Universidade de Aveiro Departamento de Engenharia Mecânica
2015

Rui Miguel Ferreira Paulo

Modelação de processos de soldadura por fricção e sua influência no comportamento estrutural de painéis reforçados em alumínio

Modelling of friction stir welding processes and their influence on the structural behaviour of aluminium stiffened panels

Tese apresentada à Universidade de Aveiro para cumprimento dos requisitos necessários à obtenção do grau de Doutor em Engenharia Mecânica, realizada sob a orientação científica do Doutor Robertt Angelo Fontes Valente, Professor Auxiliar do Departamento de Engenharia Mecânica da Universidade de Aveiro e do Doutor Filipe Miguel Horta e Vale Teixeira-Dias, Senior Lecturer, School of Engineering, The University of Edinburgh.

Apoio financeiro da FCT e do FSE no âmbito do III Quadro Comunitário de Apoio.

o júri / the jury

presidente / president

Prof. Doutora Anabela Botelho Veloso
professora catedrática da Universidade de Aveiro

Prof. Doutor Adrian Murphy
senior lecturer, Queen's University Belfast, United Kingdom

Prof. Doutor Pierpaolo Carlone
assistent professor, University of Salerno, Italy

Prof. Doutora Dulce Maria Esteves Rodrigues
professora auxiliar da Faculdade de Ciências e Tecnologia da Universidade de Coimbra

Prof. Doutor Robertt Ângelo Fontes Valente
professor auxiliar da Universidade de Aveiro

Prof. Doutor António Gil D'Orey de Andrade-Campos
professor auxiliar da Universidade de Aveiro

acknowledgements

First of all, I would like to express my sincere gratitude to Doctor Robertt Valente, my supervisor, for his friendship, support and constant optimism during all the years we worked together.

To Doctor Filipe Teixeira-Dias, my co-supervisor, for his friendship, encoragement and support.

To Doctor Pierpaolo Carlone, for receiving me at the University of Salerno, where I developed most of the experimental work. I would like to thank him for all his support and guidance.

To Doctor Antonino Squillace and his working group, for their availability during the experiments performed at the Department of Chemical, Materials and Industrial Production Engineering at University of Naples “Federico II”.

To *Fundação para a Ciência e Tecnologia, Ministério para a Educação e Ciência,* Portugal, for the support under the grant SFRH/BD/82456/2011.

To all my colleages from GRIDS reaserch group and from the Department of Mechanical Engineering, for the friendship and support.

To my friends, for all the encoragement during this journey.

To my family, for everything.

palavras-chave

Painéis reforçados, encurvadura, *Friction Stir Welding*, AA2024-T3, Método dos Elementos Finitos.

resumo

Os painéis reforçados em alumínio são os elementos básicos de muitas estruturas que requerem alto desempenho em termos da relação resistência/peso. São usados numa ampla gama de aplicações como asas e fuselagem de aviões, navios e estruturas off-shore. Os processos de soldadura por fricção tem sido usados na manufatura dessas estruturas em substituição de outras técnicas de ligação, como a rebitagem ou processos de soldadura por fusão, com inúmeras vantagens. A compreensão dos efeitos da soldadura por fricção no comportamento estrutural de painéis reforçados é uma importante área de investigação, já que permite evitar soluções conservativas na fase de projeto, frequentemente consideradas para compensar incertezas na análise estrutural.

O presente trabalho centra-se na simulação numérica do processo de soldadura por fricção, de forma a prever os seus efeitos, e na simulação numérica da compressão longitudinal de painéis reforçados em alumínio incluindo esses efeitos. O modelo numérico da soldadura por fricção foi inicialmente desenvolvido para simular a ligação de duas placas e subsequentemente validado usando dados experimentais obtidos também no âmbito deste trabalho. O modelo validado foi posteriormente adaptado para simular o processo de soldadura por fricção em painéis reforçados. Estudos de sensibilidade revelaram uma variação insignificante nos resultados provenientes de simulações que usaram diferentes distribuições de calor relativas à geometria da ferramenta. Pelo contrário, ambos os modelos mostraram grande sensibilidade às variações das condições de fronteira mecânicas que reproduziam o sistema de fixação. O modelo numérico da placa mostrou ser muito mais afetado por este parâmetro de modelação.

As simulações relacionadas com a compressão longitudinais dos painéis incluíram o estudo da influência de cada um dos efeitos da soldadura (distorção, tensões residuais e amaciamento do material) no comportamento estrutural. A modelação numérica destes efeitos da soldadura foi feita adotando duas diferentes metodologias: usando os resultados das análises numéricas do processo de soldadura por fricção; e usando uma modelação simplificada baseada na literatura. Ainda relativamente à compressão dos painéis, foram testados e comparados outros detalhes relativos à modelação, como: a metodologia numérica de resolução do problema; a definição do comportamento plástico do material e os efeitos da soldadura junto das extremidades transversais. Todos os efeitos da soldadura mencionados mostraram a capacidade de afetar o comportamento dos painéis, nomeadamente a sua carga de colapso. Finalmente, foi realizado um estudo complementar relativo as imperfeições geométricas iniciais atráves do uso configurações de deformação distintas, obtidas de análises de valores próprios e aplicadas com diferentes magnitudes. A variação da carga de colapso com o aumento da magnitude da imperfeição revelou-se dependente do padrão geométrico dessa imperfeição.

keywords

Stiffened panels, buckling, Friction Stir Welding, AA2024-T3, Finite Element Method.

abstract

Aluminium stiffened panels are the basic elements of many structures with requirements of high strength/weight ratio. They are used in a wide variety of applications such as airplane wings and fuselage, ships and off-shore structures. Friction Stir Welding (FSW) process has been used in the manufacturing of such structures as an alternative of other joining techniques, such as riveting or fusion welding processes, with many advantages. The understanding of the effects of FSW processes in the structural behaviour of stiffened panels is a relevant research area, useful to avoid conservative design choices often motivated by an attempt to compensate for structural analysis uncertainties.

The present work focus on the numerical simulation of FSW processes, aiming to predict its effects, and also on the numerical simulation of the longitudinal compression of aluminium stiffened panels, including these effects. The numerical model for FSW was firstly developed to simulate single plates' joining and subsequently validated using data from experiments, also performed in the scope of this work. The validated model was afterwards adapted to simulate FSW operations on stiffened panels. Sensitivity analyses performed showed an insignificant variation in the results coming from models using distinct heat input distributions related to the geometry of the toll. On the contrary, both models showed significant sensitivity to the variations of the mechanical boundary conditions that simulate the clamping system, although the single plate model was seen to be more affected by this modelling parameter.

The simulations regarding the longitudinal compression of the panels included the study of the influence of each one of the welding effects (distortion, residual stresses and material softening) on the structural behaviour. The numerical modelling of these welding effects was performed adopting two different procedures: using the results from FSW numerical analyses; and using a simplified methodology based on the literature. Regarding the compression of the panels, other modelling details were also tested and compared, such as: the numerical solving methodology; the plastic behaviour definitions of the material and the welding effects on the transversal edges. All the mentioned welding effects were able to affect the panel behaviour and, namely, the collapse load. Finally, a complementary study on initial geometrical imperfection was performed using distinct deformed shapes obtained from eigenvalue analyses and applied with different magnitudes. The variation of the collapse load with the increase of the imperfection magnitude revealed to be dependent on the shape of that imperfection.

Contents

List of figures

List of Tables

Chapter 1
Introduction

1.1. Overview

Stiffened panels are often the basic structural building blocks of airplanes, ships and other structures with high requirements in terms of strength/weight ratio. They typically consist of a plate with equally spaced longitudinal stiffeners on one side and often with intermediate transverse stiffeners, as represented in Figure 1.1. The cross-section of the stiffeners can have different shapes, such as blade (flat bar), T, L and box sections, only to mention some commonly used ones in aluminium structures.

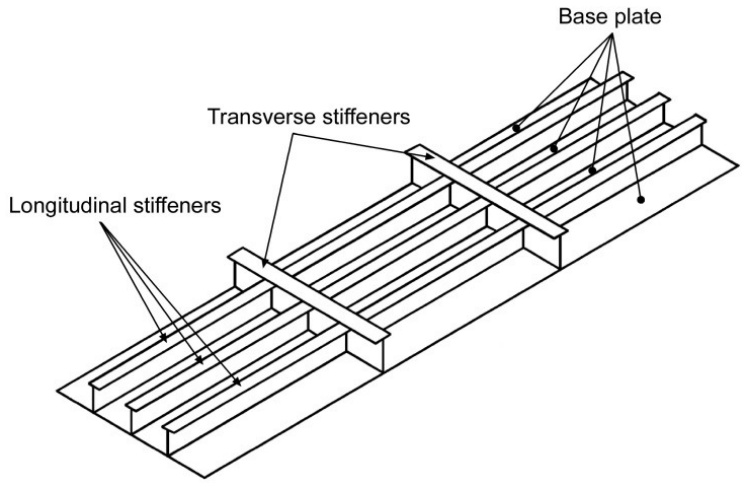

Figure 1.1: Stiffened panel.

Aluminium stiffened panels have been used in a large variety of marine structures, such as hull and decks of boats (Figure 1.2(a)), superstructures for ships, and offshore modules and containers. In airplanes, they are both used in wings and fuselage structures (Figure 1.2(b)).

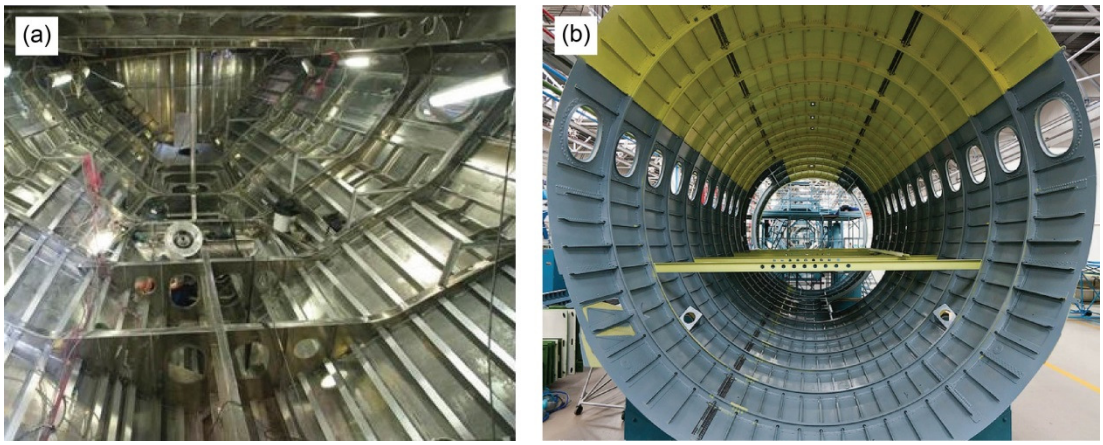

Figure 1.2: Structures including stiffened panels: (a) boat hull structure [1] and (b) an airplane fuselage [2].

These panels are primarily required to withstand longitudinal compressive forces, although transverse loads, in-plane shear forces and/or those perpendicular to the base plate, may in general also be present and interact with each other [3].

The structural stability of such thin-walled structures, when subjected to compressive loads, is highly dependent on the buckling strength of the structure as a whole and of each structural member individually. A typical load/end shortening curve, as obtained from a stiffened panel subjected to longitudinal compressive loads, is illustrated in Figure 1.3, where distinct regions are visible. The stiffness of the panel is reduced after buckling, as it enters a post-buckling regime in which a phenomenon of mode-switching may occur, with the panel changing the buckling shape patterns with the increase of the load level [4, 5]. For higher compressive forces, the ultimate load is reached with the consequent failure or collapse of the structure [6].

The manufacturing of stiffened panels often involves the use of joining processes, such as riveting and/or welding, to join the base plates, build the stiffeners and/or join the stiffeners to the base plate. An attractive solution in this field is the use of integrally stiffened panels (ISP), which are basically modular structures that include the base plate and the stiffeners in a single component, directly obtained by extrusion and/or by

machining operations. Nonetheless, joining processes are also required for the production of large parts from modular ISP.

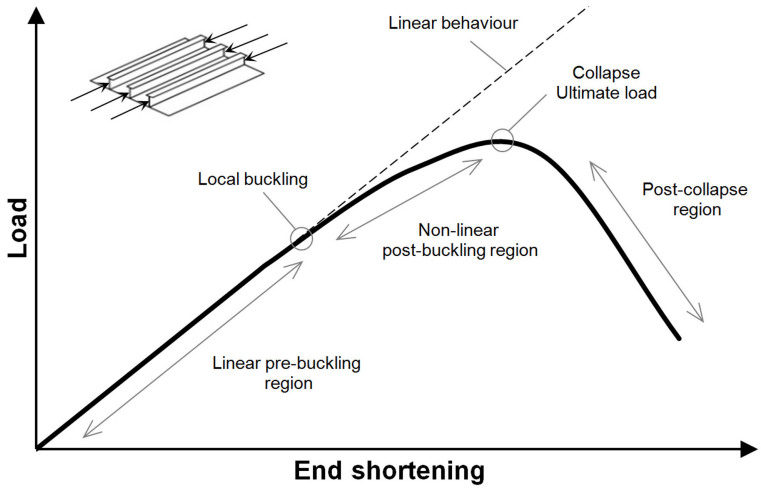

Figure 1.3: Typical behaviour of a stiffened panel subjected to longitudinal compressive load [7].

In joining processes involving welding, the heat added and conducted into the parts can influence the structural performance of the final set, since it affects the quality of the panels, namely in terms of: geometrical imperfections, build-up of residual stresses and significant changes in the properties of the materials in the welded zone. These changes are less significant for Friction Stir Welding (FSW) processes than in the traditional welding processes, like metal inert gas (MIG) welding, due to the lower temperatures involved [8, 9]. Basically, FSW is a solid-state joining process in which a rotating tool moves along the joint line, with the combined effect of heating and stirring of the material leading to a weld with high quality. Due to this, and many other advantages, FSW has been used in a wide number of applications related to the construction of stiffened panel structures [10-12].

Aluminium stiffened panels have been used for a long time in airplane structures, as aluminium alloys have been the primary materials of choice in the aeronautical industry since the 1930s [13]. Compression design methods in this field were initially based on Euler's column buckling theory, as well as on Timoshenko's theory on the elastic stability of plates and shells. Many of the initial design methodologies developed by NACA (nowadays NASA) [14-16] are still part of the current bibliography dedicated to the analyses and design of aeronautical structures [17-19].

The use of aluminium in the construction of high speed commercial and military vessels rapidly expanded since the early 1990s, mostly due to their higher strength/weight ratio when compared to steel structures [20]. Naval structural design analyses have been typically simplified and experience-based [6], mainly relying on empirical methods.

In the meanwhile, specific software packages have been developed, (*e.g.* DNV GN software [6, 21], ALPS/ULPAC [6, 22], Hypersizer [23]) in order to reduce the calculation time of ultimate loads. The EUROCODE 9 [24] and the design codes of the U.S. Aluminium Association Specifications [25] can also be used on the calculation of the ultimate strength of stiffened panels. Paik *et al.* [6] compared predictions of the compressive strength obtained using distinct methods (including some of those previously mentioned) in different stiffened panels. The predictions had a large variation for some panel geometries.

The methods listed before may have limited applicability related to: the simplicity of the boundary conditions that can be used, the constitutive models (often assumed as elastic), the geometry of the panels, and the effects of the welding processes. Therefore, the prediction of critical loads does not always show good accuracy when compared to experimental results [6]. The use of the Finite Element Method (FEM) can lead to higher levels of accuracy and generality, being *a priori* suitable for all case studies.

The FEM is a numerical method used to solve problems in different fields of engineering, including structural, heat transfer and electromagnetic analyses, being an alternative to analytical and empirical methods. It is frequently used to complement or replace complex experimental procedures, often leading to significant cost reduction.

With FEM, a given body is divided into equivalent smaller parts (the finite elements) interconnected by common points (the nodes) in a process called discretization. Then, equations that individually describe each finite element are combined to obtain a solution for the whole body.

In the context of the present work, the Finite Element Analyses (FEA) has been used in two distinct applications, by means of the Abaqus FEA package [26]. The first consists in the simulation of FSW processes to infer about the effects that can directly affect the static strength of aluminium structures. This complex process required the use of a thermo-mechanical model and material properties that were defined as temperature and temperature history dependent. The second application was the structural analysis of

stiffened panels under compressive loads, which includes an extensive study about the influence of the welding effects and modelling decisions on the simulation results.

1.2. Objectives

The understanding of the relationship between the effects of the FSW process and the structural behaviour of the stiffened panel is important to avoid conservative design, often caused by an attempt to compensate for structural analysis uncertainties. The present work focuses on the prediction of the effects of FSW and on the assessment of their impact on the structural strength of stiffened panels.

The main aims and objectives are:

- To experimentally characterize the FSW process and of the resulting welded joint;
- To develop and validate a numerical model, able to simulate the FSW process on an aluminium plate;
- To predict the effects of FSW process on the joining of stiffened panels joining using numerical simulation;
- To develop a set of structural numerical models for elasto-plastic buckling analyses of stiffened panels;
- To understand the impact of welding effects on stiffened panels' structural behaviour under longitudinal compressive loads;
- To study the influence of geometrical imperfections on the structural behaviour of aluminium stiffened panels.

1.3. Reading guide

The present work is organised in 8 chapters. In **Chapter 1** the work is introduced and the main objectives are presented. **Chapters 2** to **5** are related to the FSW process, while **Chapters 6** and **7** are related to the structural analysis of stiffened panels. Finally, the main conclusions are pointed out and possible future lines of research are suggested in **Chapter 8**.

In the **Chapter 2,** the FSW process is described and a review of the literature is presented focusing on variants of the process, their applications and effects on welded parts. **Chapter 3** describes the experimental work performed within this thesis, which included the characterisation of the welding process and welded joint. The study of the

welded joint includes: (i) residual stress field determination, using the Contour Method; (ii) microharness measurements; and (iii) observations in the microstructure. The experimental data concerning the temperature distribution during the welding process is also presented. **Chapter 4** describes the development of a numerical model, based on the FEM, able to simulate the FSW process on an aluminium plate and infer the corresponding welding effects. The validation of the model using experimental data is also described, as well as a study on the influence of different modelling approaches. **Chapter 5** focuses on the simulation of the FSW process on aluminium stiffened panels, including sensitivity analyses on some relevant modelling parameters. A description of FSW effects on panels with distinct cross-section configurations is presented. **Chapter 6** presents a literature review about the methodologies involved in the analyses of the structural behaviour of aluminium stiffened panels under longitudinal compressive loading, using the FEM. It includes a review of methods used for modelling the welding effects. **Chapter 7** presents a study about the impact of the effects of FSW on the structural behaviour of panels subjected to longitudinal compressive loads. Distinct methodologies to include the effects of the welding, as well as other modelling details, are tested and thoroughly compared. An extended study on the effects of the shape and magnitude of the geometrical imperfections is also presented.

Chapter 2
Friction Stir Welding process

The FSW process was developed and patented by The Welding Institute (UK) in 1991 [27]. It is an efficient solid-state joining technique that was initially applied to aluminium alloys. Later, its application was extended to a wide range of materials, such as titanium, copper and magnesium alloys, after developments of the tool design and optimisation of welding parameters. FSW can also be used to join parts from dissimilar metals such as: aluminium alloys from different series [28], aluminium alloy to steel [29, 30] or aluminium alloy to titanium alloy [31]. This joining technique is energy efficient, environment friendly and versatile, being considered one of the major developments in metal joining technology in recent years [11].

It what follows, the welding technique will be described in detail. Also, the main effects of the process will be presented, focusing on the welding of aluminium alloys, with a particular focus on the heat treatable ones.

2.1. Basic principles

The basic concept of the FSW process is quite simple. A non-consumable rotating tool, usually composed by a shoulder and a pin, is inserted into the adjoining edges of the plates to weld and then moved along the joint line. A photograph of the process is shown in Figure 2.1 and a schematic representation in Figure 2.2.

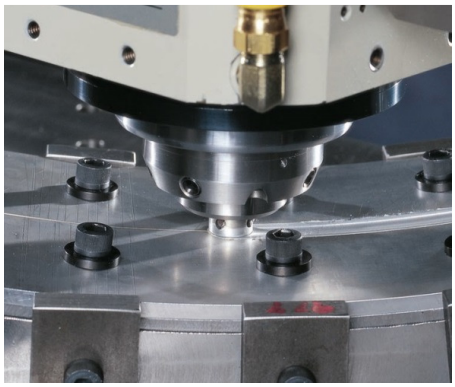

Figure 2.1: FSW of two aluminium alloy curved plates [32].

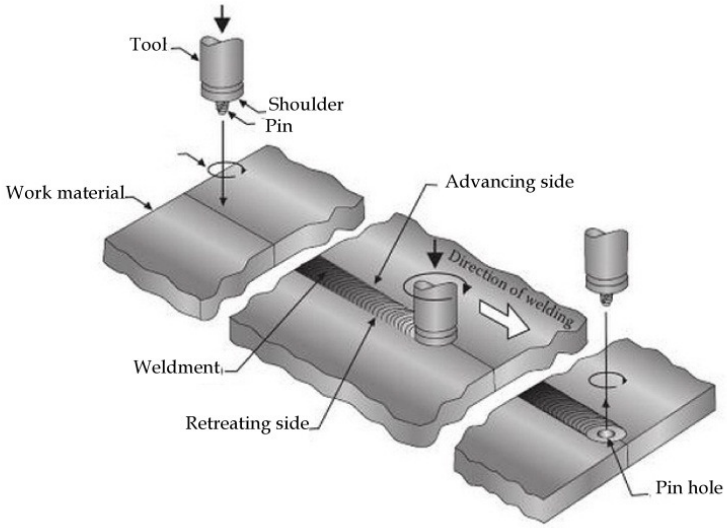

Figure 2.2: Schematic representation of the FSW process [33].

The tool has two primary functions: heating the workpiece and stirring the material. The heating is accomplished by friction between the tool and workpiece, and also by the plastic deformation of the material. Heat softens the material around the tool, while the combination of the tool rotation and translation, on its turn, leads to the movement of the material from the front of the pin (the leading edge) to its back (the trailing edge), leading to the joining of the parts.

2.2. Advantages and disadvantages

The use of FSW presents a large number of advantages when compared to alternative conventional fusion welding processes, such as:

- It allows the welding of aluminium alloys that are considered non-weldable by conventional techniques (such as, 2xxx and 7xxx series);
- Good mechanical properties of the welded zone and low distortion of the workpiece;
- Absence of melt-related defects;
- Improved safety, due to the absence of toxic fumes or the spatter of molten material;
- No consumables are needed, since no filler or gas shield is required;
- FSW can be performed using conventional milling machines, taking advantage of the lower setup costs and need of less training;
- Good dimensional stability and repeatability;
- Can be performed in all positions (vertical, horizontal, over-head and orbital) as there is no weld pool;
- Less joint preparation is needed;
- Lower environmental impact, as there is no need of shielding gases, cleaning or degreasing products;
- Lower energy consumption [10-12].

Also, there are some advantages in the replacement of fastened joints for FSW joints, namely:

- FSW can lead to significant weight and cost savings;
- The joining speed is much higher than automatic or manual riveting;
- Elimination of the stress concentration effects associated with fasteners;
- Improvement of corrosion performance;
- Elimination or minimisation of the need of sealants and locking compounds [10-12].

However, the FSW process has limitations and disadvantages when compared to other join processes, namely:

- Larger forces can be involved in FSW, with requirements for heavy-duty clamping necessary to hold the parts together;
- It is less flexible than alternative manual and arc processes, namely concerning difficulties with thickness variations and non-linear welds;
- There is an exit hole left when the tool is withdrawn [10-12].

2.3. Process parameters

Factors such as joint design, tool geometry and welding parameters have a significant effect on the material flow pattern and temperature distribution, thereby influencing the material properties of the welded parts. In order to create a sound weld, each one of these parameters has to be carefully selected and taken into account.

2.3.1. Joint configuration

FSW is applicable to a different number of joint configurations. Some of these configurations are shown in Figure 2.3. The most common ones are the square butt joint (a) and the lap joint (d). The remaining configurations can usually be produced from variations of these two.

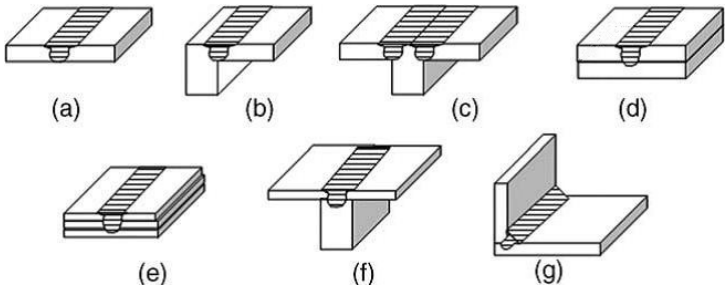

Figure 2.3: Joint configurations for FSW: (a) square butt joint, (b) edge butt joint, (c) T butt joint, (d) lap joint, (e) multiple lap joint, (f) T lap joint and (g) filled joint [11].

On a square butt joint, two plates are placed on a backing support and firmly clamped to prevent the faces to be joined from separating. The tool is plunged and afterwards moved along the weld line with the shoulder in contact with both plates. On a simple lap joint, a plate is overlapped to other and clamped on a backing support. The rotating tool is vertically plunged through the upper plate into the lower plate and moved along the desired direction [11].

A square butt FSW joint was experimentally performed and studied in detail within the scope of this thesis.

2.3.2. Tool design

The geometry of the tool is one of the most influential aspects of the FSW process, as the uniformity of the microstructure, the resulting material properties and the process loads are dependent on it [11, 34, 35].

The earliest tool designs consisted of a flat featureless shoulder and a cylindrical, sometimes threaded, pin. However, the tool geometry has evolved significantly with the increasing experience and understanding of the process, namely about the material flow. Complex geometrical features have been developed in order to alter the material flow and mixing, as well as to reduce process loads. The selection of a tool is essentially based on the configuration of the joint, the plate material(s) and thicknesses. Some distinct designs of FSW tools are shown in Figure 2.4.

Figure 2.4: Different FSW tool designs [36].

Some interesting variants have emerged with the development of the process, such as tools in which the pin and the shoulder rotate independently (including non-rotating shoulders), retractable pin tools, and bobbin tools, with a shoulder on both ends of a pin [12].

2.3.3. Welding parameters

Concerning the movement and position of the tool during welding, four parameters are often used to control the process. These are:

- The rotation speed or angular velocity of the tool;
- The transverse speed, advance speed or linear velocity;
- The penetration depth or target depth;
- The tilt angle.

The first two parameters are usually the most important in FSW. Concerning the rotational speed, higher values usually increase the temperature due to increased friction heating and more intense stirring and mixing of the material. However, it is important to mention that the heating is dependent on the frictional coupling between the tool and the workpiece. Therefore, a linear relation between the increase of rotation speed and the increase of

heating is not expected, as the coefficient of friction changes with the rotation speed of the tool [11]. In terms of the transverse speeds, higher magnitudes of this parameter tend to decrease the heat input and, consequently, the welding temperatures [37].

The target depth is associated with the pin height and is an important factor when producing sound welds. When the insertion depth is too shallow, the shoulder of the tool does not have enough contact with the workpiece surface. In this case, the welds may present inner channel(s). When the penetration of the tool in too deep, a significantly concave weld is produced leading to a local thinning of the welded plates.

Concerning the tilt angle of the tool, it is usually small and towards the trailing direction. Developments on the tool shoulder allows FSW with a 0º tool tilt, that are particularly preferred for curved joints [11].

During a FSW process the tool is subjected to significant loads. On the one hand, these forces precondition the equipment in terms of power on the machinery and strength of the used supports. On the other hand, together with the welding parameters, they affect the properties of the welded joint.

Some other variables of the FSW process are related to heating or cooling of the workpiece. Preheating or additional external heating during the FSW process can be used in materials with high melting points (such as steel and titanium) or high conductivity (such as copper). In these situations, the heat produced by the tool may not be sufficient to soften and plasticize the material and obtain a defect-free weld. In materials with lower melting point (such as aluminium and magnesium), cooling can be used to reduce the extensive growth of recrystallized grains and dissolution of strengthening precipitates around the stirred zone [11].

2.4. Process variants

Searching for new applications, low cost and better results, conventional FSW has evolved and expanded into a number of process variations, such as: self-reacting FSW (SR-FSW), stationary shoulder FSW (SSFSW), friction stir processing (FSP), friction stir spot welding (FSSW), assisted FSW and pulsed FSW. Some details and applications of these methods can be found in the literature [10].

2.5. Applications

Applications of FSW have been reported across many industries branches. The increasing versatility of FSW is a great benefit compared to other joining processes, making it suitable to be used in the manufacture of distinct products such as airplanes, cars, spacecraft, military vehicles, ships, trains and electronic devices. The main applications of the FSW are compiled in the literature [10-12]. Nonetheless, some representative examples of the use the FSW process in important areas of industry (aerospace, maritime and automotive) will be described below.

Aerospace

FSW has been widely developed and applied in the last years by the aerospace industry. One of the first implementations of this joining technology in aerospace applications dates to 1998, when NASA began to develop the process for use on the manufacture of the space shuttle main external tank. The change in the alloys of the external tank required a more robust joining process to replace Variable Polarity Plasma Arc (VPPA). FSW was used in more than 210 m of welds, with advantages in terms of repeatability and reliability. NASA continues to use FSW in the construction of hardware and it is anticipated that the next generation of heavy-launch vehicles will make extensive use of this process.

Private space companies had also adapted the FSW technology for their own space applications. United Launch Alliance uses FSW for welds on the Delta II, Delta IV and Atlas V launch vehicles. Also, both circumferential and longitudinal welds were made using this technology on the SpaceX Falcon IX. The Orion Multi-Purpose Crew Vehicle was also completed using FSW. As the market of launch services continues to evolve with entrants such as Blue Origin, Virgin Galactic and Sierra Nevada on the horizon, FSW is expected to continue to play an important role in the space vehicle industry [10, 12].

Within the context of aviation structures, FSW is also rapidly gaining acceptance of the major airframe manufacturers, often to replace riveted joints in current structures. Since the most common materials in these structures are AA2xxx and AA7xxx, the use of FSW is fundamental since they cannot be joined by conventional fusion welding, as mentioned before [10].

Eclipse Aviation makes extensive use of FSW in the Eclipse 500 business jet. In this aircraft, over 7378 fasteners (60% of the total) were replaced by 263 friction welds, in

a total of 123 m. The process enabled to construct the cabin, aft fuselage and wings. The cabin structure of the Eclipse 500 (see Figure 2.5) is built using the ISTIR Aero FSW system produced by MTS [32], show in Figure 2.6. The primary motivation for using the FSW process was that it enables joining speeds 6 times faster than automated riveting and 60 times faster than manual riveting. This factor is preponderant regarding the high volume of manufacturing of this aircraft, with more than 1500 units produced every year [10].

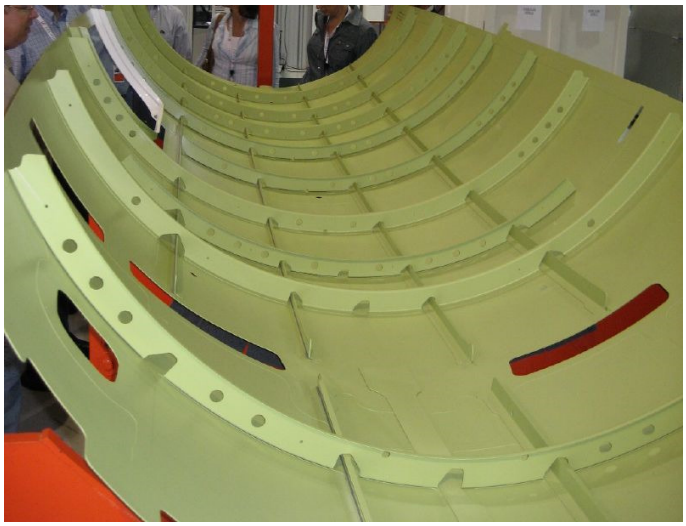

Figure 2.5: Cabin structure of the Eclipse 500 aircraft [32].

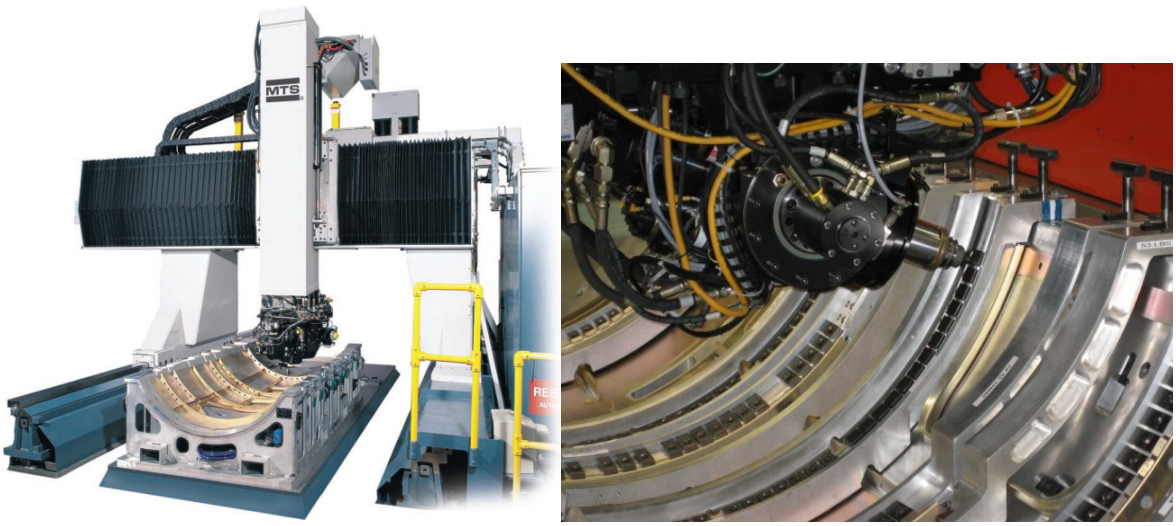

Figure 2.6: FSW setup used for the construction of the Eclipse 500 cabin [32].

Most of the commercial aerospace manufacturers have also implemented and evaluated the FSW technology. Boing has reported virtually zero defect incidence and significant cost savings over the previous VPPA process. At Airbus, FSW has replaced rivets on longitudinal fuselage skin joints and wingspans for the A340, A350 and A380 aircraft. This manufacturer is also using this welding technology on the floor panels of the A400M military aircraft. Embraer has been evaluating the FSW technology for use on the Legacy 450 and Legacy 500 models, and Bombardier tested the technology for use in the manufacture of regional aircrafts [10, 12].

Maritime

FSW has also been extensively used in commercial applications within the maritime field. The range of use includes the manufacture of fish freezing plants for fishing vessels, joining extrusions for bulkheads and decks, in various high speed aluminium vessels, and the production of large steel cruise ships, which now often include light-weight aluminium superstructures. An example of application of FSW is the cruise ship Seven Seas Navigator, which contains many kilometres of friction stir welds, mostly in 6xxx aluminium alloy extrusions. Figure 2.7 represents an example of stiffened panel profiles joined by FSW for a ship building application.

Figure 2.7: AA6062 stiffened panel profiles for ship structure joined by FSW.

The US Navy has been using FSW with AA5083, AA5456 and AA6082 parts on the construction of combat ships and vessels (see example in Figure 2.8). It was also tested for the Advanced Amphibious Assault Vehicle construction with good results in terms of final tensile strength and ductility, when compared to the gas metal arc welding process,

allowing the welded plates to withstand ballistic impact tests. The Royal Navy (UK) is also studying the FSW for military marine applications [10, 12].

Figure 2.8: Littoral Combat Ship USS Freedom, built using FSW technology for aluminium alloy joining [10].

Automotive

In the automotive sector, FSW is also becoming a widely implemented method of joining. This market has driven the development of robotic FSW to cope with complex shapes and high volume production, with low cost requirements. The investigation regarding the application of FSW into automotive manufacturing began in 1998, when The Welding Institute (TWI) partnered with BMW, Daimler-Chrysler, Ford, General Motors, Land Rover, Volvo, Tower Automotive and EWI to explore the FSW concepts applied to aluminium tailored blanks for door panels, drive shafts and space frames. Nowadays, after many advances have been made, FSW is being used to manufacture automobile parts and structures worldwide.

Mazda used FSSW on the rear door structure of the RX-8 model since 2003. Ford used the continuous FSW lap joints to construct the central tunnel of the GT model from aluminium stampings and extrusions. FSW was also used by Audi, for a similar application, in the R8 high-performance sport car. Mercedes used FSW to join the centre tunnel and the extruded aluminium floor panels of the full aluminium body of the 2012 SL model. One of the latest applications of FSW in the automobile industry was the manufacture of the engine cradle for the Honda Accord (see Figure 2.9). In this structure, aluminium and steel were joined by means of continuous FSW lap welds, resulting in a 25% weight saving [10, 12, 29, 30].

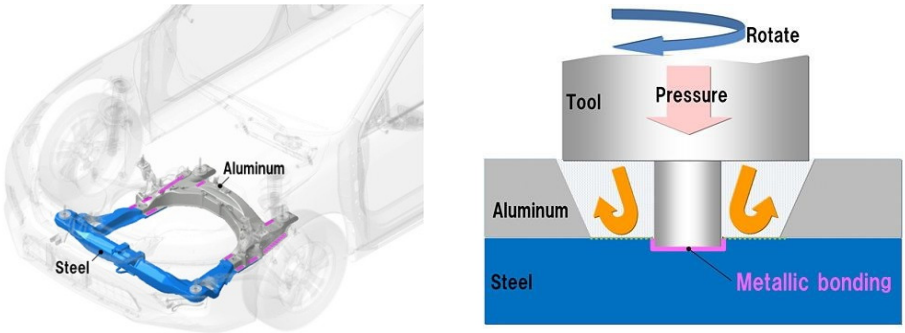

Figure 2.9: Aluminium and steel joined by FSW in the Honda Accord (welded parts marked in pink) [29, 30].

2.6. Metallurgic aspects of the FSW joint

Based on the microstructural characterisation of grains and precipitates, different areas can be found in a FSW joint: the nugget zone (NZ), the thermo-mechanical affected zone (TMAZ), the heat affected zone (HAZ) and the parent material. Figure 2.10 represents the location and microstructural aspect of each one of these zones, in a cross-section perpendicular to the weld line in a FSW plate. The macrograph shows the lack of symmetry along the centre line. A zone named “flow arm” is commonly present, in which the material was dragged across the nugget top, by the pin and tool shoulder, in the advancing side.

Nugget zone (NZ)

In this region, also denominated stirred zone or dynamically recrystallized zone (DXZ), the intense plastic deformation and frictional heating during FSW results in a recrystallized fine-grained microstructure. Under specific conditions, an onion ring pattern can be observed in the nugget zone, consisting of a banded microstructure [38].

Various shapes of the nugget zone have been observed depending on the processing parameters, tool geometry, temperature of the workpiece and thermal conductivity of the material. The size of recrystallized grains in the FSW materials is significantly influenced by the processing parameters, tool geometry, material of the workpiece, temperature of the workpiece, vertical pressure and active cooling [11]. Additionally, the grain size may have variations inside the nugget zone [39].

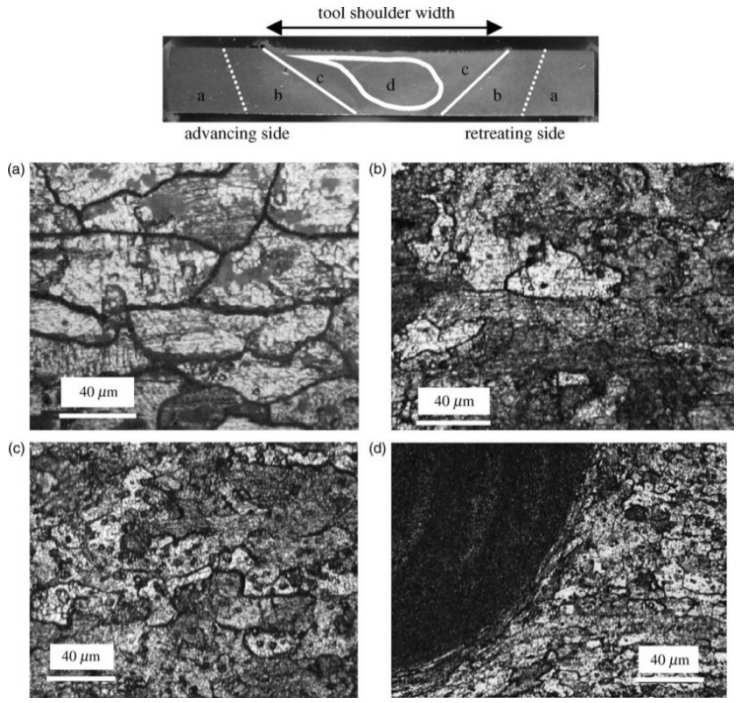

Figure 2.10: Microstructure in a AA6082-T6 transverse section, perpendicular to the welding direction, joined by FSW: (a) parent material, (b) HAZ, (c) TMAZ, and (d) nugget transition zone [40].

Thermo-mechanical affected zone (TMAZ)

In this zone the material is plastically deformed by the tool and the heat flux exerts some influence on the material. The grains become elongated, deformed in an upward flowing pattern around the nugget zone. However, although the TMAZ shows evidence of plastic deformation, recrystallization does not occur. The dissolution of precipitates happens in this zone due to the exposure to high temperatures [11, 40].

Heat affected zone (HAZ)

This zone is subjected to a thermal cycle but does not show any plastic deformation. The grain size structure is the same as in the parent material, but the thermal exposure exerts a significant effect on the precipitate structure [11, 40].

Parent material

In the parent material, also denominated base material or unaffected material, no deformation occurs and the material is not significantly affected by the heat flux in terms of microstructure or mechanical properties [40].

2.7. Properties of the FSW joint

2.7.1. Hardness

The hardness profiles across a FSW section are highly dependent on the alloy type and also on the welding parameters and tool. Figure 2.11 shows the typical hardness variation on a transverse FSWed cross-section for different aluminium alloys. Heat treatable (precipitation-hardnable) aluminium alloys, in which the strength derives from the presence of fine precipitates formed during pre-heat treatment, can be more affected by the FSW process than the non-heat-hardened (solid-solution-hardened) alloys [11]. Depending on the temperature and duration, the thermal cycles during welding can lead to precipitate coarsening or dissolution, reducing the hardness of the alloy [12]. The centre of the weld, corresponding to the nugget zone, can have higher hardness compared to the HAZ or even to the parent material. This fact can be explained by the properties of the material after recrystallization [41]. Thus, the heat treatable aluminium alloys present a W-shaped distribution on the hardness after FSW.

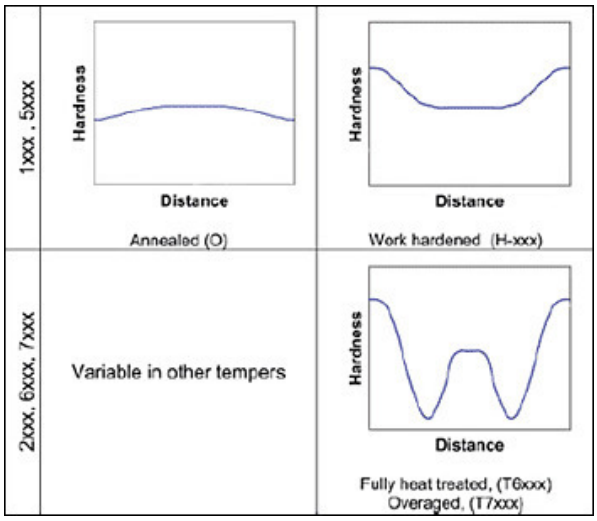

Figure 2.11: Generic hardness profiles on transverse FSW cross-sections for different aluminium alloys [12].

In heat treatable alloys, ageing is an important factor in the evolution of the hardness profile with time. It can occur at room temperature (natural ageing) or at elevated temperature (artificial ageing) and consists on the formation of extremely small uniformly dispersed particles (precipitation hardening). The precipitate particles act as obstacles to

the movement of dislocations, consequently increasing the hardness of the material. Due to a coarsening effect, which reduces the solute available for natural ageing, some permanent softening of the material occurs even after a long period [42]. Figure 2.12 represents the variation of hardness with time concerning natural ageing on a AA7075-T6 plate after FSW [43]. Similar evolution was also reported by other authors [44, 45].

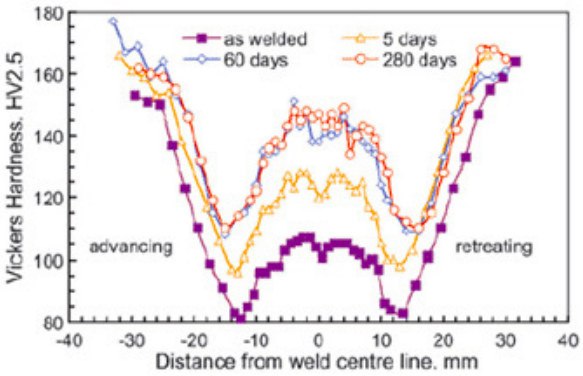

Figure 2.12: Hardness profiles variations showing natural ageing in FSWed AA7075-T6 plates [43].

2.7.2. Mechanical properties

As with hardness, other mechanical properties of aluminium alloys can be highly affected by a FSW process. Many authors (*e.g.* Genevois *et al.* [46] and Carlone and Palazzo [47]) studied the variation of some mechanical properties such as the yield strength, the ultimate strength and the elongation, after FSW processes. As an example, Figure 2.13 shows the evolution of mechanical properties in AA2024, with T351 and T6 heat treatment, and in AA5251-O. Differences between the heat treatable alloys and AA5251-O are obvious in terms of changes in properties in the welding zone. For the AA2024, the decrease on the magnitude of the yield and ultimate stresses, close to the weld centre line, is evident and significant.

As previously described for the hardness, for heat treatable alloys the mechanical properties also suffer an evolution associated to the natural ageing process. In particular, the magnitude of the yield stress (related to the hardness) increases with time due to the occurrence of precipitation processes [11, 12, 46].

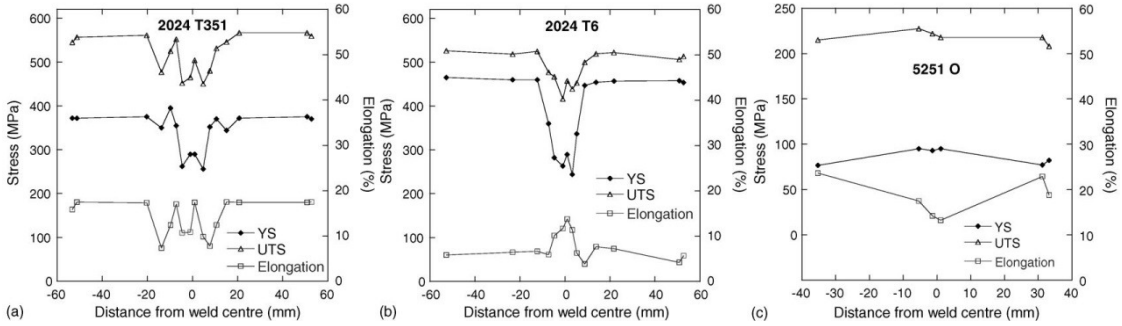

Figure 2.13: Mechanical properties (yield strength, ultimate strength and elongation) profiles for FSW aluminium alloy plates: (a) AA2024-T351, (b) AA2024-T6 and (c) AA5251-O [46].

2.7.3. Residual stresses

The measurement of FSW residual stresses is important to assess the performance of the weld, even taking into account that these stresses are usually substantially lower when compared to those from fusion welding processes. The distribution and magnitude of the residual stresses are dependent on some parameters, namely, the tool shape and dimensions, welding parameters and also the specific design of the fixing tools [48-51].

Most of the works in the literature evaluate the longitudinal residual stresses (*i.e.* parallel to weld line) in the mid-length cross-section of the welded plates (*i.e.* along a direction perpendicular to the weld line) where usually the situation can be described as steady state. In this zone the longitudinal residual stresses are typically (i) high tensile in the HAZ; (ii) tensile, but lower, in the NZ; and (iii) compressive in the region with parent material properties (beyond the diameter of the tool shoulder), as shown in Figure 2.14 for measurements performed in distinct welded aluminium alloys. Usually the maximum magnitude of the longitudinal residual stresses occurs close to the shoulder radius and is often slightly higher in the advancing side. The authors usually refer to this distribution as having an M-shape, although in some cases another peak can appear close to the weld line (*e.g.* see AA7449 curve in Figure 2.14).

In the mid-length transverse cross-section, the transverse residual stresses (*i.e.* acting in a direction perpendicular to weld line) are typically much lower when compared to the longitudinal stresses [12, 52, 53].

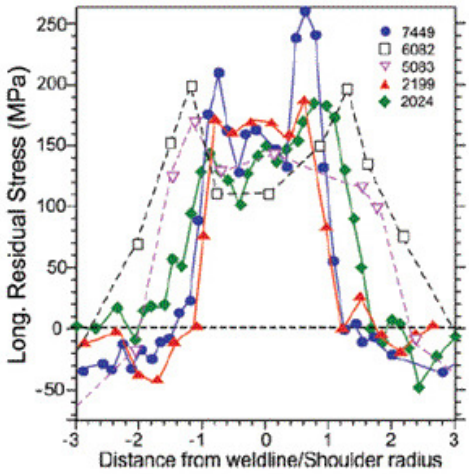

Figure 2.14: Longitudinal residual stresses profile for different aluminium alloys joined by FSW [12].

The residual stress distribution results from the differential heating and cooling rates in the welded material, in combination with changes in the material properties. In a brief explanation, the hotter region is plastically deformed in compression, due to dilatation induced by the temperature increase in the tool position. When it cools down, after the tools passes, tension stresses arise. To ensure overall equilibrium, when these tensile stresses are developed close to the weld line, they are balanced by compressive stresses in the zones farthest from the weld line. The variations in the tensile stress distribution on the tool shoulder zone are mostly related to the material changes due to heat and mechanical action of the tool. It should be mentioned that the longitudinal residual stresses originated from a FSW process usually have a variation along the plate length [52, 53] and also across its thickness [28, 50, 54].

Measurement of residual stress

The methods that allow measuring the residual stresses, in particular macro-residual stresses (often referred as type I), may be classified as destructive, semi-destructive or non-destructive.

The destructive and semi-destructive techniques, also called mechanical methods or stress-relaxing methods, are dependent on inferring the original stress from the displacement incurred by completely or partially relieving the stresses by removing material. The main mechanical methods used to measure residual stresses are: the hole-drilling technique (semi-destructive), the ring-core method (semi-destructive), the deep-

hole method (semi-destructive), the sectioning technique (destructive) and the Contour Method (destructive).

Non-destructive methods include: the x-ray diffraction method, the neutron diffraction method, the ultrasonic method, the magnetic method and Barkhausen noise techniques. The non-destructive techniques usually measure some parameter that is related to the stress. They allow, for example, to assess the fatigue related damage that becomes increasingly important in many structural components, such as bridges or airplane structures, which need to be periodically inspected.

Further details, range of application and comparison between the measurements performed with each of these methods can be found in the literature [55, 56]. The Contour Method, described in detail in section 3.2, is used within the scope of this work to determine the residual stresses in FSWed plates.

2.7.4. Flaws in FSW

The most common flaws from FSW process are related to the use of under-optimised parameters, ineffective tool design or lack of process control [12]. A typical flaw is the formation of voids, which can occur at different locations and have different shapes. Another typical flaw is named “kissing bond”. It consists of two surfaces lying extremely close but not close enough for atomic bonds to be created. Depending on their location and extent, they may have detrimental effects on the fatigue life and through thickness load capacity [57].

Also the bad quality of the surface after FSW may be considered a flaw since it can significantly deteriorate the fatigue strength [11]. Obtaining a smooth welded surface, with lower tendency for crack initiation, is known to be highly dependent on the welding parameters [50, 58, 59].

2.7.5. Distortion

The differential on plastic strains during the FSW process, and the resulting residual stress fields, are responsible for the global distortion of the welded structure. An inverted saddle shape is typically obtained (as shown in Figure 2.15), consisting of a shape that is concave along the direction perpendicular to the weld line (usually a V-shape) and convex in the longitudinal direction, being reported in works that experimentally measured the out-of-

plane displacement after the FSW process [60, 61]. Nonetheless, other shapes have been reported, as the distortions in the plates prior to the welding process also influence the final assembly shape. The distortion should be minimised in the welded parts, since it can influence the strength of the structures, namely when buckling effects are involved [7, 62].

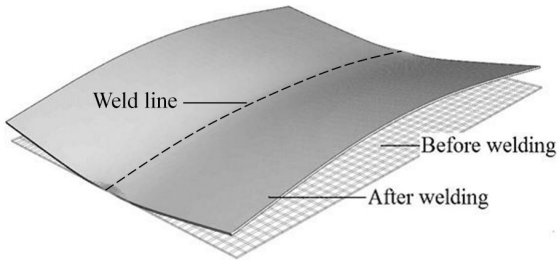

Figure 2.15: Typical distortion shape in a plate after the FSW process (adapted from [60]).

Chapter 3

Experimental characterization of Friction Stir Welding

In the present experimental procedure, two plates were joined using the FSW process. Afterwards, the characterisation of the welded plates was made in terms of residual stresses (using the Contour Method), microstructure and hardness. Relevant data concerning the temperature distributions during the welding process was obtained from the literature [63]. The main purpose of the experimentally obtained results was to use them in the validation of a numerical model for the FSW process simulation.

3.1. Experimental FSW join procedure

Two AA2024-T3 rolled plates, shown in Figure 3.1, were joined using the FSW process. The nominal composition of the plates' material is provided in Table 3.1. Each plate had initial dimensions of $194 \times 30 \times 4$ mm^3, with the final welded plate having a width of 60 mm.

The welding operation was executed on a MCX 600 ECO machining centre. The adopted HSS unthreaded tool, with its dimensions, is represented in Figure 3.2.

Figure 3.1: AA2024-T3 plates to be welded.

Table 3.1: AA2024-T3 nominal composition (% wt).

Al	Cu	Mg	Mn	Si	Fe	Zn	Ti	Cr	Others (total)
90.7 - 94.7	3.8 - 4.9	1.2 - 1.8	0.3 - 0.9	max 0.5	max 0.5	max 0.25	max 0.15	max 0.1	0.15

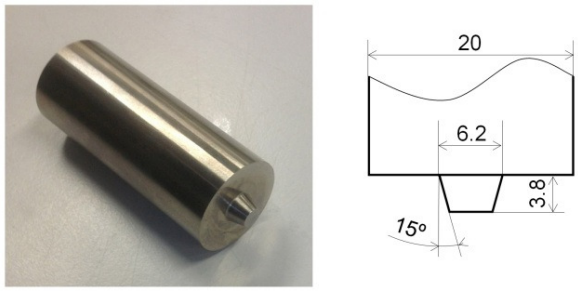

Figure 3.2: Tool used in the FSW process (dimensions in mm).

The optimum welding parameters were selected based on preliminary tests and studies reported by Carlone and Palazzo [47, 50, 63]. The tilt angle and penetration depth were defined as 2° and 0.2 mm, respectively. Additionally, an angular tool velocity of 1400 rpm and a linear velocity of 70 mm/min were used. On the one hand, and according to these studies [47, 63], the use of lower angular tool velocities can lead to some internal defects in the joint, such as voids and kissing bond effects, typically related to insufficient material stirring and lower process temperature. On the other hand, the use of higher angular tool velocity increases the temperature during the welding process and therefore has more impact in the material properties.

The correct positioning of the plates during the welding procedure was ensured by the clamping system shown in Figure 3.3. The welding process can be seen in Figure 3.4 while Figure 3.5 represents in detail the surface aspect after the tool passage.

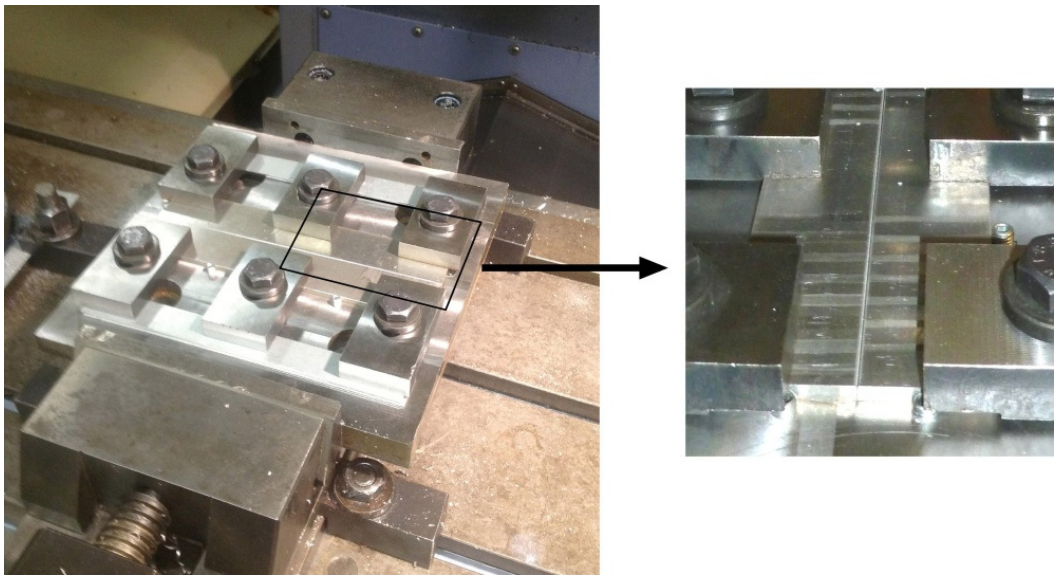

Figure 3.3: FSW experimental setup regarding the plates' clamping system.

Figure 3.4: FSW process.

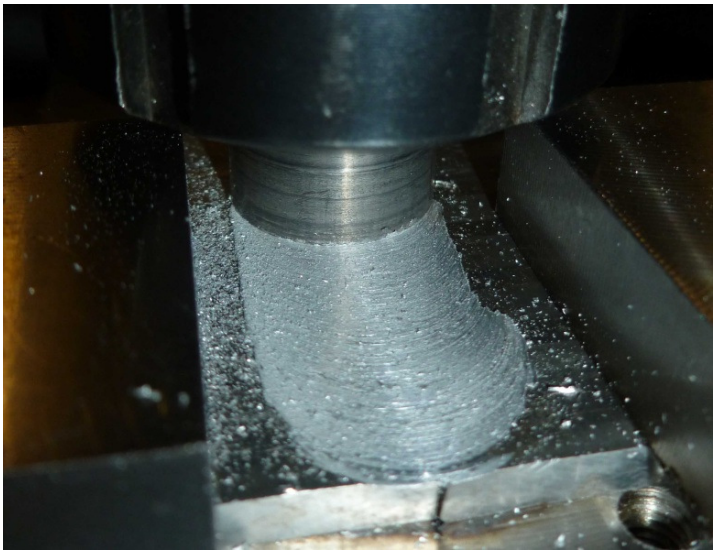

Figure 3.5: Detail of the surface of the plate after the passage of the tool.

As shown in Figure 3.6, the tool was plugged into the weld line, with the tool centre positioned at approximately 10 mm from the transverse edge of the plate. This position corresponds to the shoulder limit matching the beginning of the plate. The tool moved along the joint line until the shoulder reaches the other transverse edge of the plate. Therefore, the tool travelled approximately 174 mm along the joint line.

It is important to mention that the nomenclature shown in Figure 3.6 will be used in what follows, regarding the directions, positions and edges.

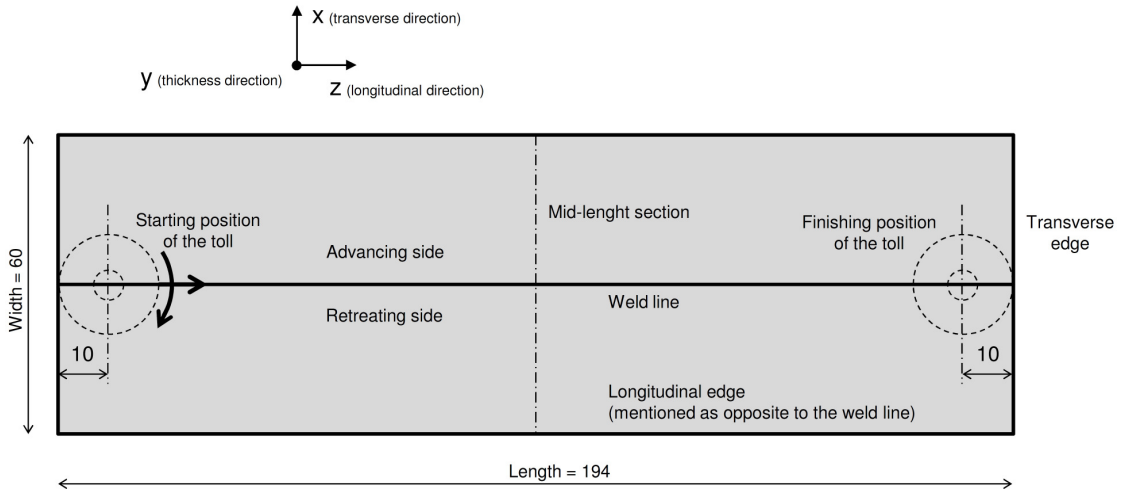

Figure 3.6: Schematic representation of the experimental FSW process and used nomenclature.

Figure 3.7 shows the welded plate after the FSW process before its removal from the clamping system. In this image it is possible to see the exit hole (top left corner) created after the tool exit. The welded plate was removed from the support after a cooling stage of about 15 minutes.

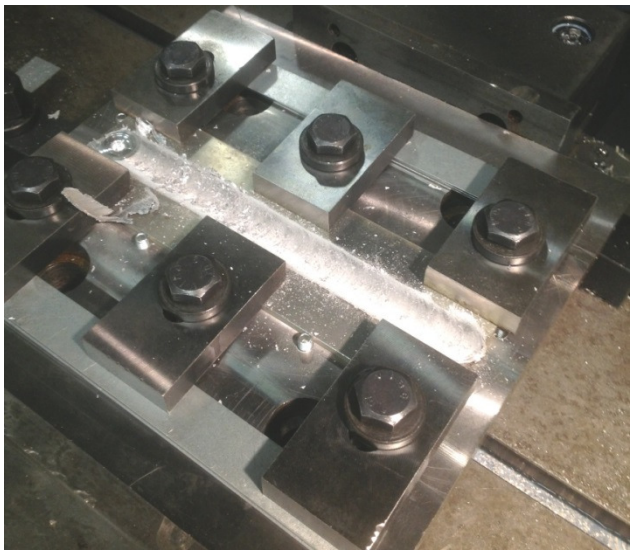

Figure 3.7: Plate after the welding process, before being removed from the support.

3.2. Residual stress measurement by the Contour Method

The Contour Method is a relaxation method introduced by Prime [64] that allows the evaluation of the residual stress field in a cutting plane of a given specimen. A complete map of the normal stresses in this plane can be obtained with this method. It was successfully applied in the measurement of residual stresses in the cross-sections of FSWed plates by several authors [50, 51, 54, 65]. This measuring technique is relatively simple in experimental terms and the required equipment is widely available in engineering laboratories. The basic theoretical principles of this method, following the complete description proposed by Prime [64], and also the experimental application are presented below.

3.2.1. Contour Method: principles

The Contour Method is based on a variation of the Bueckner's superposition principle [66]. Figure 3.8 represents this principle in two dimensions, for simplicity reasons, although it can be equally applied in three-dimensional cases. Figure 3.8(a), step A, represents the undisturbed part containing the residual stresses to be determined. In Figure 3.8(b), step B, the part was cut in two and deformation occurs due to the relaxation of residual stresses after the cut. In Figure 3.8(c), step C, the free surface created by the cut is forced back to its original shape (a straight line). Superimposing the stress state in B with the change in stress resulting from step C, originates the original residual stresses throughout the part, assuming the absence of plasticity.

As performed in the Contour Method, the shape of the free surface in step B is measured after the cut. The surface is then forced back to its original position, although, since the stresses in B are unknown, it is not possible to determine the original stresses throughout the body. However, since the normal stresses in the free surfaces in step B are null, in step C it is possible to determine the normal stresses (σ_z) along the cutting plane. [55, 64]. The boundary conditions in step C consist on displacements on the cutting plane, with the remaining boundary conditions being imposed only to avoid rigid body motions.

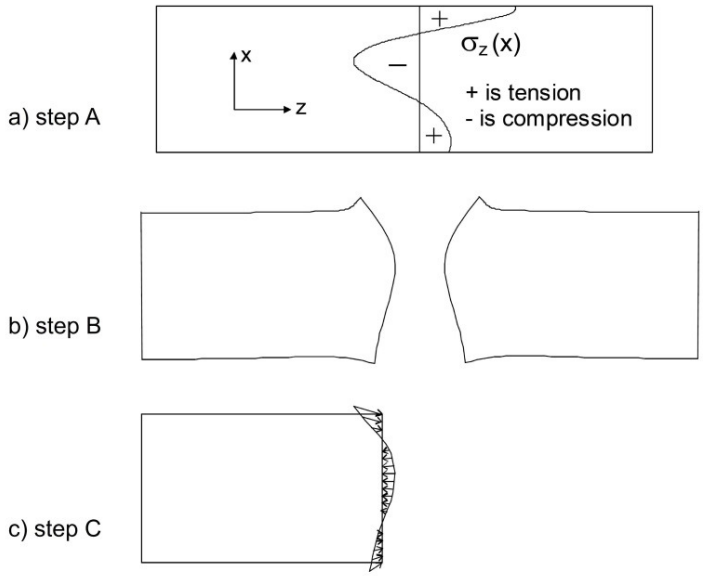

Figure 3.8: Superposition principle used to calculate a residual stress field: (a) original residual stress distribution, (b) profiles after the part is cut, and (c) force field necessary to bring the cut surface to the undeformed position (adapted from [64]).

Bueckner's superposition principle also considers that any residual stresses away from the cutting plane, as well as the stress components, σ_x, σ_y, and τ_{xy}, acting on the cutting plane, will not influence the deformations in the cut part (represented in B). Therefore, it is assumed that these stresses will not lead to errors in the Contour Method measurements [64].

3.2.2. Contour Method: assumptions and approximations.

The superposition principle assumes that (i) the material behaves elastically during the relaxation of the residual stresses and that (ii) the material removal process, during the cut, does not introduce additional stresses of sufficient magnitude to affect the measured displacements. These two assumptions are common to other relaxation methods.

Additionally, the cut must occur along a flat plane (concerning the original configuration). As the body slightly deforms when stresses are released during cutting, the validity of this assumption can be argued even if the cut is perfectly straight. However, Prime [64] showed that the flat cut assumption can be seen as reasonable if the specimen is adequately constrained during cutting.

It should also be mentioned that the Contour Method only allows measuring the normal stresses, perpendicular to the cutting plane, not the shear stresses. The measurement of the surface contour only provides information about the displacements in the normal (Oz) direction, not those in the transverse (Ox) direction (and Oy direction for the 3D case). Therefore, there is an approximation comparing to what is shown in Figure 3.8(c). The surface will be forced back to its original configuration only in the Oz direction, leaving the Ox displacements (and Oy direction for the 3D case) unconstrained. If the residual shear stress component, τ_{xy} (and τ_{xz} for the 3D case), was originally zero along the cutting plane, the calculated stresses would be correct. In the general case, when shear stresses are present on the cut plane, it is necessary to first average the contour measured on the two halves represented in B to correctly determine the normal stresses (σ_z). Prime [64] demonstrated that this approximation is reasonable and that the averaging procedure can correctly handle the shear stress field.

3.2.3. Experimental application of the Contour Method

In the present work, the Contour Method has been applied for the measurement of the normal residual stresses in the mid-length section of the welded plate, perpendicular to the weld line, according to the following consecutive steps:

i) cutting of the welded specimen;

ii) shape acquisition;

iii) data processing;

iv) stress computation.

Each one of these steps is described in detail in the following paragraphs.

Cutting of the welded specimen

The cutting step is crucial in the implementation of the Contour Method, since subsequent procedures and final results are dependent on how well this step is performed. The capacity to correctly infer the normal stress field requires that the cutting process respect some pre-requisites to avoid, or at least to reduce, posterior measuring errors: (i) the cut should be flat with a high quality surface finish, which requires a proper constraint during the specimen cutting; (ii) the cut thickness should be constant and as small as possible, requiring a cutting process that minimises the effects on pre-existing stresses.

The technology most suitable to accomplish this step is the Wire Electro Discharge Machining (WEDM), which uses electric discharges (spark erosion) instead of mechanical tools to remove the material. This cutting process is a noncontact one, avoiding the plastic strain from the large contact forces originated in conventional machining [50, 55, 64]. Following these requirements, and within the present work, the cutting of the welded plate was performed using a Mitsubishi FA-20 WEDM equipped with a 0.25 mm diameter cooper wire. To avoid thermal deformations, the cut was performed in a temperature controlled deionized water bath. Skim-cut parameters have been used to minimise effects on pre-existing stresses. Also, efforts were made to properly constrain the movements, in both longitudinal ends of the plate, to ensure a good quality of the cut. The experimental apparatus used for the specimen cutting is shown in Figure 3.9 and the resulting cut parts are shown in Figure 3.10.

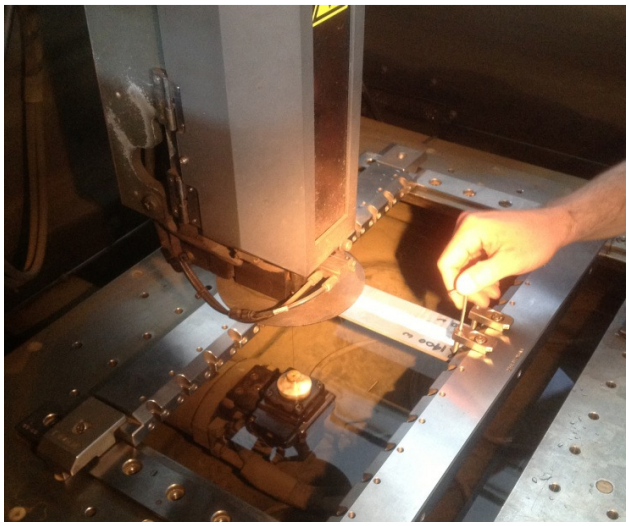

Figure 3.9: Fixing of the plate for posterior cutting using WEDM.

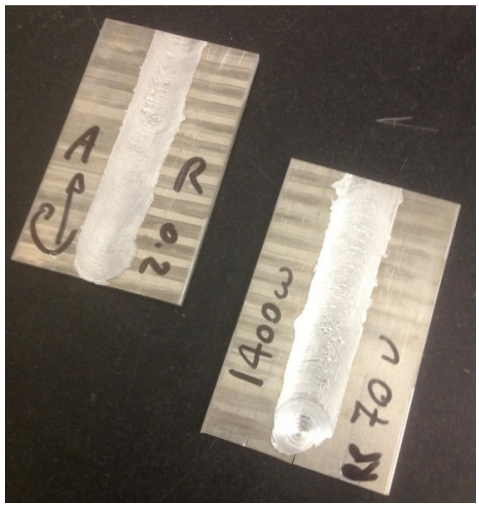

Figure 3.10: Plate parts after cut.

Shape acquisition

After the sectioning process, the residual stresses relaxation leads to a dimensional distortion on the cut surfaces. Following many works that apply the Contour Method (*e.g.* [50, 54, 67]), the out-of-plane displacements were acquired using a Coordinate Measuring Machine (CMM), in this case a Dea Image Global Clima. The resolution of this equipment is 0.1 µm, and the machine was equipped with a contact probe with a 30 mm height steel stylus and a 3 mm ruby pin (see Figure 3.11). Each acquisition was preceded by a machine-probe system calibration to properly compensate stylus deflection. A measurement grid with 0.25×0.25 mm^2 was programmed in a reference coordinate system

associated with the sample, shown in Figure 3.11, resulting in approximately 4100 data points. Both surfaces (corresponding to the two sides of the cut part) were measured since, as aforementioned, the eventual presence of shear stresses should be compensated by averaging the contour displacements from opposite parts. Figure 3.12 represents the measurements results for both surfaces (that will be mentioned as part A and part B).

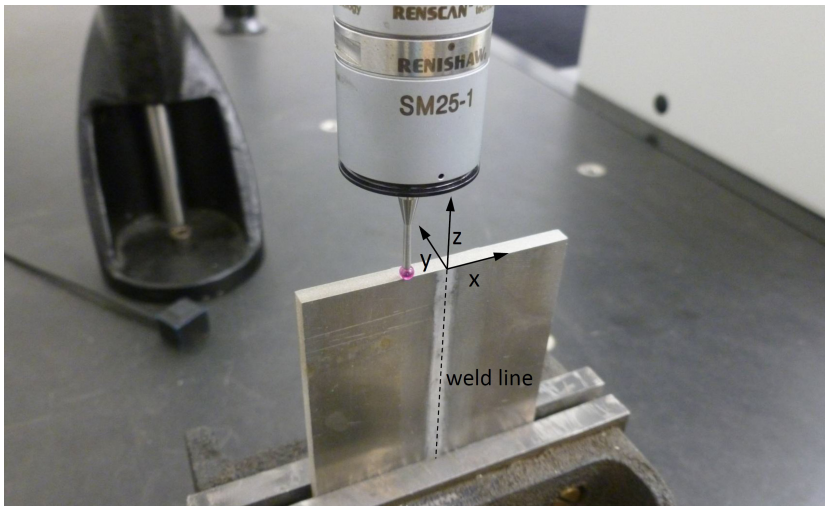

Figure 3.11: Surface acquisition using a CMM and the reference coordinate system used.

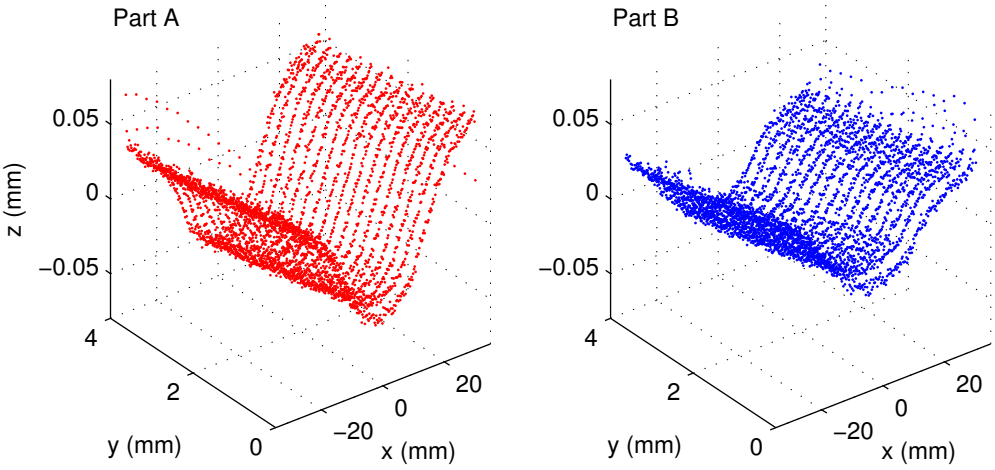

Figure 3.12: Surface profile measurement in both sample surfaces.

Data processing

The data processing included several steps, performed using MATLAB software, which are briefly described in the following paragraphs.

The first step consisted in obtaining the base plane for each one of the measured surfaces that allowed eliminating any rotation effects. After that, the average shape of the two surfaces was calculated, as shown in Figure 3.13. Since the position of each point (*Oxy*) may not coincide in the two surfaces, interpolation was used to match the theoretical position before averaging. The differences in the shapes of the two surfaces are significant, resulting from the existence of shear stresses and, possibly, associated with slight deviations during the cut. Variations with similar magnitude have been reported by other authors [54, 65, 67] in measurements performed on welded plates.

Finally, the averaged results were filtered in order to obtain a smooth surface, as shown in Figure 3.14, thus eliminating irregularities associated with roughness and measuring errors.

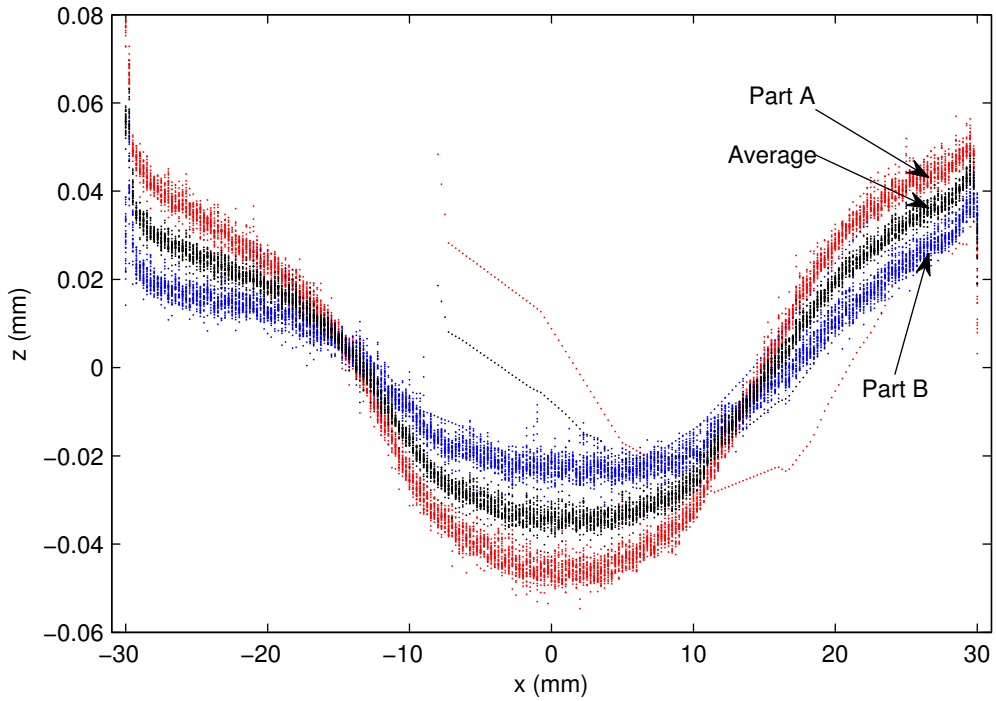

Figure 3.13: Displacement obtained from both surfaces measured and average (all values along *Oy* direction are shown).

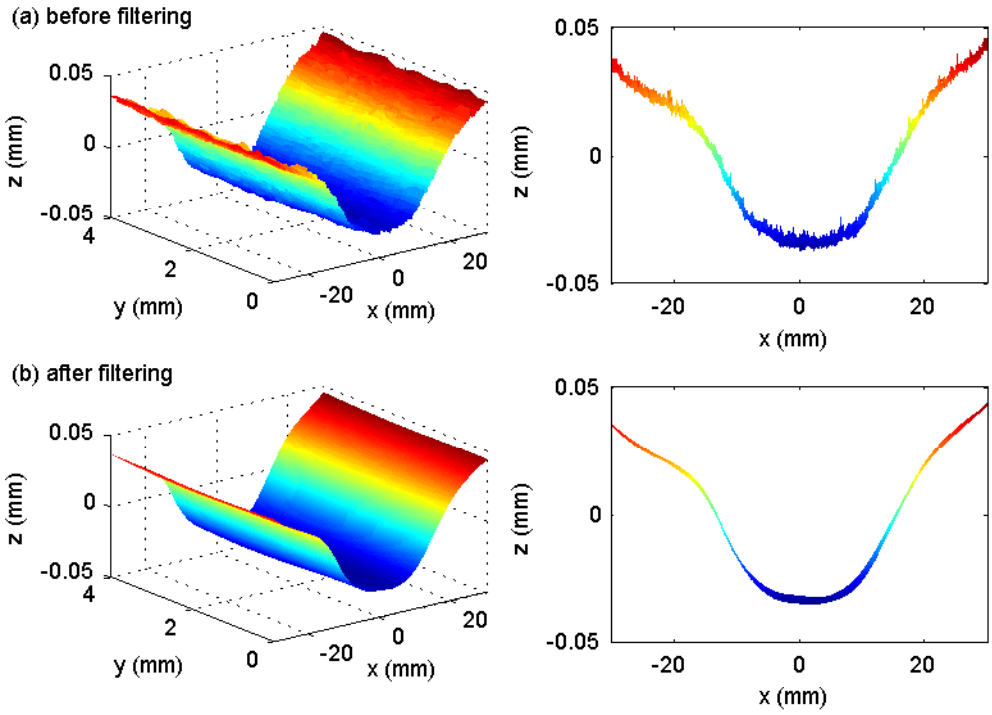

Figure 3.14: Displacement surface (a) before and (b) after filtering.

Residual stress computation

The last step of the Contour Method involves the use of the FEM to compute the residual stresses from the displacements obtained after the data processing. The commercial FEM software ANSYS [68] was used to solve the linear elastic problem, with the material properties defined in the model as corresponding to the parent material.

The discretization of the model, corresponding to half-length of the welded plate, was made using a SOLID185 formulation (solid hexahedral elements with 8 nodes and 3 degrees of freedom per node) [68]. Concerning the mesh, all the elements have a dimension of 0.5 mm along the Ox and Oy directions. Thereby, a mesh with 8×30 elements, with 9 layers of nodes across the thickness, was used on the cutting plane surface. Concerning the Oz direction, the elements have a length of 0.5 mm close to the face where the displacements were applied, and become progressively more slender moving away from that face, as shown in Figure 3.15.

The displacements, with reversed sign, were directly applied to the nodes of a model of the plate with flat faces, as shown in Figure 3.15. This procedure is commonly used in the Contour Method [28, 50, 54, 64, 69] since it is less labour-intensive when

compared to creating the deformed model and forcing the relaxed surface to become flat. The displacement of the nodes induced a stress field in the plate, as shown in Figure 3.16, where the longitudinal stresses at the top surface were the ones intended to be measured.

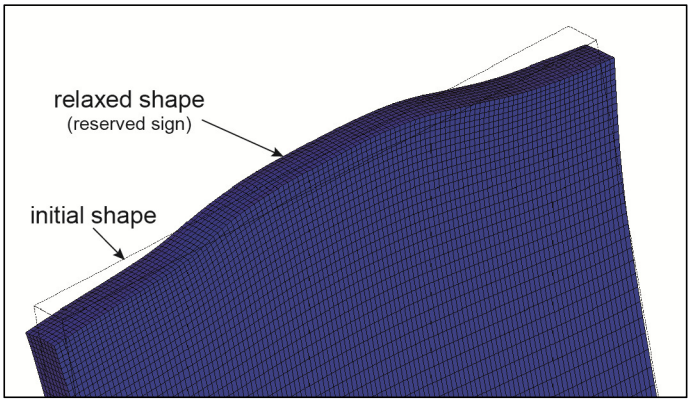

Figure 3.15: Initial shape and finite element mesh after displacement input.

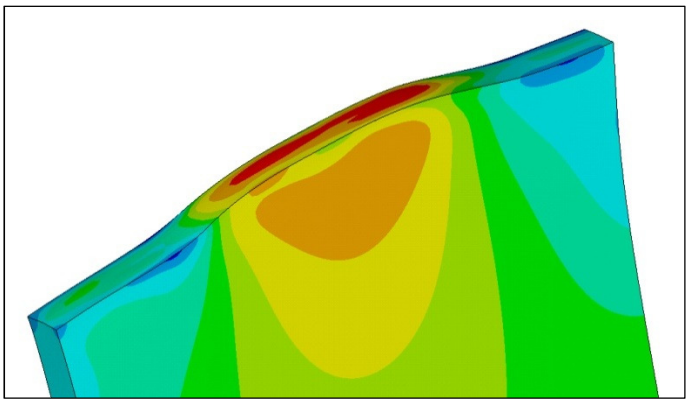

Figure 3.16: FEM results for the longitudinal stress distribution.

3.2.4. Final results

Figure 3.17 represents the distribution of the longitudinal residual stresses (*Oz* direction) on the mid-length cross-section, and Figure 3.18 shows the detailed stress profiles along the thickness of the plate, with the several *Oy* lines corresponding to the nodes' *Oy* positions. The averaged values across thickness were calculated and are also shown (solid thick black line). As can be seen, the experimental results follow the typical M-shape distribution, with two stress peaks within the tool shoulder area. As often happens in FSW joins, the longitudinal stress magnitude is slightly higher in the advancing side.

The maximum stress is 163 MPa and the maximum in the average profile is 124 MPa. There is an expected variation across thickness [50, 51, 54, 65].

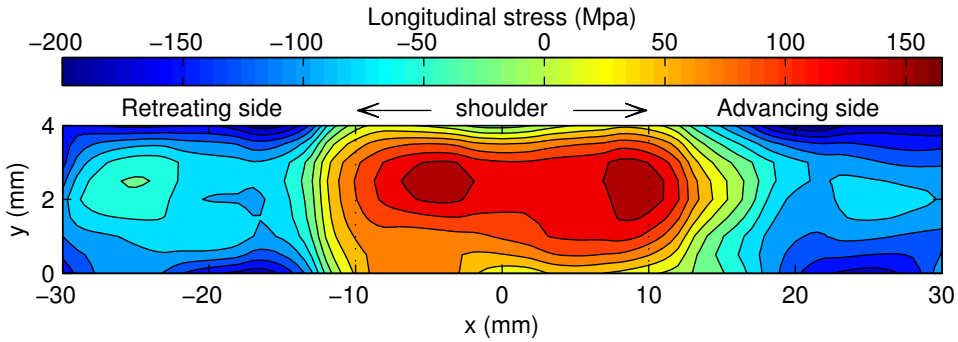

Figure 3.17: Longitudinal residual stress map (σ_z) on the cross-section of the plate, obtained by the Contour Method.

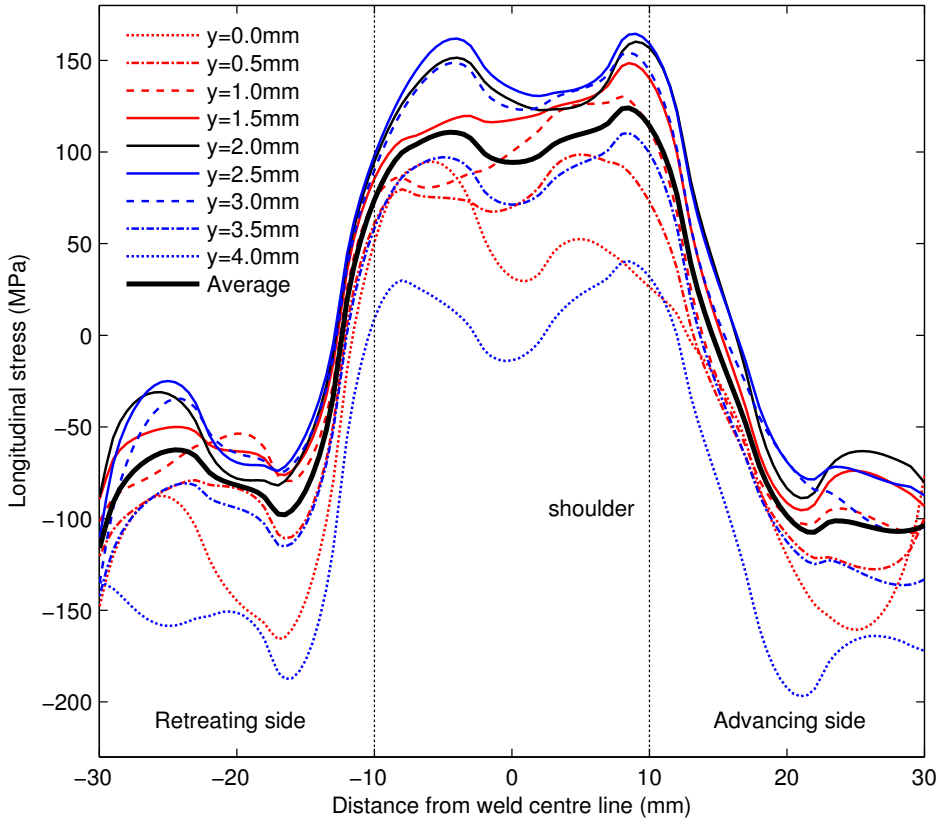

Figure 3.18: Longitudinal residual stress profiles (σ_z) obtained by the Contour Method for different positions across thickness and respective average across thickness.

3.3. Temperature distribution during the FSW process

The information about the temperature distribution during the welding process is important for the development and validation of a FSW numerical model, although it was not possible to obtain this data during the experiments performed. However, relevant data was provided by Carlone and Palazzo [63] using a sample of the same material with the same width. The machine and the tool used were also the same. The temperature measurements were achieved using an IR thermal-camera (see Figure 3.19), and the measured temperature profile, along the weld centre line in the trailing side is represented in Figure 3.20.

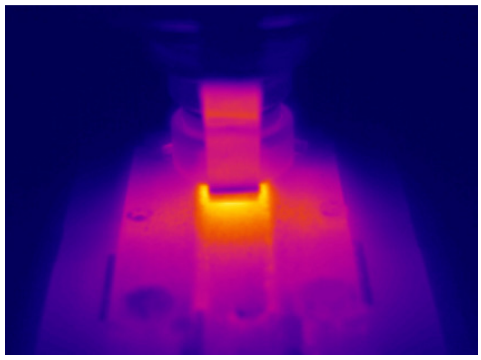

Figure 3.19: Thermography image of the FSW process [63].

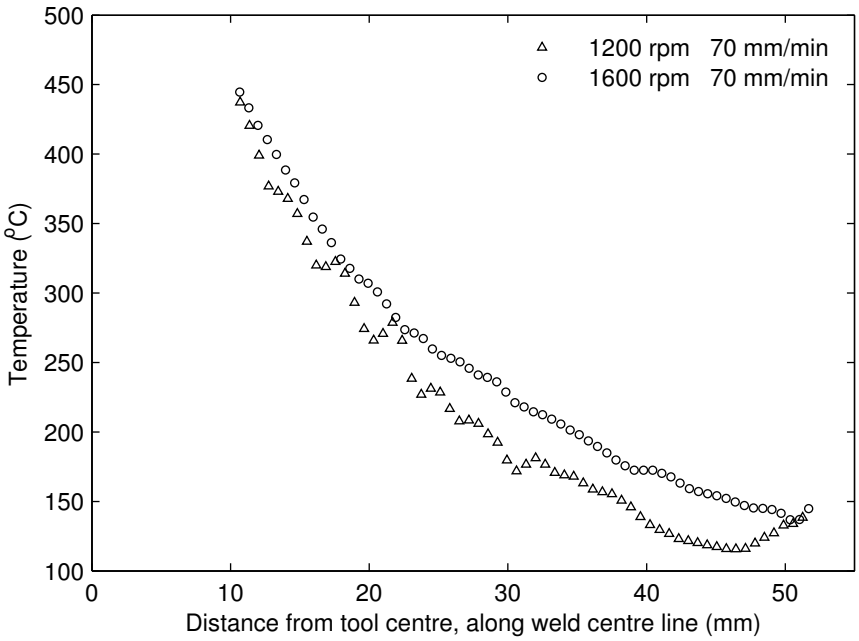

Figure 3.20: Temperature profile along the weld line, in the trailing side [63].

Unfortunately, results for the same combination of welding parameters used in the present work (1400 rpm and 70 mm/min) were not available. However, those authors [63] presented results for higher (1600 rpm) and lower (1200 rpm) angular tool velocities, with the same linear speed (70 mm/min), tilt angle and penetration depth. The expected temperature profile for the current welding parameters should fit between the two available profiles.

3.4. Hardness measurement

Vickers micro-hardness measurements were carried out after 1 year of natural ageing. They were performed in the same samples and cut surfaces used for the residual stress measurement, *i.e.,* located at mid-length of the plate. Since the surface obtained from the WEDM was too rough for the micro-hardness determination, the samples were previously prepared using a sequence of abrasive disks.

A LEICA VMHT AUTO micro-hardness tester was used for the measurements. The equipment was set-up with the following parameters: load of 200 gf (1.96N), loading time of 15 s and an indentation speed of 60 μm/s.

The hardness was determined in the mid-thickness of the samples, covering all the width (60 mm), using a distance of 1 mm between each measured point. After each indentation, the size of the diagonals were measured and used to determine the harness by means of the software provided by the equipment manufacturer. The procedure was performed on both sides of the cut plate (see Figure 3.21(a)) and, after that, the average values for each location had been calculated, with the results being presented in Figure 3.21(b). The hardness profile follows the typical W-shape (Figure 2.12), characterised by a decrease of the hardness in the HAZ, and an increase at the centre of the joint, due to the particular properties in the TMAZ and NZ.

3.5. Microstructure observation

A sample was cut from the mid-length zone of the plate with 32 mm width (transverse direction), centred in the weld line, and 8 mm long (longitudinal direction). This sample was mounted in a mixture of epoxy resin and copper, allowing electric conductivity.

Afterwards, it was metallographically prepared according to standard preparation technique using grinding and polishing, followed by etching to reveal the microstructure.

A macrograph image collected from the sample is presented in Figure 3.22, showing the typical aspect obtained after FSW and no macroscopic defects in the joint. The first observations were performed on a Leitz Weslar optical microscope. After, detailed observations were done in a Hitachi TM300 Scanning Electron Microscope (SEM). This microscope was equipped with a National Instruments Energy-Dispersive X-ray Spectroscopy (EDS) detector, which allows for an evaluation of the composition of the material in specific zones of the sample.

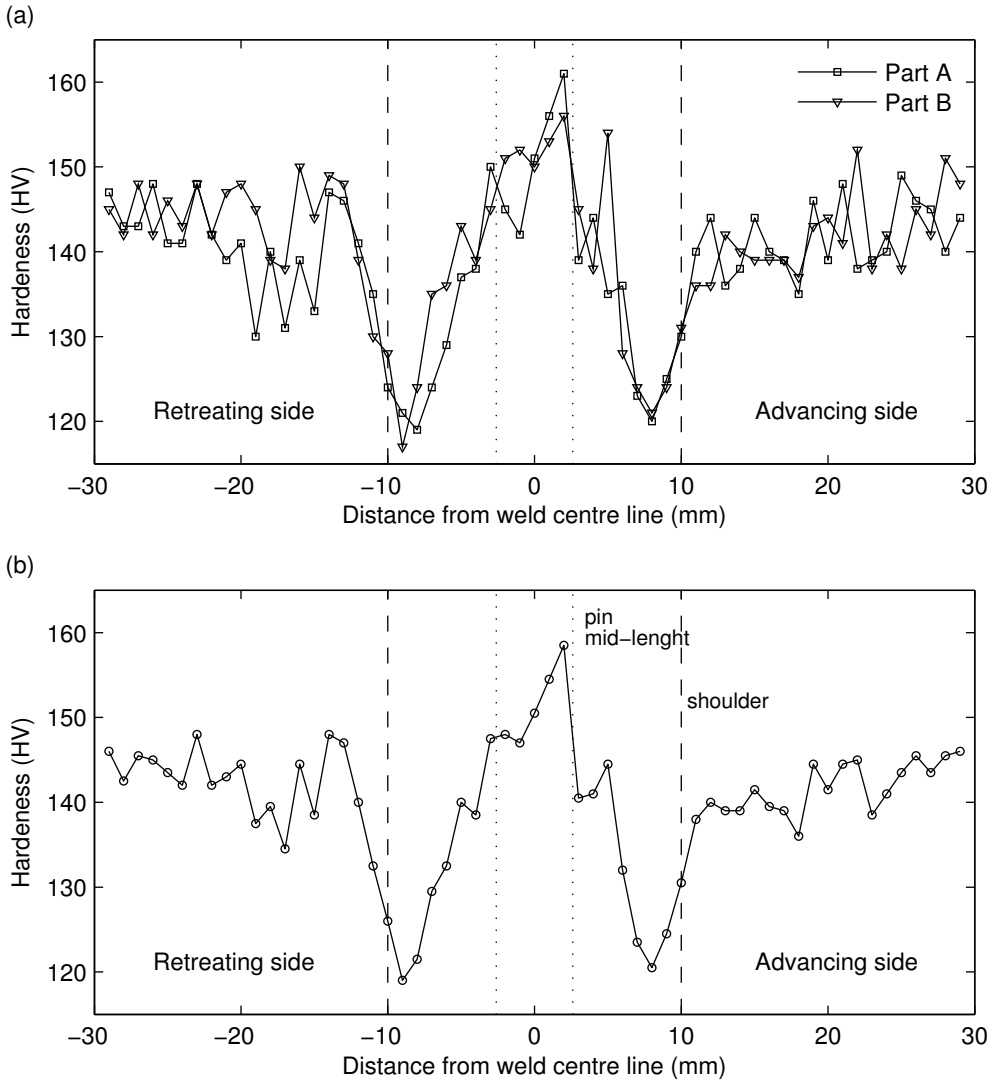

Figure 3.21: Micro-hardness profile along the width of the plate (mid-thickness): (a) measurements in each part, and (b) averaged values.

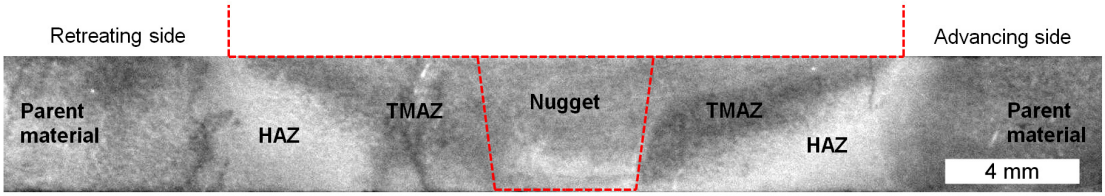

Figure 3.22: Macroscopic image of the transverse cross-section of the welded plates (tool position represented in red).

The microstructure observations from the optical microscope and SEM are shown in Figure 3.23 and Figure 3.24, respectively. In the parent material and HAZ it is possible to see a similar microstructure, with elongated grains along the rolling direction (horizontal direction in Figure 3.23). The NZ is characterised by a smaller grain size. Furthermore, in Figure 3.24, it is possible to observe bands in the microstructure. Analyses performed with the EDS detector revealed a high percentage of copper in the light-coloured lawyers, corresponding to a concentration of the major allowing element.

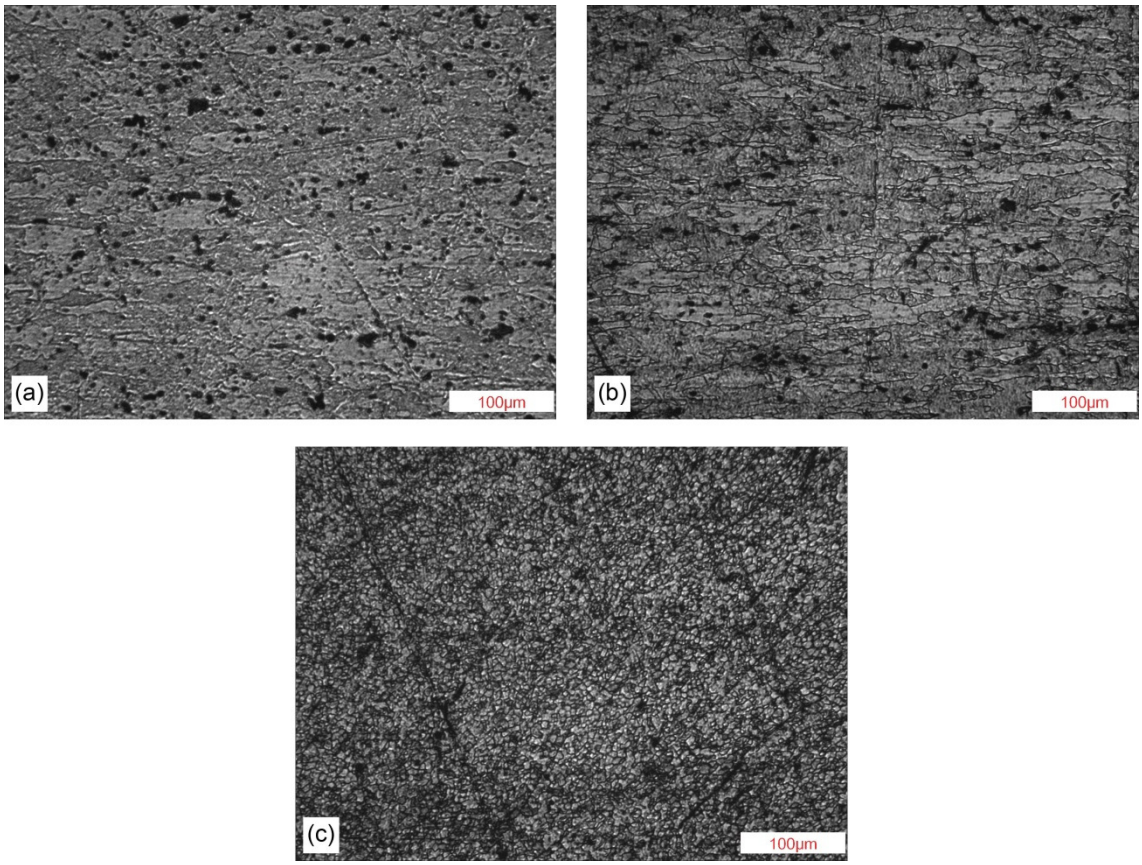

Figure 3.23: Microstructure of the FSW plate (obtained with the optical microscope) from: (a) parent material, (b) HAZ, and (c) NZ.

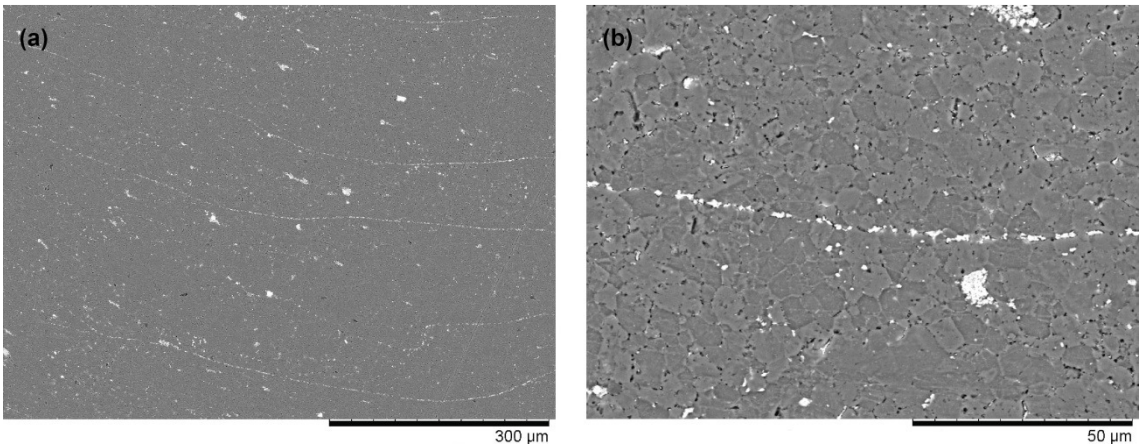

Figure 3.24: Microstructure of the NZ (obtained with the SEM): (a) 250× amplification and (b) 1500× amplification.

As mentioned before, the experimental data, namely the residual stress field, the temperature and the hardness profile will be used in the following chapter for the validation of a numerical model to simulate the FSW process.

Chapter 4

Numerical modelling of the Friction Stir Welding process

The modelling and numerical analyses of FSW were performed using the FEM commercial software package Abaqus [26]. A 3-stage procedure was adopted by means of a coupled thermo-mechanical model and a sequence of *quasi*-static analyses. In the first stage, a heat source crossed the plate following the weld line and, on the second stage, the cooling of the joined structure occurred. During these two initial stages, mechanical boundary conditions were applied to simulate the clamping system. The third (and last) stage of the simulation corresponds to the release of the joined plate from the supports, with the boundary conditions being replaced by minimal constrains, only preventing rigid body movements.

The implemented material model considers the variation with temperature of several parameters. The thermal softening of the material was considered as not only temperature dependent but also temperature history dependent.

The model of the welded plate, with the same dimensions of the one used in the experiments, was discretised using shell elements. When compared to solid elements, this type of formulation allows a simpler discretisation of thin-walled structures, aiming to use this methodology in the welding simulation of stiffened panels (Chapter 5) and subsequent

structural analyses (Chapter 7). A sensitivity study was carried out on the mesh density, the type of shell element to be chosen and the optimum number of integration points across thickness, seeking for a reasonable calculation time without compromising the accuracy of the results. Different types of heat source distribution were tested and the sensitivity of the model to distinct mechanical boundary conditions, simulating the clamping system, was also assessed.

Details concerning material modelling, element formulation, discretization, and boundary and loading conditions are presented in the following sections.

4.1. Material modelling

In the present work, the thermal and mechanical properties of AA2024-T3 were defined following previous references in the literature [63, 70, 71]. It should be noted that most of these parameters (such as thermal conductivity, thermal expansion coefficient, specific heat, Young's modulus and yield stress) were considered as being temperature dependent. The variation of their magnitude with temperature is shown in Figure 4.1. Outside the plotted range, the variables assume a constant value equal to the border ones. The density and Poisson's ratio, assumed as temperature independent, are listed in Table 4.1. The material model was considered to be isotropic.

Thermal softening effects induced by the thermal cycle were also considered, being assumed as a result of the manufacturing process. A softening model was therefore included into the numerical analyses to properly account for the effects of the temperature and the temperature history on the magnitude of the yield stress, based on the proposal by Myrh and Grong [72], and relying on the level of precipitates dissolution and coarsening. The effects of the natural ageing and mechanical alterations in the grains in the TMAZ and NZ are not considered in this model. Sonne *et al.* [70] showed that the use of the implemented softening model in the AA2024-T3 FEM numerical analyses can lead to important changes in the prediction of residual stresses, compared to the exclusive use of temperature dependent material properties.

This particular softening model was previously used in the numerical simulation of FSW process on AA2024-T3 plates to predict the residual stress field [49, 70, 73-75]. It was also used when modelling the FSW process using other aluminium alloys [48, 53].

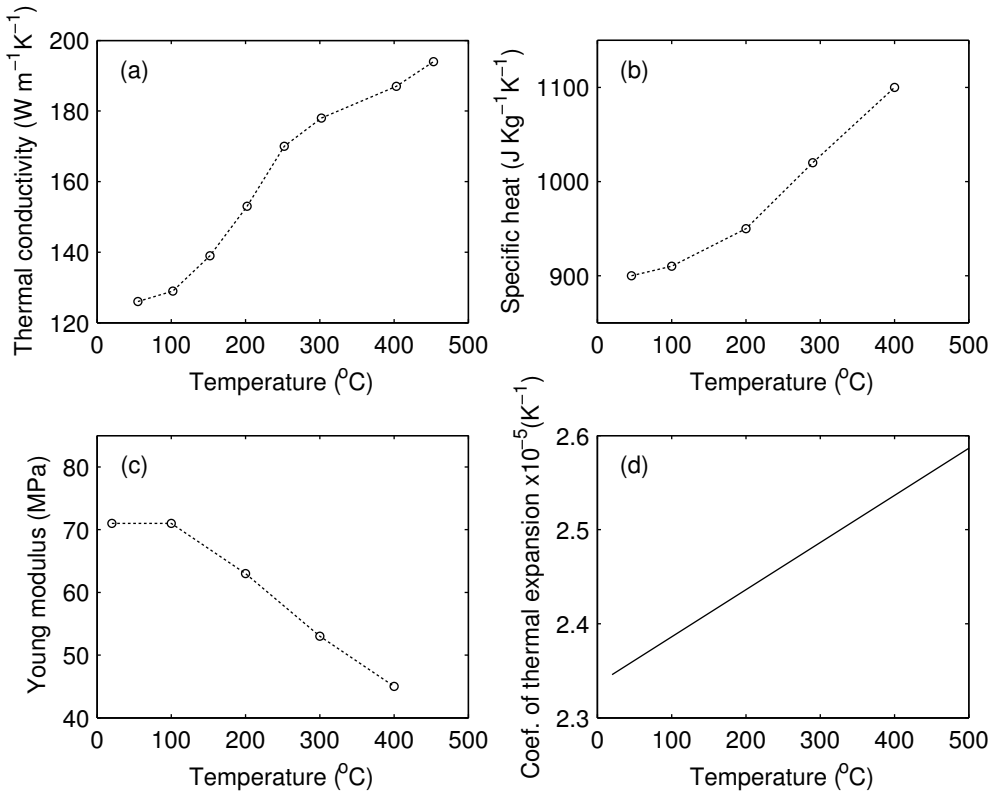

Figure 4.1: Temperature dependent material parameters used in the FSW numerical analyses [63, 70, 71].

Table 4.1: Temperature independent parameters used in the FSW numerical analyses [63, 70, 71].

Parameter	Magnitude
Density	2770 kg m^{-3}
Poisson's ratio	0.33

Following the work of Feng *et al.* [53] and Sonne *et al.* [70], the yield stress (σ) can be defined by

$$\sigma = (\sigma_{\max} - \sigma_{\min})(1 - X_{\mathrm{d}}) + \sigma_{\min} \ , \tag{4.1}$$

where $\sigma_{\max}$ is the yield stress of the material in the T3 condition, $\sigma_{\min}$ is the yield stress in the fully softened state (both shown in Figure 4.2) and X_{d} is a dissolved precipitates fraction, defined by

$$X_{\mathrm{d}} = \sqrt{t_{\mathrm{eq}}}\,. \tag{4.2}$$

In this equation, t_{eq} is given by

$$t_{\mathrm{eq}} = \sum_{i=1}^{N_{\mathrm{total}}} \frac{\Delta t_i}{t_{\mathrm{ref}}\ \exp\left[\frac{Q_{\mathrm{ref}}}{R}\left(\frac{1}{T_i} - \frac{1}{T_{\mathrm{ref}}}\right)\right]}, \tag{4.3}$$

where Δt_i is the size (time) of the increment, T_i is the current temperature, t_{ref} is the time for total dissolution at the reference temperature (T_{ref}), R is the universal gas constant and Q_{ref} is the effective activation energy for the dissolution of precipitates. The constants were defined as: t_{ref} = 16 s, T_{ref} = 673 K, Q_{ref} = 70.52 kJ mol^{-1} [70]. For every numerical analysis increments, X_{d} is updated for each integration point, starting from a value of 0 (corresponding to the material in the T3 condition) and going up to 1 (fully softened material), according to equations (4.2) and (4.3). The calculation of X_{d} was performed using an Abaqus USDFLD user subroutine [26] and this magnitude was defined as a field variable. The actual value of the yield stress was obtained by interpolation between the upper (σ_{max}) and lower (σ_{min}) bounds of the yield stress values (see Figure 4.2), according to equation (4.1) and taking into account the current temperature. The curves corresponding to the upper and lower boundaries were based on the literature, although there are some differences in the information provided by different authors [42, 49, 70, 76]. In particular, for the lower bound curve, the values presented by distinct authors [49, 70] are quite different. The σ_{min} curve presented in Figure 4.2 was plotted based on the general pattern of the variation with temperature from the available information and assuming a yield stress, at room temperature, of 205 MPa. This magnitude corresponds to 60% of the yield stress of the base material, being within the range values presented in the literature [42, 49, 70]. The σ_{max} was plotted following a similar procedure, although in this case the differences from distinct references were much smaller. The maximum yield stress at room temperature was set with a value of 345 MPa, as defined by many authors [42, 49, 70, 77].

As an example, the plot in Figure 4.2 shows the evolution of the yield stress in a point of the plate during the heating and cooling phases of the FSW process. It should be noted that, although the temperatures are expressed in Kelvin in the previous equations, they will be expressed in degrees Celsius in the following for convenience purposes.

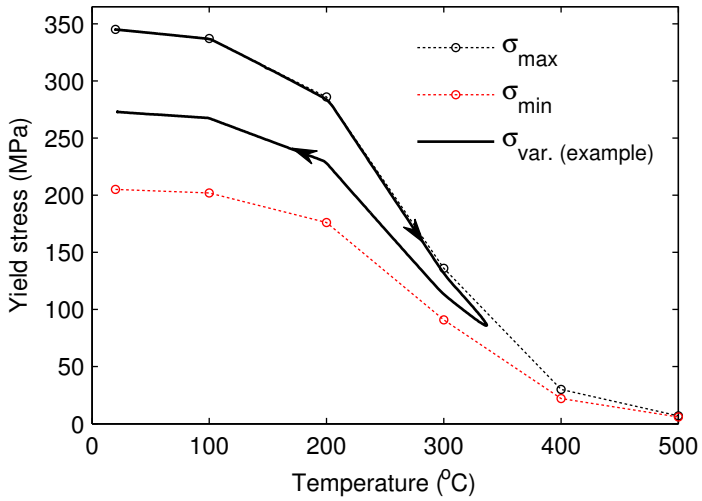

Figure 4.2: Yield stress curves used in the softening model and example of the yield stress variation during the FSW process.

No hardening law was defined in the constitutive model, as the material was considered to be perfectly plastic. To support this assumption, Preston *et al.* [42] showed an insignificant effect of the work hardening settings, compared with perfectly plastic case, on the prediction of residual stresses in the numerical analyses of FSW process with AA2024-T3. This is because most of the plastic strain occurs at high temperatures, when the work hardening rate is negligible. Additionally, the assumption of a perfectly plastic behaviour can lead to significant gains in terms of computational time, since there is no need for a incremental update in the hardening variables.

Apart from the effects on the residual stress and distortion, the softening model is also important in terms of the final yield stress prediction. This is an important issue considering the structural analyses to be performed afterwards in subsequent steps of this study.

4.2. Finite element discretization

As previously mentioned, a shell element formulation was used to discretize the plate. Two types of elements from the Abaqus library were tested: S4RT and S4T. These are 4-node thermo-mechanical coupled elements, where S4RT adopts a reduced integration scheme while S4T a fully integrated one [26]. Further details about these shell element formulations are presented in Section 6.1, focusing on mechanical aspects only. However, those details are shared with the thermo-mechanical coupled elements, mentioned here,

which have an additional degree of freedom per node (the temperature) when compared to the mechanical-only versions.

Regarding the distribution of the integration points across thickness, a Simpson's rule is used by default in Abaqus [26]. This means that the integration points are evenly distributed, with the position of the top and bottom integration points corresponding to the top and bottom surfaces of the plate. Two different numbers of integration points were tested using the S4RT elements: 5 and 9 points across thickness (which corresponds to the same number of integration points per element, due to the reduced in plane integration). For the S4T shell element, only 5 integration points across thickness were used, resulting in a total of 20 integration points per element (5 layers of 4 in plane integration points). For this element, the option of 9 integration points across thickness was not tested since the previous results using the S4RT element did nor showed any advantages on using more than 5 integration points in the thickness direction.

In terms of refinement levels, three different meshes were assessed, all of them composed by equal sized square elements. Meshes with elements with 0.5, 1 and 2 mm width were used. The total number of elements obtained for each mesh refinement is listed in Table 4.2. Coarser meshes were not tested, since they would not offer enough resolution in the results for the intended application.

Table 4.2: Number of elements in each model depending on the mesh refinement level.

Element size (mm)	Number of elements
2	1455 (97 × 15)
1	5820 (194 × 30)
0.5	23280 (388 × 60)

4.3. Loading and boundary conditions

The FSW numerical analyses included three different steps that are listed in Table 4.3, together with the duration of each one. The term "pseudo-time" is used, since the simulations are a sequence of *quasi*-static analyses, in which the time has no real meaning. It consists of the summation of the size of the performed increments. Mechanical and thermal boundary conditions vary from step to step during the simulation following the experimental conditions.

Table 4.3: FSW simulation steps.

Step	Action	Pseudo-time (s)
1	Tool passage (heat input)	135 [0, 135]
2	Cooling	50 [135, 185]
3	Clamping system release	1 [185, 186]

4.3.1. Mechanical boundary conditions

First, it is important to mention that the mechanical loads produced by the tool in contact with the plate were not considered in the model, for the sake of simplicity. The modelling of these kinds of loads can have influence on the residual stresses, namely leading to some degree of asymmetry between the leading and retreating sides [77]. However, Richards *et al.* [49] mentioned that these mechanical loads have a small impact when compared with the thermal effects. The considered simplification is computationally efficient and was used by other authors, leading to accurate results [49, 70, 74, 75].

The current model presents a symmetry plane (in the weld line) in terms of geometry, loading conditions and boundary conditions, therefore only half of the plate (one of the parts to be welded) was modelled, with obvious benefits in the total computational time. Thus, as represented in Figure 4.3, the nodes in the weld line were considered to have a symmetry boundary condition on the *Oyz* plane.

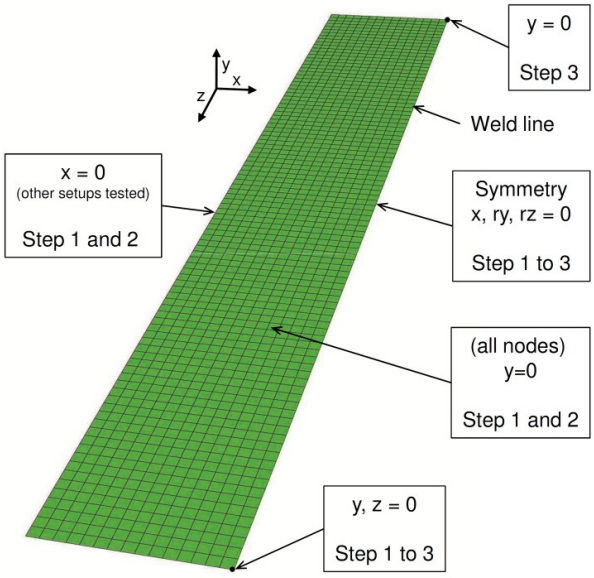

Figure 4.3: Mechanical boundary conditions for the FSW final numerical model.

Another concern was about the modelling of the clamping system. In this work a simplifying approach was performed without physically defining the clamping tool, using only constrains in the displacement/rotations in some sets of nodes. This simple modelling was adopted in many similar works in the literature (see for example [70, 74, 77]) with good final results. It avoid the need to model contact surfaces, define friction and consider clamping forces. These details, apart from being difficult to measure and apply in the model, would also make it much more complex, with associated problems in terms of computational time and convergence of the results. Therefore, using only displacement/rotation boundary conditions in the nodes, the best approach was found by trying several setups in preliminary analyses. Different boundary condition combinations were tested, including restrictions on the longitudinal edges, transverse edges and on all the nodes. Some of the obtained results using different setups are presented in Section 4.4.2. The set of boundary conditions represented in Figure 4.3 was chosen to reproduce the experimental clamping setups shown in Figure 3.3.

In steps 1 and 2 (when the clamping system is present), the displacement normal to the plate surface (along the *Oy* direction) is restricted. This reproduces the effects of the base support and the compression forces from the clamps. The displacement of the nodes in the edge opposite to the weld line was constrained in the *Ox* direction, in the first two steps, reproducing the effects of the clamps, whose shape restrict the displacement in that direction (see Figure 3.3).

In step 3 of the simulation, the boundary conditions related to the clamping were removed and minimal boundary conditions (necessary to avoid rigid body movements) were applied to the model (see Figure 4.3).

4.3.2. Thermal boundary conditions

In terms of thermal boundary conditions, the modelling of the heat transfer (in and out) during the first two steps of the simulation was performed according to information provided in the literature and taking into account the dimensions of the adopted tool. These boundary conditions are represented in Figure 4.4. In step 3 of the numerical analyses, which occurs after the cooling of the plate, no heat transfer was considered.

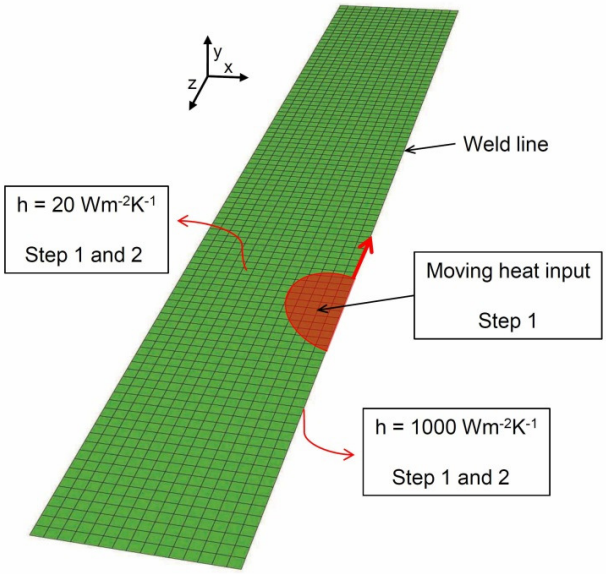

Figure 4.4: Thermal boundary conditions for the FSW numerical model.

During the first two steps, the heat flux output was modelled using distinct effective heat transfer coefficients for the top and for the bottom of the plate, following the equation,

$$q = -h(T - T^0), \tag{4.4}$$

where q is the heat flux across the surfaces, h is the heat transfer coefficient, T is the current temperature at the analysed point, and T^0 is the room temperature, which was set to 20º C. On the bottom surface of the plate, the heat transfer coefficient (h), related to the heat transfer between the plate and the steel base, was assumed to be 1000 $Wm^{-2}K^{-1}$, according to references in which similar analyses were performed [70, 78, 79]. At the top, the heat transfer coefficient (h) was set to 20 $Wm^{-2}K^{-1}$, accounting for convection heat transfer to the surrounding air [70, 79] and also for some heat losses through the clamps.

It is worth mentioning that the 50 seconds defined the duration of step 2 were determined after preliminary tests. That amount of time for the cooling stage was enough to achieve temperatures lower that 1º C from room temperature in the whole plate.

The total heat input was also determined in preliminary analyses, by trial and error, approximating the numerical results in terms of the maximum temperature to the ones obtained experimentally. A good agreement was found using a total power of 1300 W.

In terms of heat input distribution, according to the tool geometry, different approaches are mentioned in the literature concerning the FSW numerical modelling (*e.g.*

[49, 70, 77]). For this reason, distinct heat input distributions were tested to assess the influence of this factor on the final results.

According to the work of Schmidt *et al.* [80], taking into account the geometry of the tool and the independence of the contact conditions, the ratio of heat generation (f), *i.e.* the contribution from the different surfaces of the tool compared to the total heat generation, can be calculated using the following analytical equations:

$$f_{\text{shoulder}} = \frac{Q_{1\,(\text{shoulder})}}{Q_{\text{total}}} = \\ = \frac{(R_{\text{shoulder}}^3 - R_{\text{shoulder}}^3)}{(R_{\text{shoulder}}^3 - R_{\text{shoulder}}^3) + 3R_{\text{pin}}^2 H_{\text{pin}} + R_{\text{pin}}^3}, \tag{4.5}$$

$$f_{\text{pin side}} = \frac{Q_{2\,(\text{pin side})}}{Q_{\text{total}}} = \\ = \frac{3R_{\text{pin}}^2 H_{\text{pin}}}{(R_{\text{shoulder}}^3 - R_{\text{shoulder}}^3) + 3R_{\text{pin}}^2 H_{\text{pin}} + R_{\text{pin}}^3}, \tag{4.6}$$

$$f_{\text{pin tip}} = \frac{Q_{3\,(\text{pin tip})}}{Q_{\text{total}}} = \\ = \frac{R_{\text{pin}}^3}{(R_{\text{shoulder}}^3 - R_{\text{shoulder}}^3) + 3R_{\text{pin}}^2 H_{\text{pin}} + R_{\text{pin}}^3}. \tag{4.7}$$

The total heat input is then

$$Q_{\text{total}} = Q_1 + Q_2 + Q_3\,. \tag{4.8}$$

The variables in these equations are represented in Figure 4.5, where Q_1, Q_2 and Q_3 are the heat generation contributions of the tool shoulder, pin side and pin tip, respectively.

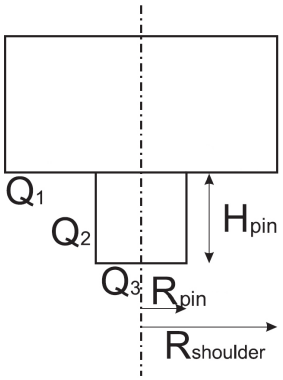

Figure 4.5: Heat generation contributions (adapted from [80]).

Considering the tool geometry shown in Figure 3.2 and a pin radius of 2.6 mm (representing the radius in the pin mid-length) the results obtained using the analytical relations are listed in Table 4.4.

Table 4.4: Heat distribution obtained from the analytical equations.

Zone	1 (shoulder)	2 (pin side)	3 (pin tip)	Total
Ratio (f)	0.912	0.072	0.016	1
Power (W)	1185.6	93.6	20.8	1300

The heat input, depending on the position of the part of the tool, can be classified as:

i) horizontal (perpendicular to the rotation axis with an circular surface);

ii) vertical (parallel to the to the rotational axis with an cylindrical surface).

The horizontal heat input varies with the radius (r), increasing from the centre of the tool to the periphery, and can be defined by:

$$q(r) = \frac{3Qr}{2\pi(R_1^3 - R_0^3)}, \tag{4.9}$$

for $R_0 \leq r \leq R_1$ [77]. This equation can be used for the heat input corresponding to the tool shoulder (on the top surface of the plate) and pin tip (on the bottom surface of the plate), with the values R_0 and R_1 defined for each heat distribution case in the following paragraphs.

The vertical heat input, relative to the pin side, does not change radially. In the present model this heat flux was applied on a predefined area with a constant magnitude

equally divided between the top and bottom surfaces of the plate. This is a simplistic approach, when compared to more elaborated approaches such as defining a volumetric heat input or a vertical heat flux.

The different heat input distributions (HD) are shown in Figure 4.6 using a radial profile. The positive values represent the heat applied on the top surface of the plate and the negative values represent the heat input on the bottom. The heat flux distribution was defined in each case using an Abaqus DFLUX user subroutine [26].

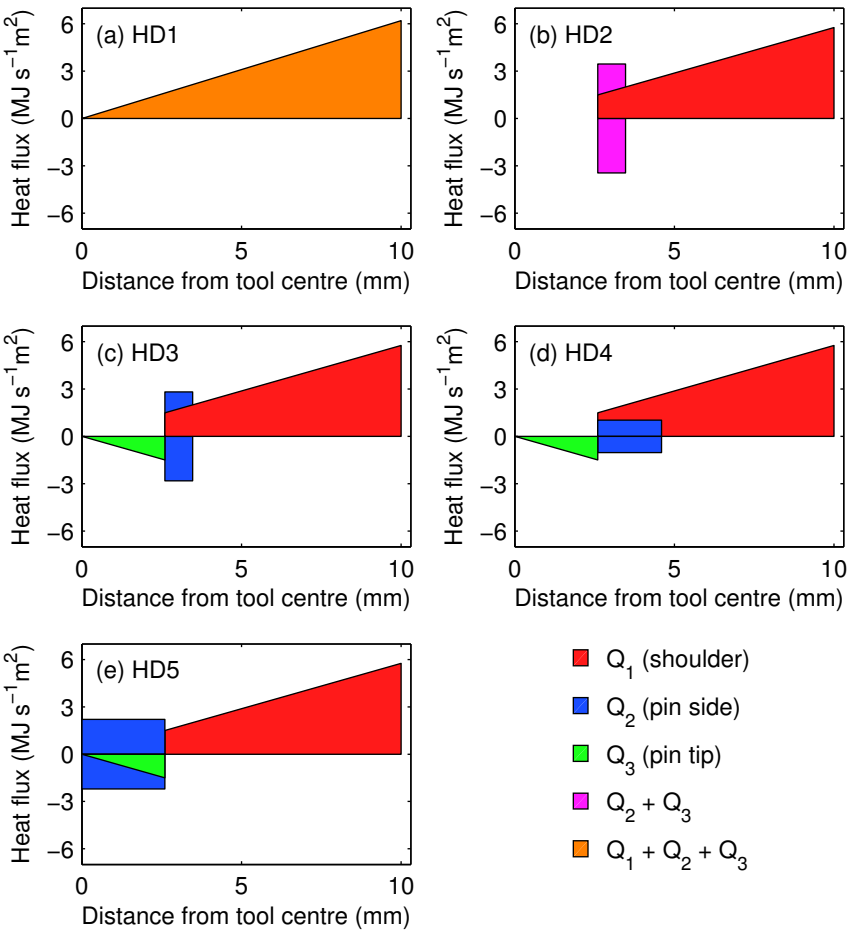

Figure 4.6: Radial distribution of the heat distributions used in the numerical modelling.

In the HD1 model, the total heat power (1300 W) is distributed using equation (4.9) between the centre of the tool (R_0 = 0) and the shoulder radius (R_1 = 10 mm). This distribution does not account for the dissimilar heat input in the tool pin, resembling a pinless tool distribution.

The HD2 is based on the work of McCune *et al.* [77]. The heat generated by the shoulder was also applied according to equation (4.9) between the mid pin radius (R_0 = 2.6 mm) and the shoulder radius (R_1 = 10 mm). The heat power corresponding to the pin ($Q_2 + Q_3$) was distributed in both sides of the plate between the pin mid-length radius (2.6 mm) and 4/3 of the pin mid-length mid radius (3.47 mm).

The HD3 setup is a variation of HD2, in which the power generated by the pin tip (Q_3) is applied, following the equation (4.9), on the bottom surface of the plate.

Taking into account the mesh refinement using 2 mm elements, a variation on the HD3 was applied in HD4. In this heat input distribution the power contribution of the pin side is considered between the pin mid-length radius and a radius of 4.6 mm, therefore defining a larger distribution area.

The HD5 case is also a variation of the HD3, in which the power corresponding to the pin side is applied inside an area defined by the pin mid-length radius.

The developed DFLUX subroutine also defined the position of the heat source, advancing along the weld line. Since the model was solved by means of a sequence of *quasi*-static increments, special care was given to the maximum increment allowed during the tool travel. On the one hand, the definition of small increments led to high computational times. On the other hand, the definition of large increments led to artificial oscillations of the temperature, which affected the reliability of the results. Preliminary convergence studies were performed to decide about the correct maximum increment magnitude for each mesh refinement.

The advance speed of the tool was modelled to match the experimental value of 70 mm/min, although the tool displacement was slightly different from the experimental setup. The starting position of the tool centre was defined as 12 mm from the starting transverse edge, instead of 10 mm used in the experimental setup, to avoid convergence problems on the coarser meshes. The tool passes along the weld line and finished his displacement at 24.5 mm from the panel edge (instead of 10 mm in the experimental setup). This early stop was chosen to avoid temperatures higher than the ones obtained steady state period of the welding (in which the maximum temperature is stable). The rise of the temperature in the end of the FSW process is related to the numerical approximations considered in the modelling of the heat output. While in the experimental setup the heat conduction occurs towards the support, at the bottom of the plate, in the

numerical model the heat output and conduction is limited to the plate surface, since the support is not part of the model. The possible artificial effects caused by the temperature increase at the end of the welding process were therefore avoided with the reduction of the tool displacement, without significant influence on the results obtained in the plate mid-section.

4.4. Results of the sensitivity analysis

4.4.1. Computation times

The analyses were performed using an Intel Core i7-2600 processor @ 3.40 GHz, with 8 Gb of RAM memory, using a total of 4 cores. The computational times using different combinations of the modelling parameters (element size, element type and number of integration points across thickness) are listed in Table 4.5. It should be noted that the use of different heat input distributions and distinct boundary conditions did not significantly affect the calculation time and, therefore, the corresponding results are not presented.

Table 4.5: Computational times for the FSW models.

Element size	Element formulation	Int. points across thickness	Relative comp. time
2 mm	S4RT	5	1 (=17 minutes)
1 mm	S4RT	5	2.9
0.5 mm	S4RT	5	14.1
2 mm	S4T	5	1.6
2 mm	S4RT	9	1.2
1 mm	S4T	5	5.2
1 mm	S4RT	9	4.4
0.5 mm	S4T	5	23.2
0.5 mm	S4RT	9	21.1

4.4.2. Influence of mechanical boundary conditions

The numerical results in terms of residual stresses showed a high sensitivity to the mechanical boundary conditions (BC) used to model the clamping system. This may be related to the small width of the plate and consequent proximity of the displacement-restricted edge to the welded zone. This sensitivity to the BC was also inferred by Sonne *et al.* [74] in a study using plates with the same width. Results in Figure 4.7 show the longitudinal stress distribution obtained in the preliminary analyses, using different mechanical boundary conditions in the longitudinal edge opposite to the weld line (see Figure 4.3) along with the experimental results. These analyses were performed on the 2 mm mesh and with the HD1.

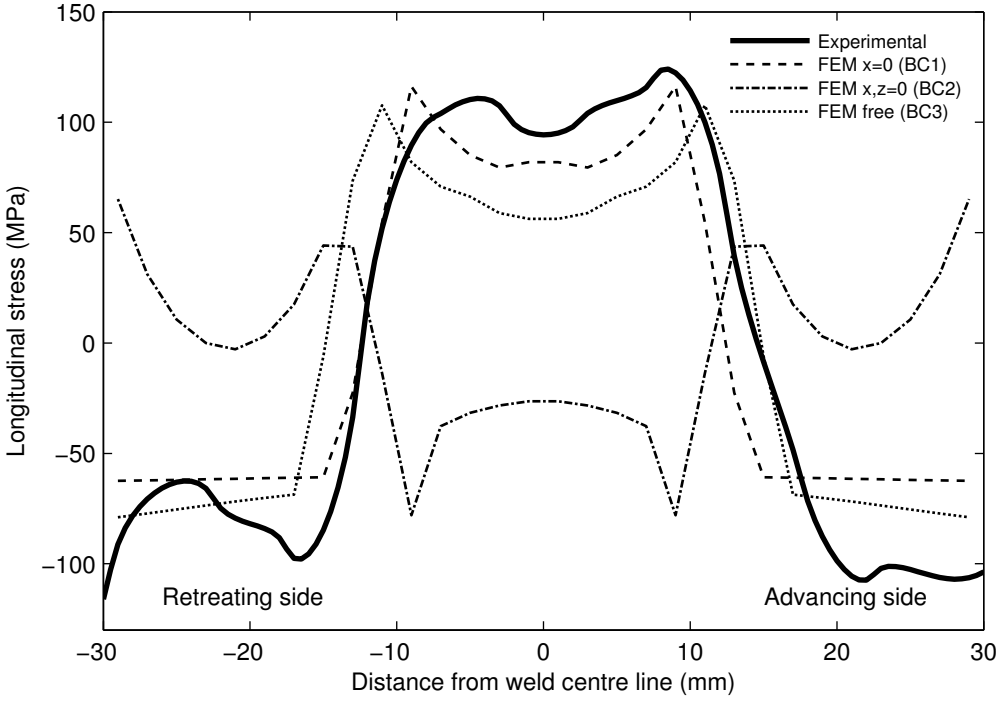

Figure 4.7: Longitudinal stress results (average across thickness) from FEM analyses for different setups of constraints on the longitudinal edge opposite to the weld line, and comparison with experimental results.

BC2 led to an overconstrained model, with results highly divergent from the experimental data. Using the BC1 and BC3 models, the typical M shape in the longitudinal stress distribution was obtained. The results with BC1 showed better agreement with the experimental observations in the retreating side, while the results using BC3 led to better agreement with the experimental results in the advancing side.

Nevertheless, it can be seen that BC1 led to higher stress levels in the shoulder zone and a smaller distance between the two higher stress peaks, therefore providing a better overall agreement with the experimental results. Additionally, BC1 is more similar to the restriction imposed by the experimental clamping system (see Figure 3.3) in terms of displacements in the *Ox* direction. Consequently, the BC1 set were used in the remaining models.

4.4.3. Mesh refinement

The study about the influence of the mesh refinement was initially performed using the HD1 heat setup. The corresponding results are described in the following paragraphs. Afterwards, the obtained conclusions were confirmed using the other heat distributions.

The temperature distribution when the tool passes in mid-length of the plate is shown in Figure 4.8, together with the experimental measurements. The numerical results obtained with different meshes are quite similar in both longitudinal and perpendicular temperature distributions. Furthermore, they are in good agreement with the experimental observations, shown in Figure 4.8(a), since the FEM results concerning the top of the plate are within the two sets of experimental data. As mentioned before, the experimental results were obtained using lower (1200 rpm) and higher (1600 rpm) rotational speeds relatively to the model in this work (1400 rpm).

The influence of the mesh refinement on the longitudinal residual stresses and softening distributions is quite small when globally analysed. Similar patterns in the stress distribution were obtained, in particular in regions close to the transverse edges. However, small differences in the results can be observed in the mid-length distributions, as can be seen from the results in Figure 4.9. This is also illustrated in Figure 4.10 and Figure 4.11, which show the complete map for the mid-length cross-section in terms of longitudinal stresses and softening, respectively.

The variations in softening in the zone corresponding to the tool shoulder radius are mainly related to the positions of the integration points (Figure 4.9 (b)), *i.e.* resolution problems associated with spatial distribution. This small variation in the softening seems to be an additional factor affecting the longitudinal stresses, as shown in Figure 4.9 (a). Nonetheless, these differences are small, with a maximum variation on the stress peak of 9 MPa and of approximately 2 MPa in the zone between 15 and 30 mm. In terms of

distribution across thickness, besides the differences already mentioned, there is no relevant variation in the results using the different meshes.

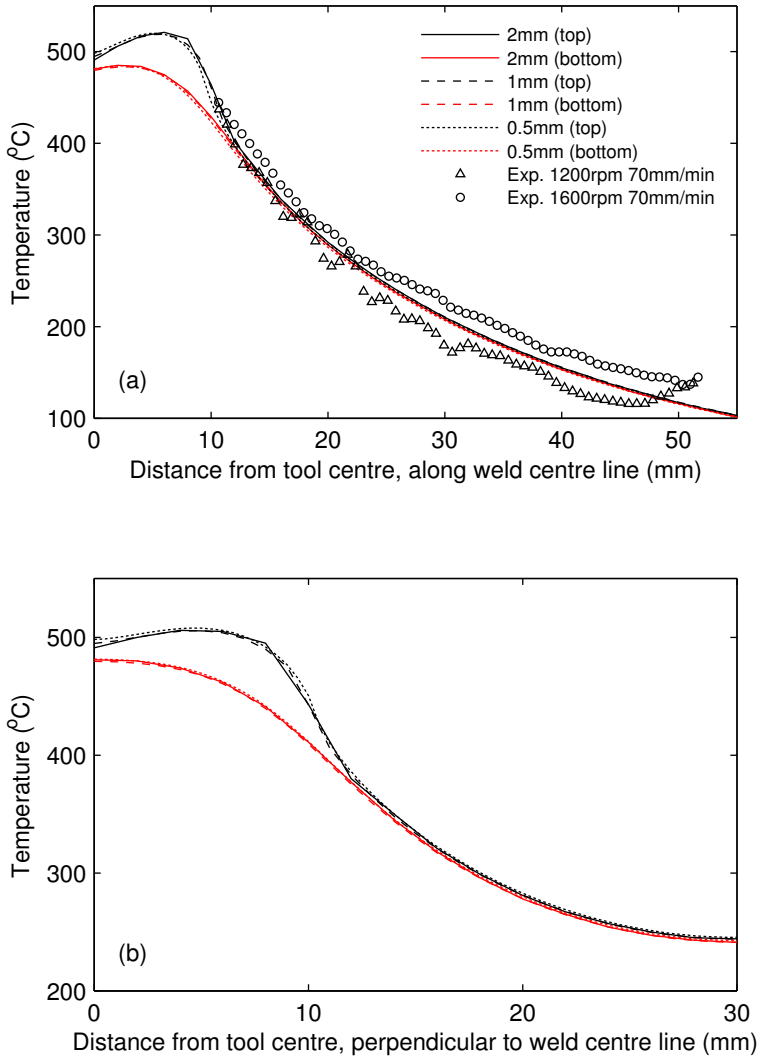

Figure 4.8: Temperature distribution using different element size meshes (and HD1): (a) along the weld line, on the trailing side, and (b) perpendicular to the weld line.

Taking into consideration that the use of meshes with 1 and 0.5 mm elements increases the computational time by factors of 3 and 14, respectively, and that the difference in results is reasonably small, the decision on which mesh to adopt in subsequent simulations has to be based on the targeted accuracy and the size of the structure.

Meshes with finite elements smaller than 0.5 mm were also tested and the results converged to those obtained with the 0.5 mm mesh. However, these models required very small increment size that consequently led to high computational times. Also, convergence problems arise with these models, requiring more effort in the tuning of the numerical parameters to control the increment.

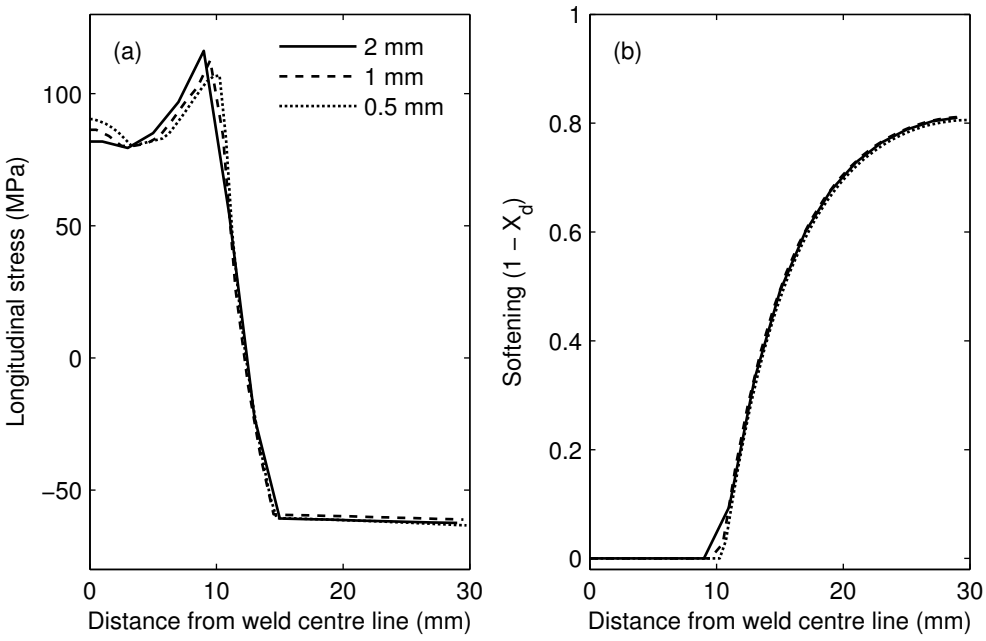

Figure 4.9: Results using different element size meshes (and HD1): (a) longitudinal stress (average across thickness) and (b) softening in the mid-thickness of the plate.

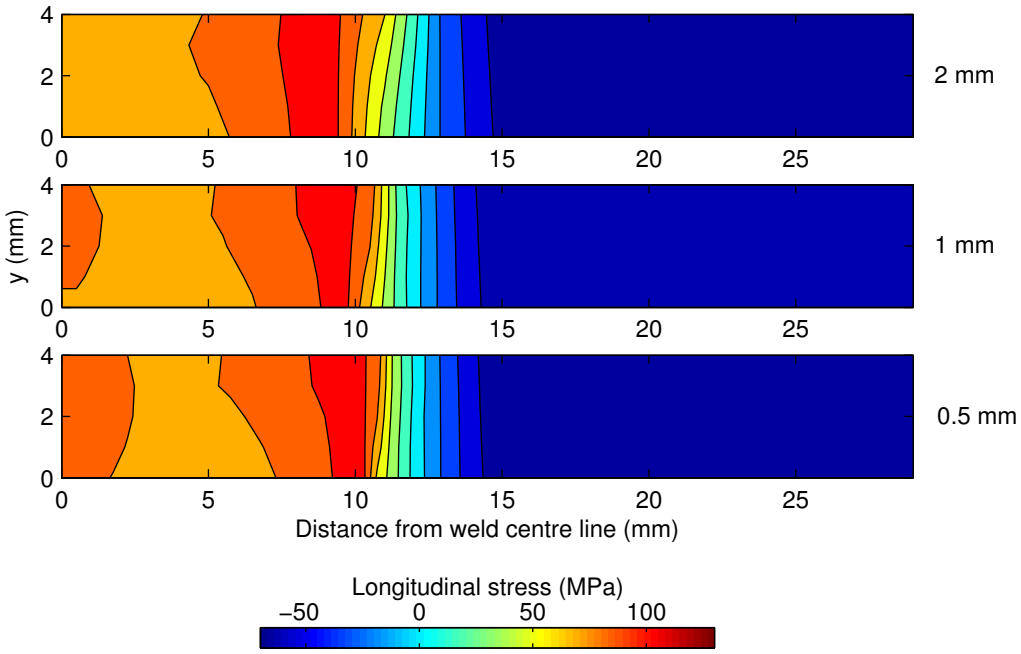

Figure 4.10: Longitudinal stress maps in the plate mid-length using different element sizes.

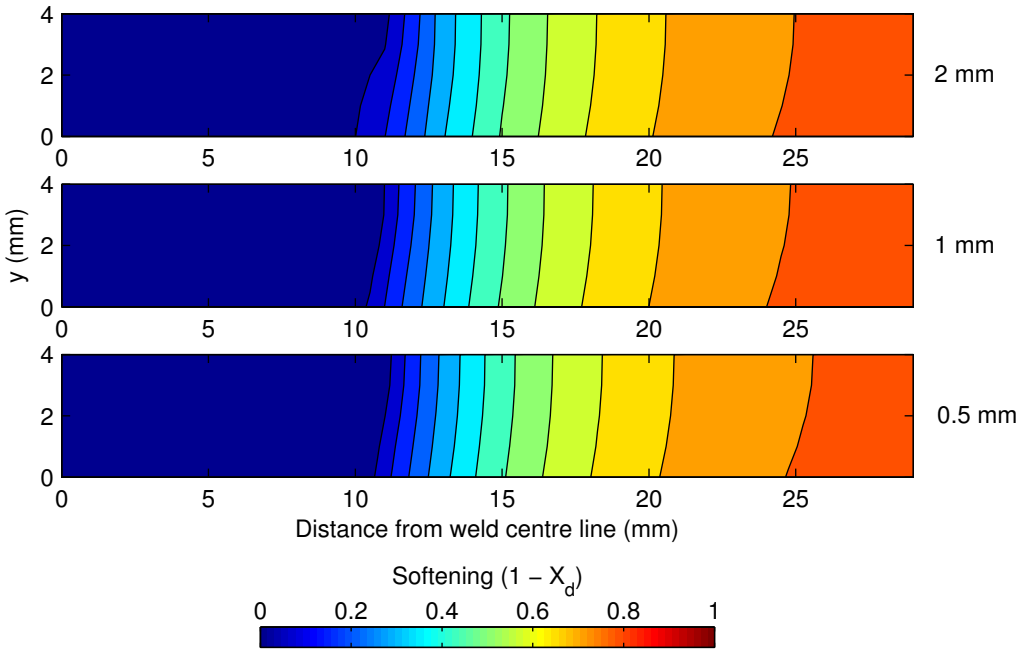

Figure 4.11: Softening distribution maps in the plate mid-length using different element sizes.

4.4.4. Heat input distribution

The influence of the heat input distribution was also tested using the different meshes. The results for the 0.5 and 2 mm discretizations are described in the following paragraphs. The results for the mesh with 1 mm led to the same conclusion obtained using the mesh with 0.5 mm and, therefore, the results are not presented.

The temperature distributions obtained with the HD1, HD3 and HD4 models are compared in Figure 4.12 and Figure 4.13 for the 0.5 and 2 mm meshes, respectively. The temperature results with the HD2 are similar to those obtained with HD3, while the results using HD5 are similar to those obtained with HD4, regarding both meshes, and, thereby, are not plotted in those figures.

Regarding the model with the 0.5 mm mesh, the temperature results obtained with HD3 and HD4 are very similar. For the HD1, lower temperatures were obtained in a zone with radius lower than 7 mm. This difference is more evident in the bottom surface, with a maximum variation of 23º C. For the 2 mm mesh, the similar trend described for the 0.5 mm model is verified, when comparing the HD1 and HD4 models. Regarding the results for HD3, the differences are not just in the central zone of the weld, but in the whole distribution, especially in the perpendicular plot, with lower resulting temperatures, as shown in Figure 4.13(b). This was expected, since in this distribution the heat input related to the pin was defined in a very small area, not compatible with the mesh refinement using 2 mm elements. Due to this fact, lower heat power was inputted in some increments, leading to lower temperatures outside the shoulder radius zone (approximately 5º C).

The impact of the heat distribution on the longitudinal stress and softening can be considered quite small, as shown in the following. A plot of these variables along the mid-length of the plate is represented in Figure 4.14 and Figure 4.15, for the 0.5 and 2 mm meshes, respectively, allowing for a detailed comparison.

For the 0.5 mm mesh models, the results in terms of longitudinal stresses and softening are very similar (Figure 4.14(b)). There is only a negligible variation in the longitudinal stress for the model using the HD1, close to the stress peak, which is most probably related to the small differences verified on the temperature.

In the models with the 2 mm mesh, the results are similar when using the HD1, HD4 and HD5 heat flux profiles. The values of softening, however, are slightly higher when using HD2 and HD3, as shown in Figure 4.15(b), due to the lower temperatures

achieved. This led to slight variations in the longitudinal residual stresses outside the shoulder radius zone, as can be observed in Figure 4.15(a).

In conclusion, different heat distributions seem not to have a significant influence on the stress and softening results in this model. However, the results for the 2 mm mesh reveal that the heat distributions, namely the ones that considered the pin contribution, should account for the mesh resolution when they are defined.

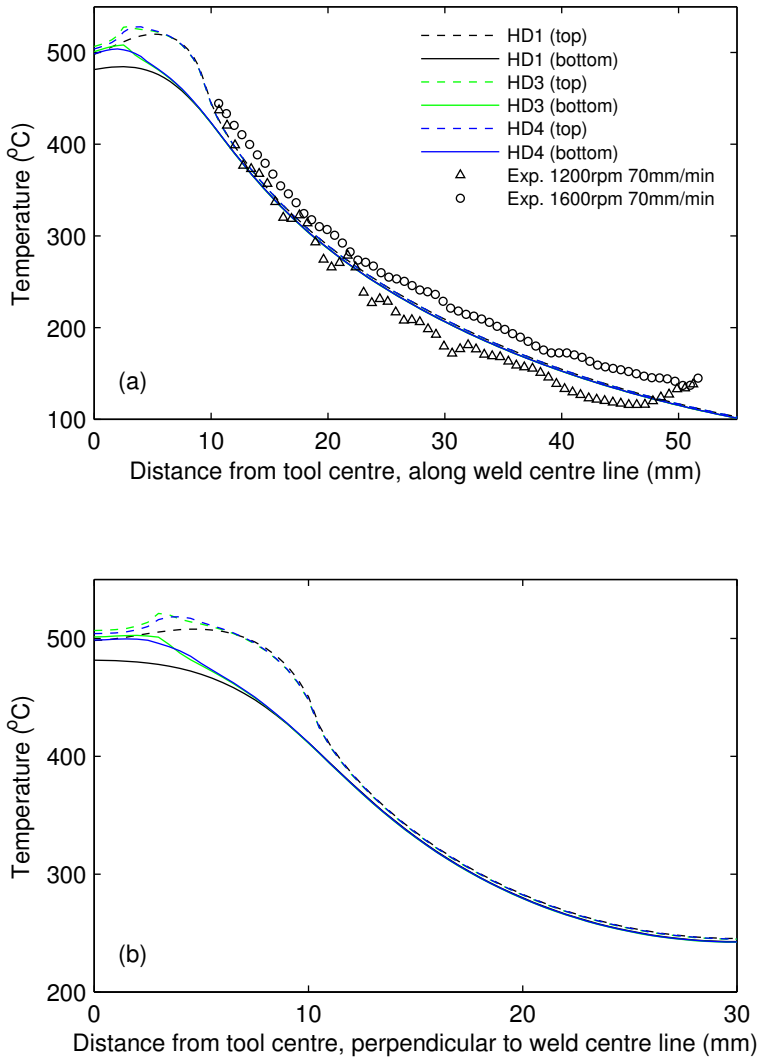

Figure 4.12: Temperature distribution using distinct heat input models (0.5 mm elements mesh): (a) along the weld line, on the trailing side, and (b) perpendicular to the weld line.

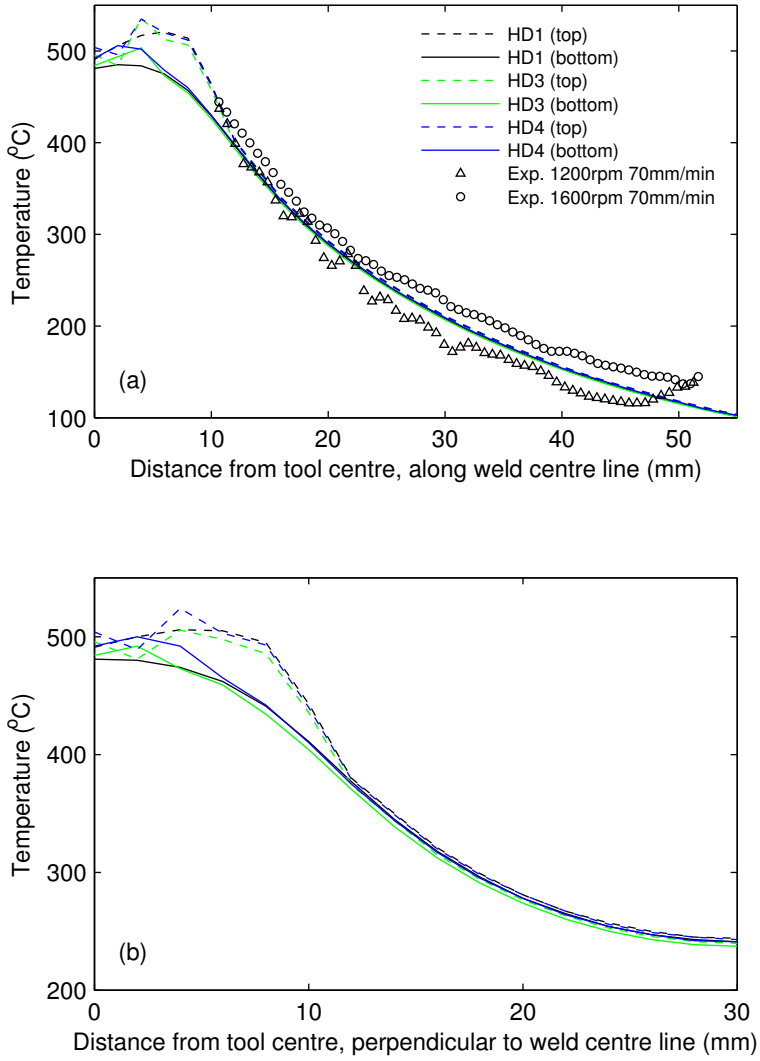

Figure 4.13: Temperature distribution using distinct heat input models (2 mm elements mesh): (a) along the weld line, on the trailing side, and (b) perpendicular to the weld line.

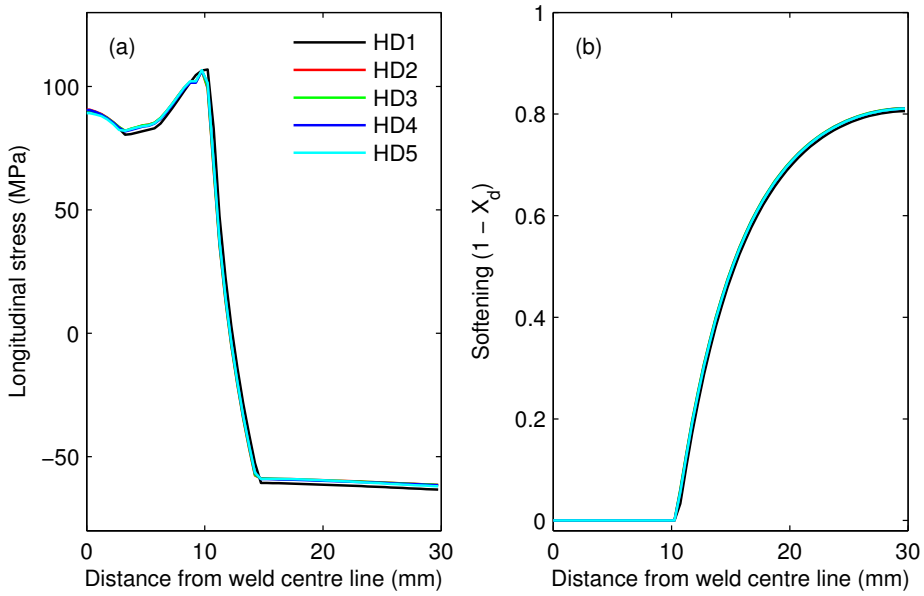

Figure 4.14: Comparison of results using different heat input distributions (0.5 mm elements mesh): (a) longitudinal stresses (average across thickness) and (b) softening in the mid-thickness of the plate.

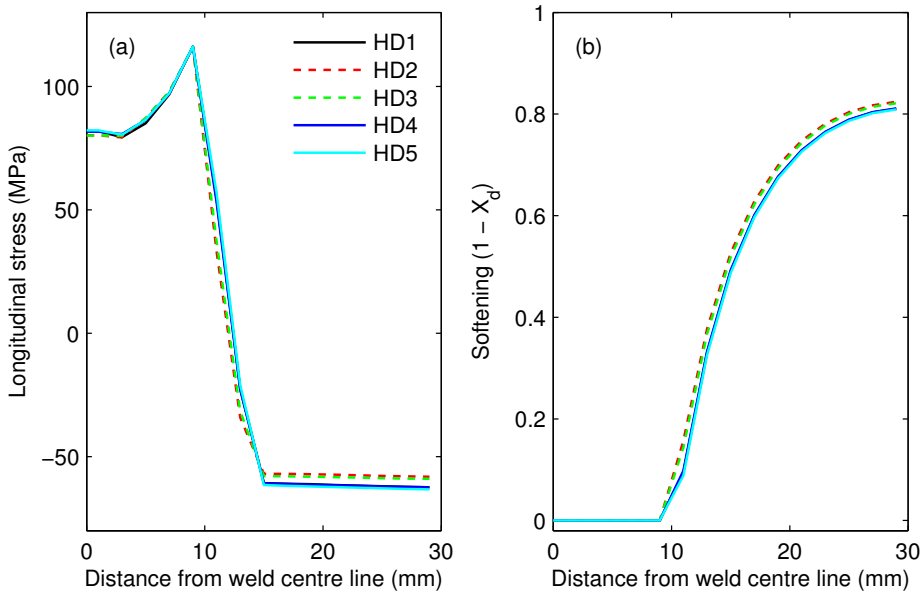

Figure 4.15: Comparison of results using different heat input distributions (2 mm elements mesh): (a) longitudinal stresses (average across thickness) and (b) softening in the mid-thickness of the plate.

4.4.5. Element type

Both shell element formulations (S4RT and S4R) were tested for all considered meshes. The variation of the results in terms of temperature, stress distribution and softening were

seen to be negligible. Figure 4.16 shows the results in the plate mid-length section, obtained for the model with 1 mm elements mesh and HD1. The use of full integration elements (S4T), with significant higher computation time (see Table 4.5), did not seem to influence the accuracy of results.

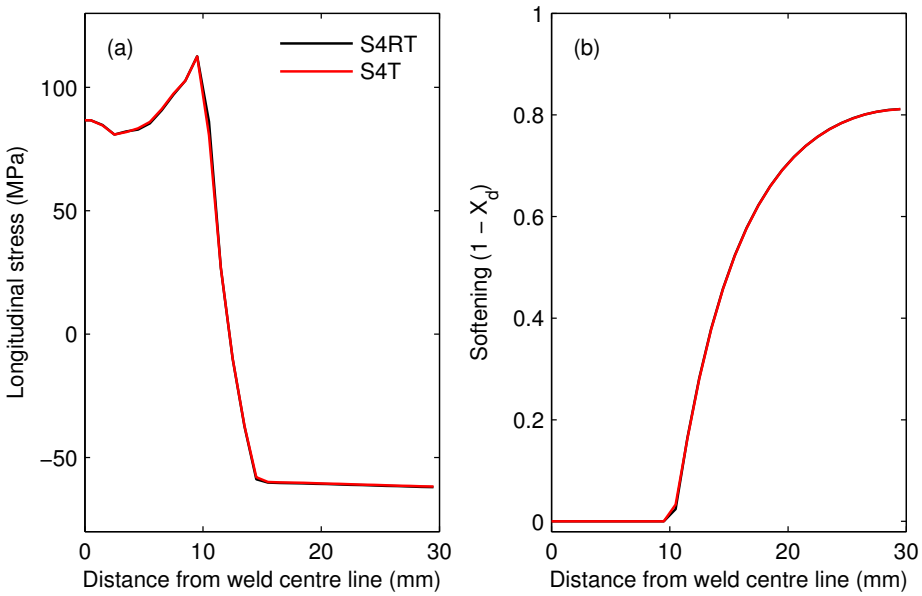

Figure 4.16: Comparison of results using different element types (1 mm elements mesh): (a) longitudinal stresses (average across thickness) and (b) softening in the mid-thickness of the plate.

4.4.6. Number of integration points across thickness

In a similar way, the use of 9 integration points across the thickness, instead of 5, did not led to any relevant influence in the final results. Figure 4.17 shows the results obtained with the 0.5 mm mesh and the HD1 heat flux profile. These results refer to the integration points with common positions in the two Simpson distributions: top, middle and bottom of the plate. There is a perfect match between the results obtained with the models using different number of integration points. Consequently, it becomes evident that the use of 5 integration points, with lower computational time (see Table 4.5), is the best option for this particular case.

4.5. Final model results

In this section a detailed description of the results is presented, including the variations during the FSW process. The following results were obtained with a model based on the

0.5 mm mesh, leading to a better resolution in mapping results, and using the HD3 heat flux profile, assumed to be a better representation of the experimental heat input. The mechanical boundary conditions used are the ones shown in Figure 4.3. The discretization of the plate was made using S4RT finite elements with 5 integration points across thickness.

In what follows, the data concerning the mapping of the full plate are relative to the top surface, where higher temperatures were achieved and the softening effect is more intense. It should also be mentioned, as a reference to better understand the results, that the tool took 72.9 s to travel until the mid-length of the plate. Plots will be used to show the variations during the welding process, referring to points in the mid-length of the plate: P1, P2 and P3, which are located at 5, 15 and 25 mm from the weld line, respectively.

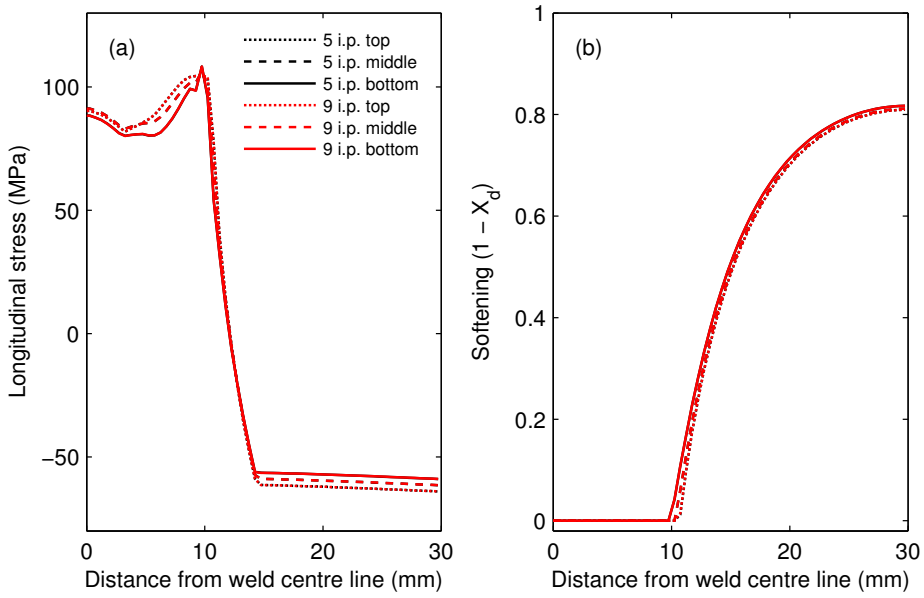

Figure 4.17: Comparison of results using different number of integration points across thickness (0.5 mm elements mesh): (a) longitudinal stresses and (b) softening.

4.5.1. Temperature and softening

Figure 4.18 shows the variation of the temperature during the welding process, regarding the passing of the tool and the cooling (step1 and 2, respectively). The temperature is responsible for variations on the softening and on the yield stress, shown in Figure 4.19 and Figure 4.20, respectively. These representations allow a better understanding of the behaviour of the softening model.

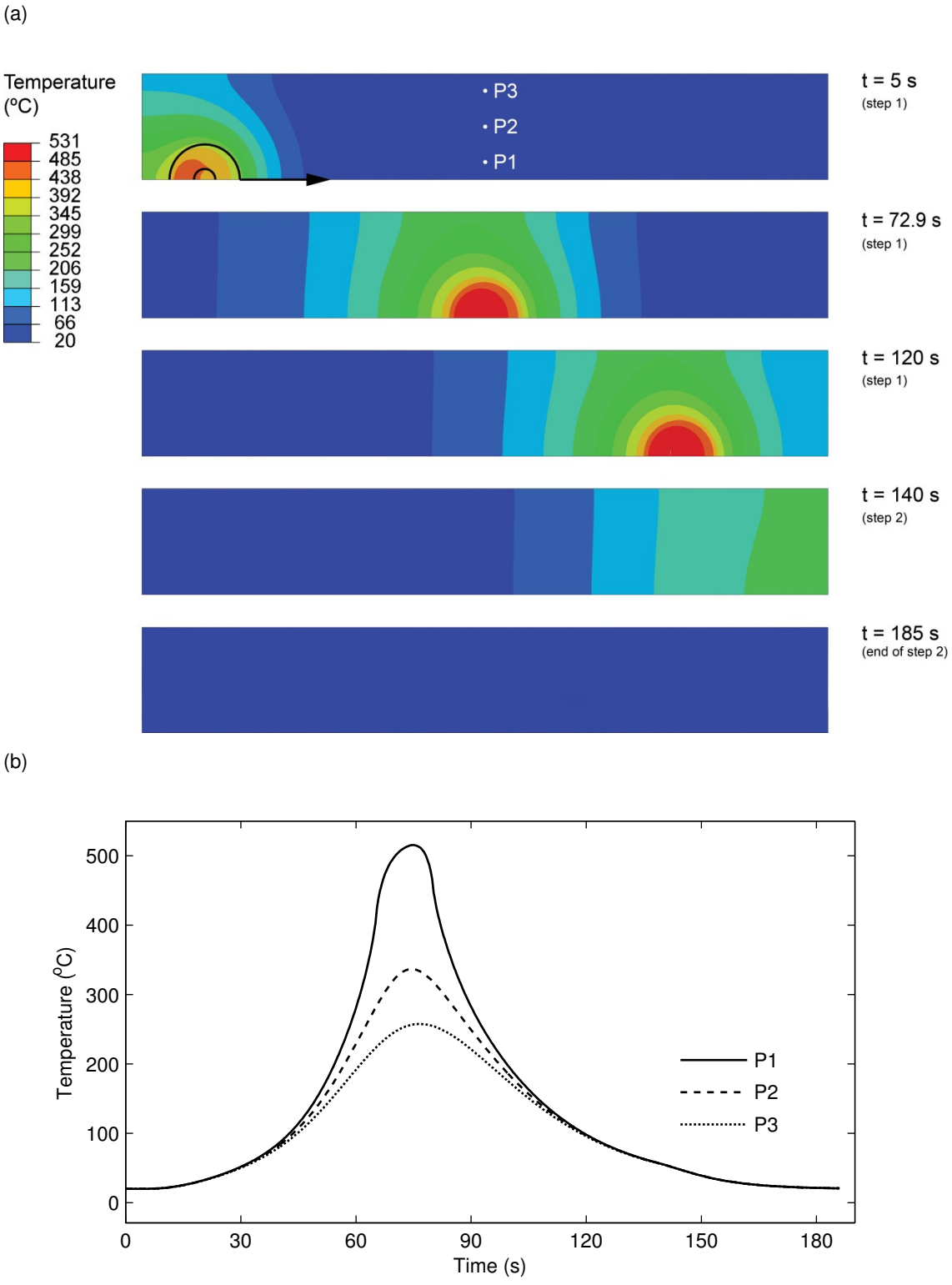

Figure 4.18: Temperature history during the FSW analyses: (a) distribution in the plate and (b) variation with time on the three marked points at mid-length of the plate.

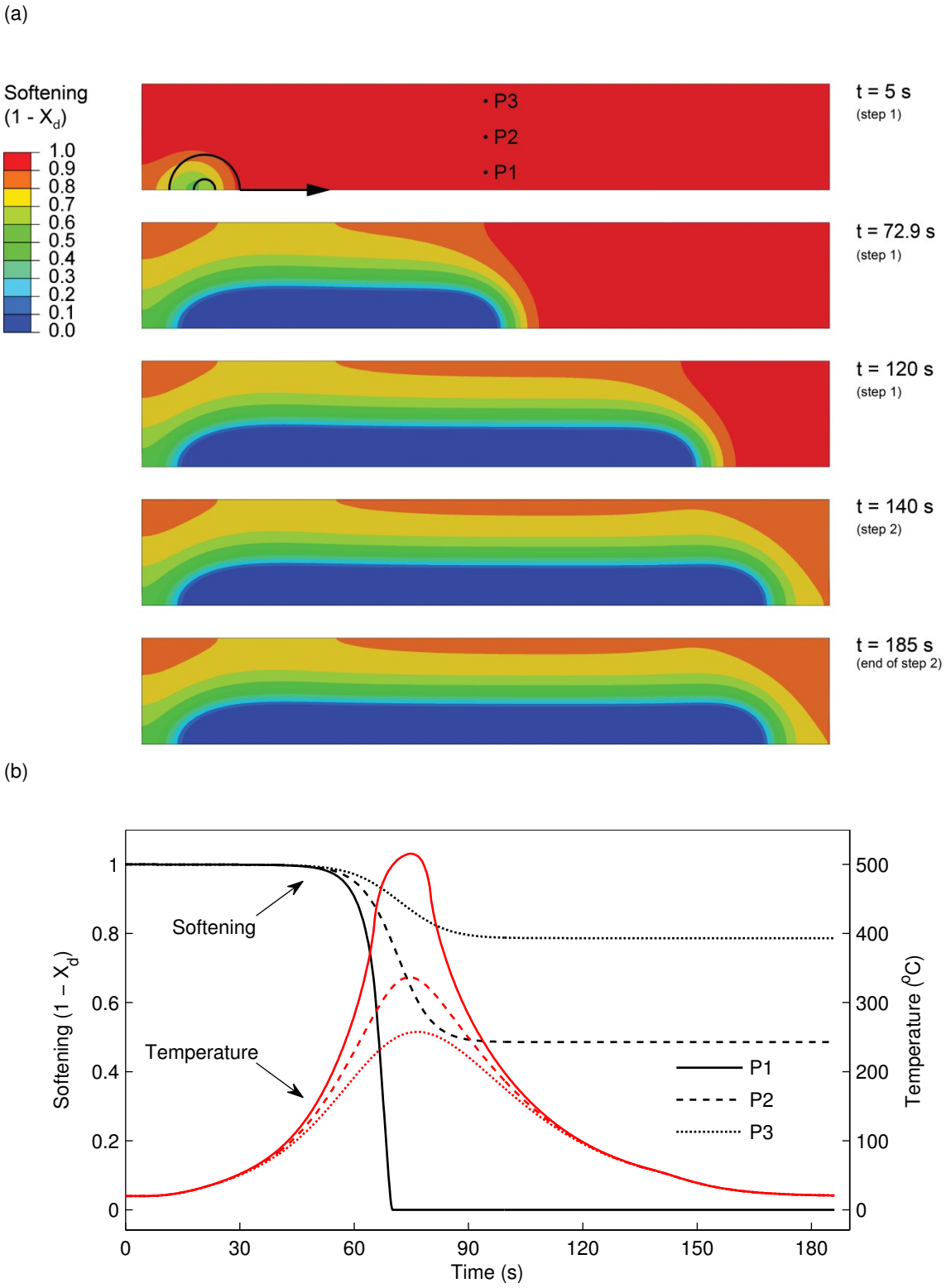

Figure 4.19: Evolution of material softening during the FSW analyses: (a) distribution in the plate and (b) variation with time on the three marked points at mid-length of the plate.

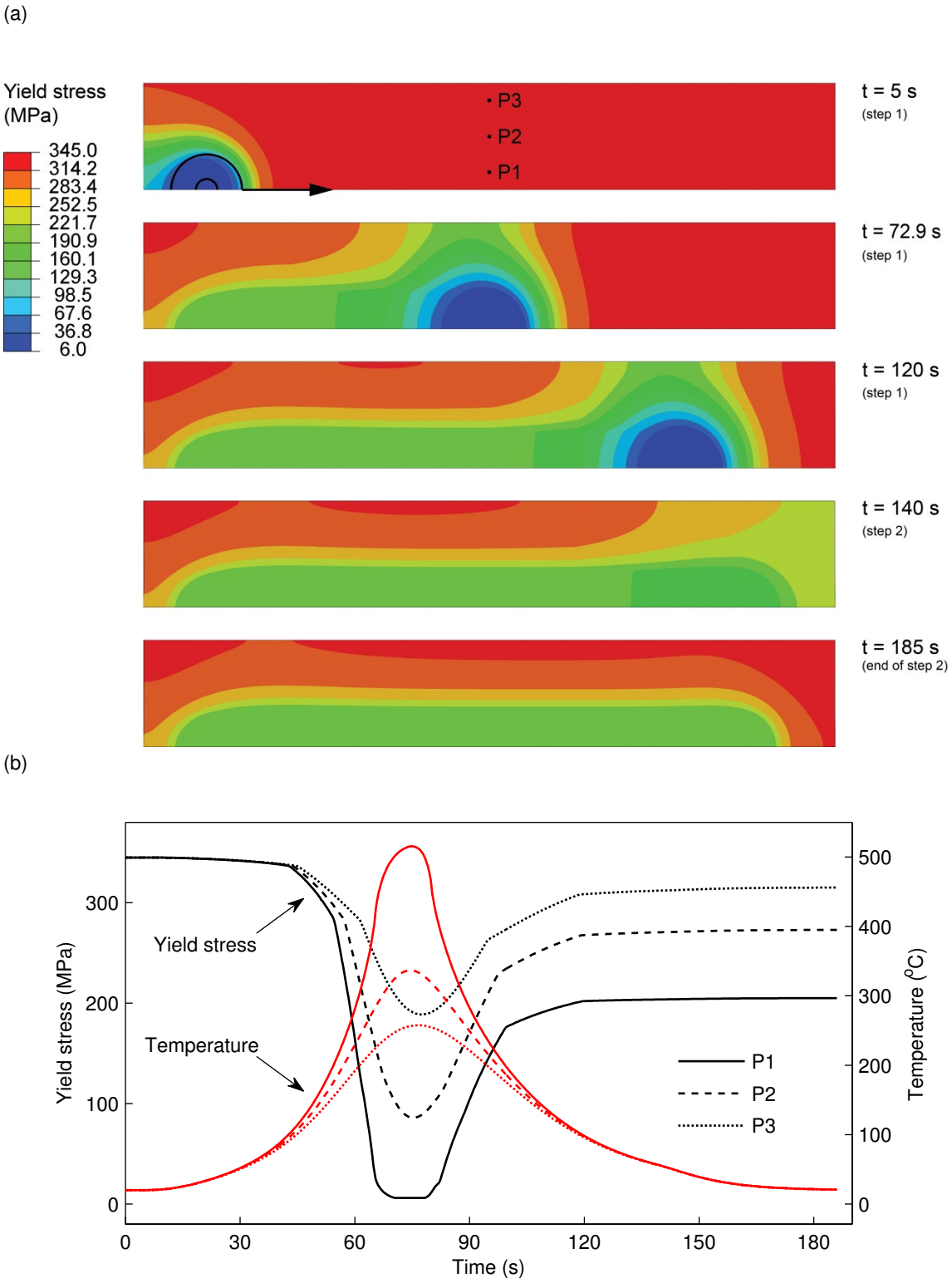

Figure 4.20: Yield stress evolution during the FSW analyses: (a) distribution in the plate and (b) variation with time on the three marked points at mid-length of the plate.

From the results in Figure 4.19(b) it becomes evident that the temperature history on the three points led to distinct evolutions in the material softening. At point P1, located at 5 mm from the weld line, the minimum value of softening (0.0) is reached after the cooling (t = 185 s) , while in the other two points, values of 0.486 (P2) and 0.787 (P3) were obtained. Results in Figure 4.20 give a clear idea that the yield stress magnitude is a result of combined effect of the temperature and of the temperature history (through the softening magnitude). In the end of the cooling stage, when the temperature of the plate is equal to the room temperature, a similar pattern in the distribution of the material softening and yield stress can be seen, since in this moment the yield stress is only dependent on the temperature history.

4.5.2. Ageing effects

The performed FSW simulation did not include natural ageing effects after the welding process, in which the re-precipitation leads to improved mechanical properties. To validate the model in terms of hardness distribution this ageing effect has to be taken into consideration, since the experimental measurements concerning the hardness were made after 1 year of natural ageing. To include the ageing effects in the hardness profile a simple methodology was applied, which will be explained in the following paragraphs.

It should be mentioned that the softening value, calculated with equations (4.2) and (4.3), can be used to determine the hardness using an equation similar to the one used for the yield stress (equation (4.1)) [53, 70]. The hardness magnitude is defined by

$$HV = (HV_{\max} - HV_{\min})(1 - X_{\mathrm{d}}) + HV_{\min} \ . \tag{4.10}$$

Assuming a linear variation between the yield stress and the hardness values, and that the maximum values for these two variables in the base material are 345 MPa and 156 HV ($HV_{\max}$) respectively, the relation between them is assumed to be

$$\sigma = 2.7\, HV. \tag{4.11}$$

The material yield stress for the fully softened material at room temperature was defined to be 205 MPa during the FSW simulation, corresponding to approximately 60% of the base material yield stress (which is 345 MPa). In terms of hardness, the magnitude of the fully softened material ($HV_{\min}$) calculated using the equation (4.11), is 93 HV.

Using equation (4.10), the hardness in the mid-thickness of the mid-length section, at the end of the FSW simulation, can be calculated using the softening values. The results are plotted in Figure 4.21 (solid red line) along with the experimental data. The experimentally measured hardness profile has higher values, especially in the [-16, 16] mm interval, than the ones obtained from the numerical model.

Another profile was determined to better approximate the experimental results by reproducing the ageing effects. Once again, the hardness values were calculated using equation (4.10) and the softening values from the FEM simulation, but now with a fully softened material hardness (($HV_{\min}$) of 117 HV, corresponding to 75% of the hardness of the base material. This second curve is shown in Figure 4.21 (solid blue line).

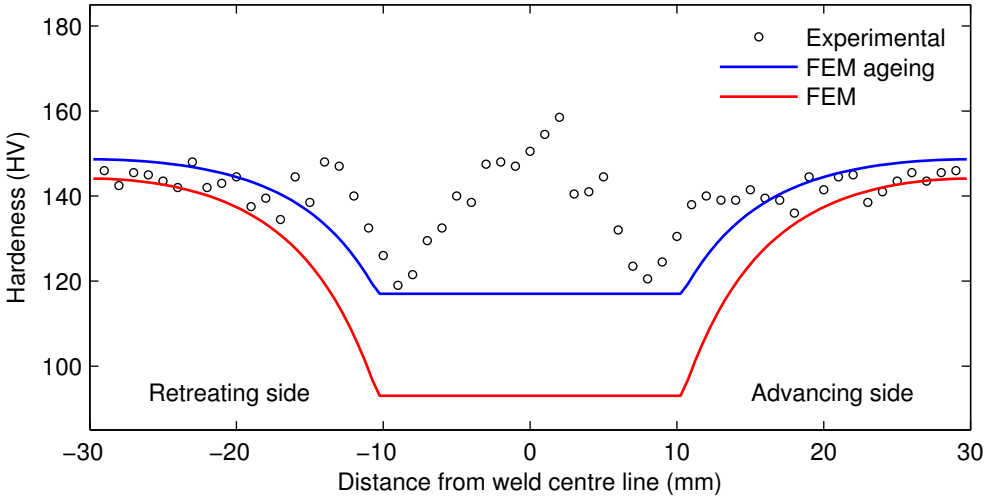

Figure 4.21: Comparison of the experimental hardness magnitude with the results obtained with the FEM model, before and after consideration of ageing effects.

This simple methodology could provide a good fitting between the FEA and the experimental results, by reproducing the ageing effects simply using an increase of 15% in the magnitude of the hardness. The imposed ageing evolution follows what is usually verified in experimental measurements, consisting in a higher increase of the hardness in the zone more affected by the welding (close to the weld line) and a lower increase in the zone where the material is less affected by the welding, as shown in Figure 2.12 [43].

Regarding the structural analyses, which will be presented later in Chapter 7, a similar methodology can be applied to the yield stress distribution in order to reproduce the ageing effects after the welding simulation, in the parts to be loaded. Since the changes in

the yield stresses will consist on an increase, it will not have any impact in the residual stress distribution or in the distorted shape.

Taking into account that the higher and lower hardness values, based on the numerical results, had some adjustments, that allowed an agreement with the experimental values, the only reliable validation that can be done about the hardness distribution concerns the width of the HAZ. In the FEA results the HAZ is slightly wider than in experimental ones, with differences of approximately 2 mm in the retracting side and 2.5 mm in the advancing side. However, the results presented by Carlone and Palazzo [63] (using exactly the same experimental conditions) had a larger HAZ and, thus, a better match with the numerical results. Considering some variability in the experimental results, it is assumed that the present numerical model can predict the HAZ with acceptable accuracy.

As expected, there is not a good agreement between the numerical values and the experimental ones in the NZ and TMAZ since the mechanical effects of the tool on the grains were not considered.

4.5.3. Stress field

The distribution of longitudinal stresses during the FSW process, along with the distribution of transverse stresses at the end of the welding process, is shown in Figure 4.22. The analysis of results is completed with the plots in Figure 4.23, which show the variations of the longitudinal and transverse stresses in three points in the mid-length of the plate, during welding.

The magnitude of the longitudinal stress during the welding process, shown in Figure 4.23, has a different evolution depending on the distance to the weld line.

A compressive peak occurred at point P1 before the heat source passed by, as a result of the thermal expansion in a position prior to this point. When the heat source got closer to P1, and with the associated increase in the temperature, the material got softer allowing plastic flow and the decrease of the compressive magnitude. Afterwards, with the cooling, occurred an increase of the magnitude of the stress, leading to a high tensile stress at the end on the analysis. These tensile stresses resulted from a contraction of this plastically deformed part restrained by an undeformed zone (far from the weld line).

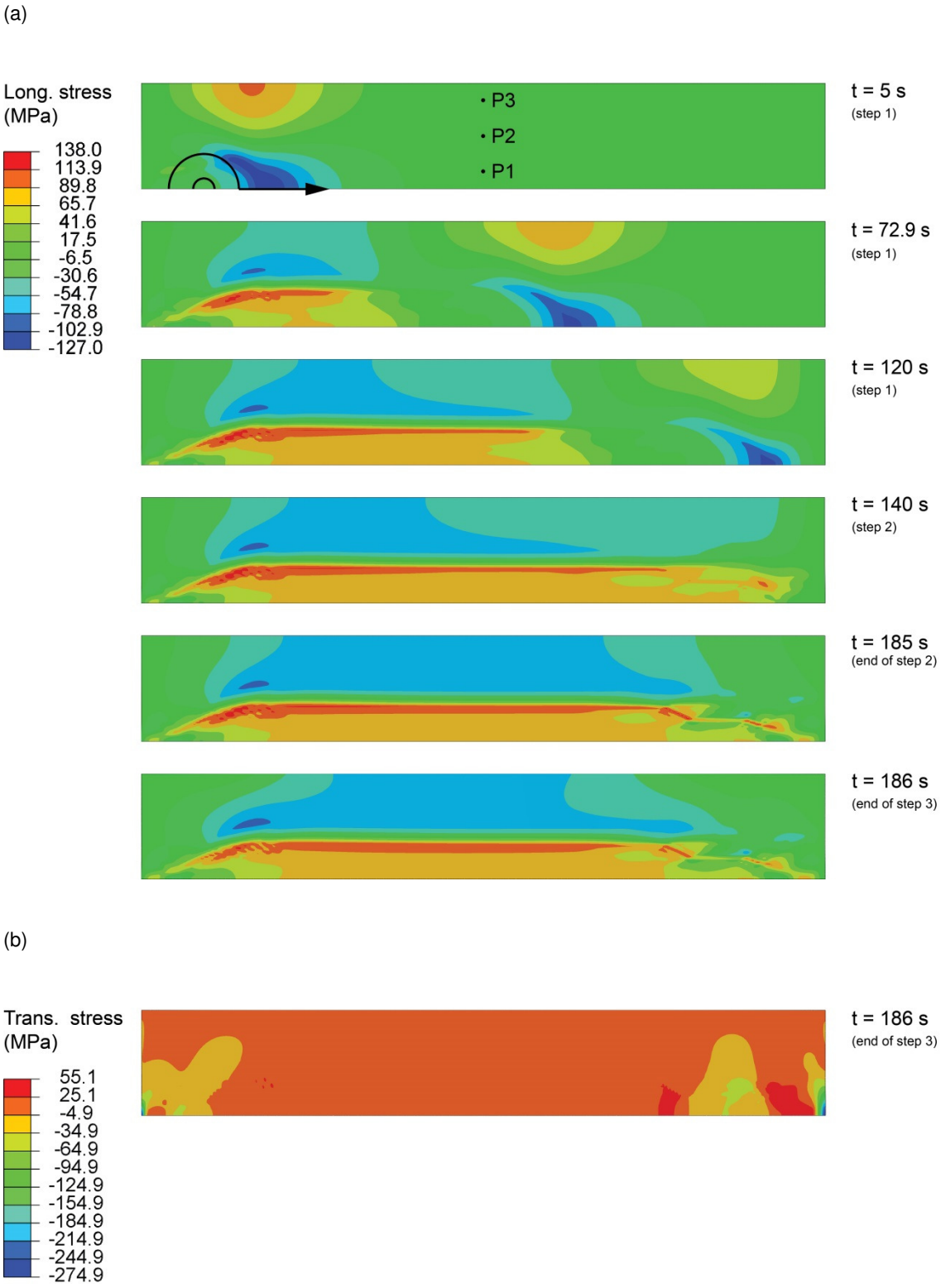

Figure 4.22: Stress results during the FSW analyses: (a) evolution of the magnitude of the longitudinal stresses, and (b) the transverse stresses at the end of the analysis.

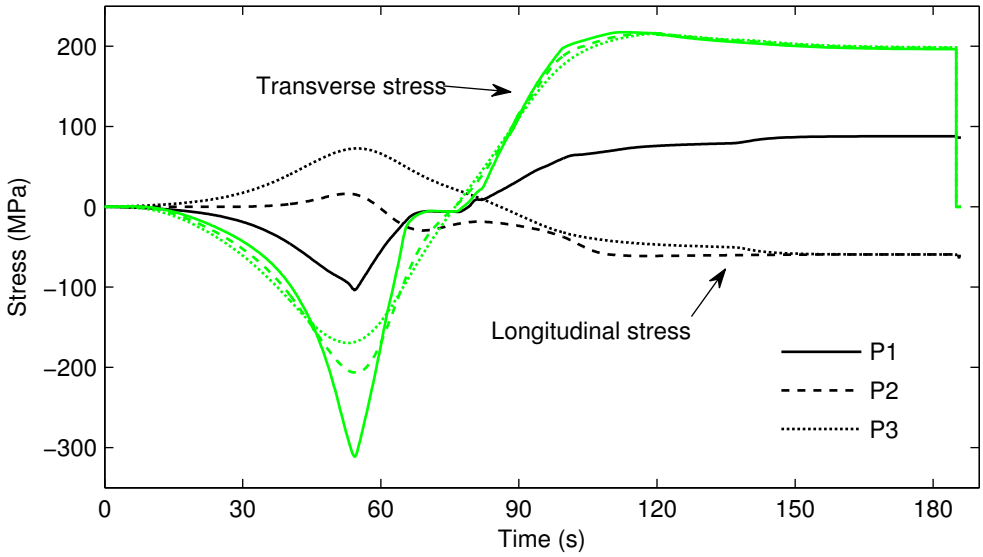

Figure 4.23: Evolution of the magnitude of the stresses on the three points located at the mid-length of the plate.

The longitudinal stress at points P2 and P3 equilibrated the stresses in P1, with mostly tensile stresses before the heat source passed by and a build-up of compressive stresses while cooling down. Since there are no restrictions in the longitudinal direction related to the clamping system, there is a small variation of the longitudinal stresses in step 3 of the simulation (when the plate support is removed) in all the three points.

In terms of transverse component of stresses, the plots for all the points follow a similar pattern, with a higher absolute magnitude achieved closer to the weld line. In this case high tensile stresses were built-up during the cooling, resulting from the previous plastic deformation in combination with the restrictions on the edge opposite to the weld line, along the *Ox* direction. Once these restrictions are removed (in step 3) there is a high variation in the transverse stresses, leading to final values close to zero. Additionally, concerning the results at the end of the analysis, as shown in Figure 4.22(b), it is possible to observe the existence of high compressive stress levels close to the transverse edges of the plate, which equilibrate the low tensile stresses in the remaining area of the plate.

The results related to the evolution of stresses during welding are in agreement with the information provided in other works involving numerical simulation of the FSW process [49, 53, 70].

Concerning the validation of the model, and focusing on the average across thickness, the longitudinal stress distribution obtained at the end of the analysis is in good agreement with the experimental results, as shown in Figure 4.24. Nevertheless, the results coming from the FEA show lower tensile peaks (difference of approximately of 17 MPa). In the zone farther from the weld centre line, with compressive stresses, the absolute magnitude is higher in the experimental curve since they equilibrate the higher tensile stresses at the centre.

Although the validation using average across thickness is reliable, results in Figure 4.25 show a map of the longitudinal stress of the entire mid-length section. It is evident that the results from the numerical analyses show a much lower variation across thickness. This can be explained taking into account the approximations made in the modelling of the clamping in the numerical analyses, that could led to an overconstrained model, and therefore to reduce the variations across thickness.

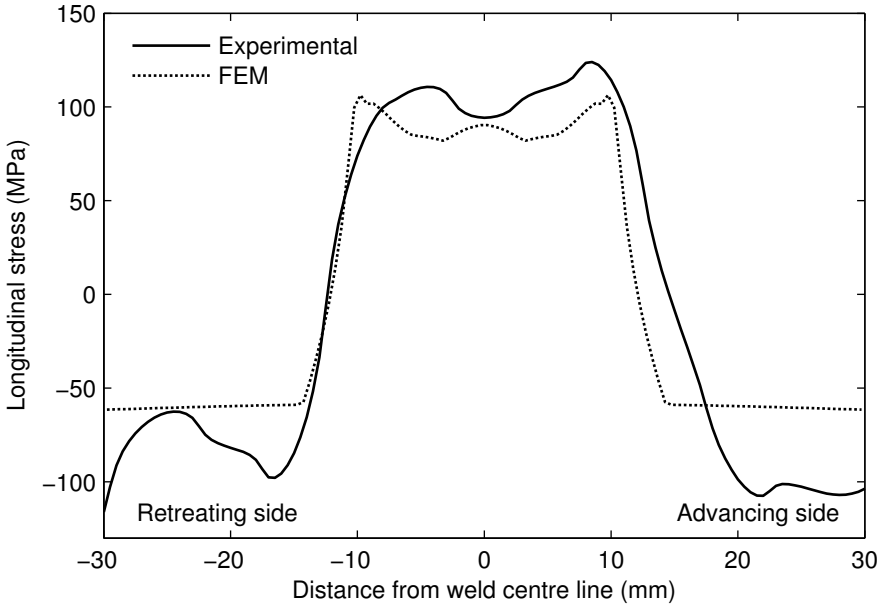

Figure 4.24: Longitudinal stress numerical results (average across thickness at the end of the simulation) from the FEM analysis and comparison with experimental results.

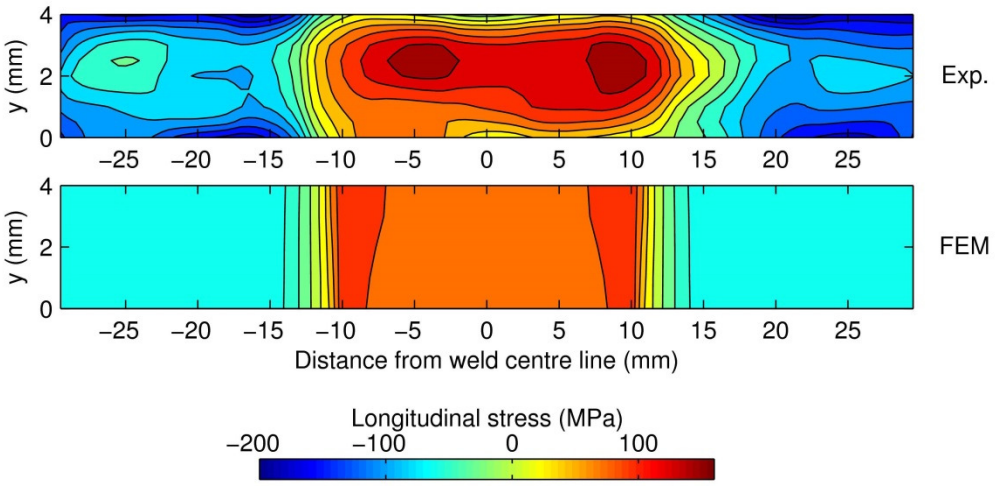

Figure 4.25: Map of the longitudinal stress in mid-length section (at the end of the simulation) and comparison with experimental results.

4.5.4. Distortion

It was not possible to make an adequate validation of the model in terms of the geometrical displacement. The overconstrain caused by of the boundary conditions used to simulate the clamping system led to very small distortions (a maximum of 0.008 mm for the out-of-plate displacement). However, a similar finite element methodology was applied in preliminary analyses to larger parts (with reduced influence of the boundary conditions) and the typical inverted saddle shape with expected magnitudes [51, 60, 61] was correctly obtained.

The distortion effects will be discussed in the next chapter, where the FEM is applied to the FSW simulation of stiffened panel structures.

4.6. Final remarks and conclusions

The numerical model developed for the simulation of the FSW process was validated using the temperature distribution, the longitudinal stress measurements and hardness measurements. Concerning the temperature distribution, although the maximum value was controlled using the power input, the good agreement between the numerical and experimental values (see Figure 4.8, Figure 4.12 and Figure 4.13) allow to conclude that heat transfer coefficient for the heat output, as well as other parameters related to the temperature, were defined with the correct values.

The proposed model was able to predict the longitudinal residual stresses and the softening with acceptable accuracy. Nevertheless, the longitudinal residual stresses showed a lower variation across thickness than what was experimentally obtained, probably due to the overconstrain of the model caused by the boundary conditions that simulate the clamping system, together with the reduced size of the plate.

In terms of softening, the width of the HAZ obtained using the numerical model was slightly wider when compared to the experimental results. However, taking into account some variability in the experimental results, the predictions obtained by means of the FEM were considered acceptable.

Concerning the distortion results, the out-of-plane displacements were reduced, again most probably due to the size of the modelled sample and the over restrictions coming from boundary conditions and did not allow an adequate validation of the model. However, a similar methodology applied to a larger part led to the typical distortion shape and displacement magnitudes in the expected range. Thus, the model seems to be able to predict the distortion of the plate, although requiring a proper validation that should be performed with experimental results from a larger plate and the respective numerical model.

In terms of sensitivity, on the one hand the results showed high variations related to the use of different boundary conditions modelling the clamping system. On the other hand, the heat distribution in the heat source proved to have an insignificant impact on the final results, in terms of residual stress fields and distribution of softening. A small influence on the temperature distribution was however observed, related to this modelling variable. The results showed that the heat distribution should be defined taking into account the refinement of the mesh. The magnitude of the inputted power and the distribution pattern should be as constant as possible along the several increments.

The adoption of fully in-plane integrated shell elements, when compared to elements with reduced integration, and the option for more than 5 integration points across thickness, did not improve the accuracy of results. In terms of mesh refinement, there were only some small variations using coarser finite element meshes. The choice of mesh refinements for posterior applications of the model will have to be based on the overall size of the structure and desired accuracy.

Considering that the results of the FSW simulation were somehow affected by the size of the plate, the sensitivity analyses will be repeated for a stiffened panel model in the following chapter.

Chapter 5
Simulation of the Friction Stir Welding process on stiffened panels

The methodology described in Chapter 4 was adapted and used to perform the simulation of the FSW process on stiffened panels, aiming to predict the welding effects, on a first stage, and allowing for a subsequent study of their influence on the overall structural strength.

5.1. Geometry of stiffened panels

Simulations of the FSW process were performed on integrally stiffened panels containing a single stiffener. Three different cross-section geometries, represented in Figure 5.1, were considered in the analyses. The line in red represents the mid-thickness, used as reference for the modelling of the stiffened panels using shell elements, and the dimensions concern the size of those mid-thickness sections. Also, the nomenclature for the panels geometries mentioned in the figure is used in what follows. The panel with a T stiffener geometry (panel T) is based on the one presented by Yoon *et al.* [81]. Although this panel was originally designed for an aluminium alloy stronger than the AA2024-T3 (used in this work) it has a 4 mm thick base plate, the same thickness of the previously validated FSW numerical model. The other two panel geometries consist in variations of the previous one, with a blade stiffener.

The length of the panels in which the structural analyses will be performed is 600 mm. Nonetheless, the FSW analyses were performed for panels not only with 600 mm but also with a length of 750 mm. In panels with 750 mm, the structural numerical analyses will focus only on the middle part of the panel (600 mm), while the remaining parts in both edges (75 mm, in each side) will serve to avoid the effects associated to the beginning and end of the weld located close to the transverse edge (see sections 5.4.1 and 5.4.2). This will allow inferring about the influence of these effects on the structural resistance of the parts.

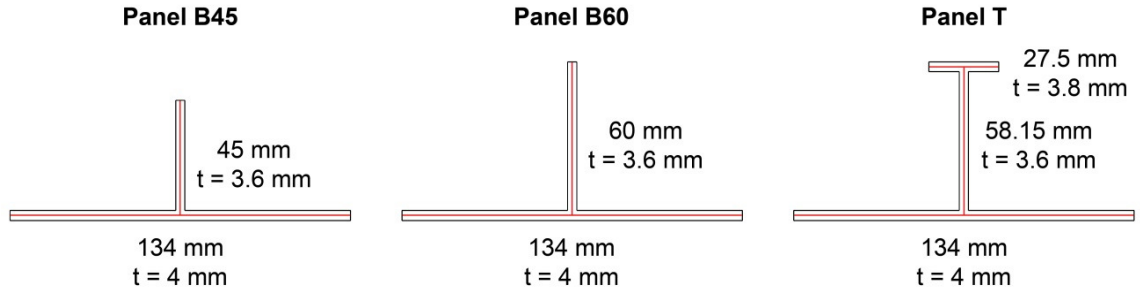

Figure 5.1: Cross-section of the stiffened panels, and mid-thickness reference lines and respective dimensions.

5.2. Finite element model

The FE model is similar to the one used for the simulation of single plate welding (presented in the previous chapter), namely concerning the material definitions. The FSW simulation included three steps, as described in Table 5.1. In the first step, the heat source (corresponding to the tool) moved along the weld line, starting from 12 mm from the starting transverse edge and finishing at 19 mm from the other transverse edge (concerning the position of the tool centre). Similarly to the single plate model, the trajectory was shortened, avoiding temperatures higher that those obtained in the steady state period of the welding process, at its end (see Section 4.3.2). The linear velocity of the heat source was the same used in the plate welding.

Concerning the second step, the 50 s defined for the panel's cooling were enough to achieve temperatures not higher than 2º C above room temperature in the whole panel. The third step simulated the removal of the welding supports. After the welding analyses, a last step was included to add the ageing effects, in which the material properties acquired the final yield stress magnitudes (the correct for structural applications).

The mechanical and thermal boundary conditions during each stage of the analysis are schematically represented in Figure 5.2, for the panel T, being the same for the remaining panel geometries. As with the previous models adopted for the plate welding, a symmetry boundary condition corresponding to the weld line was considered. In terms of the clamping system, a restriction was considered in the displacement along the *Oy* direction for all nodes located within 30 mm from the edge of the weld, reproducing a support needed to keep the base plate of the panel in contact with the support on the bottom. Different setups were tested on the edge opposite to the weld line (using the panel T configuration) and the obtained results are presented in Section 5.3.3.

Concerning the heat output, a heat transfer coefficient was set to 1000 $Wm^{-2}K$ at the bottom of the base plate of the panel. In all remaining surfaces of the panel this variable was set to 20 $Wm^{-2}K$. In terms of heat input distribution, the different setups previously tested on the single plate welding (see Figure 4.6) were also studied in preliminary analyses using the panel T.

Table 5.1: FSW simulation steps for the stiffened panels.

Step	Action	Pseudo-time (s)
1	Tool passage (heat input)	488 (600 mm panels) 617 (750 mm panels)
2	Cooling	50
3	Clamping system release	1
	Ageing	1

Additionally, sensitivity analyses were also performed for the panel T model, concerning different mesh refinement levels and finite element formulations. Mesh refinement was tested using two different discretizations of the panel, represented in Figure 5.3. One of the meshes has square elements with 2 mm side close to the weld line, while the other has square elements with 1 mm side in the same region. In the remaining area of the panels the elements are elongated, since there is no need of a refined mesh far from the weld line. In terms of number of elements, the first model has 15,600 elements while the second has 42,000 elements, leading to computational times of approximately 7 and 16 hours (using S4RT elements), respectively. The S4T element with 5 integration points across thickness was tested, as well as the S4RT element with 5 and 9 integration points

across thickness. Most of the sensitivity analyses carried out in the stiffened panels welding were already performed using the single plate welding model. However, it is important to infer and confirm the effects of those variables in the model of a larger structure.

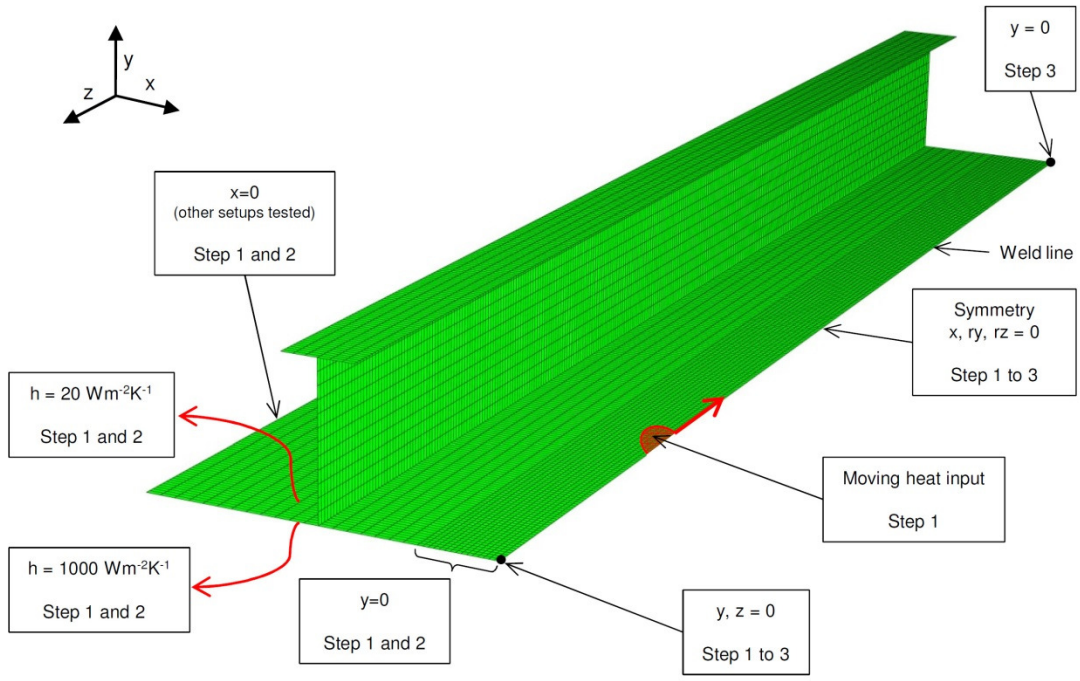

Figure 5.2: Thermal and mechanical boundary conditions for the simulation of the FSW process on the stiffened panels.

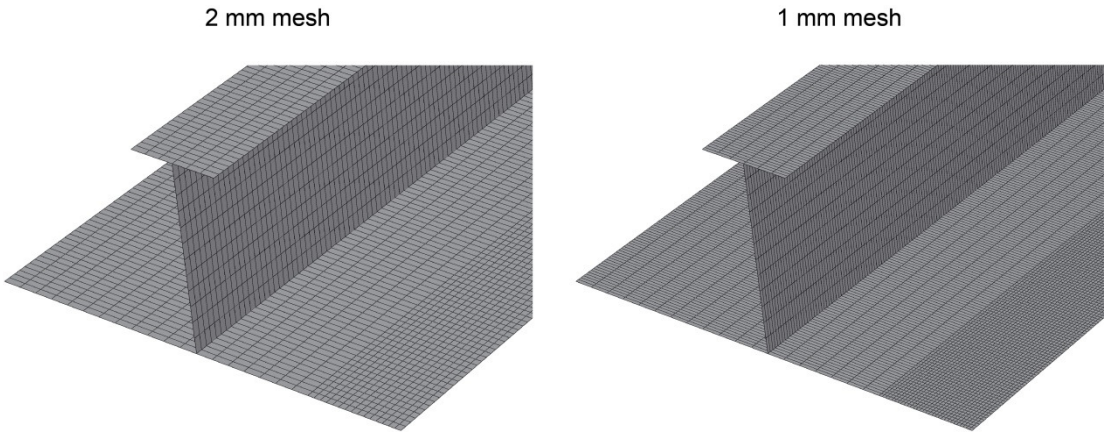

Figure 5.3: Finite element meshes tested with the panel T model.

5.3. Sensitivity study on panel T

5.3.1. Element type and number of integration points across thickness

As observed in the plate model results, the use of full integration elements (S4T) instead of reduced integration (S4RT), or the use of more than 5 integration points across thickness, did not lead to significant differences in the results. Consequently, the combination of the S4RT formulation with 5 integration points across thickness was used in all the remaining simulations, as this led to an increased computational performance.

5.3.2. Heat input distribution

All the heat distributions shown in Figure 4.6 were tested with the two mesh refinements presented in Figure 5.3. The results pointed to the same conclusions obtained for the plate welding simulation. The effects of using different heat distributions with the 1 mm mesh models were negligible. Concerning the model with the 2 mm mesh, the HD2 and HD3 led to distinct temperature distribution during the welding process, comparing to the other heat distributions. That resulted in small differences in the softening and stress distributions, as happened in the plate simulations but with a lower magnitude. The reasons for this effect were already discussed in Section 4.4.4 for the plate model.

5.3.3. Boundary conditions

Different mechanical boundary conditions on the edge opposite to the weld line were seen to lead to variations in the longitudinal stress distribution, as shown in Figure 5.4. The typical M shape distribution was obtained in all the tested setups. The main differences in the results for the distinct boundary configurations are more localized in the shoulder radius zone, compared to what happened for the single plate welding with similar boundary conditions (see Figure 4.7), due to the higher distance of the restrictions to the welded zone. The BC1, that simulates a support to keep the weld edges of the panel together during the weld, was adopted in the remaining simulations with the panels. This choice is justified to its closeness to a possible experimental setup, when compared to the BC2 and BC3 options.

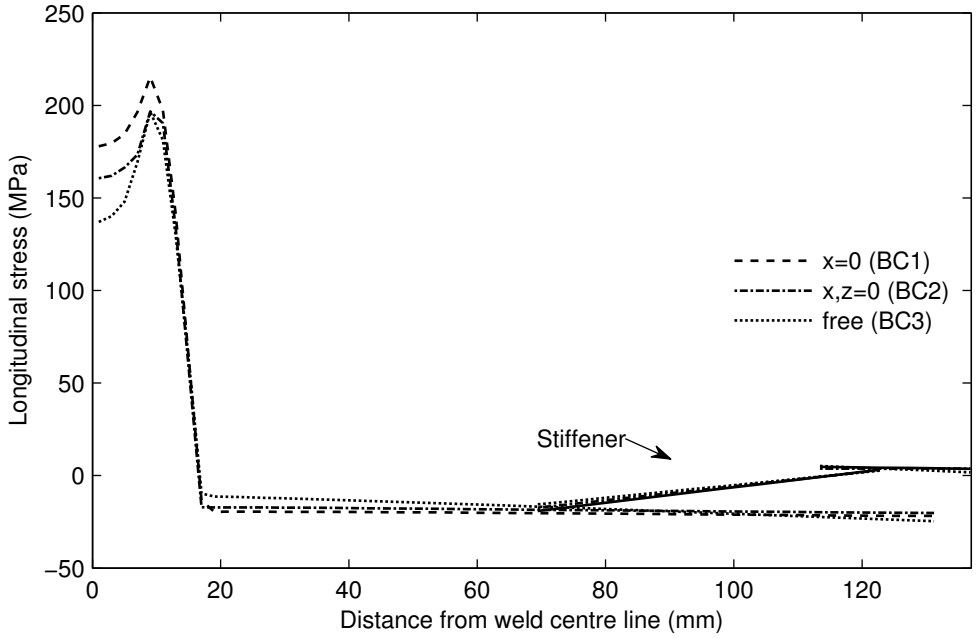

Figure 5.4: Longitudinal stress profiles in the panel T mid-length section (average across thickness) using different mechanical boundary conditions in the edge opposite to the weld line.

5.3.4. Mesh refinement

Both meshes tested led to similar results, with very small variations, as happened in the single plate FSW simulation. The results obtained in the panel mid-length are presented in Figure 5.5, in terms of softening and longitudinal stress. They are seen to be slightly affected in the coarser mesh, mainly due to spatial resolution factors. This is evident in the detail shown in Figure 5.5(a), where the location of the integration points is signalled with the × (cross) marks. It can be seen that the use of the 2 mm mesh provides less detail to define the stress peak. However, the differences in the maximum stress values, coming from the two meshes, are lower than 7 MPa. The differences concerning the softening results, as shown in Figure 5.5(b), are small and also related to the resolution associated with the spatial location of the integration points. It is thus assumed that the results obtained with the 2 mm mesh have enough accuracy for the subsequent structural analyses.

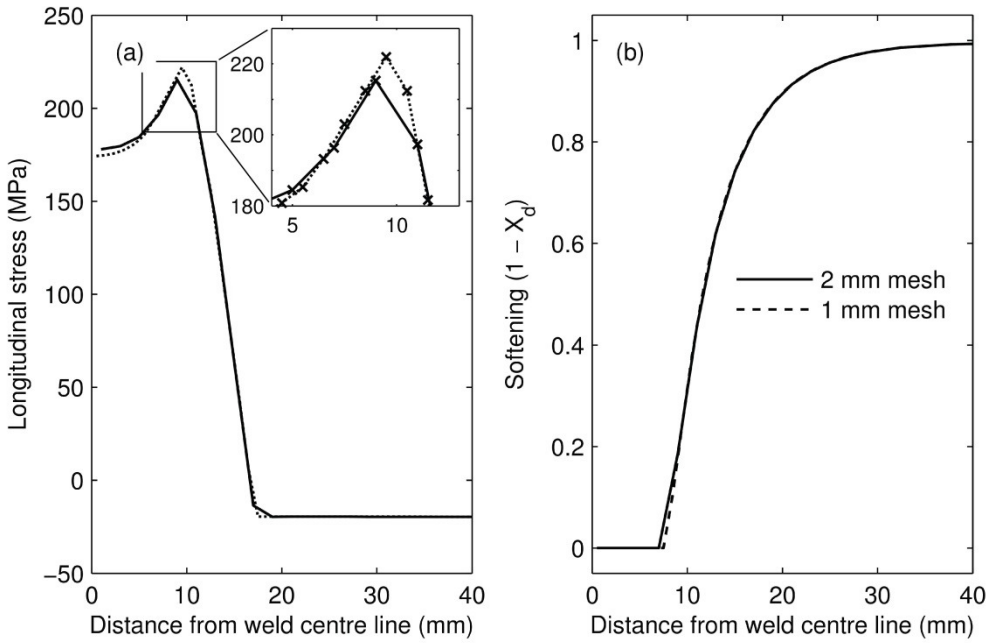

Figure 5.5: Panel T results along the mid-length section using different mesh refinements: (a) Longitudinal stress in panel T mid-length section (average across thickness) in which the × marks indicate the integration points location, and (b) softening on the mid-thickness of the base plate.

5.4. Final results

Fundamental results of the welding simulations are described in this section for the analyses performed using the panels with distinct cross-section geometries and lengths. It should be noted that, unless mentioned otherwise, the results shown are relative to the top surface of the plates. In the representation of the results of the stiffened panels with 750 mm, a dashed line is plotted defining the zone that will be submitted to loads in the structural analyses.

All the following results were obtained with the 2 mm mesh with S4RT elements with 5 integration points across thickness. The boundary conditions represented in Figure 5.2 were used and the BC1 option (see Figure 5.4) was applied on the edge opposite to the weld line. The HD1 profile (Figure 4.6) was used, since it is less complex to model and led to fewer convergence problems, with the results being the same as using a more detailed heat distribution.

5.4.1. Softening distribution

In terms of material softening, the effects of the FSW on the panels T can be seen in Figure 5.6, Figure 5.7 and Figure 5.8, for the distribution (i) along the entire panel, (ii) at mid-thickness of the mid-length section and (iii) on mid-length section, respectively. The results obtained for the panels with blade stiffeners (B45 and B60) are similar to the ones obtained for the panel T, as exemplified in the results on Figure 5.7. Consequently, they are not represented in the other distributions.

The results are presented in terms of the distribution of softening. Nevertheless, the distribution of the yield stress in the end of the welding simulation directly correlates to the one for the softening, considering minimum and maximum magnitudes of 205 and 345 MPa for softening values of 0.0 and 1.0, respectively, and according to equation (4.1).

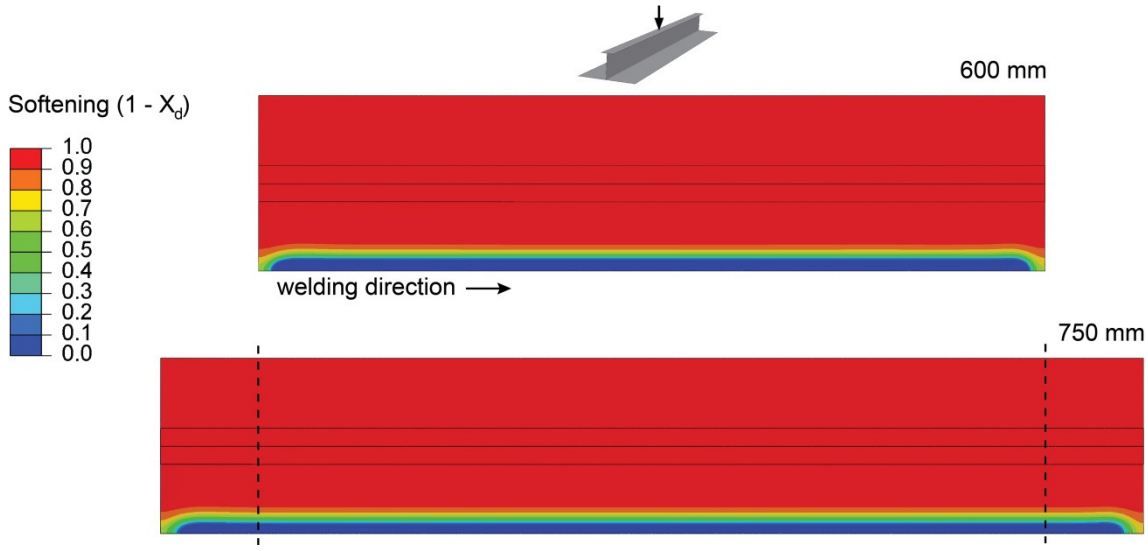

Figure 5.6: Softening distribution on the panels T with 600 and 750 mm.

Comparing the stiffened panel results with those obtained for single plate, it can be seen that the zone with lower softening value (0.0) is narrower and the softening is higher in the interval [10, 30] mm. This is related to the lower temperatures achieved in the welding simulations of the stiffened panel (see Figure 5.9) compared to the simulations of the plate (see Figure 4.18). The power of the heat input in the FSW analyses for both structures (stiffened panel and single plate) was the same. However, the stiffened panel has a much larger surface, leading to a higher heat loss, and larger volume, leading to higher heat conduction away from the location of the tool, reasons that together can explain the

lower maximum temperature. In a zone far from the weld line (for a distance higher than 30 mm) the material has properties very similar to the initial ones (base material), with a softening magnitude above 0.98.

The variation of the softening across thickness (see Figure 5.8) is more accentuated at the centre and higher than in the plate's case (see Figure 4.11). Apart from that zone, however, the differences between the top and the bottom surfaces are very small (lower than 0.001 for locations further than 30 mm from the weld line).

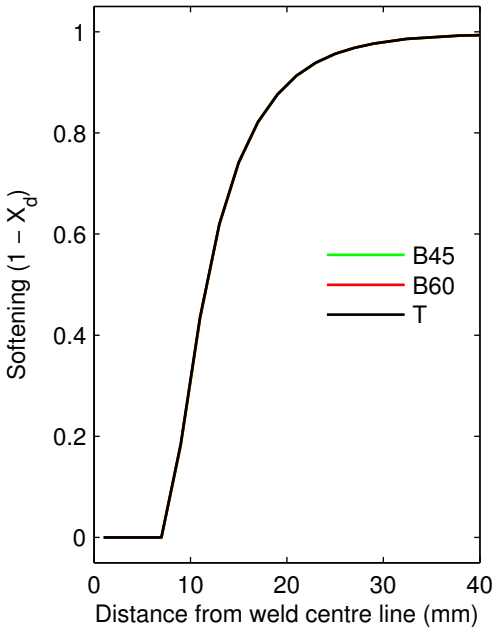

Figure 5.7: Softening on the mid-thickness of the mid-length section of the base plate of panels B45, B60 and T.

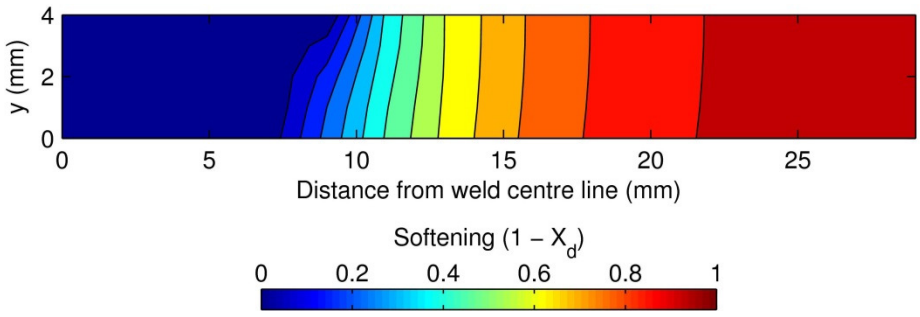

Figure 5.8: Softening on the mid-length section of the base plate of the panel T.

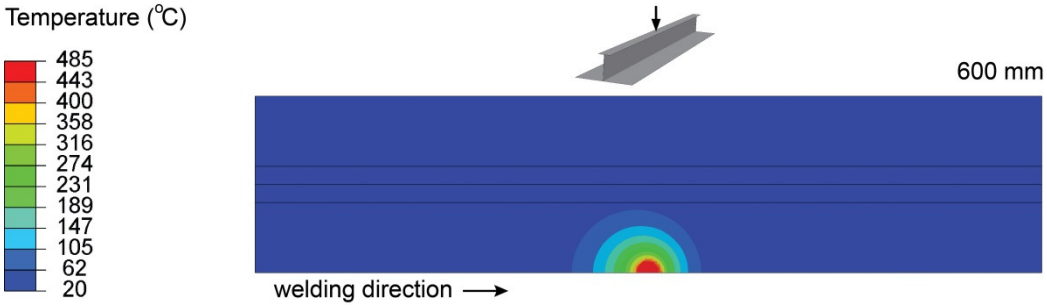

Figure 5.9: Temperature distribution when the tool passes on the mid-length of the panel T with 600 mm.

The step that allowed the simulation of material ageing (see Table 5.1), performed after the 3 stages of the FSW analyses, consisted in raising the magnitude of the minimum yield stress (associated with the fully softened material) from 205 MPa (60% of the base material yield stress) to 259 MPa (75% of the base material yield stress), according to the description in Section 4.5.2. Results in Figure 5.10 show the yield stress profile along the mid-thickness of the mid-length section, before and after the ageing effects were added to the model. As mentioned before, this procedure does not influence the residual stress distributions or the nodal displacements.

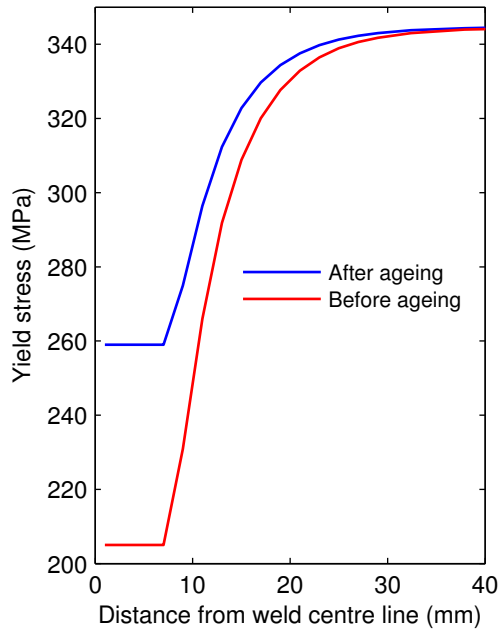

Figure 5.10: Yield stress profile along the mid-thickness of the mid-length section of the base plate of the panel T, before and after the ageing step.

5.4.2. Stress field

In terms of the residual stress field, the results of the welding simulations are globally similar for all the tested panels, considering the panels with the same length.

Figure 5.11 show the longitudinal and transverse stress distributions for the panel T. The only significant difference between the panels with different cross-section geometry can be seen in Figure 5.12, and consists in variation of the longitudinal stress on the stiffeners, in particular at mid-length. To better understand this difference it should be noted that, during the cooling on the FSW process, the arising of longitudinal tensile stresses close to the weld line is compensated by compressive stresses in the remaining part of the panel. This stress distribution forces the structure to bend, creating a convex shape in the longitudinal direction. The presence of the stiffeners minimises this effect, since they offer resistance to the distortion that, in turn, lead to a raise of the longitudinal stresses in the stiffener. As expected, in the panel with a lower (cross-section) second moment of inertia about the *Ox* direction (panel B45) the longitudinal stresses in the stiffener are higher. The results shown in Figure 5.12 are relative to the 600 mm panels. However, similar results were obtained for the panels with 750 mm.

As previously mentioned, the typical M shape distribution was obtained for the longitudinal stresses along the mid-length of the panel. The maximum tensile magnitude is much higher (approximately 100 MPa) when compared with the single plate results. This is due to the fact that in the single plate models there were no restrictions along the longitudinal direction on the edge opposite to the weld line, while in the stiffened panel, at the same location (30 mm from the weld line), the remaining part of the base plate is an additional constraint for the displacement in longitudinal direction. This restriction leads to higher compressive stresses on the panels during the tool passage, which are responsible for higher plastic strain and higher tensile residual stresses after cooling.

On the contrary, the compressive stresses that exist farther from the weld line are much lower (in terms of absolute magnitudes) on the stiffened panels than in the single plate. This can be explained by taking into consideration that the equilibrium of the tensile stresses (close to the weld line) is ensured by a much larger cross-section area on the stiffened panels, leading to larger distribution of the compressive force and, thus, to lower compressive stresses.

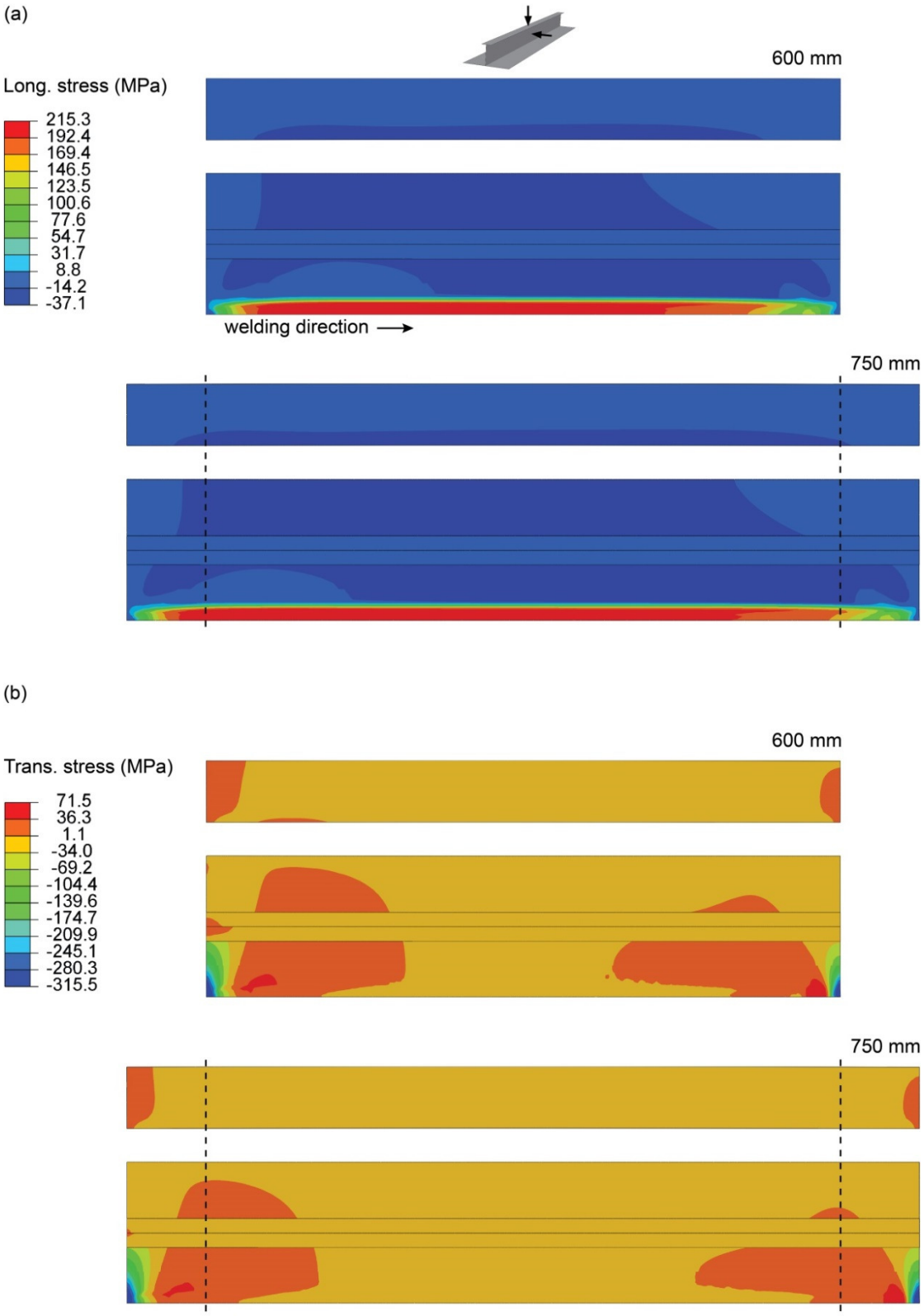

Figure 5.11: Stress distribution on the panels T with 600 and 750 mm: (a) longitudinal and (b) transverse stresses.

The distribution of the transverse residual stresses in Figure 5.11 (b) shows a high compressive stress close to both transverse edges of the panel, which equilibrates the small tensile stresses in the remaining area of the panels. The transverse stresses on the mid-length section (not represented) are close to zero, with maximum amplitude occurring on panel B45 with 600 mm, with values between -1.72 and 0.01 MPa.

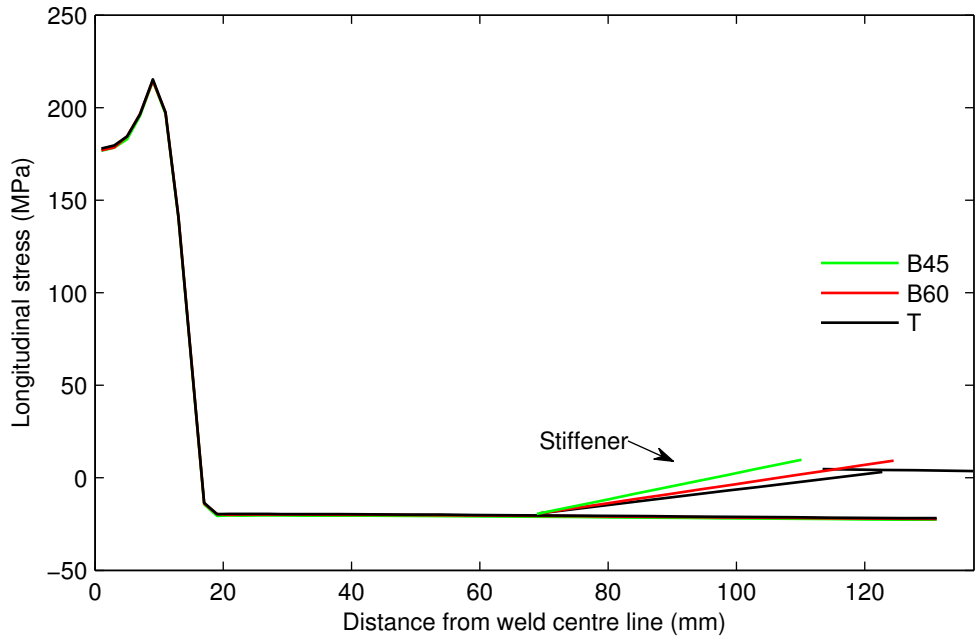

Figure 5.12: Longitudinal stresses on mid-length section of the panels (average across thickness)

The longitudinal stress distribution on the panel T mid-length section, presented in Figure 5.13, shows some degree of variation across thickness, that becomes more evident closer to the weld line, with the maximum variation (45 MPa) being achieved at 3 mm from the weld line. In the remaining parts of the panels, farther than 30 mm from the weld line (and not shown in Figure 5.13), the differences across thickness are smaller than 1 MPa. The results for panels B45 and B60 (also nor shown) are very similar to ones for the panel T, in terms of stress magnitude and distribution.

It is also interesting to realise that the variations across thickness are much higher than what was obtained for the single plate welding. This can be explained by the lower influence of the mechanical boundary conditions that reproduce the clamping system in the stiffened panel model.

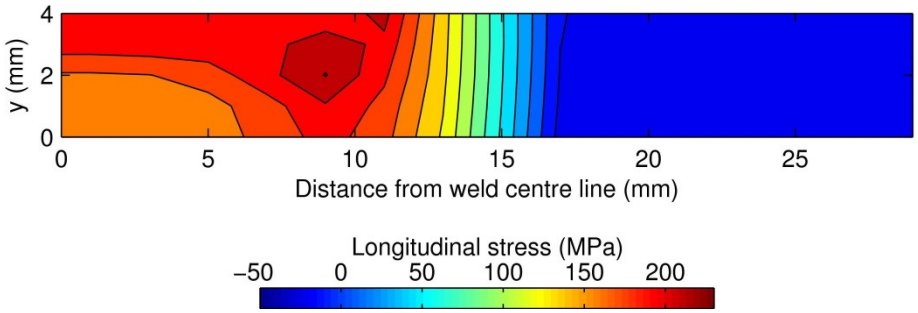

Figure 5.13: Longitudinal stresses distributions on mid-length section of the panel T (only the part closer to the weld line is shown).

5.4.3. Distortion

The deformed shape of the panels after welding is shown in the Figure 5.14 for the 600 mm panels. The out-of-plane displacements, on the weld line and on the opposite edge, are shown in Figure 5.15 for the panels with 600 and 750 mm. The typical distortion after FSW the process [60, 61], consisting of an inverted saddle shape, was obtained in the panels.

The distortion, in terms of shape and magnitude, is similar for panels with the same stiffener design but different length (considering only the central part with 600 mm in the 750 mm panels), as shown in Figure 5.15. However, small differences can be found close to longitudinal ends.

The V-shape in the transverse direction is quite similar for the whole set of tested panels, in terms of displacement magnitude, and nearly constant along the longitudinal direction in each panel. Concerning the longitudinal convex shape, the magnitude decreases for panels with higher (cross-section) second moment of inertia about the *Ox* direction, as can be seen in Figure 5.15. As previously mentioned, the stiffeners offer resistance to deformation forced by the residual stresses that arises during the welding process. Therefore, panels with higher cross-section moment of inertia exhibit lower deformation, together with lower longitudinal stresses in the stiffener.

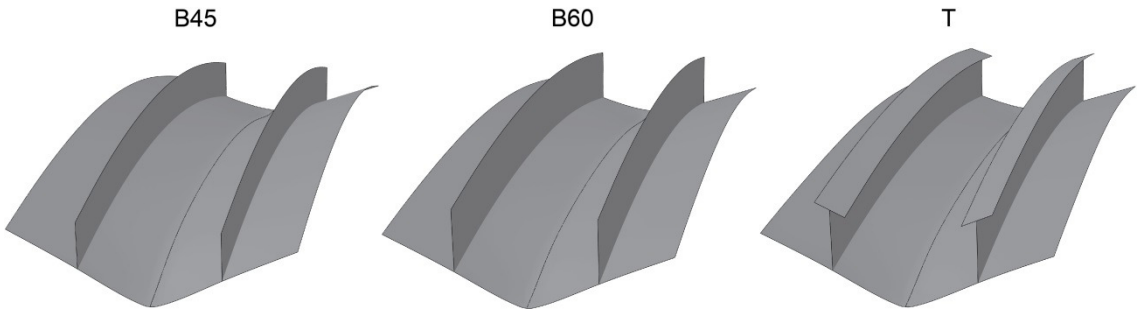

Figure 5.14: Deformed shapes obtained in the end of the FSW simulation (mirror view on the weld line symmetry plan and amplified 50 times along *Oy*).

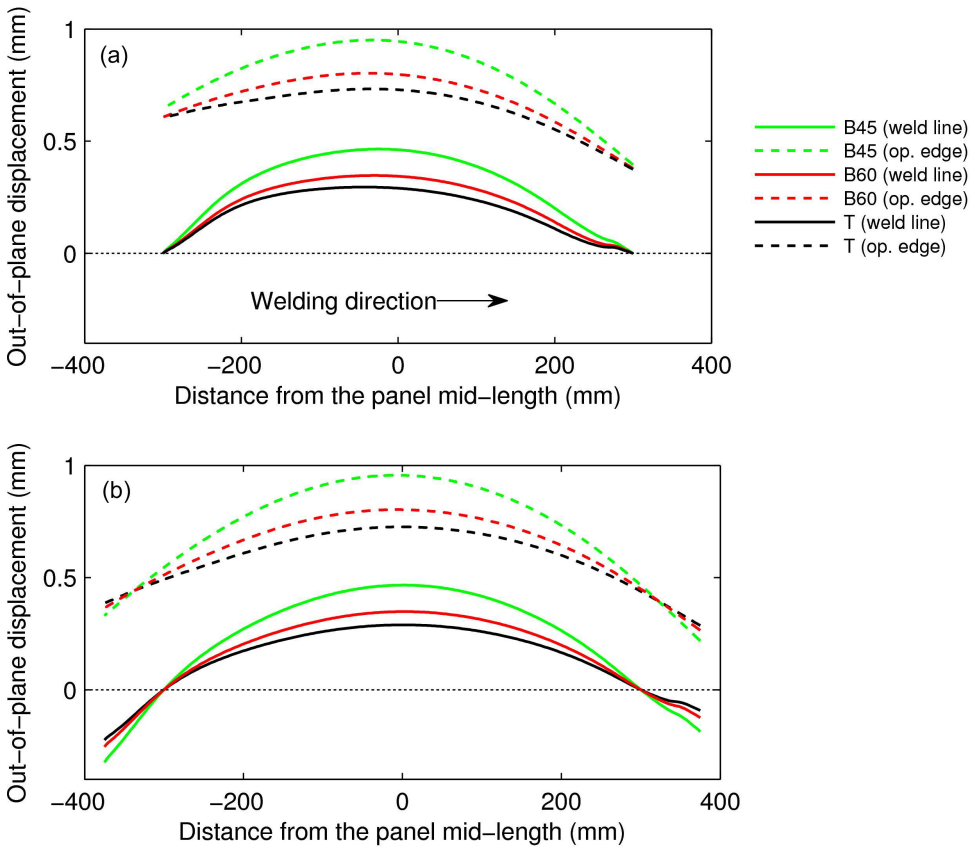

Figure 5.15: Displacements at the end of the FSW simulation along the weld line and the opposite edge in the panels with (a) 600 mm and (b) 750 mm.

5.5. Final remarks and conclusions

The model sensitivity study led to conclusions similar to those obtained for the single plate model, except in terms of the influence of the boundary conditions that reproduce the clamping system. The model of the stiffener panel showed a much smaller influence of this parameter on the final results when compared to the single plate model.

The mesh used for the final analyses was the coarser one (2 mm mesh), since the results showed insignificant differences compared to the ones obtained with the 1 mm mesh, with the computational times being much lower.

In terms of softening, the final results were similar for the panels with different stiffener geometry. The zone with a full softened material is narrower for the panels than that in the plate welding, due to the lower temperatures achieved in the stiffened panel welding.

The stress distribution results were similar for the different panels, except in the stiffeners zone. The distortion level was also similar in terms of the shape pattern but different in terms of magnitude, comparing results for panels with distinct cross-section. For panels with lower (cross-section) second moment of inertia, it was verified a higher out-of-plane displacement in the base plate and a slightly higher longitudinal stress magnitude in the stiffener. In terms of maximum magnitude, the longitudinal stresses obtained after the welding of the stiffened panels were almost twice higher than the ones obtained for the single plate.

As a last remark, it is important to comment the results for the 750 mm panels, in which is intended to exclude the effects of the welding close to the transverse edges (*i.e.,* it is intended to test just the steady state welding properties) in subsequent structural analyses (Chapter 7) by only loading the central part with 600 mm. In terms of softening (see results in Figure 5.6), the zone for the structural analyses did not include the lower magnitudes of softening observed at the edges. In terms of residual stresses (see results in Figure 5.11), the more relevant variations close to the transverse edges were not included in the zone to be considered in the structural analyses. In terms of the distortions levels (see results in Figure 5.15), the results regarding the zone considered for the structural analyses were similar in terms of shape and magnitude comparing the panels with different lengths, although there are some small differences more noticeable close to the transverse edges location (-300 and 300 mm apart from the panel centre).

Chapter 6

Review of FE modelling of stiffened panels for buckling analysis

The structural analysis of stiffened panels under longitudinal compression involves dealing with issues that, globally, cannot be properly accounted for using analytical or empirical methods. These are, for example, material nonlinearities, complex boundary conditions and structural distortions, considering a large range of panel's geometries. In these cases, the FEM is a good option and has been used by several authors with different software packages, such as Abaqus [81-86], ANSYS [87-90], LS-DYNA [90], ULSAS [90] and MSC Marc [90], only to name a few.

In the following, a review of the literature is presented focusing on the most relevant details of the numerical modelling of flat aluminium stiffened panels under longitudinal loads. Relevant data on the analysis of steel and composite stiffened panels is also presented to allow for a complete description of the modelling details. It is important to mention that similar analyses involving curved panels and/or composite structures can have specific modelling details that are not covered in the present review.

6.1. Finite element formulation and mesh refinement

A correct selection of the proper finite element formulation and mesh refinement are fundamental for a good accuracy of the results and reduced computational times. In terms of element formulation, the great majority of the works that simulate the longitudinal compression of stiffened panels use a discretization based on shell elements. Nonetheless, some authors employ solid elements in their models [81, 82, 91]. The use of shell elements in these structures makes the meshing process simpler and faster, when compared to using solid elements. Figure 6.1(a) and (b) represent the discretization of a thin plate using one solid element and one shell element, respectively. Shell elements typically rely on a reference surface, usually in the mid-thickness of plate, where the nodes are located.

Quadrilateral shell elements are those mostly used, with variations in the number of nodes and type of integration. It terms of number of nodes, elements with 4 and 8 nodes are common. The former are linear (first-order) interpolation elements while the latter are quadratic (second-order) interpolation elements. Each node has usually 6 degrees of freedom, consisting in 3 translations and 3 rotations. The distribution of nodes for these formulations is represented in Figure 6.2, which also shows the in-plane distribution of the integration points. The number of integrations points across thickness (not shown in the figure) can be defined depending on the problem, as well as its distribution along this direction, that can follow different quadrature rules, such as the Simpson or Gauss rules. These last details about the element formulation are often not mentioned in published works within this context.

Shell elements with 4 nodes and reduced integration are the most commonly used in the discretization of stiffened panels for structural analyses. Authors using the Ansys software package [68] frequently adopt the Shell43 elements (4 nodes) [87, 88, 90, 92]. Alternatively the Shell181 (8 nodes with reduced integration formulation) can be used if convergence is not obtained with the lower order elements [68, 88, 93].

Regarding the use of the Abaqus FEA package, many quadrilateral shell elements have been tested by several authors [62, 83, 84, 94]: S4R (4 nodes and reduced integration), S4 (4 nodes and full integration), S8R (8 nodes and reduced integration) and also S8R5 (8 nodes, reduced integration and 5 degrees of freedom per node, instead of the usual 6). Elements with 4 nodes and reduced integration, with advantages in terms of computational time when compared with the other element formulations, are often chosen

in such analyses (*e.g.* [62, 83, 84, 94]). Small differences in the results are reported in the literature using S4R or S8R [84]. Nevertheless, Lynch *et al.* [83] mentioned that second order elements can lead to convergence difficulties during the analyses, recommending the use of first order elements, in some cases.

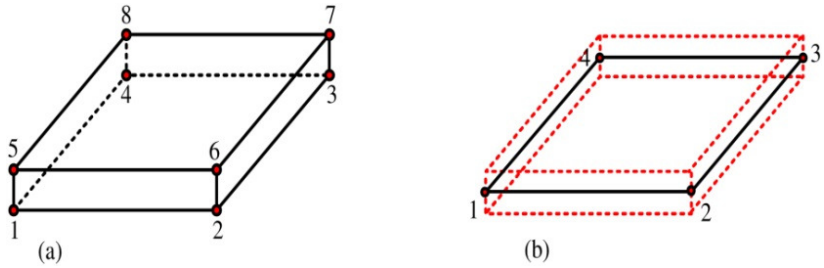

Figure 6.1: Comparison between (a) solid element and (b) shell element when modelling a thin-walled part (adapted from [95]).

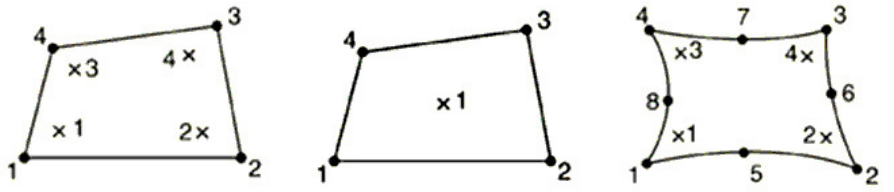

Figure 6.2: Location of nodes (●) and integration points (×) in different shell element formulations [26].

The use of specific finite elements to model the particularities of welded or riveted joints has also been studied by several authors [83, 84, 94, 96]. It should be noted that the use of distinct approximations and modelling methodologies to simulate the joints led to significant differences in the prediction of the panels' behaviour.

Regarding mesh refinements, recommendations mentioned in the literature about the optimum refinement level take into account the buckling modes of the panels. For instance, the studies performed by Lynch *et al.* [83] defined a minimum of 4 quadratic elements (9 nodes) with reduced integration per buckle half wave. Other convergence studies using first-order elements with reduced integration, performed by Quinn *et al.* [62]

and by Murphy *et al.* [97], concluded that a minimum of 4 elements (5 nodes) and 6 elements (7 nodes) per buckle half wave should be used, respectively.

6.2. Methodologies for problem solving

Modelling the behaviour of panels under compression involves dealing with instability (buckling and collapse) effects. In particular, the post buckling behaviour may include sudden changes in the mode-shape, commonly referred as mode-jump, mode-switch or mode-change [98]. These abrupt changes, where the load/displacement response may show a negative stiffness and the structure must release strain energy to remain in equilibrium, require specific modelling approaches [4, 26]. To this end, several methodologies are mentioned in the literature, such as:

- Quasi-static analysis using an arc-length method;
- Quasi-static analysis with the aid of artificial damping;
- Dynamic analysis;
- Hybrid methodologies.

Despite these possibilities, most of the works focusing on FEA of stiffened panels under longitudinal compression do not explicitly specify or describe the methodology that was used. A brief description of these methods is presented in what follows, with more emphasis on the first two, since they were applied in this work (Chapter 7).

The typical behaviour of stiffened panels under longitudinal compression, in terms of load/displacement curves, may include the effects represented in Figure 6.3. The segment of the curve on the right ("snap-back") shows the behaviour that can appear associated to a mode-change. A common *quasi*-static analysis with incremental force control, represented in Figure 6.4(a), or with incremental displacement control, represented in Figure 6.4(b), will finish in the neighbourhood of the turning point associated with force decrease or with displacement decrease, respectively. Such problems may be solved with an incremental arc-length control methodology, represented in Figure 6.4(c). In this method, an additional variable (named the arc-length) is used to measure the progress of the solution along the static equilibrium path in load/displacement space regardless of whether the response is stable or unstable [4, 5, 26]. Different formulations have been proposed for the selection of the most suitable increment, such as Riks' [99] and Crisfield's [100] methods, among others [101, 102]. A modified Riks algorithm, as

implemented in Abaqus [26], has been applied in some works in the literature that focus on the prediction of the behaviour of stiffened panels under compressive loads, including some sensitivity analyses [7, 81], and also on simulations involved in the optimisation of the cross-section geometry of stiffened panels [82, 91].

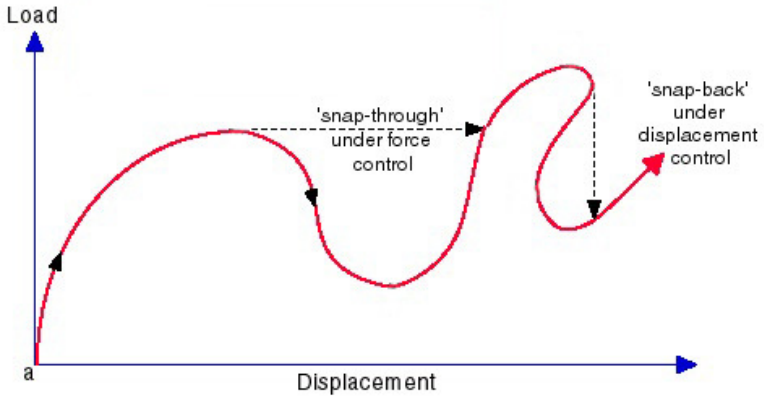

Figure 6.3: Loading path showing an unstable response [103].

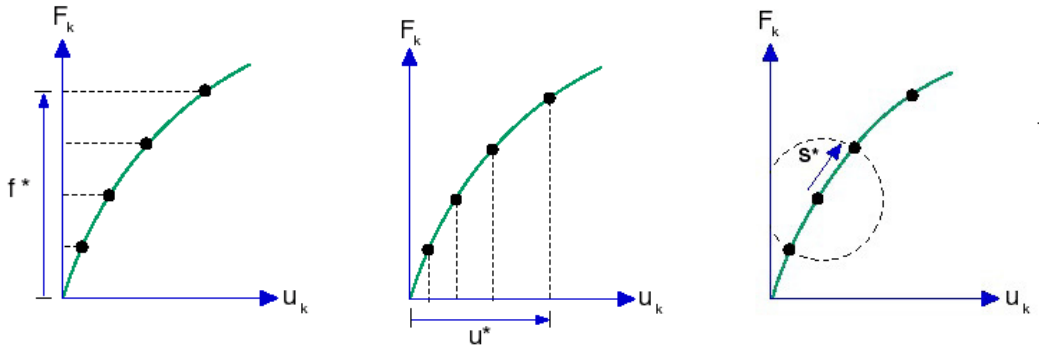

Figure 6.4: Distinct incremental methodologies (adapted from [103]).

Another approach to solve the problem is the use of a *quasi*-static analysis with an incremental displacement control, involving damping effects to stabilize the behaviour of the structure. While the simple use of incremental displacement control would fail in snap-back cases, the use of damping (dissipation of energy) can lead to a numerical solution that follows the vertical dashed line shown in Figure 6.3 (right side) until the displacement starts to increase again. This methodology has been used, for instance, in numerical analyses of aluminium panels with riveted stiffeners [94]. It has also been used in the FEA

of the mechanical response of carbon fibre composite stiffened panels [104]. This last work and also Abaqus manual [26] point out the importance of a proper adjustment of the damping parameter (ξ), since low values can lead to convergence problems while high values lead to inaccurate results. An optimal value requires a trial and error process until a converged solution is obtained and the dissipated stabilisation energy is small enough. For example, Figure 6.5 represents the load/displacement curves obtained for the compression of a stiffened panel (focusing on the mode-change zone) using different values for the damping parameter . In this case, the use of a higher magnitude than the optimal value ($\xi = 2\times10^{-6}$) clearly led to errors in the behaviour prediction [104].

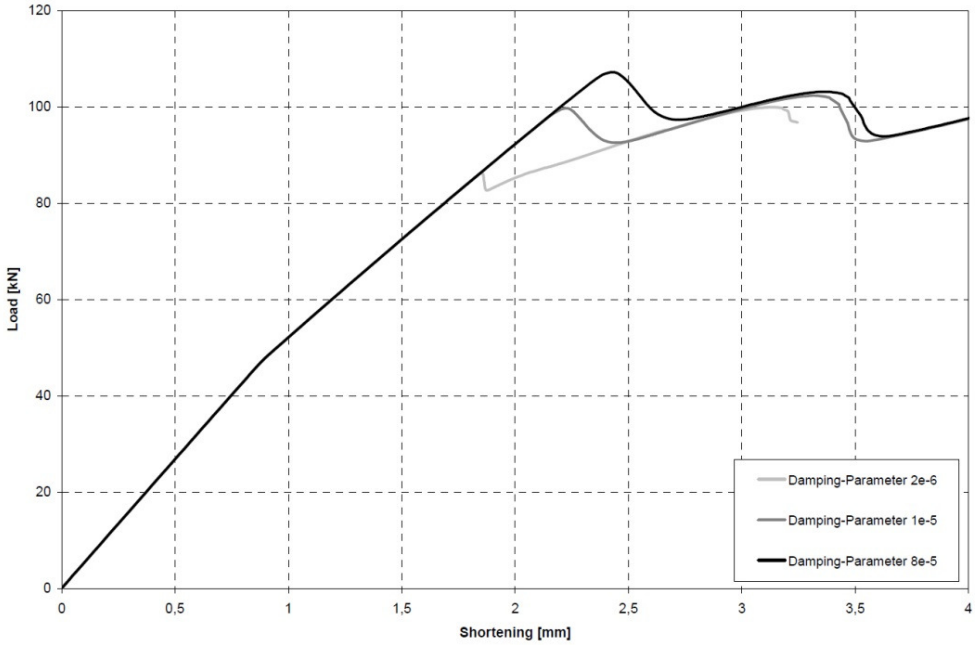

Figure 6.5: Influence of the damping parameter in the analyses results [104].

Regarding the remaining two strategies, the use of a dynamic procedure can lead to a valid solution in the analysis of instability phenomena. Implicit or explicit methodologies can be used, although implicit dynamic methods can be computationally expensive [5, 26, 90].

Finally, the use of a hybrid procedure, in which two or more of the aforementioned methodologies (or other) can be used in sequence, is referred to as an option to solve these problems, with benefits in terms of computational time [5, 26]. As an example, the Abaqus

manual suggests to start the analysis with a static procedure and, afterwards, switching to an implicit dynamic procedure as soon as the static solution becomes unstable [26].

6.3. Modelling of imperfections

Manufacturing processes can be responsible for imperfections that may affect the structural efficiency of a stiffened panel. One of those imperfections refers to geometrical distortions, which can be originated by processes such as drilling, riveting and welding, processes related to the fabrication of aluminium sheets, and extrusion and machining processes used to obtain ISP. As mentioned before, welding processes (fusion or FSW), besides the geometrical imperfections, are also responsible for material softening and build-up of residual stresses. An accurate prediction of the structural behaviour of reinforced structures using the FEA should therefore account for all these effects. Some of the most common modelling methodologies adopted for this purpose are described in the following paragraphs.

6.3.1. Geometrical imperfections

Different methodologies are used to include the initial geometrical imperfections in the models. These are associated with distinct imperfection shapes that can be applied with different magnitudes. Each methodology is separately described below.

Use of the deformed shape obtained after applying pressure to the plate

In this method a uniform lateral pressure is applied on the stiffened panel model and a linear elastic FEA is carried out, as schematically shown in Figure 6.6. In a trial and error methodology, this step is repeated until the maximum deflection of the plate reaches the intended magnitude (W_{0max}). When this condition is satisfied, the nodal positions are introduced in a new non-linear FE model to perform the compressive structural analyses. Doing this way, the geometrical imperfections are included without inducing stresses in the numerical model. This methodology is mostly used in the study of marine structures [87, 88, 90, 92, 93, 105].

Khedmati *et al.* [88] and Smith *et al.* [106] defined the value of maximum magnitude of the initial imperfection using a coefficient that varied depending on the effect

of the welding process: slight, average and severe. Varguese [107] investigated and evaluated the average value deflection in ship plating that can be used with this method.

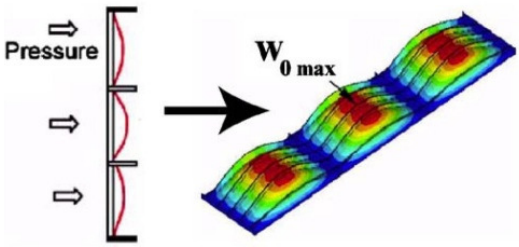

Figure 6.6: Procedure to generate initial imperfection applying pressure to a panel base plate [88].

Rigo *et al.* [90] mentioned that this procedure of introducing geometrical initial imperfections is not common, although it has been used because the modelling task is quite simple. The main objective of this work is to compare distinct FEM software and models, as well as to perform sensitivity analyses regarding several parameters, such as the existence and distribution of a HAZ, shape and magnitude of the initial geometrical imperfections, and the presence and distribution of residual stresses.

This procedure to model geometrical imperfections was also used by other authors to perform sensitivity analyses [87, 88, 92], as well as in a study carried out to create empirical formulations for the analysis of panels subjected to combined forces [105].

Offset of the nodes in the mid-length of the panel

Yoon *et al.* [81] and Caseiro *et al.* [82, 91] used a very simple method to apply initial geometrical imperfection to a given FE model. It consisted in the displacement of nodes located in the mid-length of the panel along a direction normal to the base plate, as represented in Figure 6.7. This imperfection works as a buckling trigger, leading to a perturbation in the structures that ultimately leads to buckling. In those works the geometrical imperfection was applied with a magnitude of 1/1000 of the length of the panel. This was used in the work of Yoon *et al.* [81] for a study on the effect of the existence (or non-existence) of a HAZ in the panel structural behaviour. It was also used in the optimisation process of the transverse geometry of panels, considering several types of

stiffeners' shapes, without accounting for welding effects on the material [82] and also considering FSW effects [91].

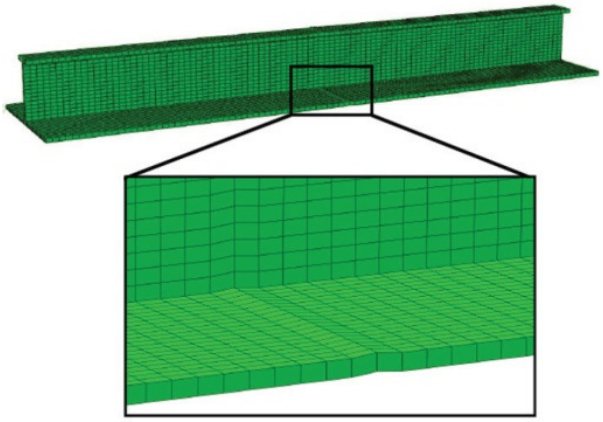

Figure 6.7: Detail of the geometrical imperfection applying an offset to the nodes in the mid-length of the panel [91].

Use of imperfection shapes defined by parametric equations

Paik *et al.* [108] presented a database of initial imperfections that can occur during welding fabrication of aluminium stiffened panels for marine applications. They mentioned different primary forms of geometrical imperfections, namely, initial distortion of the plate (between stiffeners), column type initial distortion of stiffeners, and sideways distortions of stiffeners. The present method of introducing the initial geometrical imperfections is based on sinusoidal equations that allow for the creation of multiple wave shapes. For each geometrical imperfection mentioned above, the intended shapes (with the required number of half-waves) with the intended magnitudes are separately superimposed in the model. The prediction of the shape to be applied can involve the use of eigenvalue analysis [89].

The described method was used by Paik *et al.* [89] in numerical analyses performed to develop empirical formulations. It was also used in other work that focus on the study of aluminium panels subjected to compressive loads [109].

A similar methodology was used in the study of steel stiffened panels [110]. Figure 6.8 presents the equations and corresponding shapes used as initial geometrical imperfections.

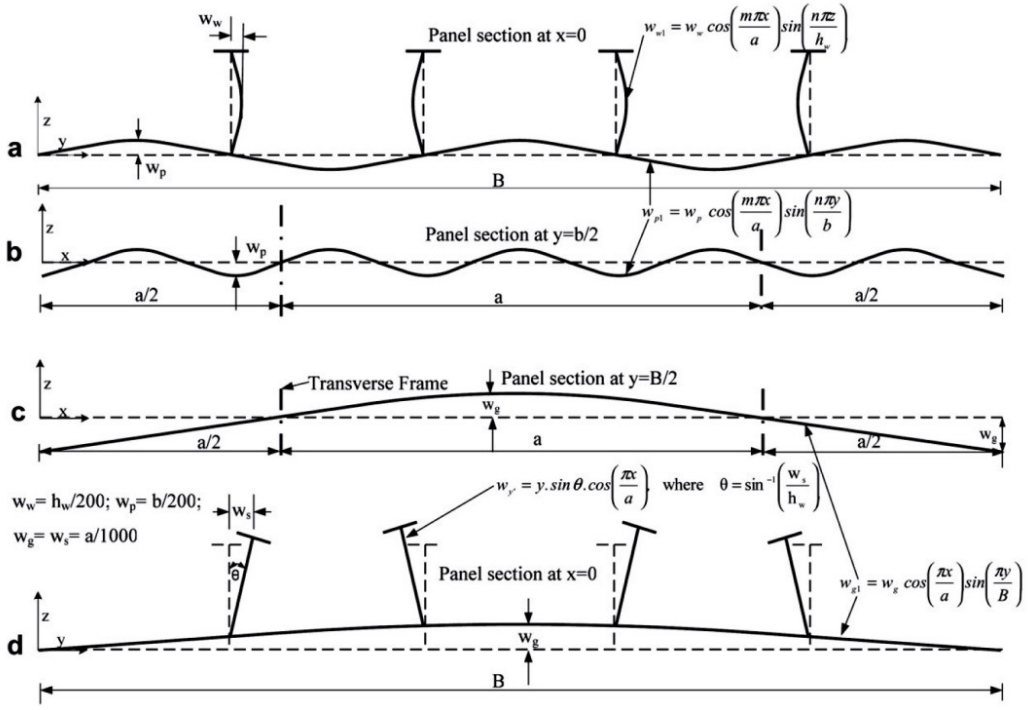

Figure 6.8: Initial geometrical imperfections shapes and the corresponding equations [110].

Use of measured distortion shapes from experimental specimens

In some studies, the geometrical imperfections introduced in the model correspond to the shape of the panel after the building process. The measurement of the distortion of a panel specimen is commonly performed before an experimental loading test and usually involves the use of a coordinate measuring machine (CMM) [62, 94, 96, 111, 112]. Some of these measurements included just the base plate, while others included both the plate and stiffeners distortions. In some cases, it is mentioned that the measured displacements were submitted to a smoothing process before being introduced into the numerical model for the structural analyses, as described by Campbell *et al.* [94], using a quadratic curve fitting, and by Wilson *et al.* [111], using a sine curve fitting by the least squares method.

This kind of initial imperfections were used in the study of compressive strength of prismatic [62] and non-prismatic [112] sub-stiffened panels. In both works, the results were compared with those obtained using an eigenmode imperfection. The experimentally measured displacements and also the eigenmode imperfections used by Quinn *et al.* [62] are shown in Figure 6.9, as an example. In this case, the use of different imperfection shapes in the numerical model led to distinct collapse load magnitudes and, in some cases, even different collapse modes.

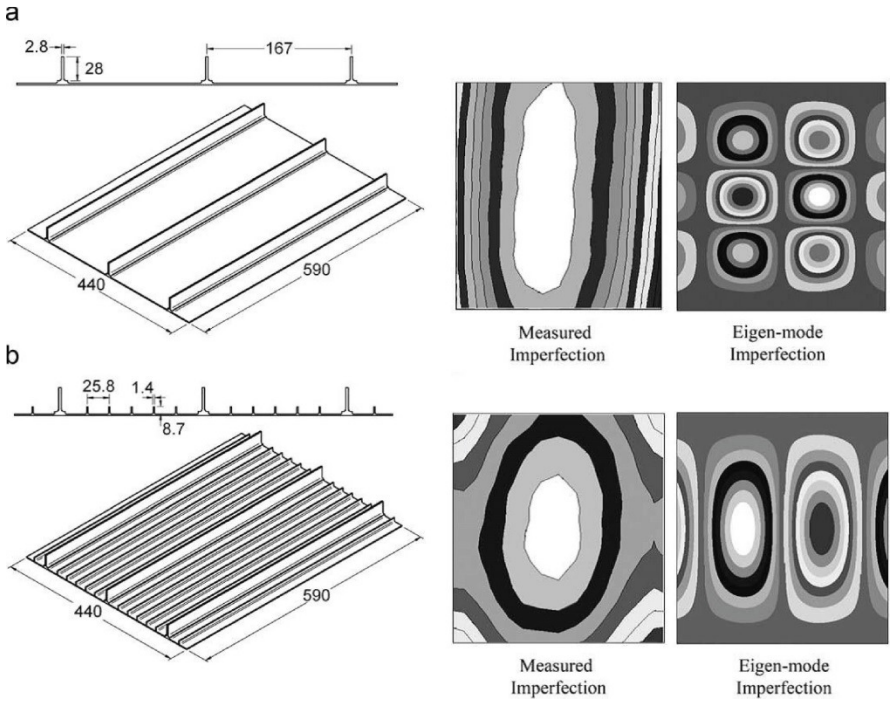

Figure 6.9: Comparison between the imperfection from experimental measurement and from eigenvalue analyses for panels (a) without and (b) with sub-stiffeners [62].

Campbell *et al.* [94] tested different imperfection shapes and magnitudes, including the one measured experimentally. The sensitivity of the panel in terms of collapse load magnitude was assessed. The measured imperfections were also introduced in the numerical model in the works of Murphy *et al.* [96] and Wilson *et al.* [111], in which sensitivity analyses on the welding effects were performed.

Use of deformed shapes generated by a residual stress input

This kind of geometrical initial imperfection results from the introduction of residual stresses, associated with the welding process, into the model and a *posteriori* numerical step to enforce equilibrium, in which the panel acquires some distortion. Thereby, the final model with geometrical imperfections included a residual stress distribution slightly different from the one initially added [96, 113, 114]. This methodology is applied and described in detail in Section 7.1.3.2.

In the work of Murphy *et al.* [113], the shapes generated using the induced residual stresses were used in the study about the influence of the location of the FSW joints and in sensitivity analyses of welding effects in the collapse load. An example of the deformed

shapes arising from different residual stress inputs (concerning different welded joint locations) is shown in Figure 6.10.

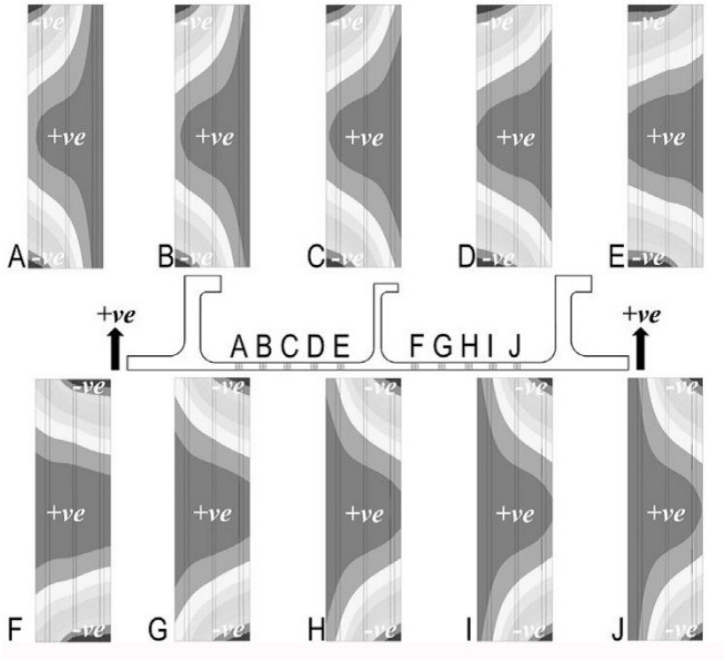

Figure 6.10: Panel deformed shapes generated by the residual stress input concerning models with distinct location of the FSW joint as indicated by the uppercase letters ("+ve" concerns out-of-plane displacements toward the stiffeners direction and "-ve" out-of-plane displacements in the opposite direction) [113].

Murphy *et al.* [96, 114] also used this methodology to perform sensitivity analyses on the welding effects on the panel strength. One of these works [96] compared the collapse load magnitudes obtained using: the described method, the shape obtained from experimental measurement and another imperfection shape that resulted from the combination of measured geometrical imperfection and the induced by residual stress field.

Use of the deformed shapes coming from previous buckling analysis

The present methodology was presented by Paulo *et al.* [7]. It required a preliminary numerical analysis, with the same model used for the final structural analysis but without any geometrical imperfection. It is important to mention that, in this case, the model included a set of rotating loaded edges that were able to create instability and therefore trigger the buckling effects even without geometrical imperfections. The deformed shapes obtained in moment of collapse were introduced as initial imperfection in the final

numerical analysis. For this purpose, nodal displacements were normalized using the maximum displacement value obtained and, afterwards, multiplied by the intended maximum initial imperfection. As an example, Figure 6.11 allows to compare the shape of initial imperfection obtained by an eigenvalue analysis (EV1) with those obtained using the present methodology (COL), for different panel models.

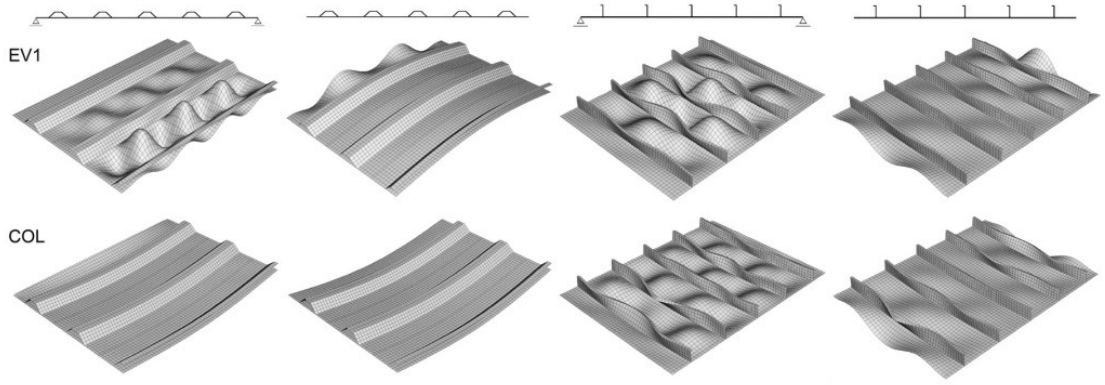

Figure 6.11: Imperfection shapes (magnified) from eigenvalue analyses, corresponding to first eigenmode (EV1), and those obtained from the onset of collapse (COL) [7].

The effects of the shape and magnitude of the initial geometrical imperfections on the collapse load were also studied by Paulo *et al.* [7]. It was concluded that the present methodology led to the lowest collapse load (in most cases) for a given imperfection magnitude.

Use of deformed shape from eigenvalue analysis

The present methodology involves carrying out an eigenvalue analysis using the same definitions as in the final structural analyses (regarding mesh, material and boundary conditions) and was adopted by several authors. The shapes corresponding to the first eigenmode for different panels and boundary conditions are shown in Figure 6.9 and Figure 6.11.

For the final structural analyses, the shape corresponding to a specific eigenmode (or more than one) is imposed with the intended magnitude. The final model is stress free before the compressive load is applied. The first buckling mode is often used as initial geometrical imperfection [62, 83, 84, 97, 112, 115]. Nevertheless, some authors [7, 94]

also use higher eigenmodes in their numerical analyses. Campbell *et al.* [94] and Paulo *et al.* [7] compare the collapse load magnitudes obtained using different eigenmodes and alternative imperfection shapes.

6.3.2. Material softening

The material softening associated with the welding processes can be included in the model considering a pre-defined zone (corresponding to the welded joint) where the material has a lower yield stress compared to the base material and, in some cases, also a distinct plastic behaviour. In the majority of published works, this zone consists in a band with fixed width along the weld line, where the affected material properties are constant [7, 81, 87, 88, 90, 92, 93, 96, 109, 111, 116]. Nevertheless, there are exceptions, such as the work of Caseiro *et al.* [91], in which the material of the welded zone was defined using different properties considering a HAZ and a NZ. The main purpose of this work was the optimisation of the cross-section of a stiffened panel.

Many sensitivity studies were performed to assess the variations on the structure's strength with respect to changes in the width of the affected zone and/or on the affected material properties [7, 81, 87, 88, 90, 92, 93, 96, 109, 111, 116]. In most works, both variables showed an influence in the panel behaviour (namely, the collapse load) when subjected to longitudinal compressive loads. A reduction in the collapse load is generaly associated to an increase of the width of the affected zone and/or a decrease in the material properties (namely, the yield stress). Nonetheless, tests carried out with some stiffened panels, as the ones performed by Paulo *et al.* [7], led to the conclusion that the existence of a HAZ did not affect the magnitude of the collapse load.

The impact of using different distributions of softened material, corresponding to different panel construction methods, has also been studied by some authors [87, 90, 92, 93, 109]. The work of Murphy *et al.* [113] focused on the variation of the collapse load with respect to the location of a single longitudinal FSW joint in a stiffened panel (see Figure 6.10). Khedmati *et al.* [87] tested and compared different panel construction methods, in which the softened material had different locations, as represented in Figure 6.12.

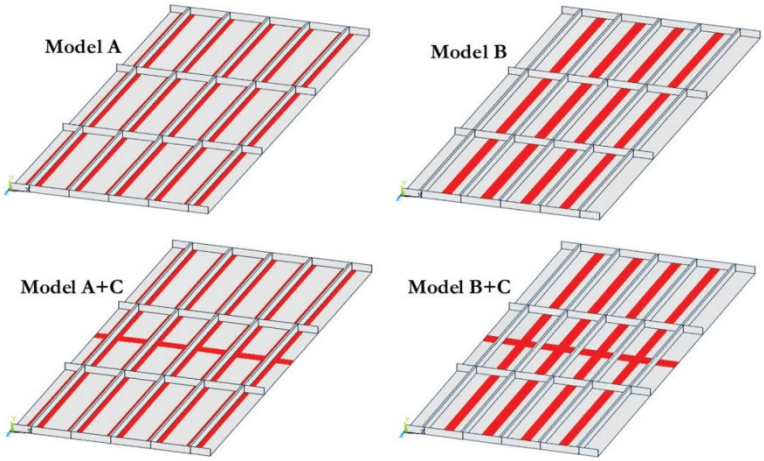

Figure 6.12: Distinct distributions of welded affected material for different panel construction [87].

6.3.3. Residual stresses

As mentioned before, the residual stress distributions coming from welding processes consist on tensile stresses close to the weld line and compressive stresses on the remaining part of the structure, regarding the stress component parallel to the weld line (longitudinal stress). Most authors do not model the transverse stress components since their magnitudes are small when compared to the longitudinal residual stresses. The modelling of the longitudinal component is usually performed by applying an uniform tensile stress in the welded zone and a uniform compressive stress elsewhere in the model. Figure 6.13 schematically represents this modelling strategy for a plate welded along its outside edges. Nonetheless, it was proposed that the stresses associated to the weld edges perpendicular to the loading direction can be ignored in the structural analysis [90, 93]. Benson *et al.* [109] compared the obtained results using only the longitudinal stresses and using both transverse and longitudinal components, and verified insignificant variations on the collapse load magnitude.

Khedmati and Pedram [93] and Benson *et al.* [109] applied the longitudinal residual stress field in their models, with the stress magnitude and the width of tensile stress zone following three different levels of damage (slight, average or severe) based on an empirical approach. Wilson *et al.* [111] tested different stress magnitudes together with variations in the HAZ in terms of width and material properties.

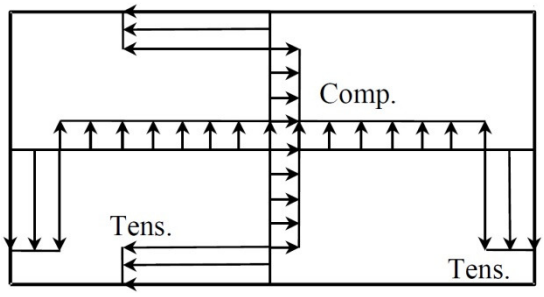

Figure 6.13: Modelling of residual stresses in a plate welded along all outside edges [108].

A specific method to model residual stresses is described in detail by Murphy *et al.* [96, 113]. As mentioned in section 6.3.1 (for geometrical imperfections resulting from a stress field), this procedure included a preliminary stage before the compression of the panel. After the residual stresses are introduced in the model, the structure in no longer in equilibrium and a numerical analysis is carried out to re-establish it, using minimum boundary conditions to prevent rigid body displacements and rotations. This stage led to distortions of the initial geometry and changes in the induced stress field, which are going to be part of the final structural analysis. The authors concluded that the existence of this stress field and its magnitude can influence the collapse load of the structures.

Chapter 7

Buckling analysis of stiffened panels

The study presented on this chapter concerns the behaviour of stiffened panels under longitudinal compressive loads. It has two distinct objectives: on the one hand, to understand the repercussions of different modelling methodologies on the structural results and, on the other hand, to assess the influence of FSW effects on the panel behaviour, namely on the collapse load magnitude. A final study including imperfection shapes from eigenvalue analyses was also performed to better understand the impact of the initial geometrical imperfection shapes and magnitude.

7.1. Model description

The stiffened panels considered in the compressive analyses are the ones previously used in the FSW simulations (see Section 5), with the same finite element discretization, allowing for an easier import of the welding effects obtained with the FSW simulations and without the need for any interpolation or extrapolation, since nodes and integration points have the same locations. This is particularly important in terms of the residual stress distribution, since it ensures model equilibrium (from the point of view of the stress fields) before the compression stage. The mesh, coming from the welding analyses, is more refined than what is recommended in the literature (see Section 6.1) and normally used.

Therefore, a new convergence study on mesh refinement was not needed for the compression analyses.

The finite element formulation used for most of the analyses was the reduced integration shell type S4R, similar to the one used for the welding analyses (S4RT) but without the thermal parameters. As previously mentioned (Section 6.1), this element formulation has good performance in terms of the accuracy/computational time ratio when compared to alternative shell formulations. Nevertheless, in some analyses, the ones performed in sequence with the FSW simulation (using a restart procedure), the S4RT formulation was used. For both shell formulations, 5 integration points were considered across thickness.

In the following, the adopted modelling is presented in detail, concerning boundary conditions, problem solving strategies as well as methodologies for the inclusion of FSW effects.

7.1.1. Boundary conditions

The mechanical boundary conditions used during the compression stage are schematically shown in Figure 7.1. Symmetry conditions were applied to nodes on the weld line and on the edge opposite to the weld line, with a symmetry plane normal to the base plate and along each one of these lines. These definitions allow simulating a larger panel with a weld join per every two stiffeners' section. However, and as a consequence of this choice, the model is capable of only reproducing the periodic buckling modes that can appear in a single section. This is however not a limitation, since those buckling shapes are those that are typically expected in these cases.

Two rigid walls were defined in each one of the transverse edges of the panels, using connector elements with 2 nodes (CONN3D2) to attach all the nodes and assuring no relative displacements between them. In one of these sections, clamped boundary conditions were applied, while in the other just the displacement along the loading direction (Oz) was allowed. On this section a load or displacement, depending on the solving methodology, was applied along the Oz direction in order to compress the panel. For the panels with 750 mm of length, only the central part (with 600 mm) was compressed. For this case, the rigid walls were defined using the nodes placed at 75 mm from each one of the transverse edges of the panel.

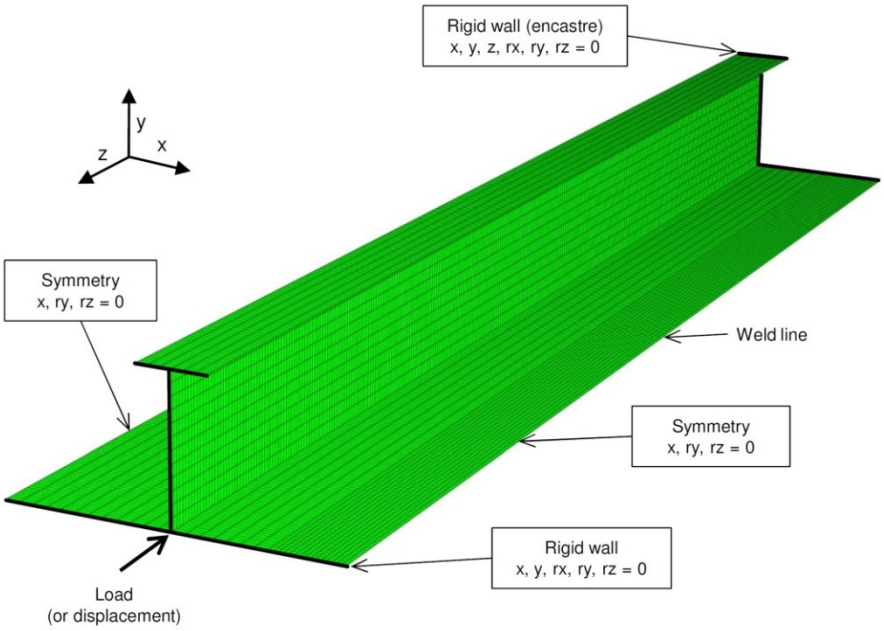

Figure 7.1: Mechanical boundary conditions for the compressive structural analyses.

7.1.2. Analysis method

During the preliminary analyses two solving methodologies were tested to predict the behaviour of the panel under longitudinal compressive loads: an arc-length method and a displacement increment control method, including damping. These two methods, based on *quasi*-static analyses, were previously mentioned in Section 6.2.

Intending to show the particularities of the results obtained using each method, two representative examples are presented in the following paragraphs. These examples concern the compression of the panels B45 and T, using stress free models with base material properties and imposing the distortion obtained after FSW numerical simulations in order to trigger the buckling.

The Riks method (arc-length method) was applied using the *RIKS command on Abaqus [26]. Either displacement or load can be impose to the moving end obtaining similar results, as expected, due to the characteristics of this methodology.

In static analyses with a displacement control method, the *STABILIZE command was used to allow for energy dissipation, and consequently to ensure stabilisation and convergence of the results. The optimal damping parameter value (ξ), *i.e.* the minimum value that leads to convergence, was determined by a trial and error approach. The collapse

loads obtained using different damping parameter values are listed in Table 7.1 and the respective load/end shortening curves are shown in Figure 7.2. The two examples show distinct buckling and collapse behaviours: for panel B45 an abrupt mode-change occurs for a load level lower that the collapse magnitude (Figure 7.2(a)), while with panel T the mode-change shown is associated with the collapse phenomenon (Figure 7.2(b)).

Concerning the results for panel B45, a convergence of results in terms of collapse load and load/end shortening curve was observed, using $10^{-6} \leq \xi \leq 10^{-11}$. With lower values of the damping parameter the analysis stopped when the mode-change occurred, as represented by the black line in Figure 7.2(a) (corresponding to $\xi = 10^{-12}$). For $\xi > 10^{-6}$ the accuracy of the results is affected, namely the prediction of the mode-change and also the collapse load, with the error magnitude increasing with the increase of the damping parameter magnitude (see Table 7.1).

Table 7.1: Variation of the collapse load magnitude using different damping parameter values.

Panel	Damping parameter (ξ)	Collapse load magnitude (MPa)	Collapse load variation (%)
B45	10^{-12}	148.04	-17.87
	10^{-6} to 10^{-11}	180.25	0.00 (ref.)
	10^{-5}	180.31	0.03
	10^{-4}	180.79	0.30
	10^{-3}	185.41	2.86
	10^{-2}	239.65	32.95
T	$\leq 10^{-7}$	256.54	0.00 (ref.)
	10^{-6}	256.61	0.03
	10^{-5}	257.02	0.19
	10^{-4}	259.33	1.10
	10^{-3}	263.58	2.77
	10^{-2}	300.04	17.09

Regarding the panel T analyses, it is possible to complete the simulation until the collapse load is reached without any energy dissipation ($\xi = 0$). However, in this kind of structural analyses it is necessary to verify if a given point corresponds to the collapse and not only to a mode-change. For that purpose, the analyses results should show an evident continuous decrease in the strength that defines the collapse of the structure. For $\xi \leq 10^{-7}$, the same collapse load magnitude was obtained. Nevertheless, the use of $\xi < 10^{-7}$ led to an

early end of the simulation after the collapse, due to convergence problems, and the results are not enough to clearly show the existence of the collapse. This fact is shown on Figure 7.2 (b) for the curves corresponding $\xi = 10^{-8}$ and $\xi = 10^{-9}$. The use of $\xi > 10^{-7}$ led to errors in the collapse load prediction (see Table 7.1).

After the optimal value of the damping parameter was determined, the two methodologies (arc-length and displacement control method with damping) could be compared. They led to similar results, in terms of the predictions of mode-changes and collapse load magnitudes. Figure 7.3 and Figure 7.4 show the results for the two examples, using panels B45 and T, respectively. The difference in the collapse load predictions using the two methods is of approximately 0.06%, for both cases. Furthermore, a similarity in the results using these two methods was observed for all the tested setups, during the preliminary and final analyses, which included different the panel geometries and distinct combinations of welding effects.

Using the displacement control with damping, the abrupt mode-change phenomenon on panel B45 was solved in a single increment without a decrease in the end-shortening due to the dissipation of energy, while using the Riks method the solution required a snap-back to deal with the same effect, as can be seen on Figure 7.3(a). The results in Figure 7.3(b) show that the deformed shape, before and after the instability, is the same using the two methodologies.

A similar pattern in the behaviour was observed for the panel T analyses, albeit in this case with the mode-change associated with the collapse, as shown in the load/end shortening curve in Figure 7.4(a), complemented with the associated deformed shapes, shown in Figure 7.4(b).

It should be noted that the definition of the parameters inherent to these methodologies (namely the initial increment value, the maximum and minimum increment sizes) can significantly affect convergence and relies mostly on the user experience. The computational costs of the two methodologies depend on the set of parameters used, although, in most of the cases, similar times can be obtained if the optimal set of increment definitions is used.

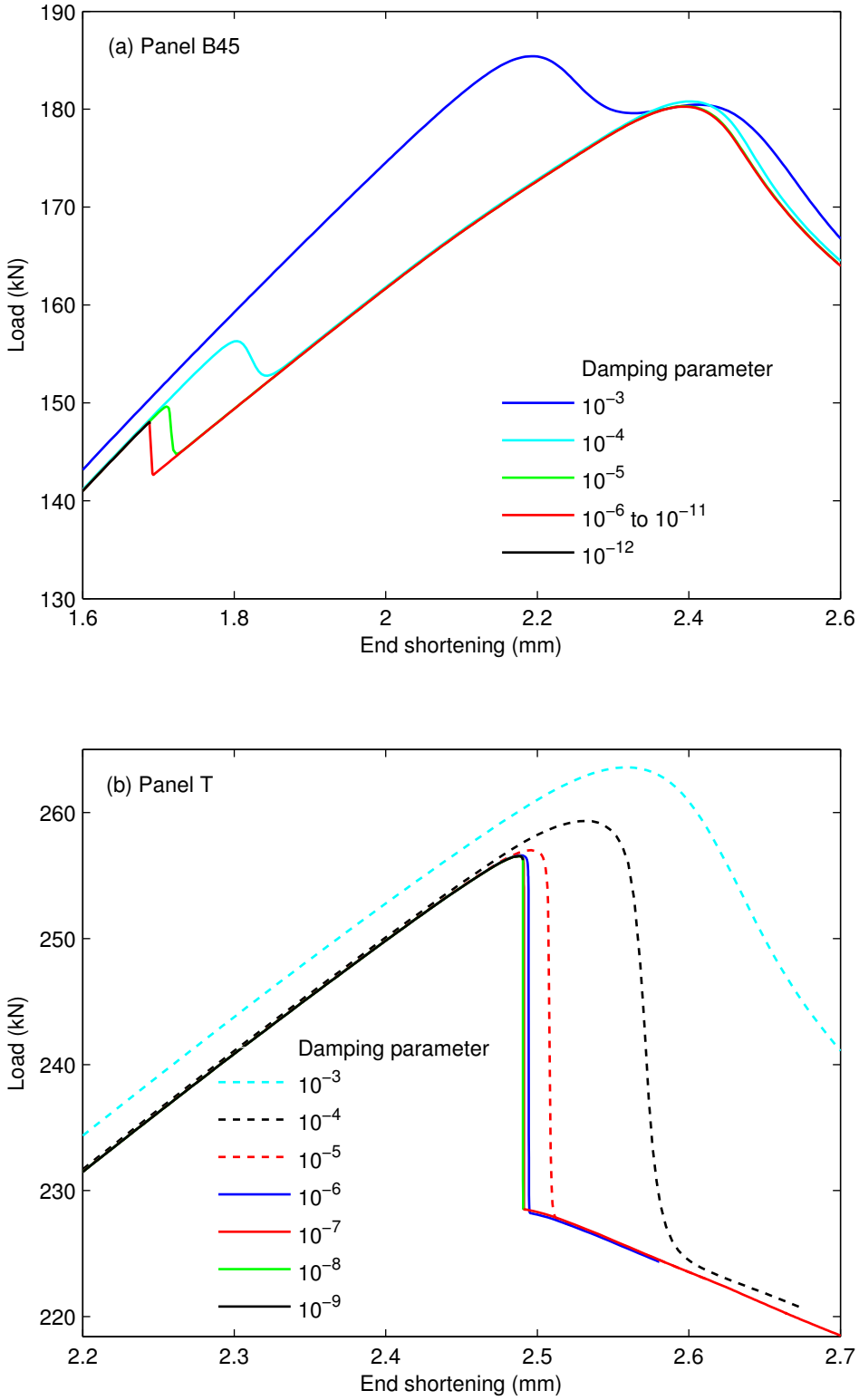

Figure 7.2: Influence of the damping parameter: (a) panel B45 and (b) panel T.

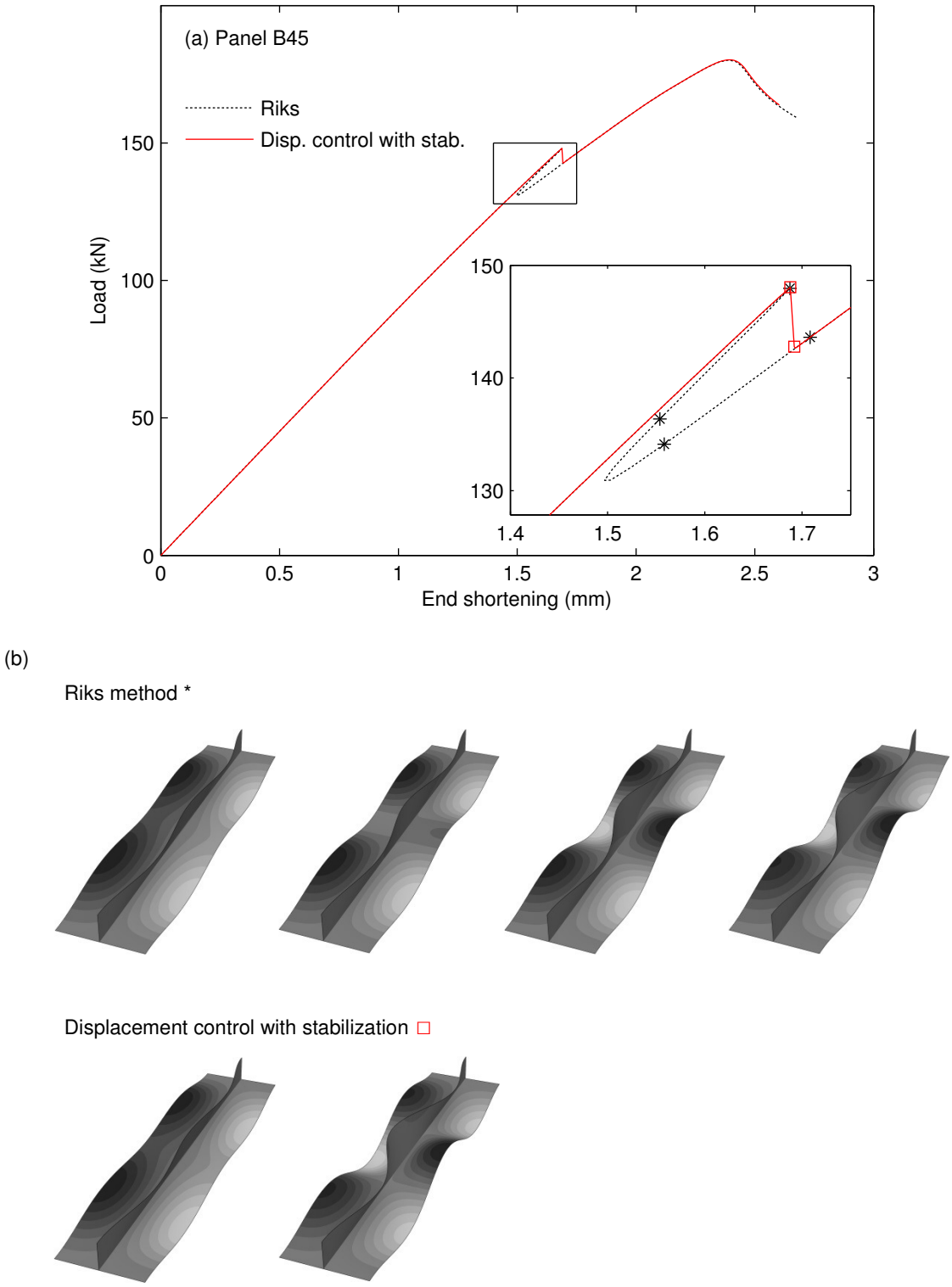

Figure 7.3: Results for panel B45 compression using distinct solving methodologies: (a) load/end shortening curves and (b) deformed shapes corresponding to the marks on the curves (displacements magnified 15 times along Ox and Oy).

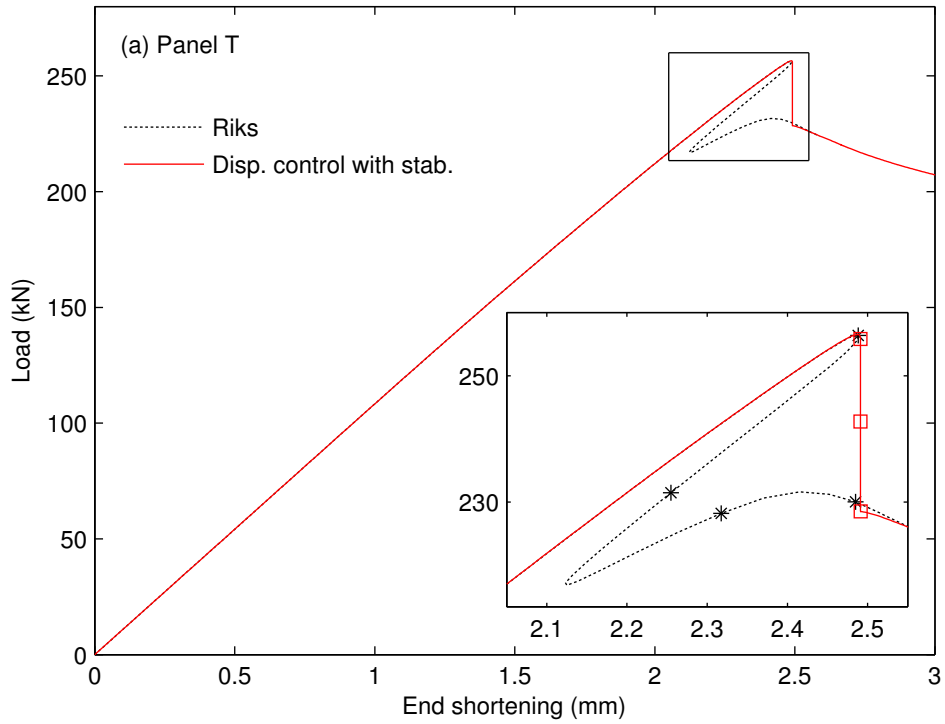

(b)

Riks method *

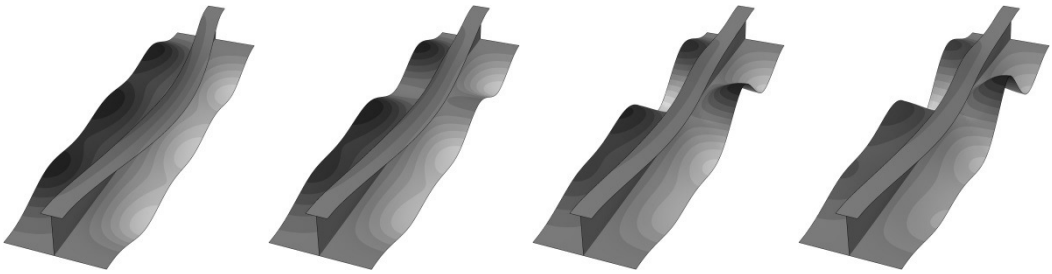

Displacement control with stabilization □

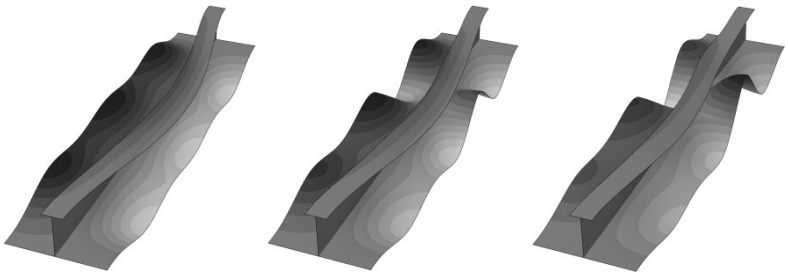

Figure 7.4: Results for panel T compression using distinct solving methodologies: (a) load/end shortening curves and (b) deformed shapes corresponding to the marks on the curves (displacements magnified 15 times along Ox and Oy).

The optimal set of parameters for the Riks method, in some cases, can be difficult to determine in order to obtain convergence up to the post-collapse region. In the displacement incremental control method with damping, this process can be easier, since the use of a small maximum increment along with the correct damping parameter value usually led to convergence, albeit at the expense of higher computational times. As showed before, this last methodology has the disadvantage of requiring a convergence study for the damping parameter. The results that are shown in what follows were obtained using the Riks method. Nonetheless, the displacement incremental control method with damping was also used in most of the models to ensure the accuracy of the results coming from the Riks method.

7.1.3. FSW effects input

The effects of the FSW process were modelled using two different methodologies. The first one consisted in importing the welding effects from the previously performed FSW numerical analyses on the 600 and 750 mm panels. The second one was a simplified methodology commonly used in the literature and previously described in Chapter 6. This second method was tested assuming perfectly plastic definitions (from the FSW analyses) and separately including work hardening effects. In this case, a linear hardening modulus was defined with a magnitude of 1.0 GPa, approximating the experimental data [117] for a plastic strain lower than 10%. Both methods tested are detailed in the following sections.

The geometrical imperfections (IMP) were included in all the models. Different combinations of the welding effects were tested, including residual stresses (RS) and material softening. For this last parameter, two distinct distributions were tested: softening before ageing (designated by SOFT60, for a minimum yield stress equals to 60% of the one for the base material) and the softening after the ageing process (designated by SOFT75, for a minimum yield stress equals to 75% of the one for the base material). All possible combinations are listed in Table 7.2, where the different models were tested with the distinct welding effects combinations. It should be mentioned that the analyses performed with the material properties before ageing (SOFT60) have no relevance in terms of practical application. Nonetheless, they will help to understand the effect of the softening on the panel behaviour.

Table 7.2 Summary of the combinations tested in the structural compressive analyses including FSW effects.

Model (FSW effects origin and model details)
FSW simulation (600 mm panels)
FSW simulation (750 mm panels)
Simplified method
Simplified method (including work hardening)

FSW effects (combinations tested)
IMP
IMP + SOFT75
IMP + SOFT60
IMP + RS
IMP + SOFT75 + RS
IMP + SOFT60 + RS

7.1.3.1. Effects from FSW simulation

The effects of the FSW process coming from the numerical analyses (presented on Chapter 5) were included into the model prior to the application of the compressive load. In the analyses including the residual stresses, a restart procedure was used on Abaqus [26], allowing to continue the simulation after the welding process without compromising the stress equilibrium. The analyses considering the material with no ageing (SOFT60) were restarted before the ageing step, while those considering the material natural ageing (SOFT75) were restarted after the ageing step. In the analyses considering the material without any softening, the original base material properties were restored before the compression.

In the analyses without the residual stress field the restart procedure was not used. Instead, the geometrical imperfections were imposed as displacements in the original mesh (using the *IMPERFECTION command [26]). The material softening was imposed using

the intended properties: base material (no softening), after welding (SOFT60) or after natural ageing (SOFT75). For that, the softening distribution was collected as a field variable at the end of the FSW numerical analyses and subsequently applied to the model for the compression stage, together with the minimum and maximum yield stress magnitude for each case.

7.1.3.2. Simplified modelling based on FSW simulation results

The use of a simplified methodology to include the welding effects follows the examples available in the literature and previously mentioned in Chapter 6. The magnitudes of the welding effects and their location on the panels were based on the FSW numerical analyses, although being added to the model with simplified distributions as described in what follows.

The yield stress distribution was modelled based on an approximation to the results of the FSW analyses. Two areas with different yield stress magnitudes were defined, as represented in Figure 7.5(a): one with the affected material properties (close to the weld line, with 12 mm width), and another with the base material properties (in the remaining area), The affected material was modelled with yield stress values corresponding to the material before (205 MPa) or after (259 MPa) ageing process, as shown in Figure 7.5(b). The plots on this figure also compare the simplified modelling approach against the distribution obtained from the FSW analyses.

The longitudinal stress was included in the model with a magnitude of 183 MPa in the zone close the weld line (with 14 mm width), as represented in Figure 7.6 (a). This value is approximately equal to the averaged stress value of the mid-length distribution on that specific location (from 0 to 14 mm). Seeking for equilibrium, a longitudinal compressive stress was applied in the remaining area of the panels. The magnitude of this compressive stress was calculated for each cross-section geometry, being applied with the absolute magnitudes of 15.96 MPa, 14.72 MPa and 12.91MPa, for panels B45, B60 and T, respectively. The stress distribution added in the simplified modelling was constant across thickness. This methodology required a relaxation step after the stress input, performed using only rigid body movement constrains (besides the symmetrical boundary condition associated to the weld line).

The relaxation step led to distortion of the panels and variations on the initial longitudinal stress distribution, as represented in Figure 7.6(b). The longitudinal stress distribution in the panel mid-length, as inputted and after the relaxation step, is compared to the one obtained from the FSW analyses in Figure 7.7. The relaxation step led to a final stress distribution similar to the one obtained from the FSW analyses, concerning a zone far from the weld line and namely in the stiffener.

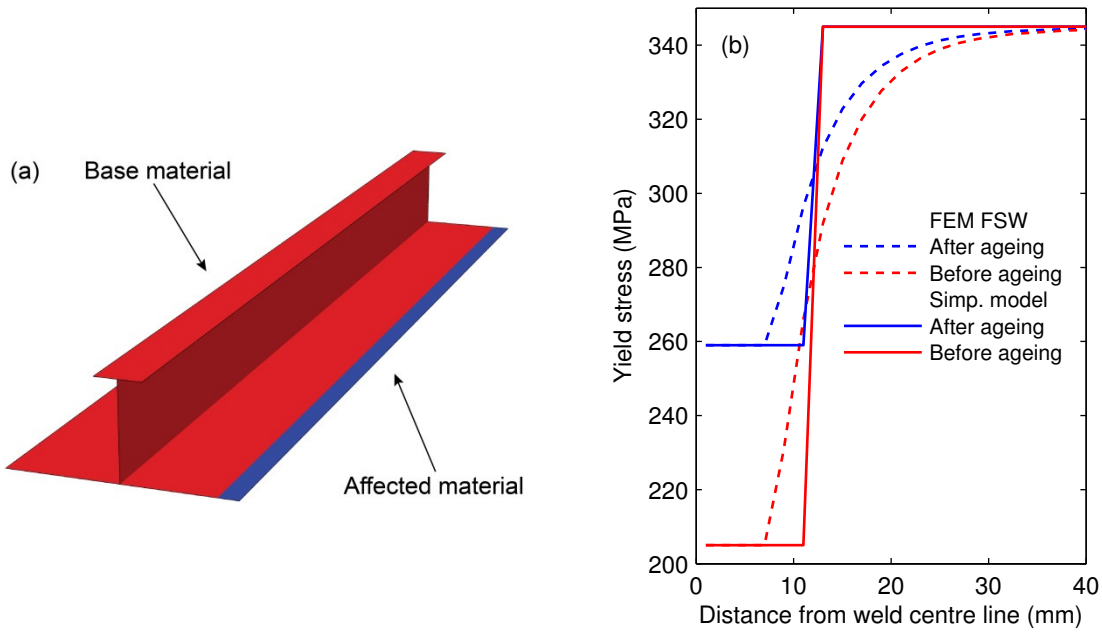

Figure 7.5: Distribution of the affected material in the simplified model: (a) full panel, and (b) along the mid-length section (compared to the results obtained from the FSW analyses).

No transverse stresses were added to the model (Figure 7.6 (c)) , although the relaxation step led to the increase of the transverse stress field, with a higher magnitude close to the longitudinal ends and the weld line, as can be seen in Figure 7.6 (d). This distribution was similar to the one obtained from the welding analyses, albeit with lower magnitudes.

The deformed shapes obtained after the relaxation stage are shown in Figure 7.8. To complement this information, the results in Figure 7.9 show the displacement magnitudes along the weld line and the opposite edge. Strictly speaking in terms of the displacement along the longitudinal direction, the obtained shapes are similar to the ones that result from the welding simulations (see Figure 5.15). However, with the current methodology the maximum magnitudes in the weld line are approximately 0.05 mm

smaller than in the results from the welding analyses. The displacements associated with the V-shape in the transverse direction have a lower variation using the present methodology compared to the ones coming from the welding simulation, in which the more accentuated V-shape was a result of the differential plastic strain across thickness.

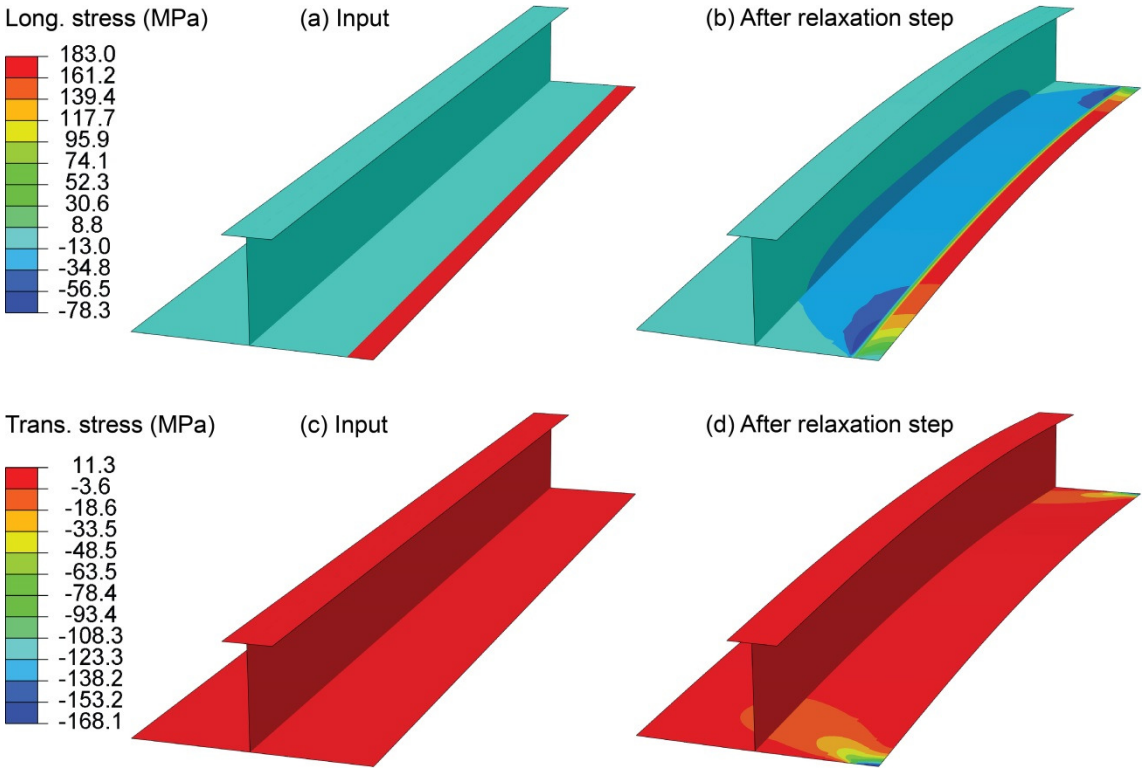

Figure 7.6: Longitudinal stress distribution in the panel T: (a) as inputted in the simplified model and (b) after the relaxation step; and transverse stress distribution: (c) as inputted in the simplified model and (d) after the relaxation step.

The methodology adopted to include the FSW effects led to symmetry of the displacements and stress fields, concerning a plane corresponding to the panel mid-length. Considering that the material distribution (in all cases) is also symmetric, the model has a full symmetry regarding the mentioned plane. This assumption can have implications on the structural buckling, since with the present models only symmetrical buckling modes can be obtained after longitudinal compression.

It should also be mentioned that the use of different softening magnitudes did not influence the results after the relaxation step, in terms of the finals stress or displacement distributions, since the stress field magnitude was lower that the yield stress in all tested cases.

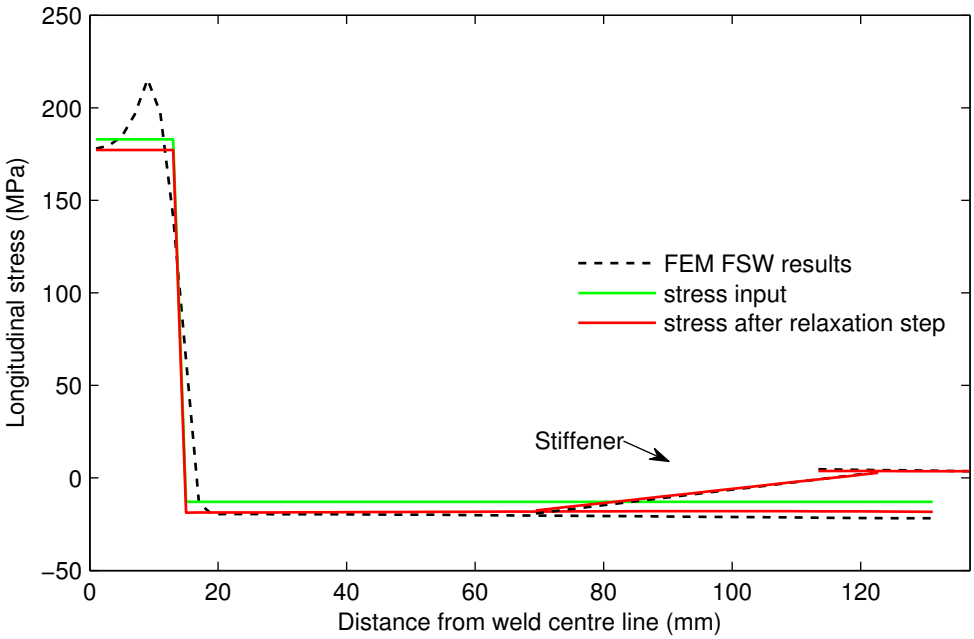

Figure 7.7: Longitudinal stress distribution in the mid–length section of panel T (average across thickness): as inputted in the simplified model and after the relaxation step, compared with the results from the FSW simulation.

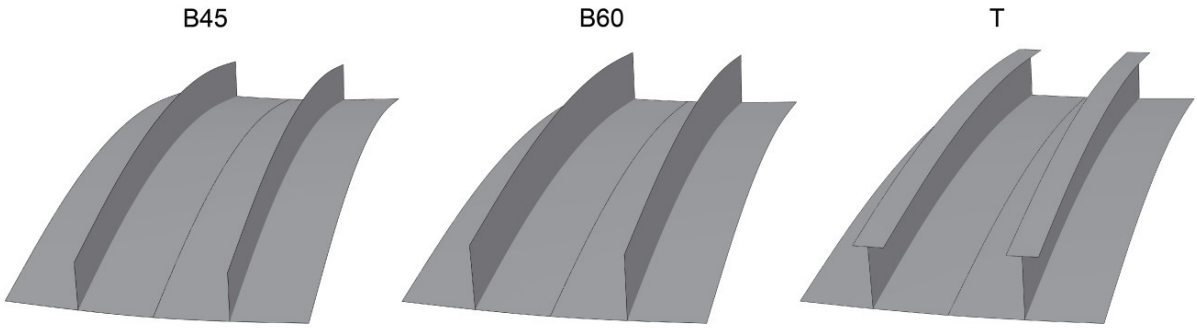

Figure 7.8: Deformed shapes obtained after the relaxation step (mirror view on the weld line symmetry plane and the displacements amplified 50 times along Oy).

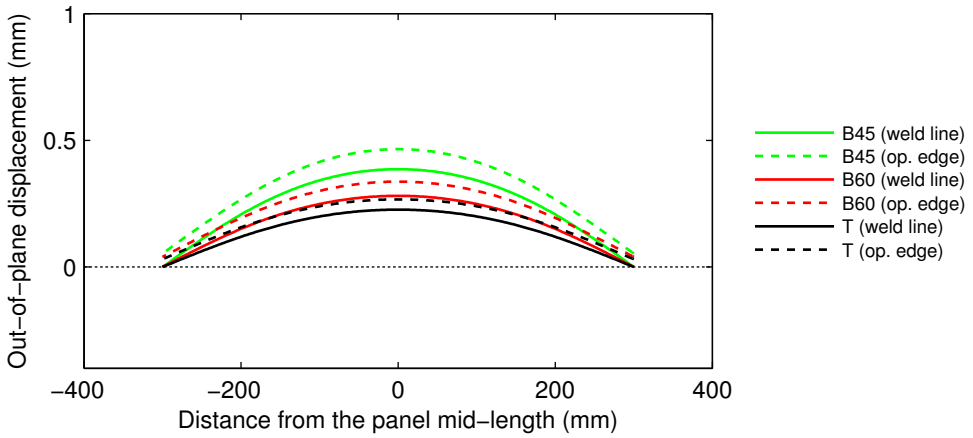

Figure 7.9: Displacement after the relaxation step along the weld line and opposite edge.

7.2. Results of the compressive analyses including welding effects

Regarding the compressive analyses, the load/end shortening curves are presented in Figure 7.10, Figure 7.11 and Figure 7.12 for the results obtained with panels B45, B60 and T, respectively. The results presented in those curves allowed the determination of the collapse loads listed in Table 7.3. The load/end shortening curves are plotted based on discrete values, dependent on the arc length increment. Thus, eventual deviations may be associated with the spatial resolution of the plot, namely in the collapse zone. The collapse load can, therefore, show intrinsic accuracy variations. In preliminary analyses, these variations were observed to be smaller than 0.06% (the same variation obtained when comparing different solving methodologies).

To properly compare the collapse load results from different panels, they are represented in Figure 7.13, after being normalized to the collapse load magnitude obtained from the model including only geometrical imperfections (IMP) for each case. Figure 7.14 shows the same results, now normalized with respect to the yield load of each panel, *i.e.* the load that the panel can support before developing plastic deformation in the absence of buckling effects. The collapse load/yield load ratio is often taken into consideration in research works involving stiffened panels analyses, since it allows the knowledge of the strength efficiency of each panel.

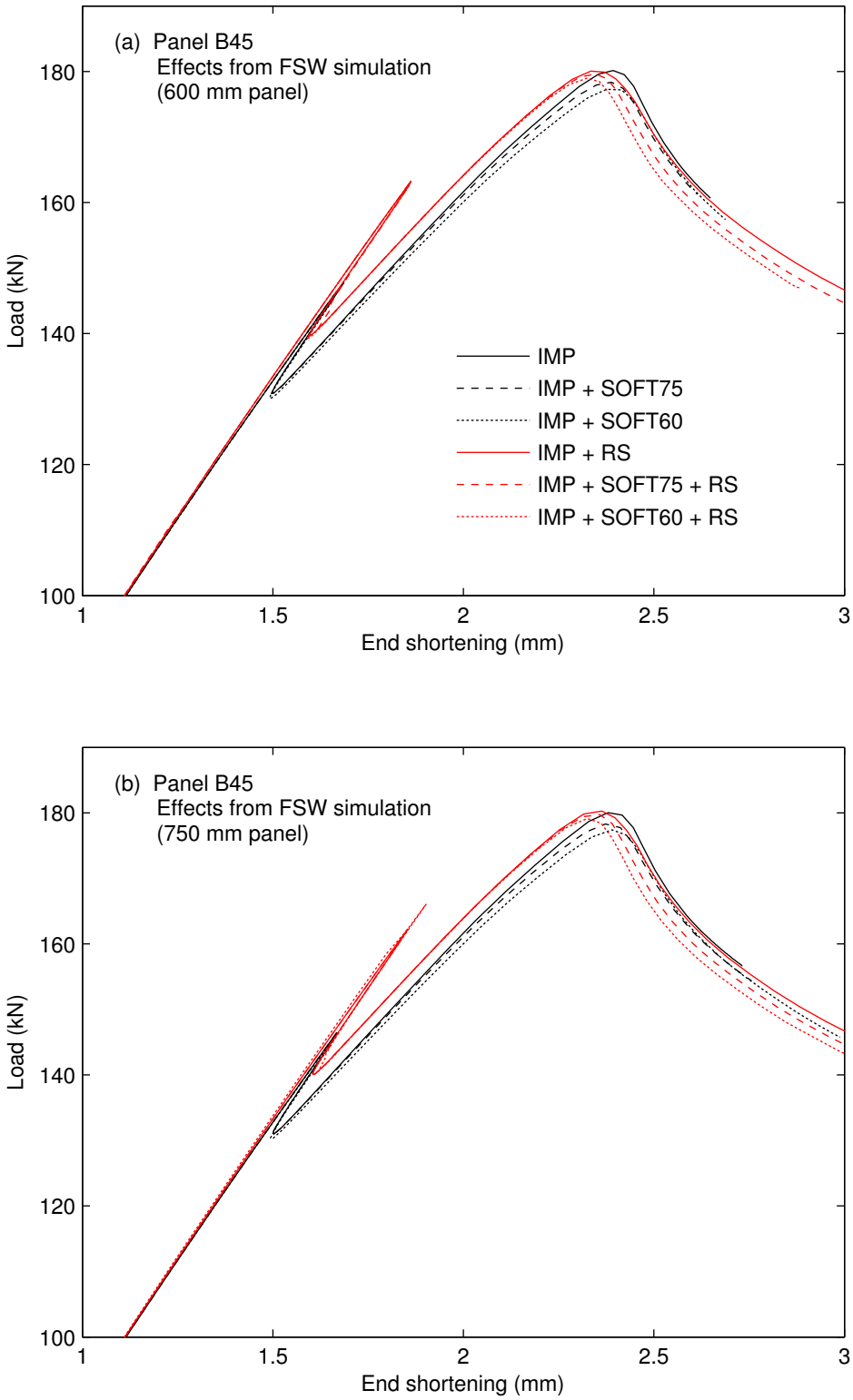

Figure 7.10: Compression analyses results for panel B45 with distinct modelling decisions: (a) FSW effects from simulation (600 mm panels), (b) FSW effects from simulation (750 mm panels), (c) simplified method, and (d) simplified method including work hardening.

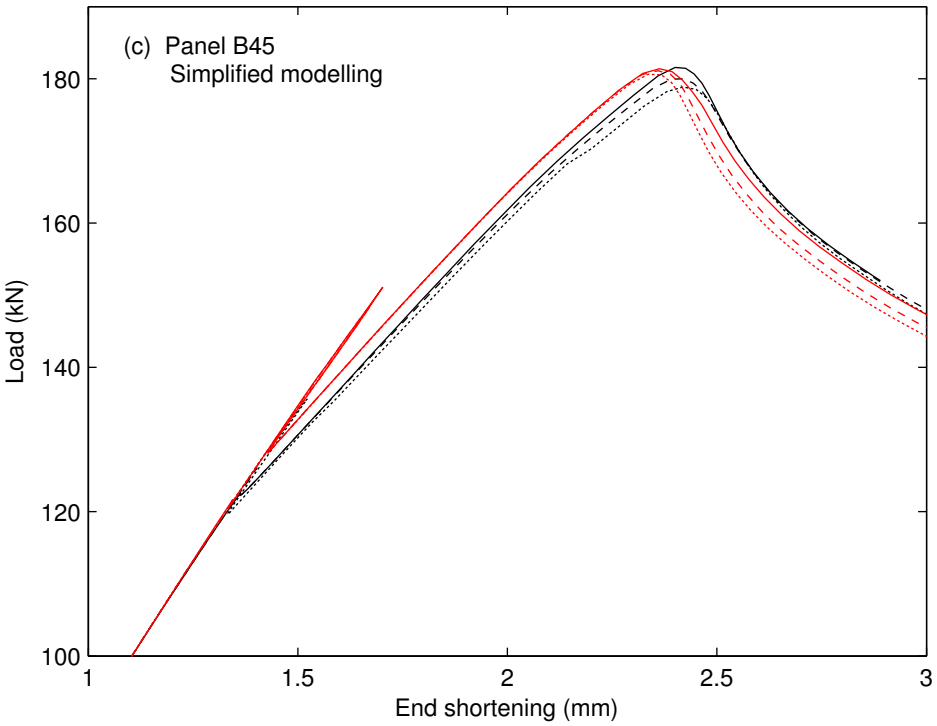

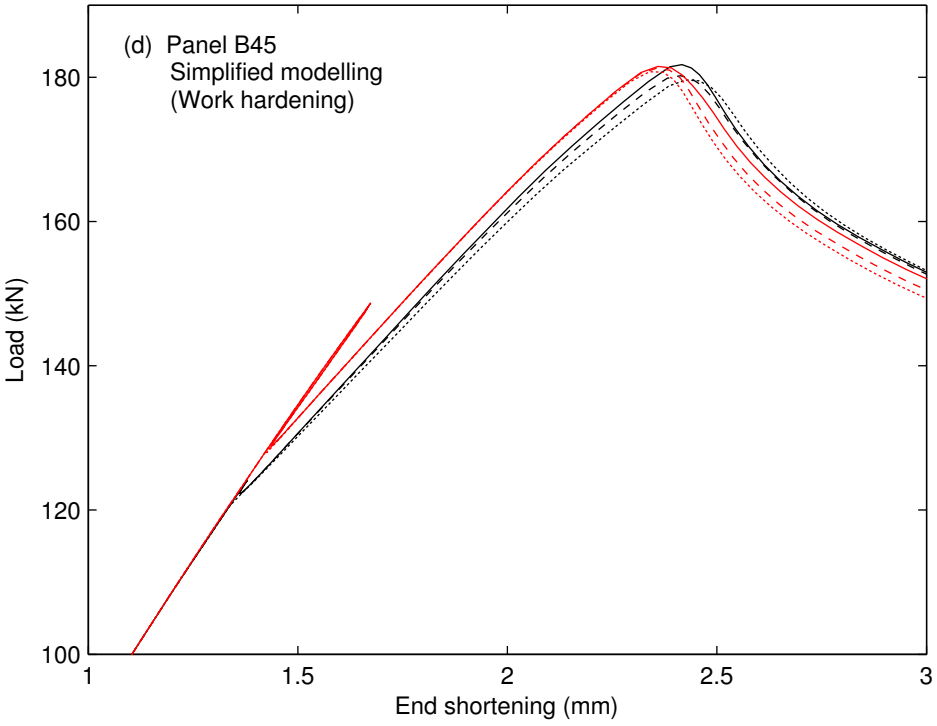

Figure 7.10 (cont.)

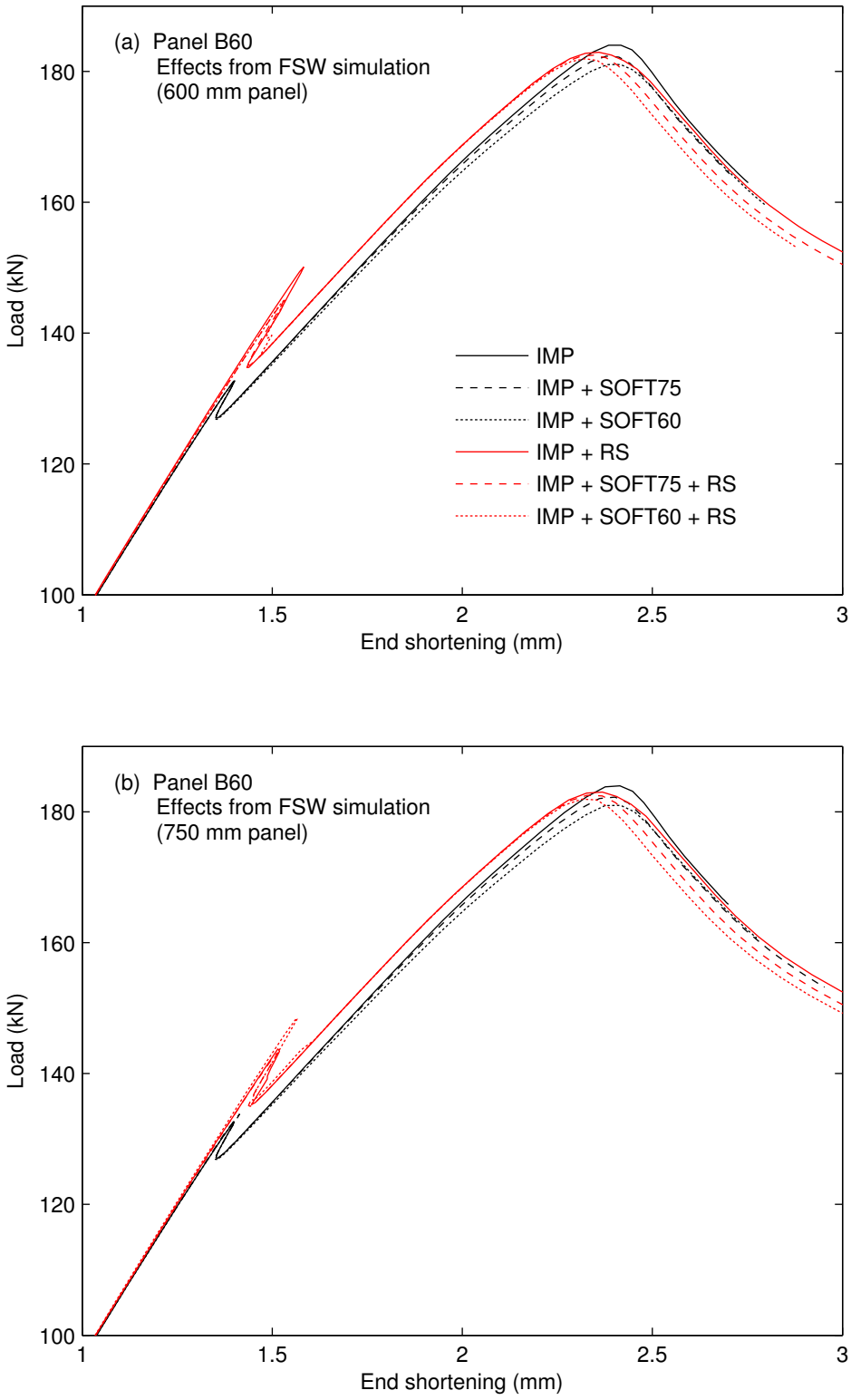

Figure 7.11: Compression analyses results for panel B60 with distinct modelling decisions: (a) FSW effects from simulation (600 mm panels), (b) FSW effects from simulation (750 mm panels), (c) simplified method, and (d) simplified method including work hardening.

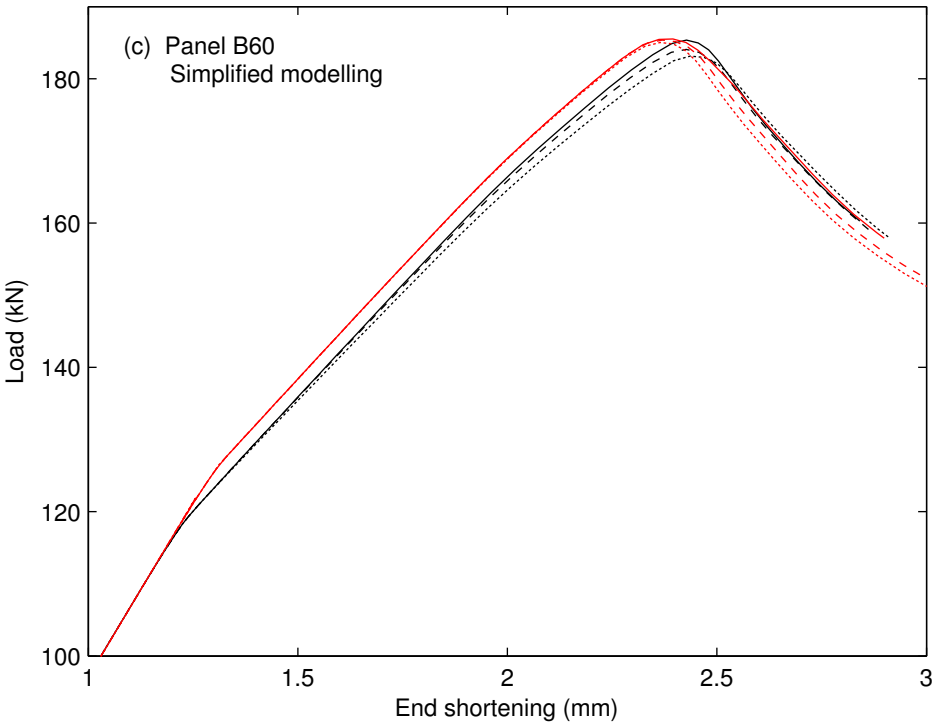

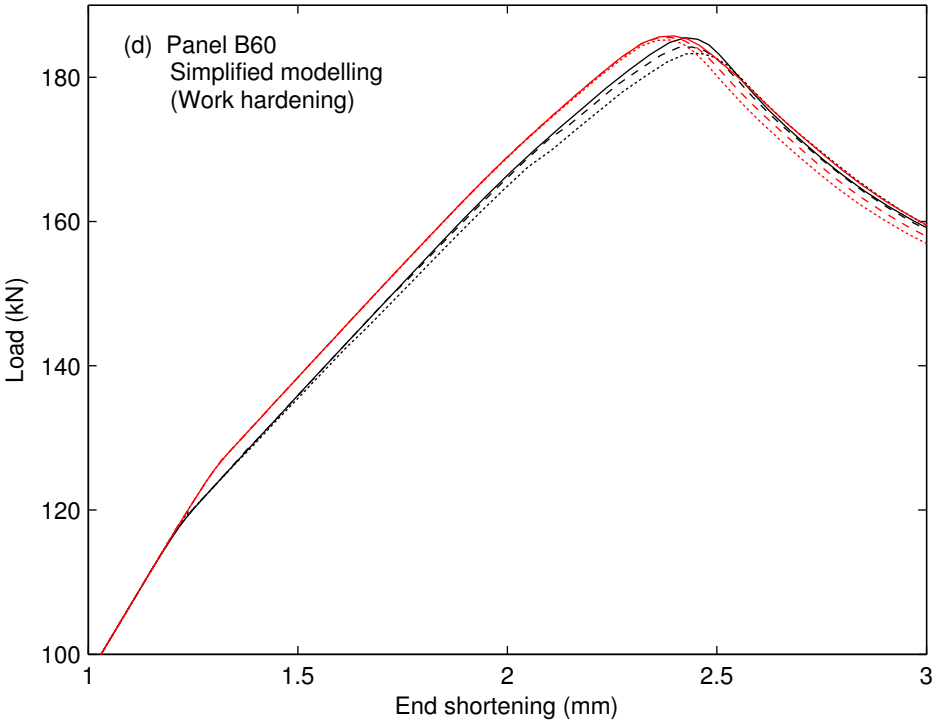

Figure 7.11 (cont.)

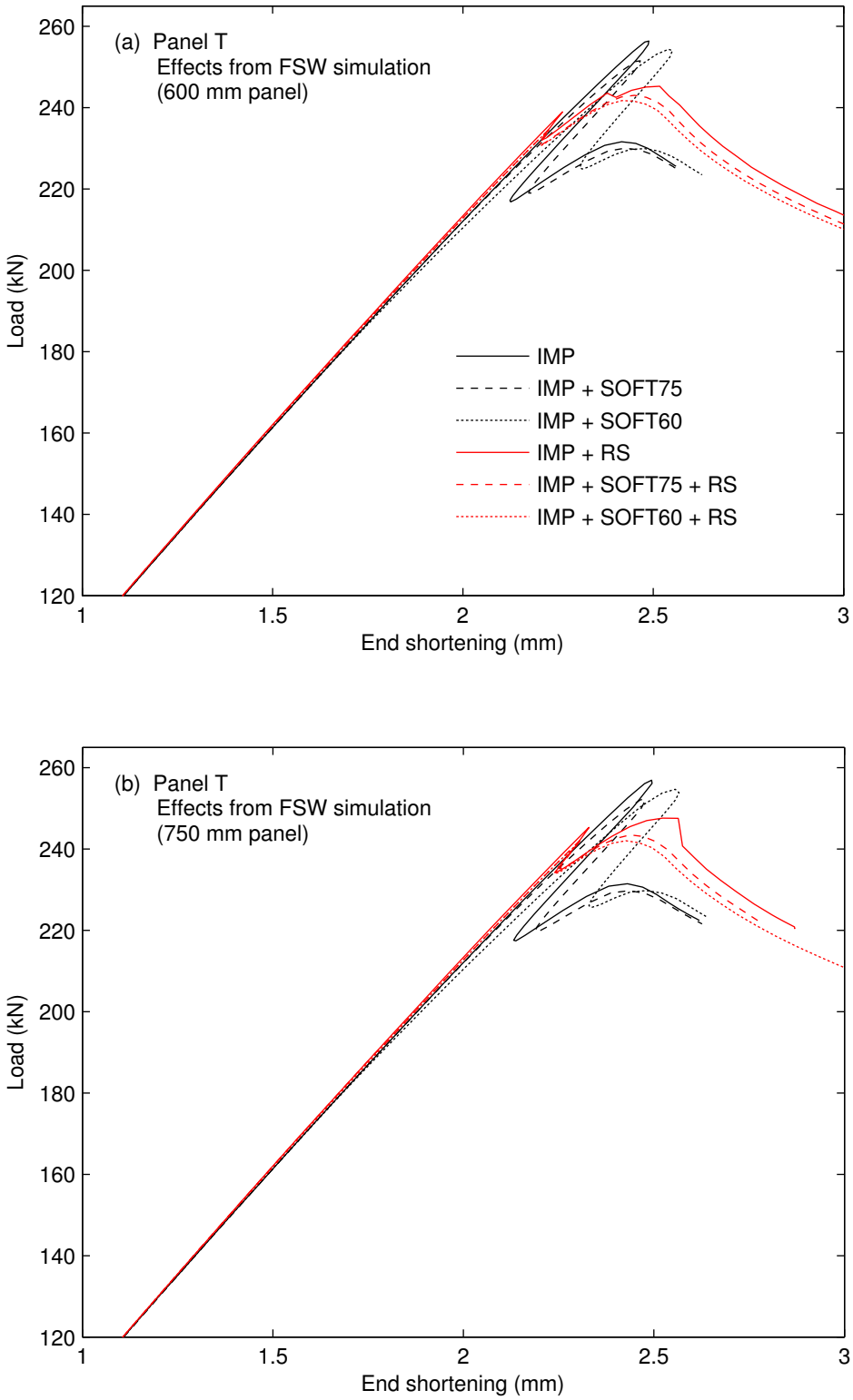

Figure 7.12: Compression analyses results for panel T with distinct modelling approaches: (a) FSW effects (600 mm panels), (b) FSW effects (750 mm panels), (c) simplified method, and (d) simplified method including work hardening.

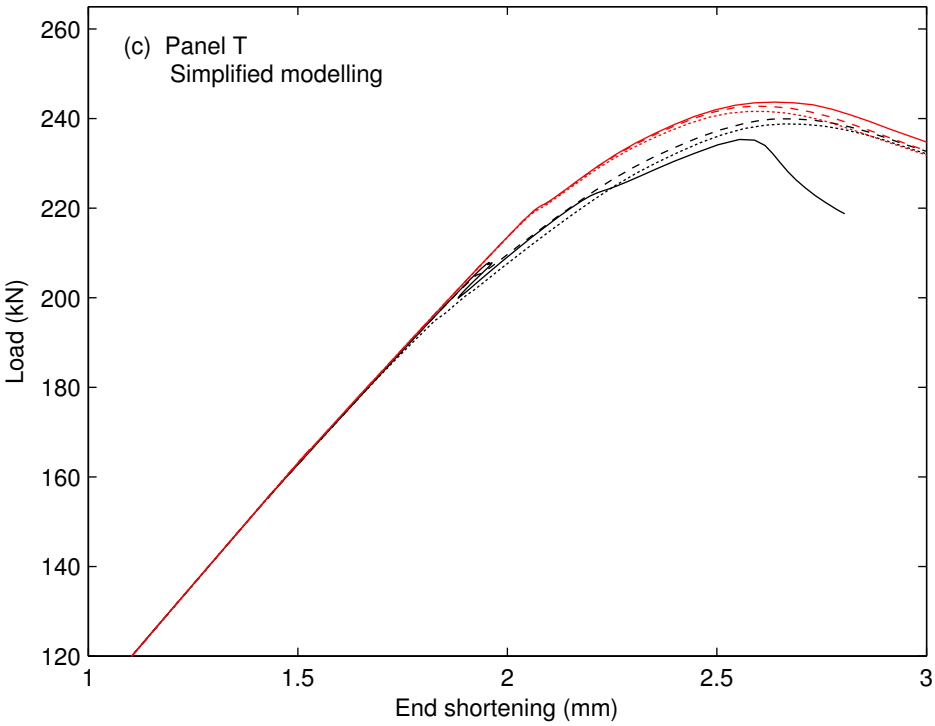

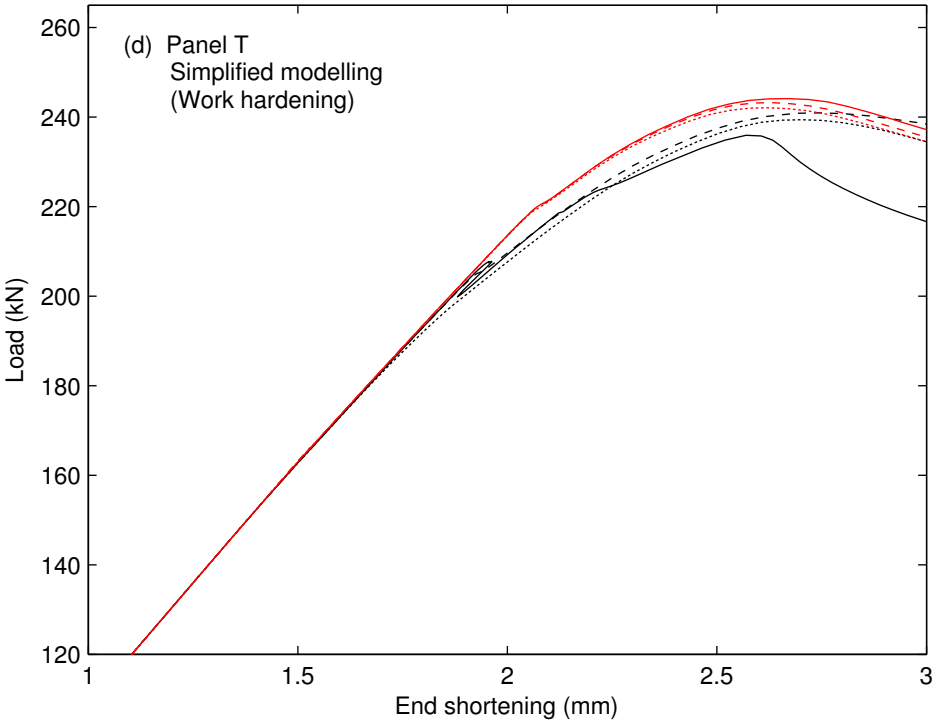

Figure 7.12 (cont.)

Table 7.3: Collapse load predictions for compression analyses including different combination of FSW effects.

		Collapse loads for distinct FSW effects combinations (kN)					
FSW effects origin (model details)	Panel	IMP	IMP SOFT75	IMP SOFT60	IMP RS	IMP SOFT75 RS	IMP SOFT60 RS
FSW simulation (600 mm panels)	B45	180.15	178.38	177.31	180.05	179.63	178.98
	B60	184.01	182.33	181.05	182.94	182.51	181.94
	T	256.38	251.53	254.36	245.28	243.06	241.76
FSW simulation (750 mm panels)	B45	180.04	178.32	177.41	180.28	179.73	179.14
	B60	183.96	182.26	180.99	183.02	182.53	181.95
	T	256.93	252.21	254.71	247.59	243.46	242.11
Simplified modelling	B45	181.57	179.99	178.85	181.38	181.12	180.61
	B60	185.35	184.06	183.14	185.53	185.36	185.03
	T	235.33	239.95	238.79	243.68	242.77	241.59
Simplified modelling (including work hardening)	B45	181.74	180.22	179.64	181.50	181.25	180.77
	B60	185.50	184.20	183.32	185.72	185.51	185.17
	T	235.92	240.94	239.43	244.14	243.23	242.11

A general overview of the results, regarding the load/end shortening curves and collapse loads, revealed two clear differences between panel T and the blade stiffened panels (B45 and B60). The first difference is that the ratio between the collapse load and the yield load is significantly higher in panel T, with a minimum ratio value of 0.805 (see Figure 7.14). The second difference is the higher sensitivity of panel T, evident in the variations in the load/end shortening curves (see Figure 7.12) and also in the higher range of variation of the collapse load from the different analyses (see Figure 7.13 and Figure 7.14).

Before proceeding to a detailed analysis of the influence of welding effects on the panels, it is important to point out the repercussions of modelling variations in the final results. In this context, it is worth comparing three distinct scenarios: (i) 600 mm panels *vs.* 750 mm panels (to assess the impact of the extremities effects on the panel strength); (ii) the use of a perfectly plastic model *vs.* the use of work hardening laws; and, finally, (iii)

the use of effects coming from FSW numerical analyses (more realistic) *vs.* the simplified modelling of these factors.

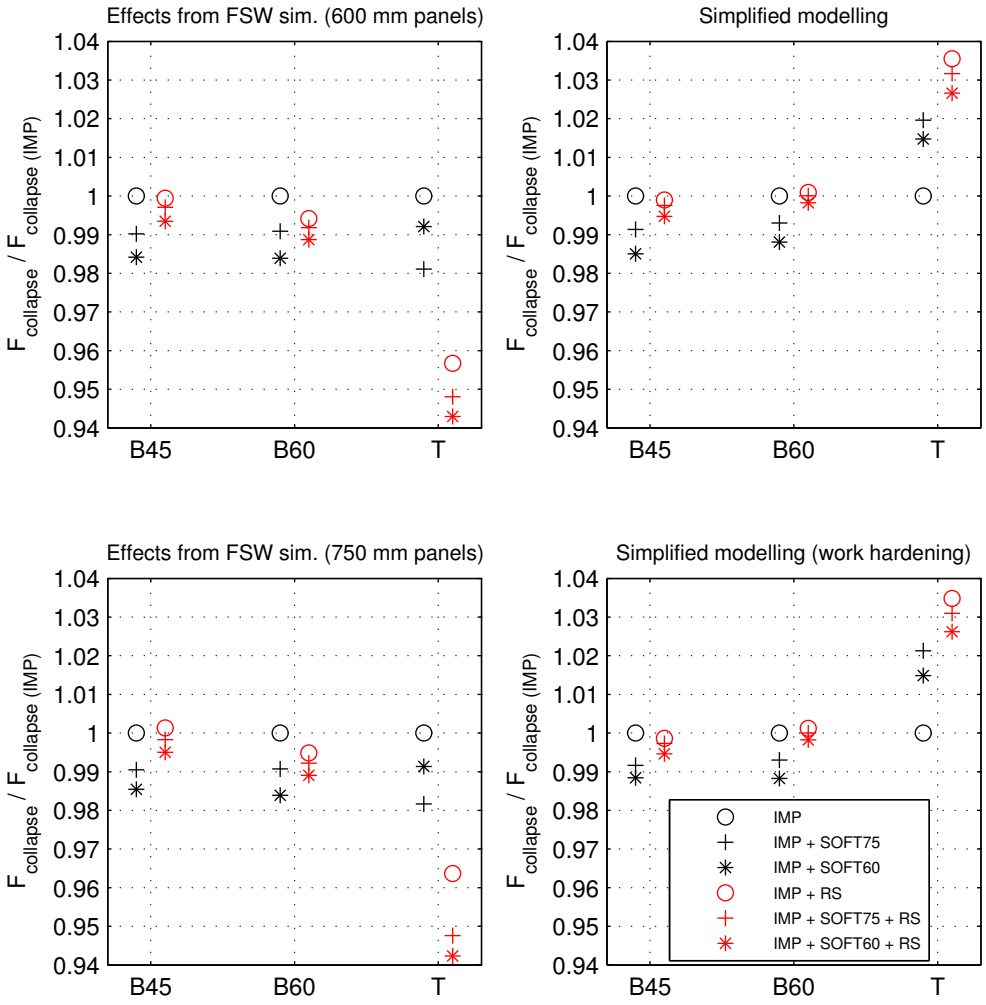

Figure 7.13: Collapse load magnitude for the panel compression analyses, normalized to the result from the model with geometrical imperfections only (IMP), for each case.

7.2.1. Influence of the longitudinal extremities welding effects

The results using the 600 mm and the 750 mm panels are not significantly different, and both led to the same conclusions concerning the welding effects. It is important to remind that in the welded panels with 750 mm, only the central part (with 600 mm) was loaded, avoiding the boundary effects of the extremities, related to the start and end points of the FSW process. The maximum variations obtained, comparing models with combination of the same welding effects, are 0.13% and 0.04%, for the panels B45 and B60, respectively.

For panel T, more sensitive to modelling variations, the differences are lower than 0.27%, except for the model with IMP + RS, that shows a variation of 0.93% due to a slight difference in the buckling evolution just before the collapse load, as can be seen in Figure 7.12 (a) and (b). All the variations are randomly negative or positive. The slight differences in the initial geometrical distortion in the panels with different lengths (see Figure 5.15) and the deviations associated with the FEA can justify these variations. There are no evidences that effects close to the transverse edges, related to the softening of the material (see Figure 5.6) or with the residual stresses (see Figure 5.11), have any influence in the collapse load of the panels.

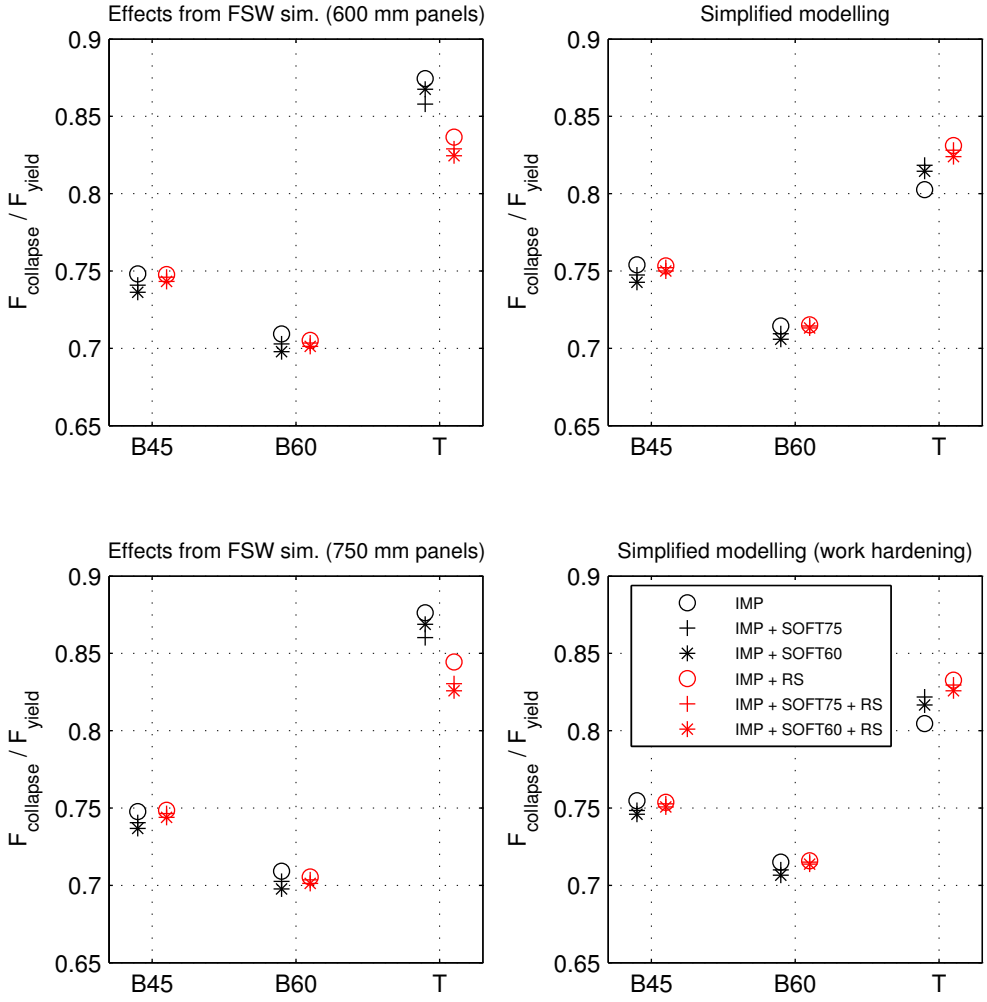

Figure 7.14: Collapse load magnitude for the panel compression analyses, normalized to the yield load magnitude of each panel.

7.2.2. Influence of using work hardening properties instead of a perfectly plastic definition

Concerning the use of work hardening properties instead of a perfectly plastic model (as coming from the FSW numerical analyses), a slight influence on the results can be seen, namely on the collapse load. Higher values of collapse load were always obtained for those models including work hardening properties, as expected. For panels B45 and B60, the variations in the collapse loads are smaller than 0.13%, except for the particular case of panel B45 with IMP + SOFT60, with a variation of 0.44%. For panel T, the differences are generally higher (between 0.19% and 0.41%) as a result of the higher ratio between the collapse load and the yield load, involving a higher plastic deformation at the moment of collapse for these panels and, therefore, a higher influence of the plastic properties of the material. Regarding the load/end shortening curves, the differences are more evident in the post-collapse zone where the plastic deformation is higher, as can be observed comparing this section of the curves in parts (c) and (d) of Figure 7.10, Figure 7.11 and Figure 7.12.

Therefore, the correct definition of the plastic deformation properties may have an important effect in the accuracy of results, especially in high efficiency panels (with a high collapse load/yield load ratio). Nonetheless, both of the material properties modelled (with and without work hardening) can lead to similar conclusions in terms of the influence of welding effects on the collapse load, as can be seen from the results in Figure 7.13.

At this point, after analysing the influence of the welding effects on the extremities of the panels and of the plastic properties hardening models, the remaining discussion will focus solely on: (i) the results obtained with the 600 mm panels, using the effects from the FSW simulations, and (ii) the results from the simplified modelling of the welding effects, using a perfectly plastic material model (no hardening effects).

The comparison between the results obtained using the effects from the FSW simulation and the results obtained with the simplified model is complex, in some cases, due to the existence of distinct initial geometrical imperfection that sometimes led to distinct collapse modes. Thus, before this discussion and also before the assessment of the influence of the welding effects, it is important to analyse the buckling shape evolution from the different models.

7.2.3. Analysis of the buckling shape evolution

Concerning the numerical analyses with panel B45, all models show a similar evolution in terms of buckling shapes. Figure 7.15 shows the typical behaviour observed with the B45 panels. The buckling mode evolves from a single curve to three half waves in the plate and stiffener, which lead to the collapse of the structure.

For the B60 panels, the shape evolution is distinct in the analyses including the effects from the FSW simulation and in the analyses using the simplified modelling. The panels with the effects from the FSW simulation show a buckling evolution similar to the one presented by the panel B45 model, as represented in Figure 7.16 (b1). The panels with the simplified modelling of the welding effects follow a similar evolution, albeit symmetric, as shown in Figure 7.16 (b2). This shows the influence of the initial geometrical imperfection on the final collapse shape.

Finally, for panel T, four distinct buckling shape evolutions are observed. For the model with welding effects from the FSW simulation, one of the evolutions is associated with all the panels without residual stresses, represented in Figure 7.17 (b1). In this case, the stiffener buckles in a single half wave. The plate buckled in a mode that combines five half waves with a single global curve induced by the stiffener displacement. As mentioned before, the collapse is associated with a mode-change and the panel fails due to localised buckling, close to one of the transverse edges.

The panel T models that included the residual stress field (with the FSW effects from numerical simulation) follow a different buckling evolution, as exemplified in Figure 7.17(b2). The stiffener also buckles in a single global curve. However, the localised buckle close to the transverse edge starts earlier than in panels without residual stresses, leading to lower collapse loads. In this case the mode-change was not associated with the collapse.

The results for panel T using the simplified modelling of the welding effects obviously had a different buckling evolution, since, as mentioned before, the modelling specificities always led to buckling shapes with symmetry considering the mid-length plane of the panel. Most of the panel T models exhibit a buckling shape evolution as shown in Figure 7.17(b4). The stiffener buckles in a single global curve and the panel in a more complex shape. The only exception to this behaviour was observed with the model including only geometrical imperfections (IMP). In this case, the stiffener showed small out-of-plane displacements and the plate evolves from a single global curve to a three half

waves shape and, later, to a five half waves shape, ultimately leading to collapse (see Figure 7.17(b4).

All the deformed shapes shown in Figure 7.15(b), Figure 7.16(b) and Figure 7.17(b) exclude the initial geometrical imperfection and the weld line had been always represented on the right side.

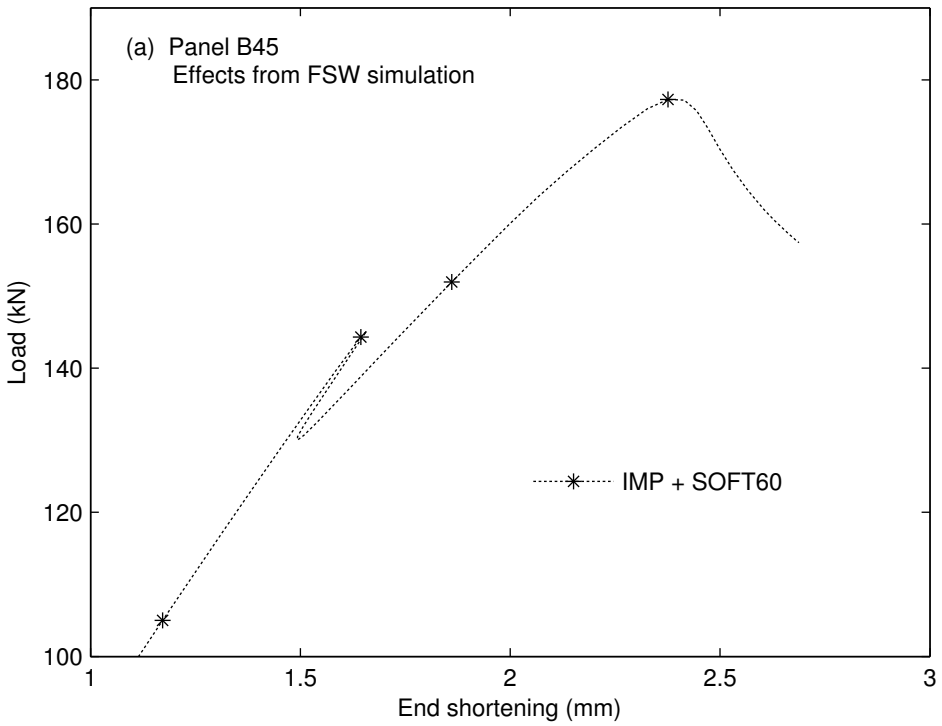

(b)

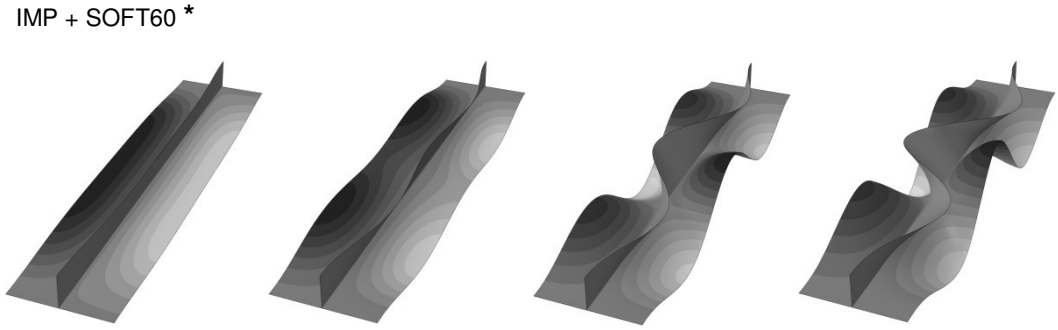

Figure 7.15: (a) Load/end shortening curves and (b) corresponding buckling modes obtained with panel B45 (displacements amplified 15 times along *Ox* and *Oy*).

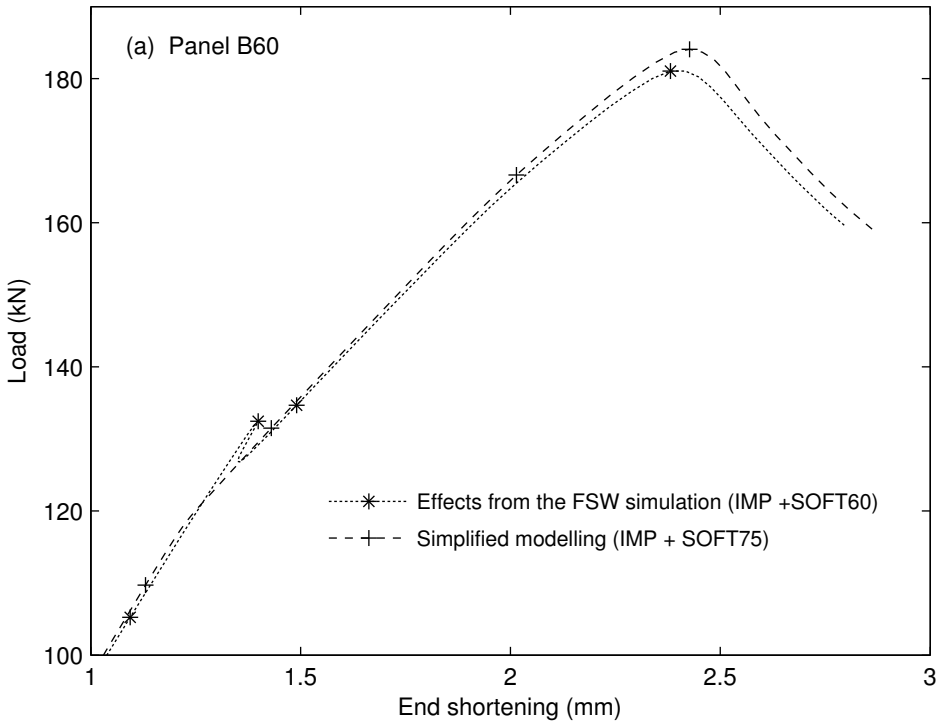

(b1) Effects from the FSW simulation (IMP + SOFT60) *

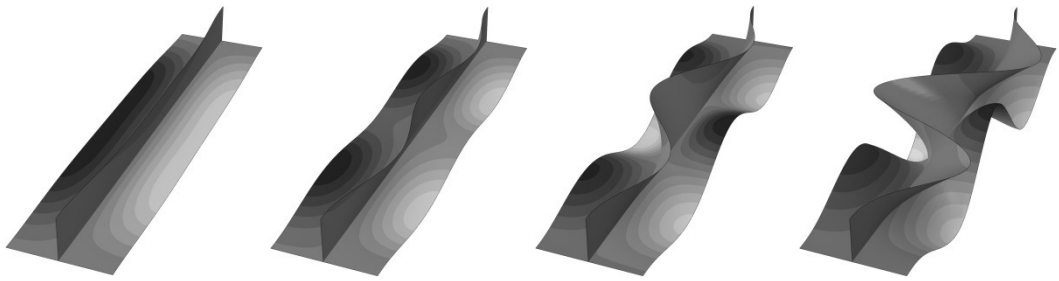

(b2) Simplified modelling (IMP + SOFT75) +

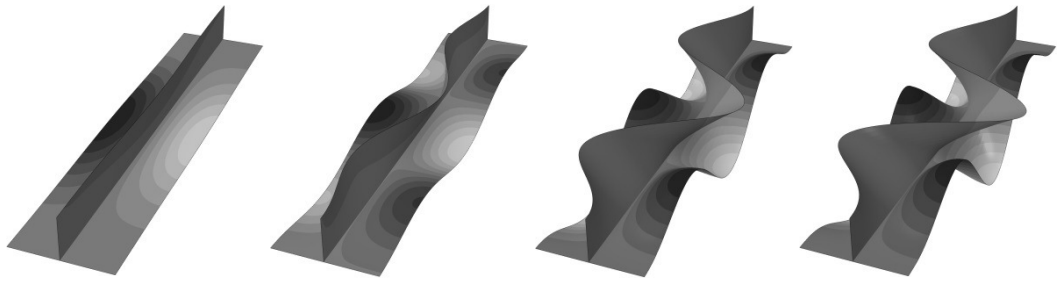

Figure 7.16: (a) Load/end shortening curves and (b) corresponding buckling modes obtained with panel B60 (displacements amplified 15 times along *Ox* and *Oy*).

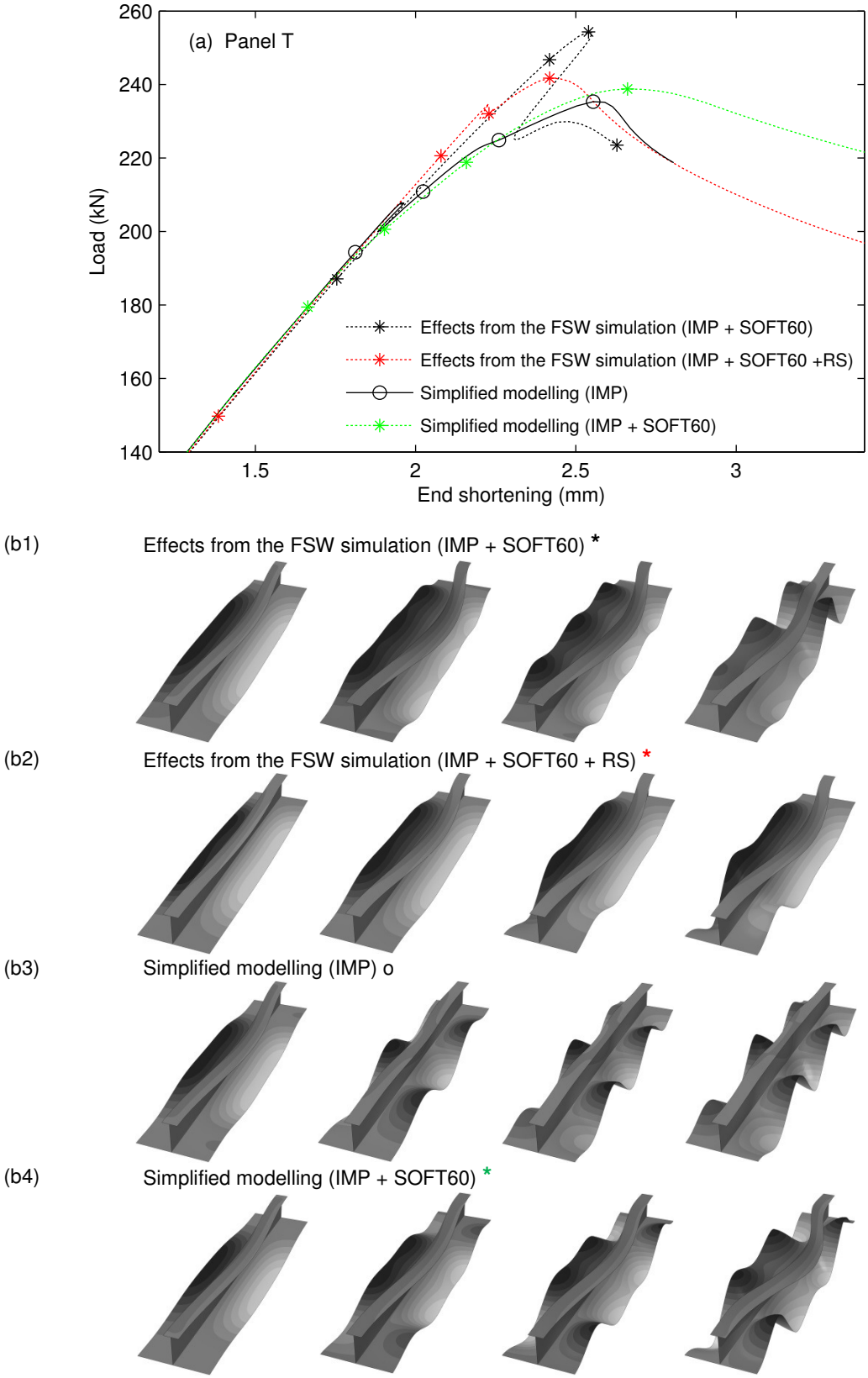

Figure 7.17: (a) Load/end shortening curves and (b) corresponding buckling modes obtained with panel T (displacements amplified 15 times along Ox and Oy).

7.2.4. Effects of residual stress field and softened material

In terms of the effects of the residual stresses on the panels behaviour, there was an occurrence that was evident in all cases (except for the panel T including effects from FSW simulation). It consisted in a delay of the first mode-change in the panels including the residual stress field, compared to the equivalent panels without the residual stresses. This delay in the mode-change, in terms of end shortening, led it to occur for a higher load magnitude. The aforementioned effect can clearly be observed in the curves of Figure 7.15 (a) to (d), Figure 7.16 (a) to (d) and Figure 7.17 (c) and (d).

In order to explain this effect, the results for panel B60 will be analysed in detail, specifically for the model with the simplified modelling of the welding effects, since the mode-change is less abrupt than in other cases. Nonetheless, the following explanation is suitable for all cases.

The curves from models with IMP and with IMP + RS effects are represented in Figure 7.18 (a) focusing on the zone associated with the mode-change. The deformed shapes corresponding to the points marked in the curve (shown in Figure 7.18 (b)), show that the deformed shape with a single global curve evolves earlier to three half waves on the model without the residual stresses. This is also evident on the results presented in Figure 7.19, that show the evolution of the out-of-plane displacement in three points located on the mid-length section of the panel. In all curves of this figure it is noticeable that the out-of-plane displacement has a later increase (in absolute terms) in the panel with residual stresses, concerning the zone with an end shortening between 1 and 1.3 mm. The evolution of the longitudinal stresses in the same three points is represented in Figure 7.20 and it also shows a delayed evolution associated with the presence of residual stresses. Particularly in this case, it is important to verify the bifurcation of the curves corresponding to the top and bottom of the base plate, and right and left in the stiffener. It is clear that the bifurcation, corresponding to the mode-change, occurs later in the model with the residual stresses.

Another interesting effect related to the mode-change in the panels B45 and B60 was that in panels including FSW effects from the numerical simulation, compared to panels with the simplified modelling, the mode change occurred later (for higher end shortening and higher load), and was more abrupt (taking into consideration the snap back). This is related to the shape and magnitude of the initial imperfection, which was

higher in the panel with the welding effects for the numerical analyses. The existence of initial geometrical imperfection (single half wave curvature) with higher magnitude, delayed the formation of the three half waves buckling mode, because this change involved the displacement of some parts of the panels to the opposite side in terms of out-of-plane position.

Before moving on to assess the effect of the residual stress field on the collapse load, it is important to explain the effect of the material softening on the panel behaviour. This effect is easier to explain in panels with the same collapse load. Looking at the results for panels B45 and B60, it is possible to relate a decrease in the collapse load with the decrease in the yield stress properties in the weld affected zone, in the models with and without residual stresses. This effect can also be seen for all panel T results that exhibited similar collapse shapes.

The results for panel B60 using the simplified modelling of the welding effects are going to be used, as example, to give an overall explanation of the softening effect in the panel behaviour. Looking at the curves load/end shortening for the models without residual stresses, represented on Figure 7.11(c), it is possible to observe that they follow a same path until the end shortening reaches approximately 1.3 mm. After that, the results show a bifurcation and the panel with the effects IMP + SOFT60 presents a lower stiffness than the other two. The same happens with the panel with the effects IMP + SOFT75, afterwards, for a higher end shortening and load. This behaviour is related to the plastic strain in the welded zone, which begins earlier for panels with lower yield stress in the affected zone. Results in Figure 7.21(a) show the stress magnitude when the panel just with initial geometrical imperfections (IMP), reaches an end shortening of 1.6 mm. The stress is higher at the centre of the base plate (close to the weld line and opposite edge) and large enough to initiate plastic deformation if the material's yield stress was the one of the affected material in the welded zone. For the same model, Figure 7.21(b) represents the stress magnitude at the moment of collapse, while Figure 7.22(a) shows the associated equivalent plastic strain. Comparing this plastic strain with the one of the model with material softening (IMP + SOFT60), represented in Figure 7.22(b), higher deformations can be observed (at the moment of collapse) close to the weld line in the model with the softened material. The earlier and higher plastic deformation leads to a lower collapse load of the panels with softened material.

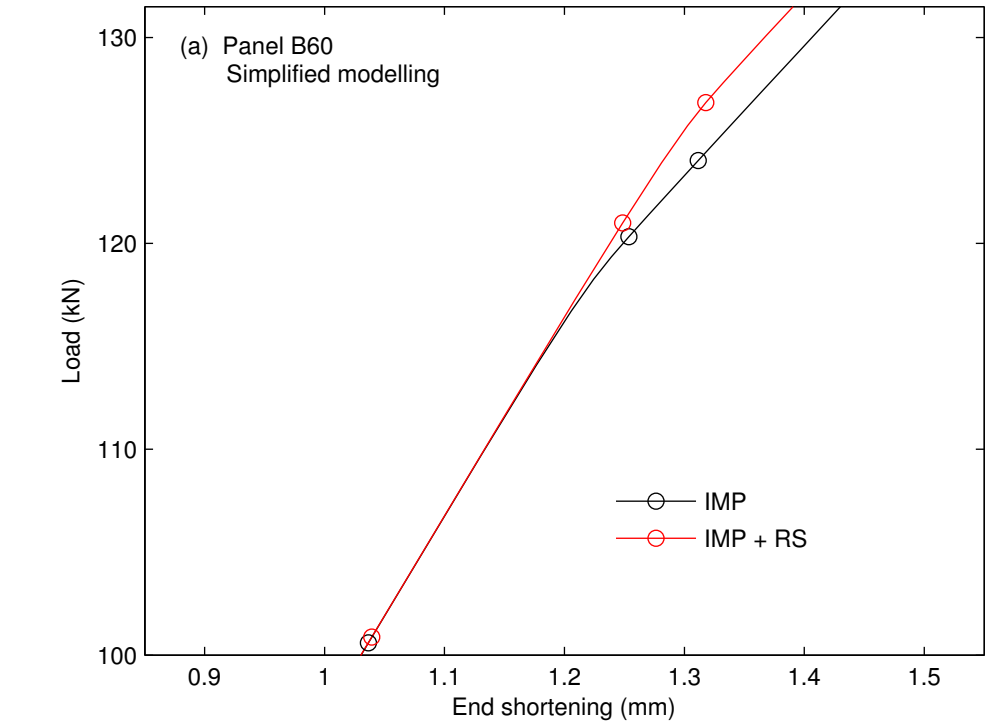

(b)

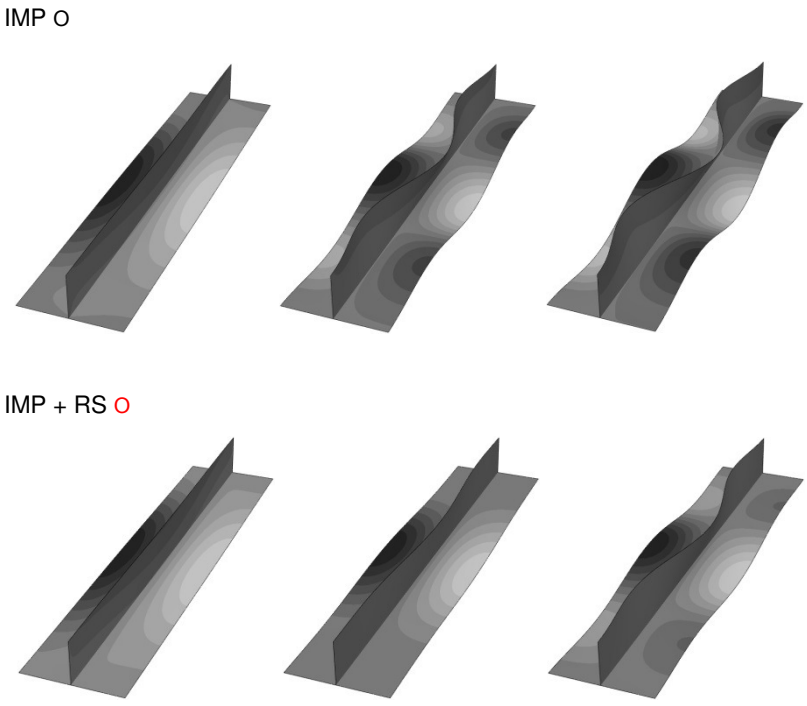

Figure 7.18: Mode-change in the panel B60, including the simplified modelling of the welding effects: (a) curve load/end shortening and (b) corresponding buckling shapes (displacements amplified 15 times along Ox and Oy).

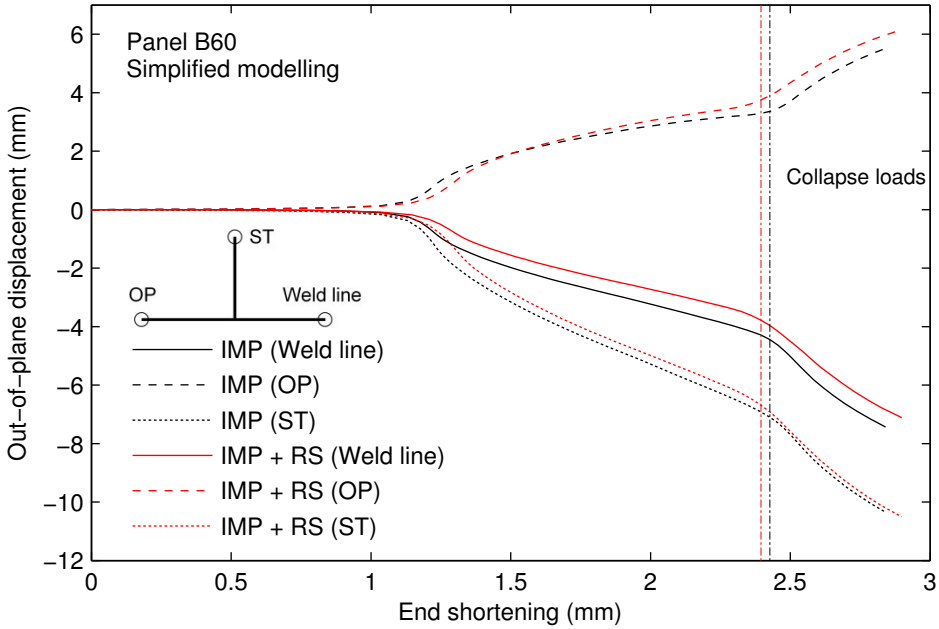

Figure 7.19: Out-of-plane displacement variation in three points located at mid-length of the panel B60, including the simplified modelling of the welding effects.

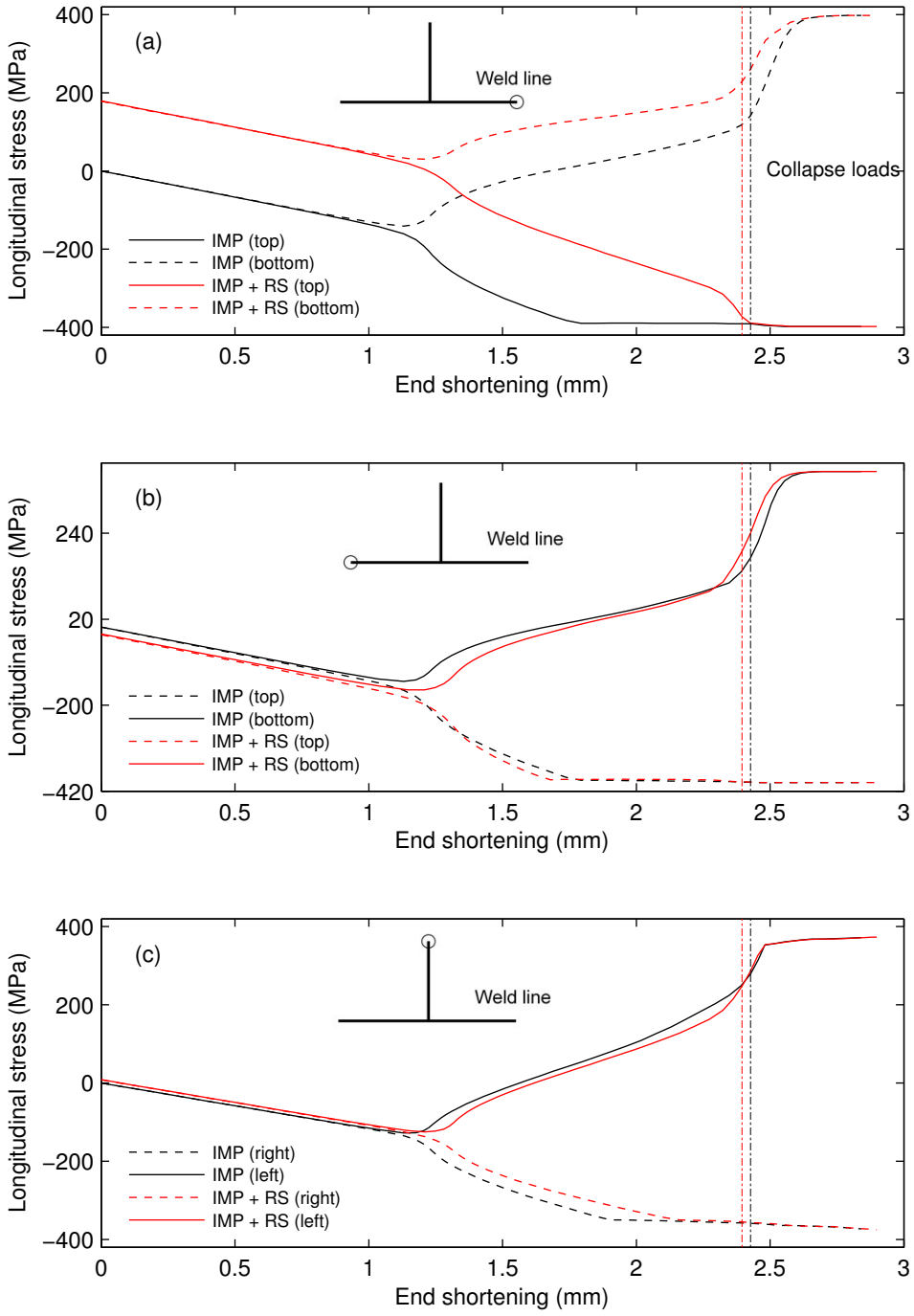

Figure 7.20: Longitudinal stress variation in three points located at mid-length of panel B60, including the simplified modelling of the welding effects: (a) in the weld line, (b) on the edge opposite to the weld line, and (c) at the top of the stiffener.

The observed effects of the softened material on the panel behaviour, without the presence of the residual stress field, is also verified when the residual stresses are considered. Nonetheless, in the presence of the residual stresses, the impact on the collapse load magnitude is lower, as can be observed in Figure 7.13 and Figure 7.14. Using panel B60 as example, with a simplified modelling of the welding effects, it is possible to verify that the difference between the models with IMP and with IMP + SOFT60 is 1.19%, while the difference between the models with IMP + RS and with IMP + SOFT60 + RS is only 0.19%.

To explain the effect of the residual stress field on the collapse load, the results obtained for panel B60 with the simplified modelling of the welding effects will be used once again, as example. Comparing the results on Figure 7.22 (a) and (c), that represent the plastic strain at the moment of the collapse, in the panels with base material properties, without and with residual stress, respectively, it is possible to observe that the existence of a zone with tensile stress (close to the weld line) reduced the plastic strain to zero close to the weld line (see Figure 7.22 (c)). Close to the edge opposite to the weld line, the plastic strain is higher in the model with residual stresses. The reason for this is that when the panel is loaded in compression the stress along the longitudinal direction decreases, as represented in Figure 7.20, until the buckling leads to a bifurcation in the stress path between the top and bottom of the metal sheet. Afterwards, in the concave zones the stress continues to decrease, while in the convex parts the longitudinal stress increases. It is important to mention that all the plastic strain at the moment of collapse happen due to compression. The initial tensile residual stress in the welded zone delays the increase of the compressive stress, as can be seen in Figure 7.20 (a), avoiding plastic deformation at the moment of collapse. On the contrary, in the opposite edge to the weld line, the existence of compressive stresses in the beginning slightly increases the compressive load in that zone, leading to an early plastic deformation and a higher magnitude at collapse. Nonetheless, in this case, the collapse load is similar in the two models (IMP and IMP + RS).

In the presence of a zone with softened material, the residual stresses have the same influence as mentioned before. Nevertheless, in this case, the presence of the residual stresses increases the collapse load (see Figure 7.13 and Figure 7.14). As mentioned before and represented in Figure 7.22 (b), the existence of the softened zone increases the plastic deformation close to the weld line. In the presence of residual stresses and softening, the

existence of the tensile stress in the welded zone strongly reduces the plastic deformation in that part. At the same time, there is not a higher plastic deformation close to the opposite edge of the line, as can be seen in Figure 7.22 (d), and the plastic deformation is similar to the one obtained with the model with geometrical imperfections only (see Figure 7.22 (a)). Therefore, the presence of the residual stresses shows two effects on panels B45 and B60: it increases the collapse load in the presence of softened material, and leads to a decrease of the impact of the softened material on the collapse load.

The increase of the collapse load in panels with a HAZ, in the presence of the residual stresses, was also shown by Murphy *et al.* [113].

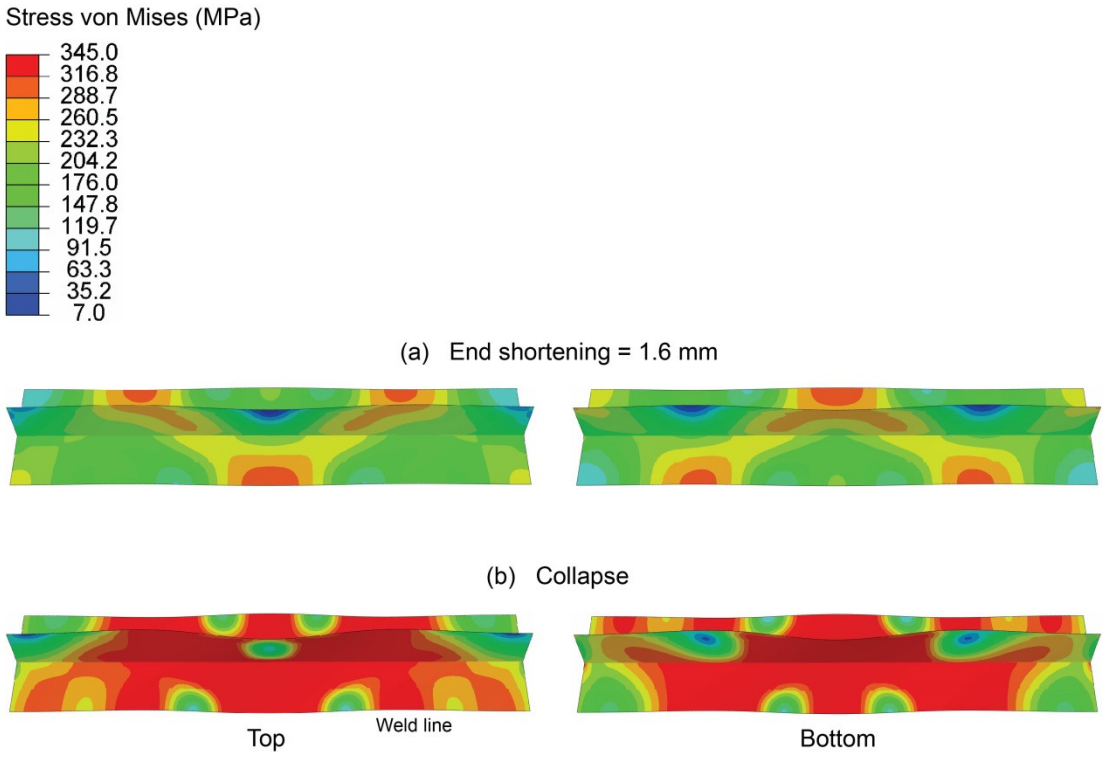

Figure 7.21: Von Mises stress distribution in panel B60 including only the geometrical imperfections (IMP) obtained using the simplified modelling of the welding effects: (a) at end shortening equal to 1.6 mm and (b) at collapse.

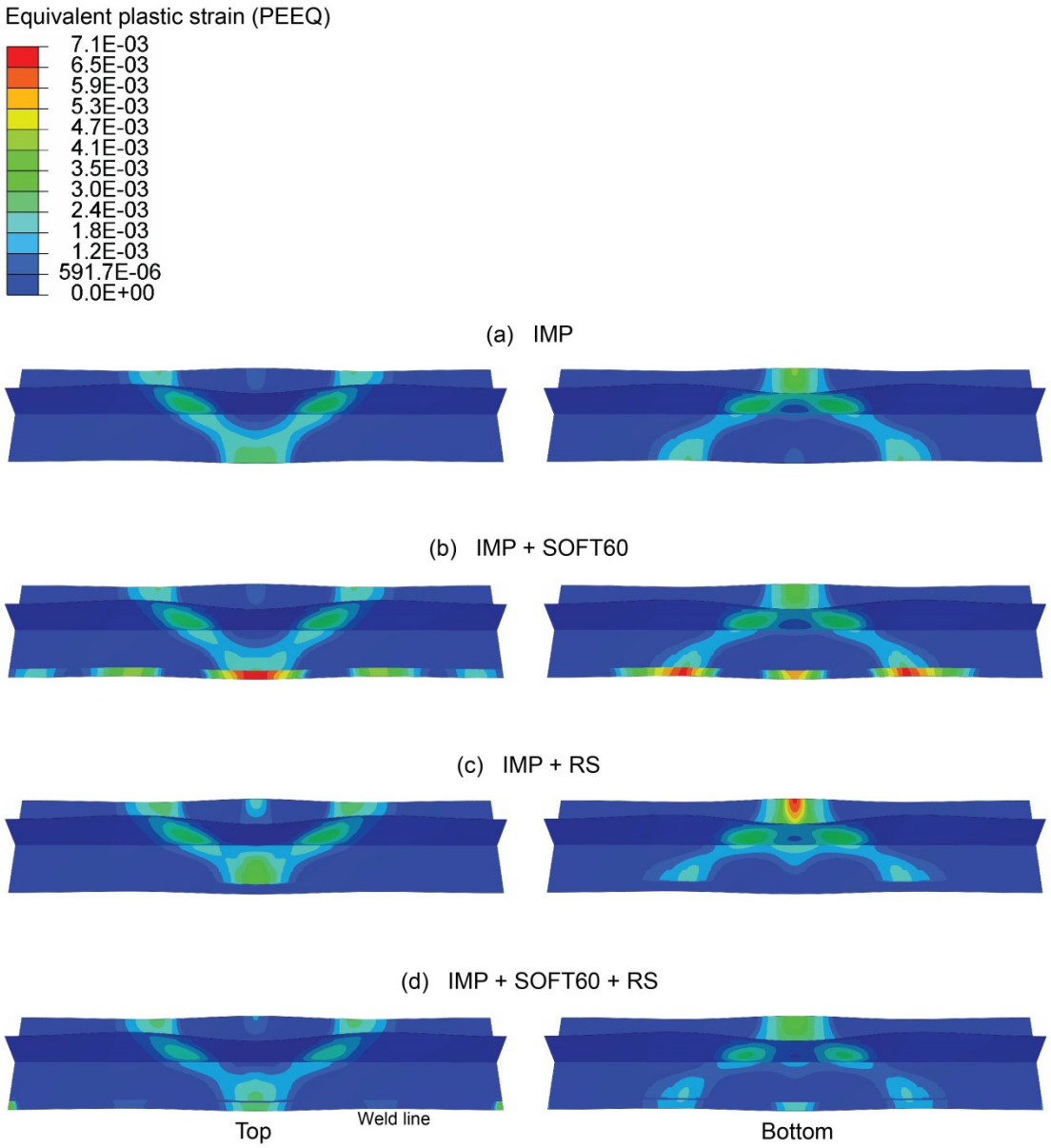

Figure 7.22 : Plastic strain in panel B60 at collapse including the simplified modelling of the welding effects with different combinations: (a) IMP, (b) IMP + SOFT60, (c) IMP + RS and (d) IMP + SOFT60 + RS.

7.2.5. Comparison of results using distinct modelling of the FSW effects

The obtained results using the two chosen methodologies to account for welding effects can now be compared (one using the effects from previously performed FSW analyses and the other using a simplified modelling approach). The initial geometrical imperfection adopted in each method is different. The one obtained in the simplified modelling (see Figure 7.8 and Figure 7.9), generated by the residual stress fields added to the model, have

a lower maximum magnitude, since the typical V-shape in the transverse direction is reduced when compared to the deformed shape from the FSW simulation (see Figure 5.14 and Figure 5.15(a)). As previously observed, this difference influences the panels' behaviour in terms of the buckling evolution and collapse mode, as happens for panels B60 and T, with obvious impact on the collapse load. Furthermore, also in the presence of the same collapse mode, as happens for panel B45, different geometrical imperfections significantly affected the collapse load. The assessment of using different residual stress and softening distributions is hampered due to the dominance of the initial imperfections effect. Nonetheless, the results in general, and especially the ones obtained with panel B45, do not show evidence of significant differences using detailed the modelling of these welding effects (from FSW simulation) instead of a simplified one.

In terms of the panel design and application, it is important to assess the influence of the welding effects in terms of residual stress and softening, comparing the IMP models with the IMP + SOFT75 + RS (since the panel with softening after ageing and residual stresses is the one that can be used in a practical application). Table 7.4 presents the collapse load variation between these two models for the different panels. The welding effects led to a slight decrease in the collapse load, in most cases, although the preponderance of the initial geometrical imperfection effects leads to different variation of the results using the two methodologies and makes it difficult to perform a valid comparison.

Table 7.4: Variation of the collapse load.

FSW effects origin	Panel	Collapse load variation (%) (comparing the model with IMP + SOFT75 +RS with model with IMP)
FSW simulation (600 mm model)	B45	-0.29
	B60	-0.82
	T	-5.19
Simplified modelling	B45	-0.25
	B60	0.00
	T	3.16

Since the initial geometrical imperfection showed such a high impact on the behaviour of the panels and also influences the impact of the other welding effects, an

additional set of analyses was performed using the deformed shapes from eigenvalue (EV) analyses to better assess the sensitivity of the panels to initial geometrical imperfections.

7.3. Panel compression using geometrical imperfections from eigenvalue analysis

A first set of analyses was performed to obtain the EV and respective deformed shapes (eigenmodes) for each panel. The deformed shapes were introduced afterwards in the final structural models with different magnitudes. Distinct material properties in the welded zone were also tested, as described in the following paragraphs.

7.3.1. Eigenvalue analysis

The EV analysis was performed using the same model (including boundary conditions) defined for the structural analyses (see Figure 7.1). For this purpose, the command *BUCKLE was used in Abaqus [26] and the subspace iteration eigensolver was invoked. The defined material properties correspond to the base material. Nonetheless, the eigenvalue analyses were performed in a linear elastic state and the plastic properties were ignored. The first three EV (EV1, EV2 and EV3) and respective buckling modes (eigenmodes) were extracted and are shown in Figure 7.23 for all the tested panels.

The eigenvalue results cannot correctly predict the collapse load in this case. However, for panels B45 and B60, EV3 gives a reasonably good prediction of the mode-change load, since the EV3 shape is similar to the one obtained in these analyses after the first mode-change.

7.3.2. Compression of the panels

The shapes associated with the EV were introduced in the models with different maximum magnitudes: 0.25, 0.5, 1, 2 and 3 mm. This range of magnitudes covers the maximum displacements magnitudes obtained in the FSW simulation and in the simplified modelling. Since the displacement field provided by Abaqus in the EV analyses is already normalised using the maximum displacement, it was simply a matter of multiplying it to the maximum magnitude intended, when introduced in the model.

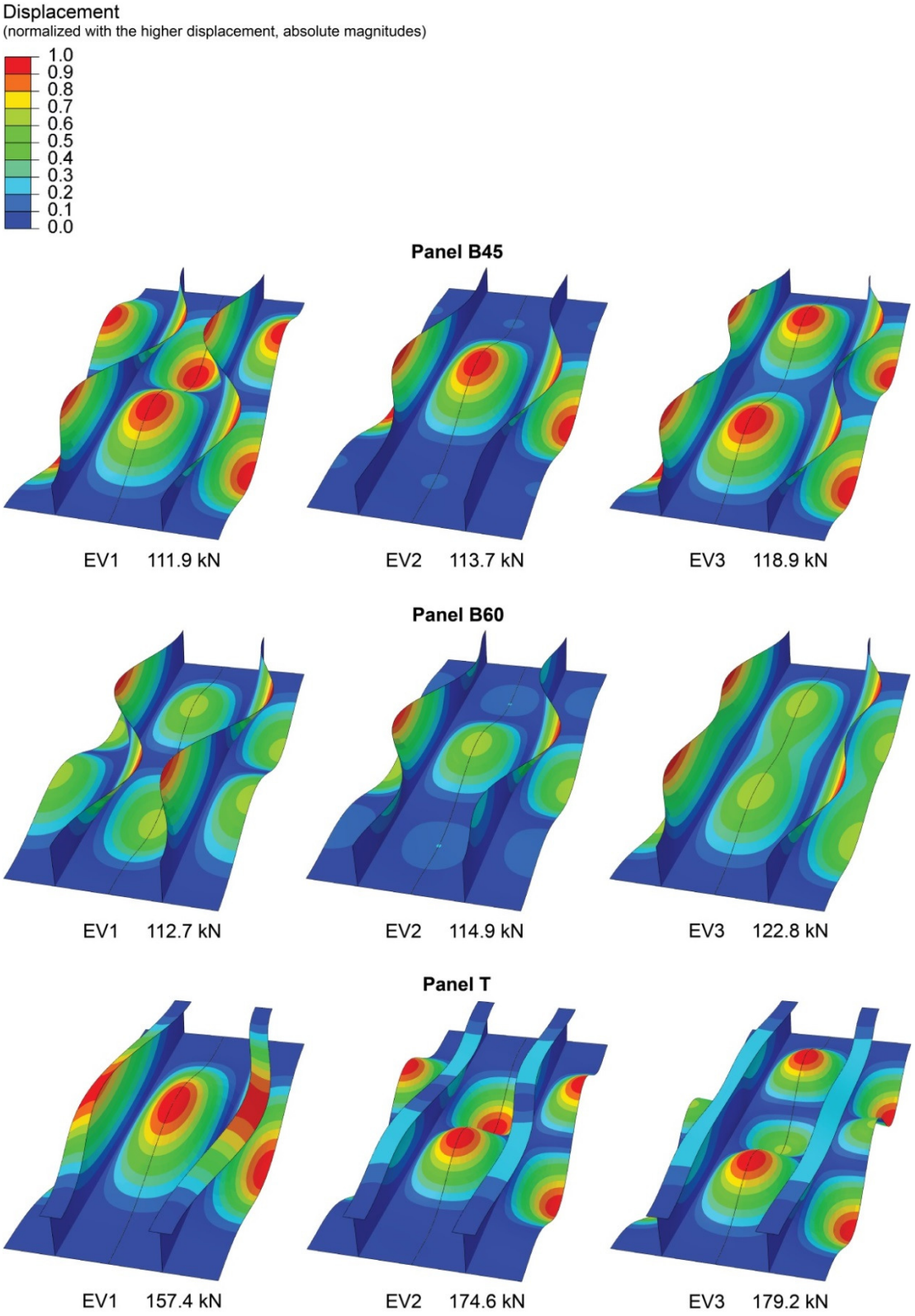

Figure 7.23: Eigenvalues and respective buckling modes (eigenmodes).

Material softening was considered in analyses (SOFT75 and SOFT60) using the simplified methodologies previously presented in section 7.1.3.2. The panels with full base material properties were also tested.

The collapse load results are compared with the ones coming from the previous analyses, in Figure 7.24. The different imperfections shapes led to a distinct variation of the collapse load with the increase of the magnitude. In some analyses, the increase in the geometrical imperfection magnitude led to a decrease in the collapse load. Nevertheless, using the EV1 and EV2 on panels B45 and B60, the collapse load increased with the increase of the imperfection magnitude, at least for some values in the tested range. This may be related to the observed small differences in the collapse shape and also to the distinct evolution of the buckling in the plate and in the stiffener, associated with distinct moment of failure of those panels' components. As an example, the shapes obtained at the moment of collapse of panel B45, using imperfection EV2, are shown in Figure 7.25. The corresponding load/end shortening curves are shown in Figure 7.26(a). The work of Paulo *et al.* [7] also shows an increase of the collapse load with the increase of the imperfection magnitude for some imperfection shapes. The remaining cases, showing a decrease in the collapse load with an increase of the imperfection magnitude, have a behaviour similar to the example presented on Figure 7.26(b) for panel B45 using the EV3 imperfection shape.

In terms of the effect of softening, Figure 7.24 shows that the results for the analyses with SOFT75 and SOFT60 have the same pattern of variation obtained without any softened material, albeit with a lower collapse load. Generally, it is possible to observe a slightly higher impact of the softened material for panels with initial imperfections that led to higher collapse loads since, in this cases, plastic strain was more intense (namely in the weld affected zone).

The variations of the collapse load, comparing the model with base material to each one with a softened zone (SOFT60 and SOFT75), is generally constant for the different imperfection magnitudes tested (considering the same imperfection shape).

It is worth noting that the collapse load results from the analyses including the welding effects is within the range obtained with the EV shapes, taking into account the magnitude of the imperfection and softening properties, as can be observed in Figure 7.24. The only exceptions are the results obtained with panel T including the effects from the FSW simulation that showed a higher collapse load due to a specific buckling evolution.

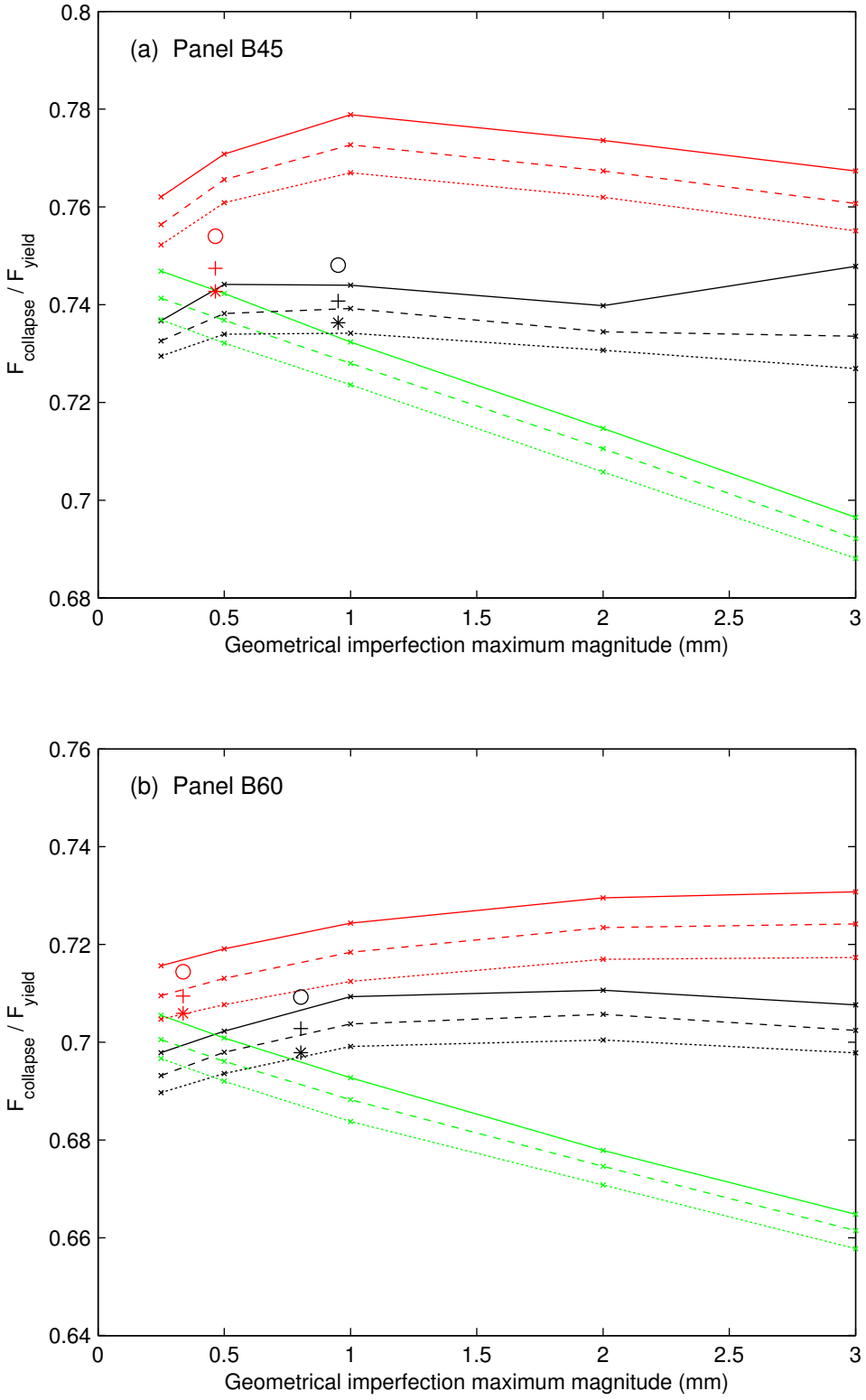

Figure 7.24: Collapse load predictions using different geometrical imperfections and material softening.

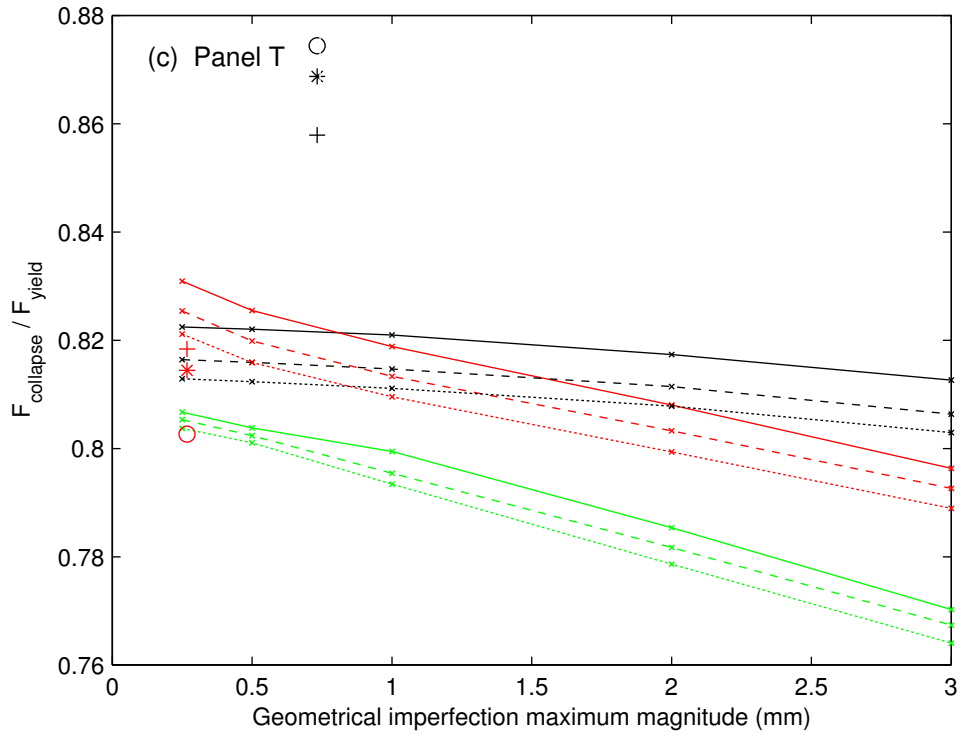

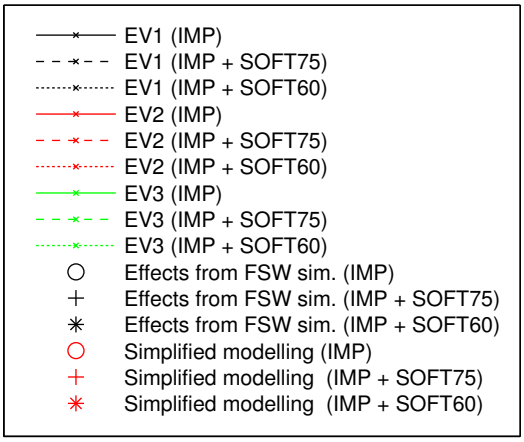

Figure 7.24 (cont.)

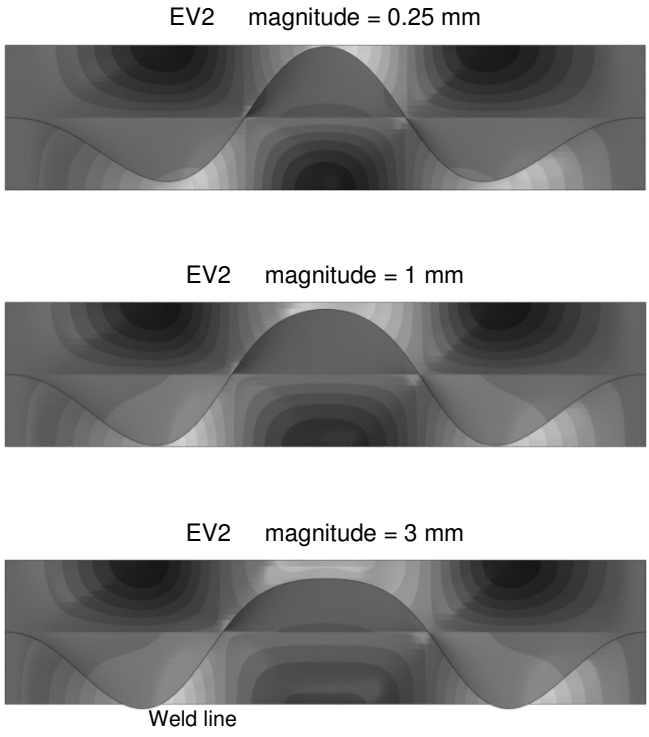

Figure 7.25: Collapse load shape obtained with panel B45 using the EV2 imperfection shape with different magnitudes.

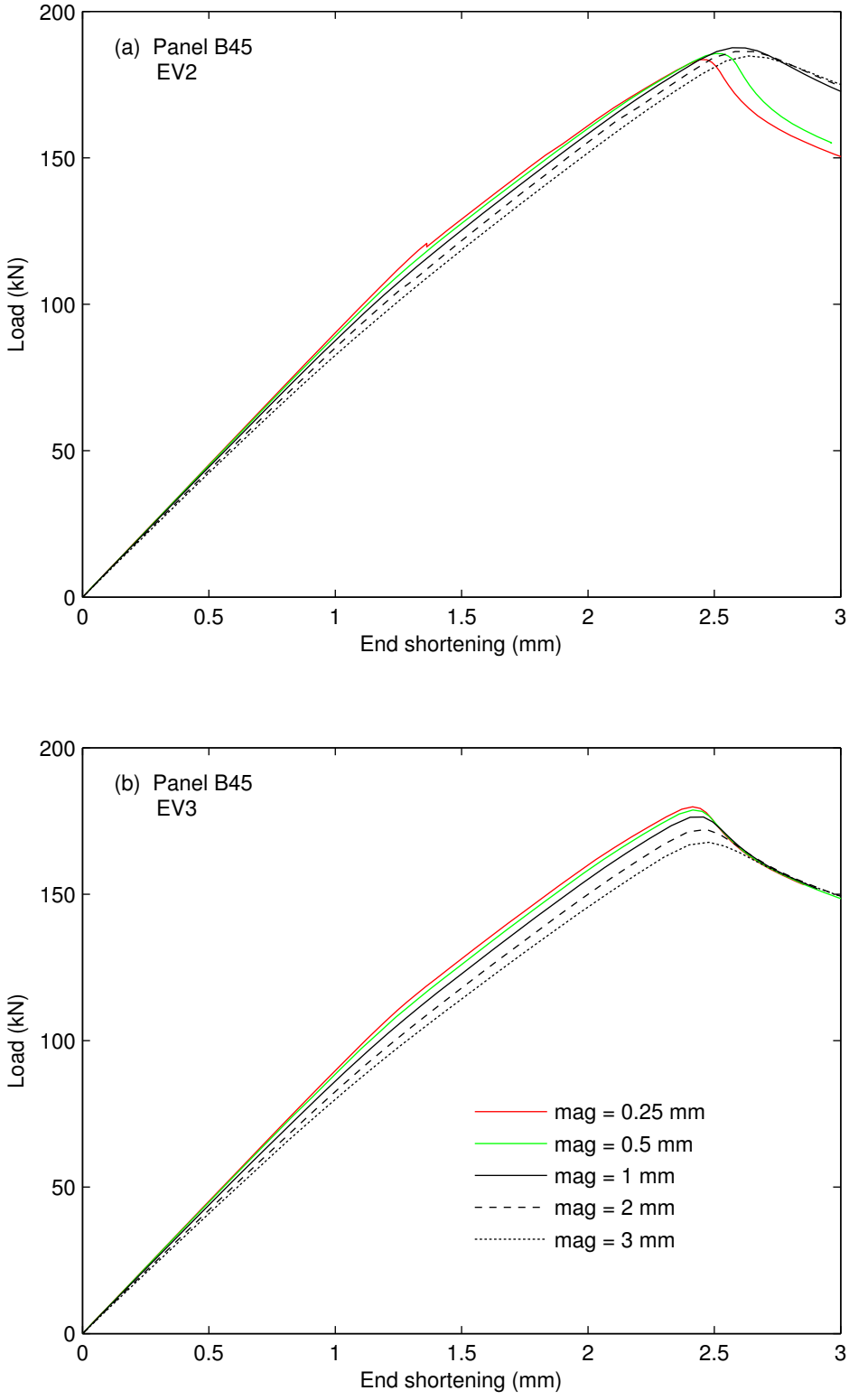

Figure 7.26: Results for panel B45 using the EV imperfections with different magnitudes: (a) EV2 and (b) EV3.

7.4. Final remarks and conclusions

The results of the compression analyses of stiffened panels allow to conclude about the impact of some modelling details on the structural behaviour prediction. Distinct distributions of the welding effects close to the transverse edges were tested using the results from the welding simulations on panels with 600 and 750 mm. In the latter, only the central part with 600 mm was compressed, avoiding the effects from the start and end of the welding process. There is no evidence that either the differences in the residual stress distribution or in softened material distribution have influence on the final results.

Regarding the use of work hardening definitions, instead of a simpler perfectly plastic relation, it led to a slight increase in the collapse load that was more significant for panels with higher collapse load/yield load ratio, since the plastic strain levels were higher.

The use of two different methodologies to model the welding effects (effects from FSW simulations and the simplified modelling) led to differences in the results mainly due to the use of different initial geometrical imperfections. The distinct modelling of the residual stress field and softened material did not show any impact on the results. Nonetheless, the detailed definition of the welding effects from the FSW simulation can be important in other studies such as, for example, fatigue analysis.

Concerning the impact of the effects associated to welding, a strong influence of the initial geometrical imperfection was observed on the panels' buckling modes and collapse loads. In panels with similar collapse mode, the existence of softened material in the welded zone led to a decrease on the collapse load. Also in the panels with the similar collapse mode, the presence of residual stress fields led to a delay in the first mode-change during loading. The results showed that in the presence of softened material in the welded zone, the existence of the residual stress field led to an increase in the collapse load. In some cases, the presence of residual stresses or softened material has shown to also affect the buckling mode.

Another interesting observation was made in the analyses using the EV buckling modes. The use of different initial imperfection shapes conducted to distinct results in terms of the collapse load. Furthermore, in most cases, an increase of the initial imperfection magnitude led to a decrease in of the collapse mode. Nonetheless, for some panels and EV shapes, the increase in the initial geometrical displacement conducted to the opposite trend, *i.e.* the increase the collapse load. The variation of the collapse load,

associated to the existence of a zone with softened material, is almost constant for the results obtained with different imperfection magnitudes (for the same imperfection shape).

Chapter 8
Conclusions and future work

8.1. Conclusions

The present work focused on the numerical simulation of two different phenomena: the FSW process and the compression of stiffened panels.

Concerning the FSW process, a numerical model was firstly developed to simulate the joining of two aluminium plates. It was validated using the temperature, longitudinal stresses and hardness distributions, obtained experimentally. The proposed model was able to predict the longitudinal residual stresses and the softening with acceptable accuracy. Concerning the distortion predictions for the FSW of simple plates, it was not possible to perform a proper validation. The out-of-plane displacements coming from the numerical analyses were much lower than expected, probably due to an overconstraining of the model related to the boundary conditions simulating the experimental clamping system and the reduced size of the plates. However, the same numerical methodology applied to a larger part led to the expected distortion. Thus, the numerical model seems to be able to predict the distortion of the plate, although requiring proper validations that should be performed based on experimental results coming from the FSW of a larger plate.

The FSW model was afterwards adapted and applied to the simulation of the welding of stiffened panels. For both models (plate and stiffened panel) sensitivity analyses were performed on several modelling parameters, seeking for good a relation between the computational time, the accuracy of the results and the simplicity of the model. It was seen that the use of fully in-plane integrated shell elements, when compared

to elements with reduced integration, as well as the option for more than 5 integration points across thickness, did not improve the accuracy of results. The use of a mesh composed by square elements with 2 mm (in the welded zone) had led to results with good accuracy when compared with more refined meshes, with gains in terms of computational time. The results showed variations related to the use of different boundary conditions associated with the clamping system. Those variations were much higher in the plate model. The modelling of the heat distribution coming from the tool proved to have an insignificant impact on the final results, in terms of residual stress fields and distribution of softening. Nevertheless, a small influence on the temperature distribution was observed, related to this modelling variable. The results allowed concluding that the heat distribution should be defined taking into consideration the refinement of the mesh. The magnitude of the inputted power and the distribution pattern should be as constant as possible in the several increments during the heat source (tool) displacement along the weld line.

In terms of final results, the maximum longitudinal stress obtained with the stiffened panel model was seen to be higher than the one obtained in the plate. Regarding the softening, the zone with fully softened material properties was shown to be narrower in the stiffened panel than in the regular plates, due to the lower temperature levels achieved in the panels.

The structural analyses concerning the longitudinal compression of the stiffened panels had two main objectives: on one hand, to understand the impact of using distinct methodologies to model the welding effects, and, on the other hand, to infer about the influence of each one of the FSW effects on the panel structural behaviour.

Distinct distributions of the welding effects close to the transverse edges were tested. One of those included the effects of the start and end of the welding process while the other included just the effects obtained in a steady state stage of the welding. There were no evidences that either the differences in the residual stress distribution or in the softened material distribution have influence in the final results.

The use of work hardening definitions instead of a perfectly plastic relation has led to a slight increase in the collapse load, which was seen to be more significant in the panels with higher collapse load/yield load ratio, since the plastic strain was higher.

Two different methodologies were used to model the welding effects: firstly, applying the welding effects as coming from previous FSW simulations (more realistic)

and, secondly, applying the welding effects using a simplified modelling. Those methodologies have conducted to some differences in the results, mainly due to use of distinct initial geometrical imperfections related to each one of the methods. The distinct modelling of the residual stress field and softened material distribution did not show any relevant influence on the results.

Concerning the impact of the welding effects on the panel behaviour, it was verified a high influence of the initial geometrical imperfection on the panels' buckling mode as well as on the collapse load. In panels with the same collapse mode, the existence of softened materials in the welded zone led to a decrease in the collapse load. Also in the panels with the same collapse mode, the presence of a residual stress field conducted to a delay in the first mode-change during loading. Furthermore, the results showed that in the presence of softened material in the welded zone, the existence of the residual stress field led to an increase in the collapse load. In some cases, the presence of residual stresses or softened material has shown to affect the buckling mode evolution.

The study about the influence of the initial distortion on the panel behaviour was extended, and tests were performed using the imperfection shapes coming from EV analyses, which were applied with different magnitudes. For most of the imperfection shapes, the increase of the initial imperfection magnitude led to a decrease in the collapse load. Nonetheless, for some panels and EV shapes, the increase in the initial geometrical displacement conducted to the opposite trend, *i.e.*, the increase of the collapse load. The variation of the collapse load, associated with the existence of a zone with softened material, revealed to be almost constant for the results obtained with different imperfection magnitudes (for the same imperfection shape).

8.2. Future work

Considering the performed work, future guidelines of research can include the improvement of the numerical models and the implementation of similar numerical simulations to other study cases.

In terms of the FSW modelling and simulation, it is fundamental to validate the model in terms of distortion results. For this purpose, the experiments are recommended to be performed on a plate larger than the one used in the present work, to reduce the sensitivity of the numerical model to the boundary conditions associated with clamping

system. The experimental measurement of the distortion should be performed before and after welding, in order to clearly verify the distortion induced by the FSW. The experimental measurements concerning the residual stresses and hardness distributions should be repeated, since they can be different for a specimen with distinct size.

In a more long-term perspective, the FSW model could also be adapted and validated for the welding of other aluminium alloys and other welding conditions, seeking for more general application. Also, it could be interesting to simulate a more complex welding process, such as involving several consecutive welds to build large parts of a structure. In addition, the author believe that the present study can be used as the starting point for a complete optimization framework of the welding sequence (involving some process parameters), in order to reduce distortion, size of the softened zone and residual stresses in the final welded parts.

Concerning the structural analyses, it could be interesting to perform similar studies in panels with the geometry optimized for the 2024-T3 aluminium alloy. Finally, since many applications involved the use of curved stiffened panels, the study presented in this work could be extended to cover this kind of structures.

References

[1] Epicos site, <http://www.epicos.com/>, (June, 2015).

[2] Technology page on Englishrussia site, <http://englishrussia.com/>, (June, 2015).

[3] A. Aalberg, M. Langseth, P.K. Larsen, Stiffened aluminium panels subjected to axial compression, Thin-Walled Structures, 39 (2001) 861-885.

[4] B.G. Falzon, M. Cerini, An automated hybrid procedure for capturing mode-jumping in postbuckling composite stiffened structures, Composite Structures, 73 (2006) 186-195.

[5] B.G. Falzon, D. Hitchings, Capturing mode-switching in postbuckling composite panels using a modified explicit procedure, Composite Structures, 60 (2003) 447-453.

[6] J.K. Paik, S. Veen, A. Duran, M. Collette, Ultimate compressive strength design methods of aluminum welded stiffened panel structures for aerospace, marine and land-based applications: A benchmark study, Thin-Walled Structures, 43 (2005) 1550-1566.

[7] R.M.F. Paulo, F. Teixeira-Dias, R.A.F. Valente, Numerical simulation of aluminium stiffened panels subjected to axial compression: Sensitivity analyses to initial geometrical imperfections and material properties, Thin-Walled Structures, 62 (2013) 65-74.

[8] L. Ronning, A. Aalberg, P.K. Larsen, An experimental study of ultimate compressive strenght of transversely stiffened aluminium panels, Thin-Walled Structures 48 (2010) 357-372.

[9] J.H. Hattel, K.L. Nielsen, C.C. Tutum, The Effect of Post-welding Conditions in Friction Stir Welds: From Weld Simulation to Ductile Failure, European Journal of Mechanics / A Solids, 33 (2011) 67-74.

[10] B.T. Gibson, D.H. Lammlein, T.J. Prater, W.R. Longhurst, C.D. Cox, M.C. Ballun, K.J. Dharmaraj, G.E. Cook, A.M. Strauss, Friction stir welding: Process, automation, and control, Journal of Manufacturing Processes, 16 (2014) 56-73.

[11] R.S. Mishra, Z.Y. Ma, Friction stir welding and processing, Materials Science and Engineering R: Reports, 50 (2005) 1-78P.

[12] P.L. Threadgill, A.J. Leonard, H.R. Shercliff, P.J. Withers, Friction stir welding of aluminium alloys, International Materials Reviews, 54 (2009) 49-93.

[13] E.A. Starke, J.T. Staley, Application of modern aluminium alloys to aircraft, Prog. Aerospace Sci., 32 (1996) 131-172.

[14] G. Gerard, H. Becker, Handbook of structural stability, Part III - Buckling of curved plates and shells, NACA, (1957).

[15] G. Gerard, H. Becker, Handbook of structural stability, Part I - Buckling of flat plates, NACA, (1957).

[16] M. Schildcrout, M. Stein, Critical axial-compressive stress of a curved rectangular panel with a central longitudinal stiffener, Technical note nº1879, NACA, (1949).

[17] M.C. Niu, Airflrame Structural Design, Conmilit Press Ltd, Hong Kong, 1st ed., (1988).

[18] M.C. Niu, Airflame Stress Analyses and Sizing, Conmilit Press, Hong Kong. 2nd ed., (1999).

[19] C.M. Wang, C.Y. Wang, J.N. Reddy, Exact Solutions for Buckling of Structural Members, CRC series in computational mechanic sand applied analysis, CRC Press, (2004).

[20] M. Collette, Strenght and Reliability of Aluminium Stiffened Panels, PhD Thesis, University of Newcastle, 2005.

[21] DNV GL site, <http://www.dnvgl.com> (June, 2015).

[22] J.K. Paik, S.J. Kim, D.H. Kim, P.A. Frieze, M. Abbattista, M. Vallascas, O.F. Hughes, Benchmark study on use of ALPS/ULSAP method to determine plate and stiffened panel ultimate strength, Advances in Marine Structures, (2011) 169-186.

[23] Hypersizer software site, <http://hypersizer.com/>, (June, 2013).

[24] Eurocode 9: Design of Aluminium Structures, European Committee for Standardization (CEN), Brussels, 1998.

[25] Aluminum Design Manual: Specification for Aluminum Structures - Load and Resistance Factor Design Specification, 7th ed., Aluminium Association, Washington DC, 2000.

[26] ABAQUS, Abaqus Documentation (v.6.14). Simulia Dassault Systémes, (2014).

[27] W.M. Thomas, E.D. Nicholas, J.C. Needham, M.G. Church, P. Templesmith, C.J. Dawes, International patent application no. PCT/GB92/02203 and GB patent application no. 9125978-9125979, (1991).

[28] M.B. Prime, T. Gnäupel-Herold, J.A. Baumann, R.J. Lederich, D.M. Bowden, R.J. Sebring, Residual stress measurements in a thick, dissimilar aluminum alloy friction stir weld, Acta Materialia, 54 (2006) 4013–4021.

[29] Gizmag web site, <http://www.gizmag.com/>, (June 2013).

[30] Honda web site, <http://world.honda.com/>, (June, 2013).

[31] U. Dressler, G. Biallas, U. Alfaro Mercado, Friction stir welding of titanium alloy TiAl6V4 to aluminium alloy AA2024-T3, Materials Science and Engineering: A, 526 (2009) 113-117.

[32] MTS Systems Corporation, <http://www.mts.com/>, (April, 2013).

[33] American Welding SocietyWelding Handbook, 9th Edition, Volume 3, Welding Process Part 2, ASW, 2007.

[34] D.M. Rodrigues, A. Loureiro, C. Leitao, R.M. Leal, B.M. Chaparro, P. Vilaça, Influence of friction stir welding parameters on the microstructural and mechanical properties of AA 6016-T4 thin welds, Materials and Design, 30 (2009) 1913-1921.

[35] R.M. Leal, C. Leitão, A. Loureiro, D.M. Rodrigues, P. Vilaça, Material flow in heterogeneous friction stir welding of thin aluminium sheets: Effect of shoulder geometry, Materials Science and Engineering A, 498 (2008) 384-391.

[36] The Welding Institute site, <http://www.twi-global.com/>, (April, 2013).

[37] T. Khaled, An outsider looks at friction stir welding, Report ANM-112N-05-06, Federal Aviation Administration, CA, USA, (2005).

[38] J.A. Schneider, A.C. Nunes Jr, Characterization of plastic flow and resulting microtextures in a friction stir weld, Metallurgical and Materials Transactions B: Process Metallurgy and Materials Processing Science, 35 (2004) 777-783.

[39] M. Mahoney, R.S. Mishra, T. Nelson, J. Flintoff, R. Islamgaliev, Y. Hovansky, Friction Stir Welding and Processing, (2001) 183-194.

[40] L. Fratini, G. Buffa, CDRX modelling in friction stir welding of aluminium alloys, International Journal of Machine Tools and Manufacture, 45 (2005) 1188-1194.

[41] Y.S. Sato, H. Kokawa, M. Enomoto, S. Jogan, Microstructural evolution of 6063 aluminum during friction-stir welding, Metallurgical and Materials Transactions A: Physical Metallurgy and Materials Science, 30 (1999) 2429-2437.

[42] R.V. Preston, H.R. Shercliff, P.J. Withers, S. Smith, Physically-based constitutive modelling of residual stress development in welding of aluminium alloy 2024, Acta Materialia, 52 (2004) 4973-4983.

[43] A.J. Leonard, Proceedings of the 2nd International Symposium on 'Friction Stir Welding', (2000).

[44] C.B. Fuller, M.W. Mahoney, M. Calabrese, L. Micona, Evolution of microstructure and mechanical properties in naturally aged 7050 and 7075 Al friction stir welds, Materials Science and Engineering: A, 527 (2010) 2233-2240.

[45] A. Pastor, H.G. Svoboda, Time-evolution of Heat Affected Zone (HAZ) of Friction Stir Welds of AA7075-T651, Journal of Materials Physics and Chemistry, 1 (2013) 58-64.

[46] C. Genevois, A. Deschamps, P. Vacher, Comparative study on local and global mechanical properties of 2024-T351, 2024-T6 and 5251-O friction stir welds, Materials Science and Engineering A, 415 (2006) 162-170.

[47] P. Carlone, G.S. Palazzo, Mechanical Characterization of AA2024-T3 FSWed Butt Joints, Advanced Materials Research, 753-755 (2013) 431-434.

[48] A. Bastier, M.H. Maitournam, F. Roger, K. Dang Van, Modelling of the residual state of friction stir welded plates, Journal of Materials Processing Technology, 200 (2008) 25-37.

[49] D.G. Richards, P.B. Prangnell, S.W. Williams, P.J. Withers, Global mechanical tensioning for the management of residual stresses in welds, Materials Science and Engineering A, 489 (2008) 351-362.

[50] P. Carlone, G.S. Palazzo, Longitudinal residual stress analysis in AA2024-T3 friction stir welding, The Open Mechanical Engineering Journal, 7 (2013) 18-26.

[51] V. Richter-Trummer, E. Suzano, M. Beltrão, A. Roos, J.F. dos Santos, P.M.S.T. de Castro, Influence of the FSW clamping force on the final distortion and residual stress field, Materials Science and Engineering A, 538 (2012) 81-88.

[52] A. Steuwer, M.J. Peel, P.J. Withers, Dissimilar friction stir welds in AA5083-AA6082: The effect of process parameters on residual stress, Materials Science and Engineering A, 441 (2006) 187-196.

[53] Z. Feng, X.L. Wang, S.A. David, P.S. Sklad, Modelling of residual stresses and property distributions in friction stir welds of aluminium alloy 6061-T6, Science and Technology of Welding and Joining, 12 (2007) 348-356.

[54] C. Liu, X. Yi, Residual stress measurement on AA6061-T6 aluminum alloy friction stir butt welds using contour method, Materials and Design, 46 (2013) 366-371.

[55] P.J. Withers, M. Turski, L. Edwards, P.J. Bouchard, D.J. Buttle, Recent advances in residual stress measurement, International Journal of Pressure Vessels and Piping, 85 (2008) 118-127.

[56] N.S. Rossini, M. Dassisti, K.Y. Benyounis, A.G. Olabi, Methods of measuring residual stresses in components, Materials and Design, 35 (2012) 572-588.

[57] A. Oosterkamp, L.D. Oosterkamp, A. Nordeide, 'Kissing bond' phenomena in solid-state welds of aluminum alloys, Welding Journal (Miami, Fla), 83 (2004) 225-231.

[58] H. Bisadi, A. Tavakoli, M. Tour Sangsaraki, K. Tour Sangsaraki, The influences of rotational and welding speeds on microstructures and mechanical properties of friction stir welded Al5083 and commercially pure copper sheets lap joints, Materials and Design, 43 (2013) 80-88.

[59] J. Adamowski, C. Gambaro, E. Lertora, M. Ponte, M. Szkodo, Analysis of FSW welds made of aluminium alloy AW6082-T6, Archives of Materials Science and Engineering, 28 (2007) 453-460.

[60] D. Yan, A. Wu, J. Silvanus, Q. Shi, Predicting residual distortion of aluminium alloy stiffened sheet after friction stir welding by numerical simulation, Materials and Design, 32 (2011) 2284-2291.

[61] Q.Y. Shi, J. Silvanus, Y. Liu, D.Y. Yan, H.K. Li, Experimental study on distortion of Al-6013 plate after friction stir welding, Science and Technology of Welding and Joining, 13 (2008) 472-478.

[62] D. Quinn, A. Murphy, W. McEwan, F. Lemaitre, Stiffened panel stability behaviour and performance gains with plate prismatic sub-stiffening, Thin-Walled Structures, 47 (2009) 1457-1468.

[63] P. Carlone, G.S. Palazzo, Influence of process parameters on microstructure and mechanical properties in AA2024-T3 friction stir welding, Metallogaphy Microstrucure and Analysis, 2 (2013) 213-222.

[64] M.B. Prime, Cross-sectional mapping of residual stresses by measuring the surface contour after a cut, Journal of Engineering Materials and Technology, 123 (2001) 162–168.

[65] V. Richter-Trummer, P.M.G.P. Moreira, J. Ribeiro, P.M.S.T. de Castro, The contour method for residual stress determination applied to an AA6082-T6 friction stir butt weld, Materials Science Forum, 681 (2011) 177-181.

[66] H.F. Bueckner, The propagation of cracks and the energy of elastic deformations, Transaction of the ASME, 80 (1958) 1225-1230.

[67] N. Murugan, R. Narayanan, Finite element simulation of residual stresses and their measurement by contour method, Materials and Design, 30 (2009) 2067-2071.

[68] ANSYS, Documentation for ANSYS, Release 11.0, (2007).

[69] M.B. Prime, R.J. Sebring, J.M. Edwards, D.J. Hughes, P.J. Webster, Laser surface-contouring and spline data-smoothing for residual stress measurement, Experimental Mechanics, 44 (2004) 176-184.

[70] M.R. Sonne, C.C. Tutum, J.H. Hattel, A. Simar, B. de Meester, The effect of hardening laws and thermal softening on modeling residual stresses in FSW of aluminum alloy 2024-T3, Journal of Materials Processing Technology, 213 (2013) 477-486.

[71] Aerospace Specification Metals Inc., <asm.matweb.com> (March, 2012).

[72] O.R. Myhr, Ø. Grong, Process modelling applied to 6082-T6 aluminium weldments - I, Reaction kinetics, Acta Metallurgica et Materialia, 39 (1991) 2693-2702.

[73] R.M.F. Paulo, P. Carlone, R. Valente, F. Teixeira-Dias, G.S. Palazzo, Buckling analysis of aluminium alloy structures accounting for friction stir welding effect, Proceedings of the Ninth International Conference on Engineering Computational Technology, (2014).

[74] M.R. Sonne, P. Carlone, G.S. Palazzo, J.H. Hattel, Numerical modeling of AA2024-T3 friction stir welding process for residual stress evaluation, including softening effects, Key Engineering Materials, 611-612 (2014) 1675-1682.

[75] D.G. Richards, P.B. Prangnell, P.J. Withers, S.W. Williams, T. Nagy, S. Morgan, Efficacy of active cooling for controlling residual stresses in friction stir welds, Science and Technology of Welding and Joining, 15 (2010) 156-165.

[76] G. Heimerl, J. Inge, Tensile properties of 7075-T6 and 2024-T3 aluminium-alloy sheet heated at uniform temperature rates under constante load, Technical note nº3462, NACA, (1955).

[77] R.W. McCune, A. Murphy, M. Price, J. Butterfield, The influence of friction stir welding idealization on residual stress and distorsion predictions for future airflame assembly simulations, Journal of Manufacturing Science and Enginnering, 134 (2012).

[78] M.Z.H. Khandkar, J.A. Khan, A.P. Reynolds, M.A. Sutton, Predicting residual thermal stresses in friction stir welded metals, Journal of Materials Processing Technology, 174 (2006) 195-203.

[79] H. Schmidt, J. Hattel, A local model for the thermomechanical conditions in friction stir welding, Modelling and Simulation in Materials Science and Engineering, 13 (2005) 77-93.

[80] H. Schmidt, J. Hattel, J. Wert, An analytical model for the heat generation in friction stir welding, Modelling and Simulation in Materials Science and Engineering, 12 (2004) 143-157.

[81] J.W. Yoon, G.H. Bray, R.A.F. Valente, T.E.R. Childs, Buckling analysis for an integrally stiffened panel structure with a friction stir weld, Thin-Walled Structures, 47 (2009) 1608-1622.

[82] J.F. Caseiro, R.A.F. Valente, A. Andrade-Campos, J.W. Yoon, Elasto-plastic buckling of integrally stiffened panels (ISP): An optimization approach for the design of cross-section profiles, Thin-Walled Structures, 49 (2011) 864-873.

[83] C. Lynch, A. Murphy, M. Price, A. Gibson, The computational post buckling analyses of fuselage stiffened panels loaded in compression, Thin-Walled Structures, 42 (2004) 1445-1464.

[84] A. Murphy, M. Price, C. Lynch, A. Gibson, The computational post-buckling analysis of fuselage stiffened panels loaded in shear, Thin-Walled Structures, 43 (2005) 1455-1474.

[85] R.M.F. Paulo, Numerical simulation of the behaviour of reinforced structures, MSc Thesis (in Portuguese), University of Aveiro, Portugal, 2011.

[86] Y. Zha, T. Moan, Ultimate Strength of Stiffened Aluminum Panels with Predominantly Torsional Failure Modes, Thin-Walled Structures, 39 (2001) 631-648.

[87] M.R. Khedmati, A. Bayatfar, P. Rigo, Post-buckling behaviour and strenght of multi-stiffened aluminium panels under combined axial compression and lateral pressure, Thin-Walled Structures, 23 (2010) 39-66.

[88] M.R. Khedmati, M.R. Zareei, P. Rigo, Sensitivity analyses on the elastic buckling and ultimate streght of continuous stiffened aluminium plates under combined in-plate compression and lateral pressure, Thin-Walled Structures, 47 (2009) 1232-1245.

[89] J.K. Paik, J.K. Seo, Nonlinear finite element method models for ultimate strength analysis of steel stiffened-plate structures under combined biaxial compression and lateral pressure actions - Part II: Stiffened panels, Thin-Walled Structures, 47 (2009) 998-1007.

[90] P. Rigo, R. Sarghiuta, S. Estefen, E. Lehmann, S.C. Otelea, I. Pasqualino, B.C. Simonsen, Z. Wan, T. Yao, Sensitivity analysis on ultimate strength of aluminium stiffened panels, Marine Structures, 16 (2003) 437-468.

[91] J.F. Caseiro, R.A.F. Valente, A. Andrade-Campos, J.W. Yoon, On the elasto-plastic buckling of Integrally Stiffened Panels (ISP) joined by Friction Stir Welding (FSW): Numerical simulation and optimization algorithms, International Journal of Mechanical Sciences, 76 (2013) 49-59.

[92] M.R. Khedmati, K. Ghavami, A numerical assessment of the buckling/ultimate strength characteristics of stiffened aluminium plates with fixed/floating transverse frames, Thin-Walled structures, 47 (2009) 1373-1386.

[93] M.R. Khedmati, M. Pedram, A numerical investigation into the effects of slamming impulsive loads on the elastic–plastic response of imperfect stiffened aluminium plates, Thin-Walled Structures, 76 (2014) 118-144.

[94] J. Campbell, L. Hetey, R. Vignjevic, Non-linear idealisation error analysis of a metallic stiffened panel loaded in compression, Thin-Walled Structures, 54 (2012) 44-53.

[95] W. Xu, A.M. Waas, A Novel Shell Element for Quasi-Static and Natural Frequency Analysis of Textile Composite Structures, Journal of Applied Mechanics, 81 (2014).

[96] A. Murphy, W. McCune, D. Quinn, M. Price, The characterisation of friction stir welding process effects on stiffened panel buckling performance, Thin-Walled Structures, 45 (2007) 339-351.

[97] A. Murphy, M. Price, A. Gibson, C.G. Armstrong, Efficient non-linear idealisations of aircraft fuselage panels in compression, Finite Elements in Analysis and Design, 40 (2004) 1977-1993.

[98] B.G. Falzon, A. Faggiani, The use of a genetic algorithm to improve the postbuckling strength of stiffened composite panels susceptible to secondary instabilities, Composite Structures, 94 (2012) 883-895.

[99] E. Riks, An incremental approach to the solution of snapping and buckling problems, International Journal of Solids and Structures, 15 (1979) 529-551.

[100] M.A. Crisfield, A fast incremental/iterative solution procedure that handles "snap-through", Computers and Structures, 13 (1981) 55-62.

[101] E.A. de Souza Neto, Y.T. Feng, On the determination of the path direction for arc-length methods in the presence of bifurcations and 'snap-backs', Computer Methods in Applied Mechanics and Engineering, 179 (1999) 81-89.

[102] H.B. Hellweg, M.A. Crisfield, A new arc-length method for handling sharp snap-backs, Computers and Structures, 66 (1998) 705-709.

[103] Solidworks help site, <http://help.solidworks.com/>, (July, 2014).

[104] R. Degenhard, H. Klein, H. Temmen, R. Zimmermann, Buckling and postbuckling analysis of shells under quasistatic and dynamic loads, DLR Report, (2002).

[105] M.R. Khedmati, M.R. Zareei, P. Rigo, Empirical formulations for estimation of ultimate strength of continuous stiffened aluminium plates under combined in-plane compression and lateral pressure, Thin-Walled Structures, 48 (2010) 274-289.

[106] C.S. Smith, P.C. Davidson, J.C. Champman, P.J. Dowling, Strenght and stiffness of ship's plating under in-plane compression and tension, Trans RINA, (1987) 277-296.

[107] B. Varguese, Buckling/plastic collapse strenght of plates and stiffened plates under combined loads, PhD Thesis, Hiroshima University, Japan,, 1998.

[108] J.K. Paik, A.K. Thayamballi, J.Y. Ryu, J.H. Jang, J.K. Seo, S.W. Park, S.K. Seo, C. Renaud, H.P. Cojeen, N.I. Kim, The statistics of weld induced inicial imperfections in aluminium stiffened plate structures for marine applications, International Journal of Maritime Engineering, 148 (2006) 19-63.

[109] S. Benson, J. Downes, R.S. Dow, Load shortening characteristics of marine grade aluminium alloy plates in longitudinal compression, Thin-Walled Structures, 70 (2013) 19-32.

[110] S. Zhang, I. Khan, Buckling and ultimate capability of plates and stiffened panels in axial compression, Marine Structures, 22 (2009) 791-808.

[111] R. Wilson, A. Murphy, M. Price, C. Glazebrook, A preliminary structural design procedure for laser beam welded airframe stiffened panels, Thin-Walled Structures, 55 (2012) 37-50.

[112] D. Quinn, A. Murphy, W. McEwan, F. Lemaitre, Non-prismatic sub-stiffening for stiffened panel plates - Stability behaviour and performance gains, Thin-Walled Structures, 48 (2010) 401-413.

[113] A. Murphy, T. Ekmekyapar, D. Quinn, M. Özakça, G. Moore, J. Niblock, The influence of assembly friction stir weld location on wing panel static strength, Thin-Walled Structures, 76 (2014) 56-64.

[114] A. Murphy, M. Price, R. Curran, Integration of strength and process modeling of friction-stir-welded fuselage panels, Journal of Aerospace Computing, Information and Communication, 3 (2006) 159-176.

[115] M. Özakça, A. Murphy, S. Van der Veen, Buckling and post-buckling of sub-stiffened or locally tailored aluminium panels, in: ICAS-Secretariat - 25th Congress of the International Council of the Aeronautical Sciences 2006, 2006, pp. 2367-2382.

[116] J.K. Paik, A. Duran, Ultimate Strength of Aluminum Plates and Stiffened Panels for Marine Applications, Marine Technology, 41(3) (2004) 108-121.

[117] N.D. Alexopoulos, P. Papanikos, Experimental and theoretical studies of corrosion-induced mechanical properties degradation of aircraft 2024 aluminum alloy, Materials Science and Engineering A, 498 (2008) 248-257.